Harnessing time-frequency qudits using integrated nonlinear processes

Der Naturwissenschaftlichen Fakultät
der Universität Paderborn
zur
Erlangung des Doktorgrades Dr. rer. nat.
vorgelegt von

Laura Serino

A Fabio
per aver sempre creduto in me

Summary

The rapid advancement of quantum technologies has driven major progress in quantum communication. A new frontier in this field is the use of high-dimensional quantum states (qudits), which unlock capabilities beyond what is possible with conventional binary systems. In this thesis, we develop and demonstrate a complete experimental framework for quantum communication using qudits encoded in the time-frequency domain of photons.

Two main elements form the core of this work: the development of a programmable source of high-dimensional entangled time-frequency states, and the realization of a versatile high-dimensional quantum decoder, the multi-output quantum pulse gate. We implement these devices using integrated nonlinear optical processes, namely parametric down-conversion for state generation and sum-frequency generation for state manipulation and detection. We achieve precise control over these processes by tailoring them via dispersion engineering of nonlinear waveguides and spectral shaping of pump pulses.

We then showcase the versatility of this framework through a range of applications in quantum communication and beyond. We realize a complete high-dimensional quantum key distribution system, introduce improved quantum state characterization techniques, and provide new experimental insights into fundamental aspects of quantum information, such as the connection between uncertainty relations and the properties of mutually unbiased bases in high dimensions.

Zusammenfassung

Die rasante Entwicklung der Quantentechnologien hat die Quantenkommunikation maßgeblich vorangetrieben. Eine neue Grenze ist der Einsatz hochdimensionaler Quantenzustände (Qudits), die Fähigkeiten jenseits konventioneller binärer Systeme erschließen. Diese Arbeit entwickelt und demonstriert ein vollständiges experimentelles Framework für die Quantenkommunikation mit Qudits, die in der Zeit-Frequenz-Domäne von Photonen kodiert sind.

Zwei Hauptelemente bilden den Kern dieser Arbeit: die Entwicklung einer programmierbaren Quelle hochdimensional verschränkter Zeit-Frequenz-Zustände und die Realisierung eines vielseitigen, hochdimensionalen Quantendecoders, des Multi-Ausgangs-Quantenpulsgatters. Wir implementieren diese Bauteile mittels integrierter nichtlinearer Prozesse wie parametrischer Fluoreszenz und Summenfrequenzerzeugung. Präzise Kontrolle wird durch Dispersionsanpassung in Wellenleitern und spektrale Formung von Pump-Pulsen erreicht.

Anschließend demonstrieren wir die Vielseitigkeit dieses Frameworks anhand einer Reihe von Anwendungen in der Quantenkommunikation und darüber hinaus. Wir realisieren ein vollständiges System zur hochdimensionalen Quantenschlüsselverteilung, führen verbesserte Methoden zur Quantenzustandscharakterisierung ein und gewinnen neue Einblicke in grundlegende Aspekte der Quanteninformation, wie die Verbindung zwischen Unschärferelationen und den Eigenschaften von wechselseitig unvoreingenommenen Basen in hohen Dimensionen.

Contents

Introduction

Think of a number between zero and five. If you had to communicate this number using only your hand, the most natural approach would be to raise the corresponding number of fingers. Simple, direct, and instantly understood. Now, imagine trying to convey the same number only by blinking: perhaps you would blink a specific number of times, or use a more complex binary code. This immediately appears less efficient and more cumbersome than simply raising fingers. This simple analogy introduces a fundamental concept in information theory: the dimensionality of an encoding alphabet.

In any communication system, information is first encoded onto an information carrier by the sender, then transmitted through a channel, and finally detected and decoded at the receiver's end. In classical communications, these carriers are typically electromagnetic fields, such as radio waves or light pulses. The chosen degree of freedom of the carrier, along with the form in which information is encoded, defines an *encoding alphabet*. Classical communication systems often exploit high-dimensional alphabets, e.g., by using multiple amplitude or phase levels in wireless transmissions, or by sending many different wavelengths (colors) of light down a single optical fiber [1]. This enhanced information capacity per carrier is clearly advantageous, allowing for faster data rates and more efficient use of the available bandwidth. Nevertheless, despite the effectiveness of high-dimensional encoding, binary encoding remains the universal standard in classical information processing: for many classical applications, using a larger number of binary signals is often easier and more cost-effective than engineering complex high-dimensional systems.

The quantum world, however, operates under a different set of rules. In quantum communication, information is ultimately carried by individual photons, that is, the fundamental particles of light. These particles enable protocols with interesting and useful properties that are impossible to achieve classically—as long as the information carriers are *truly* quantum [2, 3]. This typically means that only a single photon is transmitted in each "shot" of the communication. With this intrinsic constraint on the available resources, using a higher-dimensional alphabet is immediately beneficial: encoding more information per photon allows more information to be transmitted in each shot. But the benefits of high-dimensional

quantum encodings extend far beyond this. Utilizing a d-level quantum system, known as a *qudit*, instead of binary qubits leads to quantum cryptography protocols that are inherently more secure against eavesdropping attempts and more robust to noise [4, 5]. Certain quantum computational tasks might also find more efficient solutions when leveraging the larger state space offered by qudits [6]. Furthermore, quantum concepts, such as mutually unbiased bases and entropic uncertainty relations, reveal richer and more intricate properties in higher dimensions, providing new directions for fundamental research [7].

Then, if high dimensions are so promising, why are high-dimensional quantum systems not yet the standard? As is often the case in applying quantum technologies to reality, the challenge lies in the "how". Well-established quantum technology platforms, such as those based on the polarization of photons [8], the spin of trapped ions [9], or discrete energy levels in quantum dots [10] or superconducting circuits [11], were initially developed and optimized for qubits. These systems have been invaluable for demonstrating fundamental quantum properties and proof-of-principle quantum computation or communication protocols. However, these platforms were not designed with dimensional scalability in mind, and extending them to high dimensions presents both fundamental and technological limitations, even as research progresses [12, 13]. While photons are the ideal (in fact, the only) information carriers for quantum communication, their most utilized degree of freedom, polarization, is intrinsically two-dimensional. Spatial modes of light offer an infinite-dimensional Hilbert space, which has been explored for high-dimensional quantum information; however, spatial modes are notoriously difficult to transmit faithfully over long distances, whether through optical fibers or even free space [14]. This is a crucial obstacle when aiming to implement a "quantum internet" for secure communication and distributed quantum computing [15].

In this thesis, we turn our attention to a more resilient and practical alternative: the time-frequency degree of freedom of photons. By encoding quantum information in so-called temporal modes, which leverage the timing and spectral composition (color) of photons, we gain access to an inherently infinite-dimensional encoding space. Unlike their spatial counterparts, time-frequency encodings are robust against degradation during transmission and are compatible with standard single-mode optical fibers, making them exceptionally well-suited for practical quantum communication [16]. The work presented here analyzes the key experimental tools and underlying physics necessary to harness these time-frequency qudits effectively, from generation to detection, leveraging integrated nonlinear processes. With the development of this framework, we demonstrate a range of applications that showcase the practical utility of time-frequency qudits for both quantum communication and fundamental science.

One recurring lesson I have learned throughout my doctoral studies is that progress in experimental physics, particularly in cutting-edge fields like quantum

optics, always involves trade-offs. You might gain more dimensions, at the cost of more errors. More output channels, but less efficiency. You might boost laser power to enhance efficiency but introduce instabilities in the process, or learn everything about one physical variable only to be bound by the uncertainty principle to know absolutely nothing about its conjugate. In this thesis, we will frequently encounter and juggle these kinds of trade-offs. The challenge, and indeed the art, lies in understanding them, and in finding the optimal balance to achieve something genuinely new and useful.

This thesis is structured as follows:

Chapter 1 establishes the foundational concepts necessary for understanding high-dimensional quantum communication. It begins with classical notions of information and entropy, then shifts to the quantum domain, defining qubits, Hilbert spaces, and mutually unbiased bases. These concepts are then generalized to qudits. This chapter concludes by discussing the role of qudits in quantum communication through an example of a high-dimensional quantum key distribution protocol, focusing on how dimensionality and number of bases can enhance its security and efficiency.

Chapter 2 transitions to the practical realization of these high-dimensional concepts using the time-frequency degree of freedom of photons. After formally defining time-frequency qudits and exploring possible encoding alphabets, we introduce integrated nonlinear optical processes, particularly parametric down-conversion and sum-frequency generation in weakly guiding waveguides, which will be our main tools for generating and manipulating the qudits. We describe methods for tailoring these nonlinear processes through techniques like dispersion engineering in waveguides and spectral shaping of pump pulses, providing the toolkit for the experimental demonstrations that follow.

With this theoretical and practical framework established, the thesis then presents the experimental implementations of these concepts through original research contributions.

Chapter 3 focuses on the generation of high-dimensional entangled states. We describe the design and experimental realization of a programmable source of time-frequency-entangled qudits through parametric down-conversion, where the dimensionality of the entanglement can be controlled via pump shaping.

Chapter 4 addresses the task of decoding time-frequency qudits by introducing the multi-output quantum pulse gate (mQPG), a device based on dispersion-engineered sum-frequency generation which enables the simultaneous projection of a high-dimensional input state onto multiple basis states. We analyze its performance with various types of temporal-mode alphabets through quantum detector tomography, and study its capabilities and limitations.

Chapter 5 is dedicated to a proof-of-principle demonstration of a complete high-dimensional quantum key distribution system, showcasing the immediate application of the mQPG as a high-dimensional quantum decoder.

Chapter 6 presents fundamental explorations enabled by the mQPG, specifically experimental studies of how the properties of mutually unbiased bases impact quantum uncertainty relations in high-dimensional systems.

Chapter 7 showcases how multi-output detection not only enables new applications, but can also improve existing ones. Particularly, we focus on state characterization techniques: from self-guided quantum tomography, which allows for the efficient and high-fidelity estimation of qudits, to a new pulse characterization method called FIREFLY, which enables the reconstruction of complex phase and coherence profiles at the single-photon level and can be extended through the mQPG to simultaneously characterize two unknown pulses.

Finally, **Chapter 8** summarizes the main conclusions of this thesis, discusses their implications for the broader field of quantum information science, and offers an outlook on future research directions that build upon this work.

Author publications and contributions

Authors marked with † contributed equally to the manuscript.

Main publications

The following publications form the core of the experimental work presented in this thesis.

- **Realization of a multi-output quantum pulse gate for decoding high-dimensional temporal modes of single-photon states**
  Laura Serino, Jano Gil-Lopez, Michael Stefszky, Raimund Ricken, Christof Eigner, Benjamin Brecht, Christine Silberhorn
  PRX Quantum, 4(2), 020306 (2023)
  DOI: 10.1103/PRXQuantum.4.020306

  LS designed the nonlinear waveguide and constructed the experimental setup with input from JGL and MS. RR and CE fabricated the waveguides. LS performed the experiment and the data analysis. BB and CS supervised the project. LS wrote the manuscript with contributions from MS, BB and CS.

- **Orchestrating time and color: a programmable source of high-dimensional entanglement**
  Laura Serino†, Werner Ridder†, Abhinandan Bhattacharjee, Jano Gil-Lopez, Benjamin Brecht, Christine Silberhorn
  Optica Quantum, 2(5), 339–345 (2024)
  DOI: 10.1364/opticaq.532334

  LS, WR and JGL designed and constructed the experimental setup. WR and AB performed the experiment with assistance from LS. LS analyzed the experimental data. BB and CS supervised the project. LS wrote the manuscript with contributions from WR, AB, BB and CS.

- **Complementarity-based complementarity: The choice of mutually unbiased observables shapes quantum uncertainty relations**
  Laura Serino, Giovanni Chesi, Benjamin Brecht, Lorenzo Maccone, Chiara Macchiavello, Christine Silberhorn
  arXiv preprint (2024), accepted for publication in Physical Review Research
  DOI:10.1103/v24q-sl6n

  GC, LM and CM developed the theoretical framework. LS carried out the experiment and analyzed the data. GC and LM performed the simulations. CM and CS supervised the project. GC, LS and LM and wrote the manuscript with contributions from BB, CM and CS.

- **Programmable time-frequency mode-sorting of single photons with a multi-output quantum pulse gate**
  Laura Serino, Christof Eigner, Benjamin Brecht, Christine Silberhorn
  Optics Express, 33(3), 5577 (2025)
  DOI: 10.1364/OE.544206

  LS performed the experiment and the data analysis. CE fabricated the waveguides. BB and CS supervised the project. LS wrote the manuscript with contributions from BB and CS.

- **Self-guided tomography of time-frequency qudits**
  Laura Serino, Markus Rambach, Benjamin Brecht, Jacquiline Romero, Christine Silberhorn
  Quantum Science and Technology, 10(2), 025024 (2025)
  DOI: 10.1088/2058-9565/adb0ea

  LS performed the experiment and the data analysis with contributions from MR and JR. BB, JR and CS supervised the project. LS wrote the manuscript with contributions from all other authors.

- **Frequency-bin interferometry for reconstructing electric fields with low intensity**
  Abhinandan Bhattacharjee†, Laura Serino†, Patrick Folge†, Benjamin Brecht, Christine Silberhorn
  arXiv preprint (2025)
  DOI: 10.48550/arXiv.2504.08607

  AB and LS developed the method for pulse reconstruction. LS performed the experiments with coherent light. PF and AB carried out the experiment with the PDC source. AB and LS analyzed the data. AB wrote the manuscript with contributions from LS and PF. BB and CS supervised the project.

- **Experimental entropic uncertainty relations in dimensions three to five**
  Laura Serino, Giovanni Chesi, Benjamin Brecht, Lorenzo Maccone, Chiara Macchiavello, Christine Silberhorn
  arXiv preprint (2025)
  DOI: 10.48550/arXiv.2507.05025

  GC, LM and CM developed the theoretical framework. LS carried out the experiment and analyzed the data. GC and LM performed the simulations. CM and CS supervised the project. LS and GC wrote the manuscript with contributions from BB, CM and CS.

Other publications

The following publications are additional contributions from my doctoral work that fall outside the central scope of this thesis.

- **A pulsed lidar system with ultimate quantum range accuracy**
  Stephan Kruse†, Laura Serino†, Patrick Folge†, Dana Echeverría-Oviedo, Abhinandan Bhattacharjee, Michael Stefszky, J. Christoph Scheytt, Benjamin Brecht, Christine Silberhorn
  IEEE Photonics Technology Letters, 35(14), 769–772 (2023)
  DOI: 10.1109/LPT.2023.3277515

  SK conceived the original idea. LS designed and constructed the experimental setup. LS and PF performed the experiment and analyzed the data with input from DEO, AB and MS. SK wrote the manuscript with contributions from LS and PF. CSc, BB and CSi supervised the project. All authors contributed to the discussion of results and commented on the manuscript.

- **Pulse characterization at the single-photon level through chronocyclic *Q*-function measurements**
  Abhinandan Bhattacharjee, Patrick Folge, Laura Serino, Jaroslav Řeháček, Zdeněk Hradil, Christine Silberhorn, Benjamin Brecht
  Optics Express, 33(3), 5551–5561 (2025)
  DOI: 10.1364/OE.540125

  AB and PF developed the idea. LS designed and constructed the experimental setup. AB and LS performed the experiment. AB, PF and JR analyzed the data. AB wrote the manuscript with contributions from PF and LS. ZH, CS and BB supervised the project. All authors contributed to the discussion of results and commented on the manuscript.

- **Observing high-dimensional nonlocality using multi-outcome spectral measurements**
  Kiki Dekkers, Laura Serino, Nicola D'Alessandro, Abhinandan Bhattacharjee, Benjamin Brecht, Armin Tavakoli, Christine Silberhorn, Jonathan Leach
  arXiv preprint (2025)
  DOI: 10.48550/arXiv.2506.20796

  KD and JL conceived the original idea and developed the analysis framework. AB and LS performed the experiment with input from BB and CS, and contributed to the analysis framework. ND and AT developed the theoretical framework and carried out the data analysis. KD wrote the manuscript with contributions from all authors.

- **Quantum-limited detection of arrival time and carrier frequency of time-dependent signals**
  Patrick Folge†, Laura Serino†, Ladislav Mišta, Jr., Benjamin Brecht, Christine Silberhorn, Jaroslav Řeháček, Zdeněk Hradil
  Submitted to peer review (2025)
  JR and ZH conceived the original idea. LS designed and constructed the experimental setup. PF and LS planned and performed the experiment. JR, LM and ZH analyzed the data. ZH, CS and BB supervised the project. All authors contributed to the discussion of results and to writing the manuscript.

List of abbreviations

CK	cosine-kernel
EUR	entropic uncertainty relation
FWHM	full width at half maximum
HD-QKD	high-dimensional quantum key distribution
HG	Hermite-Gaussian
JSA	joint spectral amplitude
JSI	joint spectral intensity
mQPG	multi-output quantum pulse gate
MUB	mutually unbiased basis
OPO	optical parametric oscillator
PDC	parametric down-conversion
QBER	quantum bit error rate
QKD	quantum key distribution
QPG	quantum pulse gate
QPM	quasi-phase-matching
SFG	sum-frequency generation
SGT	self-guided tomography
SLM	spatial light modulator
TM	temporal mode
ToF	time-of-flight

1

Qudits in quantum communication

Communicating means transmitting information, so it seems straightforward to say that quantum communication deals with transmitting quantum information. But what does this really mean? What is quantum information? And what is information at all?

In this chapter, we start from the definition of information from classical to quantum following the treatments presented by Barnett in *Quantum Information* [2] and by Nielsen and Chuang in *Quantum Computation and Quantum Information* [3], before extending the discussion to high-dimensional quantum states, or qudits. The final section of this chapter is dedicated to quantum key distribution, introduced following the comprehensive review by Scarani et al. [17] and expanding the analysis to high-dimensional alphabets.

Please note that this chapter is not intended to give a complete, formal overview of quantum information, as such task would be well beyond the scope of this thesis. Here, we rather wish to build a "survival guide" for experimentalists dealing with qudits, introducing the fundamental concepts and key properties that will be referred to throughout this thesis, while highlighting the role of high dimensions in quantum communication.

1.1 Probability, information and Shannon entropy

Information is a subtle and elusive concept. While we intuitively grasp its meaning, finding a rigorous definition can be challenging. One way to think of

information is as a measure of "how much we know" about something. But how can we quantify knowledge? Is it even possible? As it turns out, a simple example suggests that it is. Imagine you are looking for a particular dog and are given two pieces of information: "*it has a tail*" or "*it has purple eyes*". Clearly, the second statement provides significantly more information than the first.

1.1.1 Information from measurement outcomes

To formalize this concept, we can consider a variable X that represents the object of our knowledge and can have different values $\{x_i\}$. The amount of knowledge we can gain from measuring X and observing a specific value x_i depends on its likelihood, that is, on the probability $p(x_i)$. The total probability is normalized to $\sum_i p(x_i) = 1$, because any measurement must yield one of the measurement outcomes $\{x_i\}$. Intuitively, if $p(x_i) \approx 0$ (i.e., this outcome is very unlikely), then observing x_i provides significant information. Conversely, if $p(x_i) \approx 1$ (i.e., this outcome is almost certain), we learn very little.

Now, consider measuring X along with an independent variable Y, obtaining outcomes x_i and y_j, respectively. Let us indicate with $H(x_i, y_j)$ the total information gained from this joint measurement, which should equal the sum of the information that we would gain from x_i and y_j individually: $H(x_i, y_j) = H(x_i) + H(y_j)$. At the same time, this total should depend on their joint probability $p(x_i, y_j) = p(x_i)p(y_j)$. These mathematical requirements naturally lead to a logarithmic function: the information we obtain from observing x_i is proportional to $-\log_2 p(x_i)$, where the negative sign ensures that this quantity is positive, and the base 2 for the logarithm is a convention. This way, we obtain $H(x_i, y_j) \propto -\log_2 p(x_i, y_j) = -\log_2 p(x_i) - \log_2 p(y_j)$, which satisfies both requirements.

1.1.2 Shannon entropy

This approach was formalized by Claude Shannon, who arguably introduced the first rigorous way to quantify information [18]. He defined the amount of information contained in variable X as the average information that one can obtain from all possible measurement outcomes:

$$H(X) = -\sum_i p(x_i) \log_2 p(x_i) \,. \tag{1.1.1}$$

This quantity, known as *Shannon entropy*, depends only on the probability distribution $\{p(x_i)\}$ of the possible outcomes $\{x_i\}$. Importantly, the averaging ensures that events with $p(x_i) \approx 0$ (which would contribute almost infinite information) are effectively negligible due to their low chance of occurring.

Although the Shannon entropy has profound thermodynamic implications (revealing that information is physical, and is converted to heat when erased), it is

commonly used to calculate the number of *units of information*, or *bits*, required to store or transmit the information contained in X. This is the underlying reason for the base 2 convention for the logarithm.

1.2 From classical to quantum communication

In classical information theory, a *bit* (short for BInary digiT) represents the fundamental unit of information. A bit distinguishes between two mutually exclusive states, such as "0" or "1", "yes" or "no", "on" or "off", "open" or "closed". We can combine multiple bits to encode more complex information: n bits can represent one of 2^n possible combinations of these binary states. For example, two bits together can represent the four values 00, 01, 10, or 11. Importantly, a bit always exists in a well-defined state, corresponding to the physical state of the system, e.g., a charged or uncharged capacitor. Measuring a bit does not alter its state, but simply reveals its value, which is either 0 or 1.

1.2.1 Qubits

In contrast, the probabilistic character of measurements is one of the key features of a *qubit*, or quantum bit, which is the fundamental unit of quantum information. Unlike classical bits, qubits can exist not only in one of two distinct states, denoted by $|0\rangle$ and $|1\rangle$, but also in a *superposition* of these states. In this context, 0 and 1 are state labels; therefore, being in a superposition of the 0 and 1 states does not merely mean being in the 0.5 state. Instead, the mathematical expression of a pure[1] qubit state is

$$|\psi\rangle = \alpha\,|0\rangle + \beta\,|1\rangle\,, \tag{1.2.1}$$

where α and β are complex coefficients normalized such that $|\alpha|^2 + |\beta|^2 = 1$. Through the Born rule $P(x_i) = |\langle x_i|\psi\rangle|^2$ (where $\langle\cdot|\cdot\rangle$ indicates the scalar product, or "overlap"), these coefficients encode the probability to find the qubit in $|0\rangle$ or $|1\rangle$ when measured: $P(0) = |\alpha|^2$ and $P(1) = |\beta|^2$. In this context, $|0\rangle$ or $|1\rangle$ are said to form the *computational basis* for the qubit.

This behavior introduces a fundamental difference between classical and quantum systems: measuring a qubit permanently alters its state. In fact, while classical bits remain unchanged upon observation, measuring a qubit in the computational basis forces it to "collapse" into one of the two possible states $|0\rangle$ or $|1\rangle$ in a probabilistic way. This collapse is not deterministic, meaning that even if we fully know the state of the qubit before the measurement, in general we cannot predict the exact outcome, but only the probability of each result. After the measurement, the superposition is destroyed, and the qubit remains in the state corresponding to the measurement result. This property of *measurement*

[1] A qubit can also be in a *mixed* state, which cannot be expressed as a ket, but instead requires the density matrix representation. We will not explicitly consider mixed states in this chapter.

disturbance is a key aspect of quantum mechanics and plays a central role in quantum communication together with the *no-cloning theorem*, which states the impossibility to perfectly clone a quantum state while leaving the original one unaffected [19]. Consequently, information extraction must often rely on a single measurement: in quantum communication, we only have *one shot* at measuring the qubit and, therefore, we must carefully choose which measurement to perform.

1.2.2 Hilbert space

What does it mean to choose a measurement? To understand this, we take a step back and look at the meaning of $|0\rangle$ and $|1\rangle$. In quantum mechanics, $|0\rangle$ and $|1\rangle$ represent two orthogonal quantum states that form the fundamental basis, or computational basis, of a vector space called the *Hilbert space*. This space contains all possible linear combinations of $|0\rangle$ and $|1\rangle$, that is, all superposition states $|\psi\rangle = \alpha|0\rangle + \beta|1\rangle$. The orthogonality condition $\langle 0|1\rangle = 0$, which implies that the overlap between $|0\rangle$ and $|1\rangle$ is zero, is a requirement for these two states to form a computational basis in quantum information.

The complex nature of α and β makes it so that these coefficients also contain a *phase* component, which has a very physical meaning in determining the state of the qubit. For instance, in the case of polarization encoding, the phases indicate how the horizontal and vertical components combine, resulting in a specific angle of diagonal or elliptical polarization. This phase, therefore, is necessary to describe the qubit, and needs to be addressed by the measurement.

But if measuring the state destroys the superposition, how can we access this phase information? The trick here is to "rotate" our measurement from the computational basis. We can define superposition bases containing two orthogonal states $|a\rangle$ and $|b\rangle$ from the Hilbert space defined by $|0\rangle$ and $|1\rangle$, meaning that $|a\rangle$ and $|b\rangle$ are two superpositions of the fundamental states. When we measure in a superposition basis, the qubit will collapse into one of its two basis states with probability $|\langle a|\psi\rangle|^2$ and $|\langle b|\psi\rangle|^2$, respectively. If $|\psi\rangle$ is equal to $|a\rangle$ or $|b\rangle$, we will always obtain the same measurement outcome, thus gaining full information on the state, including its phase. However, in a real experimental setting, finding the precise basis rotation that leads to a deterministic measurement outcome is a highly nontrivial task. In practice, qubit states are typically estimated using more sophisticated techniques, grouped under the term *quantum state tomography*. While many such methods exist, including the two we demonstrate experimentally in Chapters 4 and 7, they all ultimately rely on the fundamental principle of rotating the measurement basis to extract information about both the amplitudes and the relative phases of the quantum state.

1.2.3 Mutually unbiased bases

There exists a special category of superposition bases called *mutually unbiased bases* (MUBs). Two MUBs measure complementary properties of a state, meaning that there is no mutual information between them. If a qubit is completely determined in one basis, which is the case when $|\psi\rangle$ is an element of the basis, then it will be completely undetermined when measured in one of its MUBs, randomly yielding one of the two possible measurement outcomes with 50% probability. In other words, having complete information in one basis implies having no information in all other MUBs. This property is related to the so-called *entropic uncertainty relations*, i.e., a formulation of Heisenberg's uncertainty principle in terms of Shannon's entropy, which will be addressed in Chapter 6.

A two-dimensional Hilbert space always contains a set of three MUBs, which can be represented as

$$\begin{aligned}
&\{|0\rangle, |1\rangle\}, \\
&\{|+\rangle, |-\rangle\} \equiv \{|0\rangle + |1\rangle, |0\rangle - |1\rangle\}, \\
&\{|+i\rangle, |-i\rangle\} \equiv \{|0\rangle + i\,|1\rangle, |0\rangle - i\,|1\rangle\}.
\end{aligned}$$

In the polarization encoding, these correspond to the HV (horizontal-vertical), DA (diagonal-antidiagonal) and LR (left-hand and right-hand circularly polarized) bases.

1.2.4 Entanglement

Another substantial difference between bits and qubits lies in the behavior of correlations. When we have two independent qubits in states $|a\rangle$ and $|b\rangle$, we can write their joint state as

$$|\Psi\rangle = |a\rangle\,|b\rangle\ . \tag{1.2.2}$$

If the two qubits are correlated, their state is more generally written as

$$|\Psi\rangle = \alpha\,|a_0\rangle\,|b_0\rangle + \beta\,|a_1\rangle\,|b_1\rangle\ , \tag{1.2.3}$$

where $\{|a_0\rangle, |a_1\rangle\}$ and $\{|b_0\rangle, |b_1\rangle\}$ are bases for each qubit. If this two-qubit state cannot be factored into the form (1.2.2), it is called an *entangled* state: two entangled qubits cannot be described separately, but only as a joint system.

A direct implication of entanglement is immediate from the expression of (1.2.3): if we perform a measurement on the first qubit and obtain $|a_i\rangle$, then we know that the second qubit will be in the corresponding state $|b_i\rangle$. However, until we perform this measurement, the joint state will behave as a superposition of $|a_0\rangle\,|b_0\rangle$ and $|a_1\rangle\,|b_1\rangle$.

How does entanglement differ from classical correlations? Consider the entangled Bell state $|\Phi^+\rangle = (|0\rangle\,|0\rangle + |1\rangle\,|1\rangle)/\sqrt{2}$, which describes two maximally

correlated qubits. When measuring these qubits in the computational basis $\{|0\rangle, |1\rangle\}$, the outcomes are perfectly correlated: if the first qubit is $|0\rangle$, the second is also $|0\rangle$, and if the first is $|1\rangle$, the second is also $|1\rangle$. Crucially, this correlation persists even when we change the measurement basis. This is a direct consequence of the fixed phase relationship between the $|0\rangle|0\rangle$ and $|1\rangle|1\rangle$ components of the superposition. For instance, if we rotate to the diagonal basis $\{|+\rangle, |-\rangle\}$, the Bell state $|\Phi^+\rangle$ can be rewritten as $\frac{1}{\sqrt{2}}(|+\rangle|+\rangle + |-\rangle|-\rangle)$. This means that a measurement outcome of $|+\rangle$ on the first qubit guarantees an outcome of $|+\rangle$ on the second, and similarly for $|-\rangle$. This persistence of correlations across different measurement bases is a purely quantum property of entanglement.

Now, let us attempt to describe the correlations using a classical mixture. One might imagine a scenario where the two-qubit system is in the state $|0\rangle|0\rangle$ with 50% probability, or in the state $|1\rangle|1\rangle$ with 50% probability. If we measured this classical mixture in the computational basis, we would observe the same correlated outcomes as the entangled Bell state. However, the distinction becomes clear when we rotate the measurement basis: measuring the classical mixture ($|0\rangle|0\rangle$ or $|1\rangle|1\rangle$) in the diagonal basis $\{|+\rangle, |-\rangle\}$ yields independent random outcomes for each qubit. For example, if the system was in state $|0\rangle|0\rangle$, measuring the first qubit in the diagonal basis gives $|+\rangle$ or $|-\rangle$ with equal probability, and this outcome provides no information about the second qubit (which will also be random). Thus, for the classical mixture, the strong correlations observed in one basis vanish when the basis is rotated.

Indeed, correlations that resist basis rotation cannot be explained by any classical theory, and are thus unique to entangled quantum systems. Measuring the state of one of the entangled qubits instantaneously determines the state of the other, independently of the distance that separates them (*non-locality principle*). These properties lie at the heart of Bell inequalities [20], which are derived under the assumption of classical correlations and hence must always hold in a classical framework, but are violated by quantum entanglement.

1.3 Qudits

So far, we have only looked at the binary quantum systems, but quantum states are not limited to two dimensions. We can add more vectors to our fundamental basis $\{|0\rangle, |1\rangle\}$, extending it to the d-dimensional basis $\{|0\rangle, |1\rangle, \ldots, |d-1\rangle\}$. In order for these states to form a bases, they must be orthonormal:

$$\langle i|j\rangle = \delta_{ij}, \quad \forall\, i, j \in \{0, \ldots, d-1\}\,. \tag{1.3.1}$$

This new basis defines a d-dimensional Hilbert space that contains all possible superpositions of the d basis states:

$$|\psi\rangle = \sum_{i=0}^{d-1} \alpha_i |i\rangle \,, \tag{1.3.2}$$

where α_i are complex coefficients satisfying the normalization condition $\sum_{i=0}^{d-1} |\alpha_i|^2 = 1$. These states are called *qudits*, and they are the natural extension of qubits to a d-dimensional quantum system.

Measuring a qudit in the computational basis collapses its state into one of the d possible outcomes, $|0\rangle, |1\rangle, \ldots, |d-1\rangle$, with probabilities $|\alpha_i|^2$ for each state $|i\rangle$. This increased number of outcomes allows each qudit to store more information than a qubit. How much more exactly? Using the Shannon entropy (1.1.1), we find that a d-dimensional qudit with equally likely outcomes (each with probability $1/d$) corresponds to $\log_2 d$ qubits. For example, in a four-dimensional space, a single four-dimensional qudit (a so-called ququart) carries the equivalent of two qubits of information.

In classical information, analogously, a 4-level system represents two bits of information. However, if physical resources are not constrained, the complexity or performance of classical information processing does not fundamentally change when using a single 4-level system instead of two separate physical bits. In contrast, in quantum information and communication, physical resources (i.e., information carriers such as atoms or photons) are often limited, making the ability of qudits to store more information per carrier particularly advantageous. Beyond increased information capacity, employing higher dimensions in quantum communication protocols implies accessing a larger Hilbert space, which can lead to additional benefits such as noise resilience and enhanced security [14], as we will see in the remainder of this chapter.

1.3.1 MUBs in high dimensions

The concept of MUBs extends naturally to qudits. Two bases $\{|a_i\rangle\}$ and $\{|b_j\rangle\}$ are mutually unbiased if the overlap between any state from one basis and any state from the other is uniform:

$$\left|\langle a_i | b_j \rangle\right|^2 = \frac{1}{d}, \quad \forall\, i, j \in \{0, \ldots, d-1\}\,. \tag{1.3.3}$$

This means that if a system prepared in an eigenstate of the first basis is measured in the second (mutually unbiased) basis, the outcome is completely random among the d possible states $|b_j\rangle$, each occurring with probability $1/d$.

Nevertheless, the properties of MUBs in high-dimensional Hilbert spaces have not been completely explored yet. In prime-power dimensions $d = p^n$, with p prime, it is known that a complete set of $d+1$ MUBs exists [21–23], where the

word “complete” indicates the largest possible set of MUBs in that Hilbert space. In non-prime-power dimensions, however, only a set containing at least three MUBs has been identified. Even in cases where complete sets are known, many of their properties are still under active investigation, making this an exciting frontier in quantum information research [7, 24].

1.3.2 Entangled qudits

Entanglement can also extend to high-dimensional systems. Two entangled qudits, each from a d-dimensional Hilbert space, are described by a joint state of the form

$$|\Psi\rangle = \sum_{i=0}^{d-1} \sqrt{\lambda_i}\, |\psi_i\rangle\, |\varphi_i\rangle \,, \tag{1.3.4}$$

where $\{|\psi_i\rangle\}$ and $\{|\varphi_i\rangle\}$ denote the respective d-dimensional bases for each qudit, which may or may not coincide. Measuring the state of the first qudit and obtaining $|\psi_i\rangle$ immediately collapses the joint state, determining the state of the second qudit to be $|\varphi_i\rangle$.

1.4 Quantum communication with qudits

The quantum properties discussed so far open new avenues in information science. In *quantum communication*, we transmit qubits or qudits instead of bits, enabling protocols that cannot be realized in classical communication. This finds valuable application in quantum cryptography, where the unique properties of quantum mechanics are brought to their full potential.

The field of quantum cryptography arguably began in the 1980s with Wiesner’s idea of quantum money [25], which proposed exploiting the properties of quantum particles to create a form of currency that would be impossible to counterfeit. Over time, the field has evolved to encompass a wide range of applications of quantum properties related to information security, with quantum key distribution (QKD) emerging as its showpiece protocol. QKD, proposed by Bennett and Brassard in 1984 [26] and independently developed by Ekert in 1991 [27], enables secure communication guaranteed by the laws of quantum mechanics, rather than by the assumed computational difficulty of solving certain mathematical problems.

While these groundbreaking works established a completely new field of research, further analysis revealed vulnerabilities in their underlying assumptions. This motivated the development of a plethora of improved protocols designed to close these security loopholes, though often at the cost of increased theoretical complexity and more demanding experimental requirements [28–32]. Among these, protocols exploiting high-dimensional encoding alphabets have emerged as more secure options than their binary counterparts [4, 5, 33]. However,

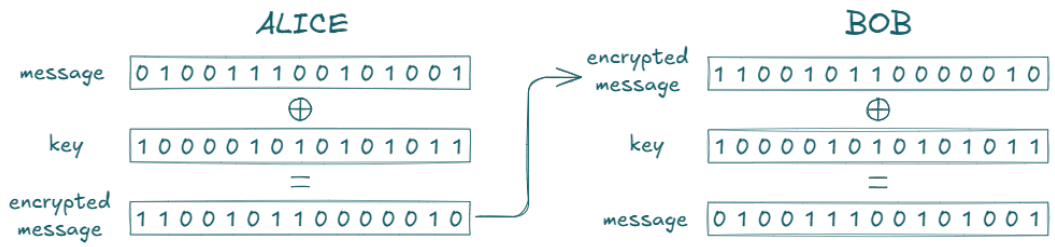

Figure 1.1: Scheme of the Vernam cypher or one-time pad: Alice encrypts a message using a modulo-2 sum with each bit of the key and sends the encrypted message to Bob, who can decode it through another modulo-2 sum with his identical copy of the key.

these high-dimensional quantum key distribution (HD-QKD) protocols were typically developed as extensions of the more sophisticated binary schemes, not the simpler original ones. As a result, much of the literature is dedicated to the rigorous security proofs of these advanced protocols, with less emphasis on a clear, intuitive introduction built from first principles. An accessible analysis of *how* and *why* higher dimensions fundamentally enhance QKD is needed.

In this section, we seek to build this essential intuition. We deliberately step back from the complexity of the most advanced protocols and, drawing inspiration from the comprehensive review of two-dimensional QKD by Scarani et al. [17], build the high-dimensional case from the ground up. We will construct a simple HD-QKD model to provide an intuitive understanding of its operation and the clear advantages of a larger Hilbert space. This model serves as an essential starting point for understanding the state-of-the-art protocols discussed later, and for appreciating the challenges of their experimental implementation.

1.4.1 Quantum key distribution protocols

Quantum key distribution is only a particular step in a broader procedure for secure communication. Consider two parties, historically named Alice and Bob, who wish to exchange a secret message. To ensure that a potential eavesdropper, called Eve, gains no useful information during transmission, they encrypt the message with a secret key. For instance, if the message is represented as a string of bits, one can mask each bit using a key string of the same length: Alice can perform a modulo-2 sum on each bit of the message and key, and Bob can decode the message applying the same operation with his copy of the key (Figure 1.1). This method, called *Vernam cypher* [34] or *one-time pad*, has been proven to be optimal: no unconditionally secure method requires less key [35]. In fact, with a truly random key, the encrypted message appears completely random to any eavesdropper. However, since the key must be discarded after its use, the double challenge of this protocol lies in sharing a key that is as long as the message, and to do so securely.

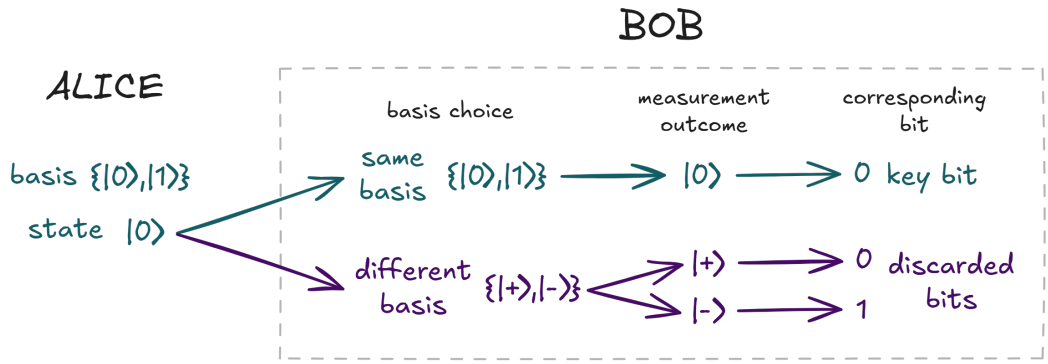

Figure 1.2: Illustration of one round of a BB84 protocol. Alice chooses an encoding basis, picks a state from it and sends it to Bob. If he measures the qubit in the same basis that Alice chose, then he successfully detects Alice's state and stores the corresponding bit in the key. If Bob chooses a different basis than Alice's, he randomly obtains one of the two possible measurement outcomes, which will be uncorrelated to Alice's state. For this reason, later Alice and Bob compare bases, and discard the bits in which they made a different choice. The remaining bits form the secret key.

Quantum physics offers a solution through QKD, where a quantum channel is used to distribute the key securely. The security arises from the principle of measurement disturbance: any attempt by Eve to intercept the key requires her to measure the quantum states, necessarily altering them. Hence, Alice and Bob are alerted to her presence and can abort the communication before disclosing the secret message. Clearly, this would not be possible in classical communication, where Eve could simply intercept the key by measuring the transmitted bits without leaving any trace of her presence.

The original protocol by Bennett and Brassard [26], known as BB84, is based on qubits encoded in the two orthogonal states from each of two MUBs. Namely, Alice is required to prepare qubits in one of the four possible states $\{|0\rangle, |1\rangle, |+\rangle, |-\rangle\}$. In each round of BB84, Alice uses a quantum channel to send one qubit to Bob, who randomly chooses a measurement basis between the same two MUBs. When Bob's basis matches Alice's, his measurement result is perfectly correlated with her encoded state; otherwise, he randomly obtains one of the two possible outcomes, as shown in Figure 1.2. By repeating this process and discarding rounds with mismatched bases, which they compare through a classical channel, Alice and Bob generate a shared key string.

Now, consider the action of an eavesdropper Eve. She can attempt an *intercept-resend* attack: Eve intercepts Alice's qubits, measures them in a randomly chosen basis, and sends a copy of her outcome to Bob. If her basis matches Alice's, the qubit is undisturbed; if not, the state is altered, introducing errors in the shared key, as shown in Figure 1.3. By publicly disclosing a subset of their key, Alice and Bob can detect these errors which indicate Eve's presence and, if necessary, abort the protocol.

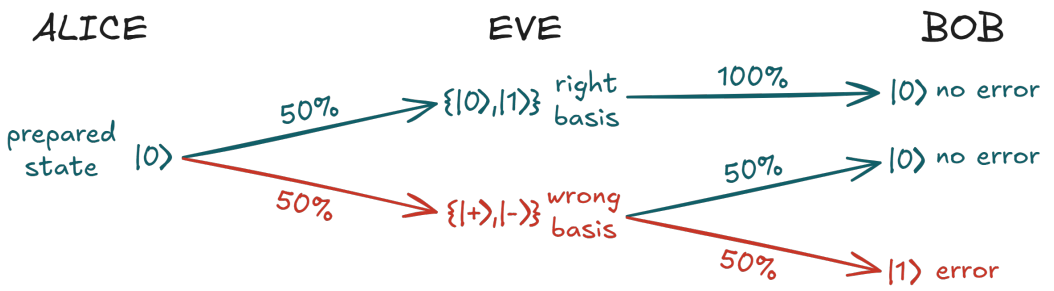

Figure 1.3: Example of eavesdropping attempt: Eve intercepts the qubit from Alice and performs a measurement to learn its value. If she chooses a different basis than Eve's, then she modifies the qubit, possibly causing Bob to obtain a measurement outcome that does not match Alice's state. Here, we only considered the case in which Bob chose the same basis as Alice, because measurements in mismatched bases are discarded.

This formulation is overly optimistic, as any realistic experimental measurement suffers from noise, which generates errors independently of Eve. This noise cannot simply be calibrated out: to guarantee unconditional security even against future technologies, we must assume an all-powerful eavesdropper who might tamper with the noise calibration. Alice and Bob can quantify the fraction of errors in their strings, called *quantum bit error rate* (QBER), to estimate the amount of information that Eve managed to extract. Based on this estimate, they can apply error correction and privacy amplification algorithms to reconcile their keys and reduce Eve's information, at the cost of discarding key bits and reducing the overall key length.

From these considerations, we can identify the main research directions in QKD: on the experimental side, developing techniques to efficiently share a key with minimal intrinsic errors; on the theoretical side, establishing robust security proofs and optimizing algorithms to maximize the final key length. For years, these efforts have advanced largely in parallel, creating a gap that has only recently begun to close, thanks to modern quantum technologies and security proofs accounting for experimental imperfections. Even now, four decades after the formulation of BB84, QKD is still a complex field in continuous evolution. Countless advanced protocols have been formulated, making the original BB84 appear almost like a toy model in comparison. One emerging direction where experiment and theory are converging is HD-QKD, which leverages qudits to enhance both information capacity and security.

Since the focus of this thesis is on qudits, here we will directly introduce the extended BB84 protocol in d dimensions rather than its binary formulation. This extension is not unique: for a prime power dimension d, we can choose up to $d+1$ MUBs. Increasing both the number of MUBs and the system dimensionality offers interesting advantages while also presenting experimental challenges. In the rest of this chapter, we will introduce the most general formulation of the

high-dimensional BB84 protocol with m bases in d dimensions, analyze a simple intercept-resend attack to study how m and d affect the secure key length, and finally summarize the main results of the latest security proofs for HD-QKD.

1.4.2 General steps of an HD-QKD protocol

An HD-QKD protocol based on the extension of BB84 to m MUBs in d dimensions requires Alice and Bob to be linked by both a quantum channel (for key distribution) and an authenticated classical channel (for post-processing). The protocol generally consists in the following steps:

1. **Raw key exchange**
   Over the course of N rounds, Alice transmits N qudits over the quantum channel, sending one qudit per round. Each qudit is randomly prepared in one of the m possible bases and in one of the d states within that basis. Bob measures each qudit in one of the m bases, also chosen randomly, obtaining one of d possible outcomes. Whenever Bob's measurement basis matches the basis in which Alice prepared the qudit, his measurement outcome will coincide with Alice's prepared state. At the end of this step, which is the only one that utilizes the quantum channel, Alice and Bob each hold a *raw key* composed of their respective sequences of N preparation choices and measurement results.

2. **Sifting**
   Alice and Bob communicate over the classical channel to compare their preparation and measurement bases. They discard rounds where their bases differ, obtaining a *sifted key* of approximately $n \approx N/m$ elements. In the absence of errors, Alice's and Bob's sifted keys should be identical; however, a potential eavesdropper Eve might try and intercept the message (e.g., via the intercept-resend attack mentioned previously), introducing errors between the two keys.

3. **Parameter estimation**
   Alice and Bob disclose a subset of the key over the classical channel to estimate the fraction of errors, or QBER. Every element they share becomes public, and must therefore be discarded from the key string. The estimated QBER allows Alice and Bob to gauge the potential information leakage to Eve.

4. **Error correction**
   If the QBER is above a predetermined threshold (that we will discuss later) too much information leaked to Eve; consequently, Alice and Bob abort the communication, and possibly retry the protocol from the first step. Instead, if the QBER is below the threshold, Alice and Bob apply an algorithm to correct the errors between their sifted keys. This process generally involves exchanging partial information on the key, hence sacrificing a part of the

key bits. At the end of the error correction step, Alice's and Bob's keys are perfectly correlated, although not perfectly secure.

5. **Privacy amplification**
   From the estimated QBER, Alice and Bob determine the maximum information that could have been intercepted by Eve. They then apply privacy amplification algorithms to reduce Eve's knowledge of the key, ideally to zero. A simple approach, for instance, is to derive a new key by computing the parity of groups of t bits from the original key. Increasing t reduces Eve's knowledge, but also shortens the final key. In general, stronger privacy amplification requires discarding more bits to further limit Eve's information. After this final step, Alice and Bob share an identical *secure key* of length ℓ, which they can use to encrypt their secret message.

Raw key exchange is the only step that requires a quantum channel, making it the main focus of experimental efforts. All subsequent steps are performed through the classical channel and are collectively referred to as *classical information processing* [17]. In a proof-of-principle demonstration of experimental QKD, the full classical information processing steps are often skipped, and the protocol performance is typically assessed by estimating the length of the final secure key.

1.4.3 Secure key rate

The efficiency of a QKD protocol is commonly analyzed in the asymptotic regime, where an infinite number of rounds $N \to +\infty$ is considered. In this limit, the protocol yields a sifted key of n states, from which secret key of length ℓ is extracted. The *secret fraction*

$$r = \lim_{N\to+\infty} \frac{\ell}{n}, \tag{1.4.1}$$

quantifies the number of secure bits per round in this limit. This value can be used to describe the efficiency of a protocol under specific noise conditions. In practical implementations, the secret fraction is typically multiplied by the repetition rate f to obtain the *secret key rate* $R = rf$, which indicates the number of secure bits generated per second.

Determining r is a challenging theoretical task even in the asymptotic regime, as it requires bounding Eve's potential knowledge of the key. This involves modeling her most effective attack strategies, while simultaneously designing efficient error correction and privacy amplification algorithms that minimize her information without excessively shortening the final key. Although a complete security proof is beyond our scope, in the following we illustrate these concepts using an intercept-resend attack as an example.

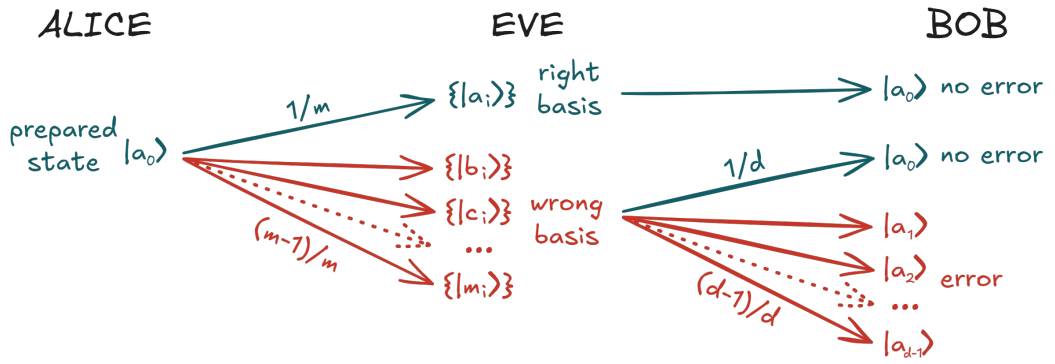

Figure 1.4: Probabilities associated to the possible outcomes of an intercept-resend attack, when using an HD-QKD protocol with d dimensions and m bases. For simplicity, we only consider the remaining measurements after sifting, in which Alice and Bob chose the same basis. If Eve chooses the right basis, with probability $1/m$, she correctly detects the state encoded by Alice, and sends an identical state to Bob. If she picks the wrong basis, with probability $1-1/m$, then she obtains a random measurement outcome and sends Bob a qudit encoded in a different basis, resulting in an error with probability $1-1/d$ (Bob will randomly obtain a measurement outcome correlated to Alice's with probability $1/d$).

Intercept-resend attack

In an intercept-resend attack, Eve intercepts the qudits, measures each in a randomly chosen basis among the m available, and sends a copy of the resulting state to Bob. Figure 1.4 illustrates the probabilities associated to the possible outcomes. With a probability $1-1/m$, Eve chooses a basis that is mutually unbiased with respect to Alice's. If Bob then measures the qudit in Alice's original basis, this measurement result enters his sifted key, where it introduces an error with probability $1-1/d$. From the probability tree diagram, we can calculate the QBER Q_{IR} (i.e., the error probability that Eve's intercept-resend attack introduces in the sifted key) as

$$Q_{\mathrm{IR}} = \frac{m-1}{m}\frac{d-1}{d}. \tag{1.4.2}$$

This error rate acts as a direct indicator of potential eavesdropping; the larger Q_{IR}, the more noticeable Eve's interference becomes. Therefore, while it may seem counterintuitive, a protocol is more robust if it forces Eve to introduce a large error when she attempts to gain information. This way, if Alice and Bob measure a low QBER, they can be more confident that it derives from experimental noise rather than from an attack. A high fundamental error rate from eavesdropping thus translates to a higher tolerance for the intrinsic experimental errors in a real-world system. In the two-dimensional case ($d = 2$) with $m = 2$ bases, corresponding to the original BB84 protocol, we find $Q_{\mathrm{IR}} = 25\%$. As d and m increase, the QBER approaches 100%, making Eve's presence easier to detect (Figure 1.5).

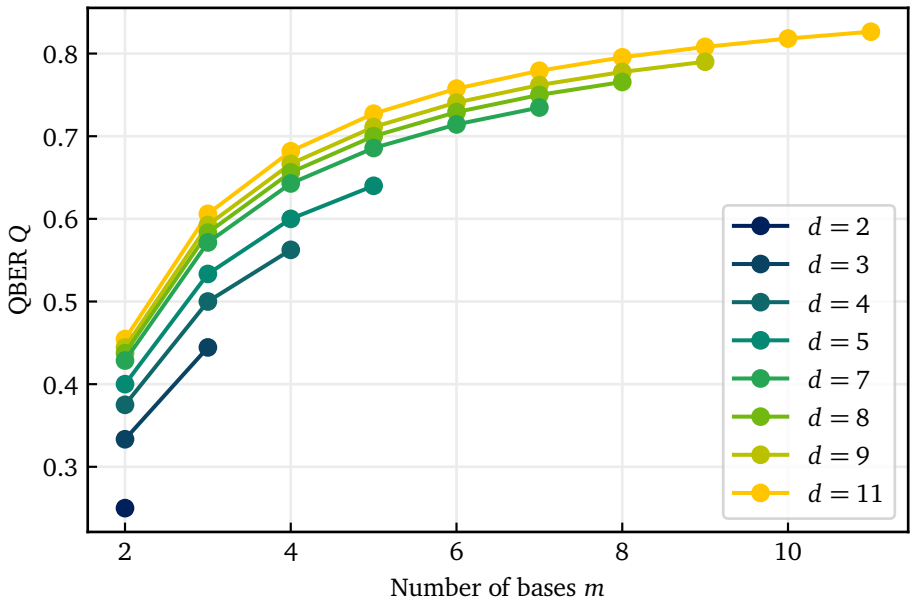

Figure 1.5: QBER (quantum bit error rate, i.e., fraction of errors) Q introduced by Eve in a complete intercept-resend attack. As the dimension d and number of bases m increase, Eve introduces additional errors, making her easier to detect.

What does this imply for Alice and Bob's mutual information? In the ideal, error-free scenario, each qudit carries $\log_2 d$ bits of information, thus, the secret fraction is simply $r = \log_2 d$, which coincides with the Shannon entropy of Bob's qudits $H(B)$ defined in eq. (1.1.1). Information theory states that, from this ideal value, we have to subtract the loss of information caused by the errors [2]. This loss is quantified by the conditional entropy $H(B|A)$, which represents Alice's and Bob's mutual uncertainty ("how undetermined is Bob's qudit, given that we know Alice's qudit?"), and vanishes when their key strings are identical. The mutual information therefore is

$$I(A:B) = H(B) - H(B|A) = \log_2 d - H_d(Q), \tag{1.4.3}$$

where Q is the QBER and $H_d(Q)$ is the d-ary entropy function,

$$H_d(Q) = -(1-Q)\log_2(1-Q) - Q\log_2(Q/(d-1)). \tag{1.4.4}$$

This function, shown in Figure 1.6, indicates the uncertainty that a QBER of Q introduces between Alice's and Bob's key strings, reflecting the $d-1$ possible ways an error can occur. For any dimension d, this quantity is maximized at $H_d(Q) = \log_2 d$ when $Q = 1 - 1/d$, which corresponds to the case of completely uncorrelated keys where the mutual information vanishes ($I(A:B) = 0$). Note that Eve could introduce such a high error only by consistently choosing the wrong measurement basis.

However, as mentioned earlier, estimating the final key length also requires accounting for the bits lost to remove Eve's information. In this specific case, we

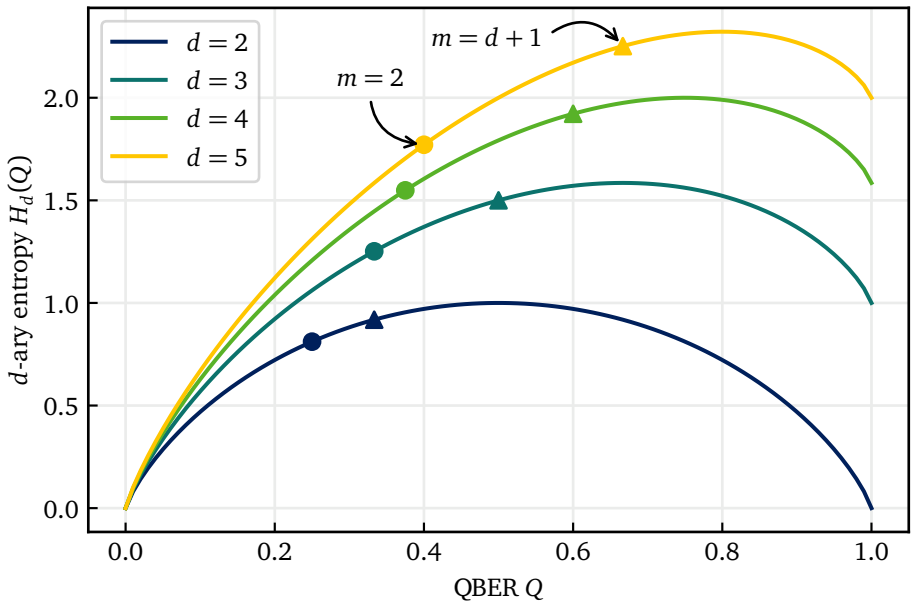

Figure 1.6: d-ary entropy $H_d(Q)$ as a function of the QBER Q for 2 to 5 dimensions. The circles and triangles correspond to the error Q_{IR} introduced by Eve in a complete intercept-resend attack in $m = 2$ and $m = d + 1$ MUBs, respectively. A larger $H_d(Q)$ indicates more uncertainty (less correlation) between Alice's and Bob's measurements.

can estimate the secret fraction by simply subtracting Eve's information I_E from Alice and Bob's mutual information [36]:

$$r = \max\{I(A:B) - I_E, 0\}, \tag{1.4.5}$$

where the lower bound is 0 because a negative secret fraction is not physical. For a complete intercept-resend attack (in which Eve attempts to measure every qudit), $I_E = \log_2(d)/m$: with probability $1/m$, Eve picks the correct basis and gains $\log_2 d$ bits of information; otherwise, with probability $1 - 1/m$, she picks the wrong basis and obtains no information at all.

For the two-dimensional BB84 protocol, Eve's information becomes $I_E = 0.5$, while inserting the intercept-resend QBER $Q_{\text{IR}} = 25\%$ for $d = 2$ into eq. (1.4.3) yields $I(A:B) \approx 0.19$. Substituting these values in eq. (1.4.5) results in $r = 0$: Eve's information is larger than Bob's! This conclusion holds for all combinations of d and m: under a complete intercept-resend attack, Alice and Bob cannot extract a secure key and must abort communication. This is because Eve's measurement of every state "breaks" the quantum channel in two, destroying the quantum correlations between Alice and Bob and essentially leaving them with the equivalent of classical correlations, from which no secure key can be extracted [17]. However, this is against Eve's best interest: her goal is for Alice and Bob to share the message while she secretly holds a copy of the key. To achieve her goal, Eve must try to minimize her disturbance, thereby aiming for a much lower QBER to remain undetected.

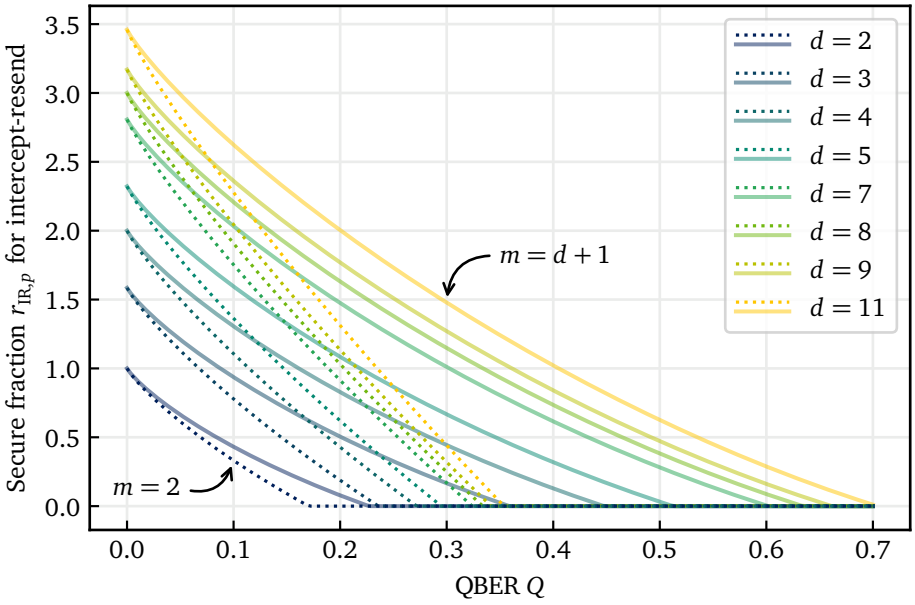

Figure 1.7: Secure key $r_{\mathrm{IR,p}}$ after a probabilistic intercept-resend attack as a function of the QBER Q for different dimensions d, using $m = 2$ MUBs (dotted lines) and $m = d + 1$ MUBs (solid lines). The starting value in absence of errors ($Q = 0$) is $\log_2 d$, giving an advantage for higher dimensions. This advantage also leads to a better tolerance to errors.

Probabilistic intercept-resend attack

To introduce less noise, Eve may adopt a probabilistic intercept-resend strategy, measuring only with probability p and leaving the qudit untouched with probability $1-p$. The QBER then becomes

$$Q_{\mathrm{IR},p} = p\frac{m-1}{m}\frac{d-1}{d}. \tag{1.4.6}$$

In exchange for introducing less noise, Eve reduces her information to

$$I_E = \frac{p\log_2 d}{m} = \log_2 d\frac{Qd}{(m-1)(d-1)}, \tag{1.4.7}$$

which, when substituted into eq. (1.4.5), gives the secret fraction

$$r_{\mathrm{IR},p} = \log_2 d - H_d(Q) - \log_2 d\frac{Qd}{(m-1)(d-1)}, \tag{1.4.8}$$

where the lower bound at 0 is implicit, and we used the mutual information expression in eq. (1.4.3). Figure 1.7 illustrates how the secret key fraction varies with the observed QBER Q for different dimensions d; Figure 1.8 shows the same quantity for a varying number of bases m in $d = 11$.

This expression highlights how larger dimensions d and number of bases m can enhance the key rate. Higher-dimensional qudits enable transmitting up to

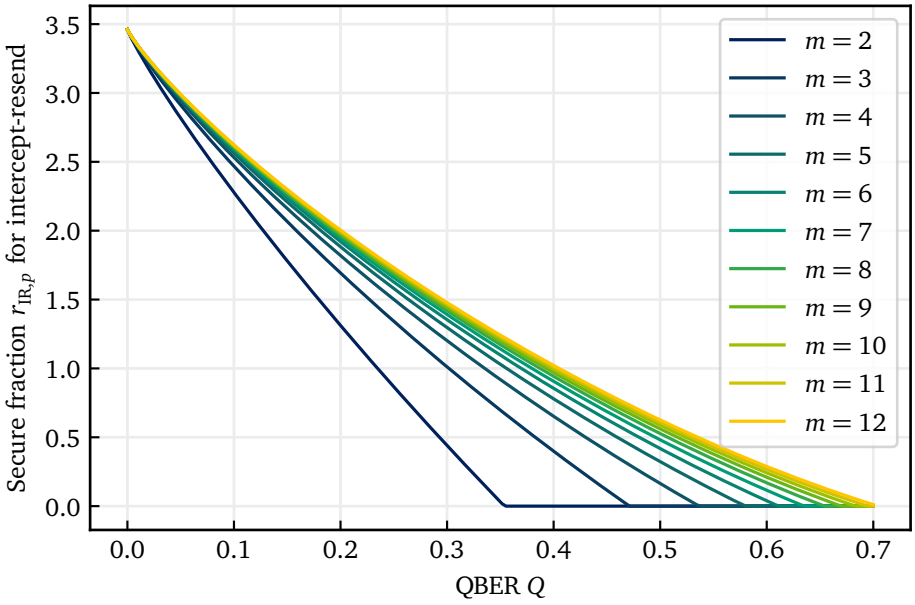

Figure 1.8: Secure key $r_{\mathrm{IR,p}}$ after a probabilistic intercept-resend attack as a function of the QBER Q for different numbers of MUBs m in dimension $d = 11$. Increasing the number of MUBs from $m = 2$ to $m = 3$ significantly improves the tolerance to errors. This improvement slowly decreases as m grows.

$\log_2 d$ bits per round instead of just 1. This gain always outweighs the increased QBER introduced by Eve: as $d \to \infty$, the secret fraction scales logarithmically as $r_{\mathrm{IR},p} \propto \log_2 d$, ensuring a continuous advantage at high dimensions.

The number of bases m appears only in the last term, representing Eve's information. Increasing m imposes stronger constraints on Eve, forcing her to introduce more errors with her measurements. However, unlike with higher dimensionalities, increasing m indefinitely causes this advantage to fade when $m \to \infty$, as the last term (Eve's information) tends to 0.

Collective and coherent attacks

So far, we have analyzed the simplest eavesdropping strategies that Eve might employ. In more advanced scenarios, she could entangle an ancilla state with each qudit and store these states in a perfect quantum memory. Later, after the classical post-processing phase, Eve could exploit the information disclosed by Alice and Bob to perform optimal joint measurements on the entire set of ancilla states. Such strategies, known as *collective* attacks, allow Eve to extract maximum information while introducing minimal disturbance [17].

The most general eavesdropping strategy involves *coherent* attacks, which include any possible strategy that Eve might ever employ. Bounding Eve's information under coherent attacks is extremely challenging, because one must assume that Eve applies the most optimal eavesdropping attack, while Alice and Bob employ

ideal error correction and privacy amplification algorithms that counteract it with minimal key loss. This problem is so complicated that a general expression for the asymptotic key rate in d dimensions and m bases has been derived only very recently [37]. Due to the complexity of the resulting formula for the asymptotic secret fraction, which involves a parameter computed through numerical minimization, we will focus on the two extreme cases, which offer analytical solutions.

The first case is the *two-basis protocol*, a direct extension of BB84 in d dimensions with $m = 2$. The corresponding secret fraction is given by [33]

$$r_{\infty}^{(m=2)} = \log_2 d - 2h(Q) - 2Q\log_2(d-1), \tag{1.4.9}$$

where $h(Q) := H_2(Q) = -(1-Q)\log_2(1-Q) - Q\log_2(Q)$ is the binary entropy function.

The second case is the *(d+1)-basis protocol*, which makes use of the complete set of MUBs and, thus, can be considered as the d-dimensional extension of the binary *six-state protocol* [38, 39]. In this case, the asymptotic secret fraction is [37]

$$r_{\infty}^{(m=d+1)} = \log_2 d - h\left(Q\frac{d+1}{d}\right) - Q\frac{d+1}{d}\log_2(d^2-1). \tag{1.4.10}$$

These rigorous formulas lead to similar qualitative conclusions as our simpler intercept-resend analysis. As shown in Figure 1.9, which plots the asymptotic key rate r_∞ for both cases in up to $d = 11$ dimensions, a higher dimensionality consistently improves the key rate, providing a robust advantage against noise. A second trend, detailed in the literature but not shown here, is that while adding the first few MUBs offers a significant increase to the key rate, the benefit for each subsequent basis diminishes. Nevertheless, since the number of available MUBs grows with the dimension, these small improvements can combine into a substantial overall advantage when all possible bases are used. Moreover, for a system with a high intrinsic QBER (due, for instance, to noise or experimental imperfections) employing more MUBs may be the only possible way to extract a positive secret key.

A useful way to visualize the advantages of the $(d+1)$-basis protocol over the two-basis protocol is through the maximum tolerable error $\overline{Q}$, i.e., the value of Q for which r drops to zero. Indeed, this quantity offers a straightforward practical interpretation: a secure key can only be extracted if $Q < \overline{Q}$, i.e., if the QBER is below the threshold. Any practical implementation of a QKD protocol, therefore, cannot work unless its intrinsic noise (independently of Eve) is below $\overline{Q}$. In Figure 1.10, we show the maximum tolerable error calculated for $m = 2$ and $m = d+1$ bases in up to $d = 11$, which match the values found in [4, 5]. The well-known value for BB84, 11%, is at the bottom of the plot. A two-basis protocol in $d = 5$ allows one to double this threshold, and a $(d+1)$-basis protocol in $d = 8$ dimensions can even triple it, enabling much stronger noise robustness.

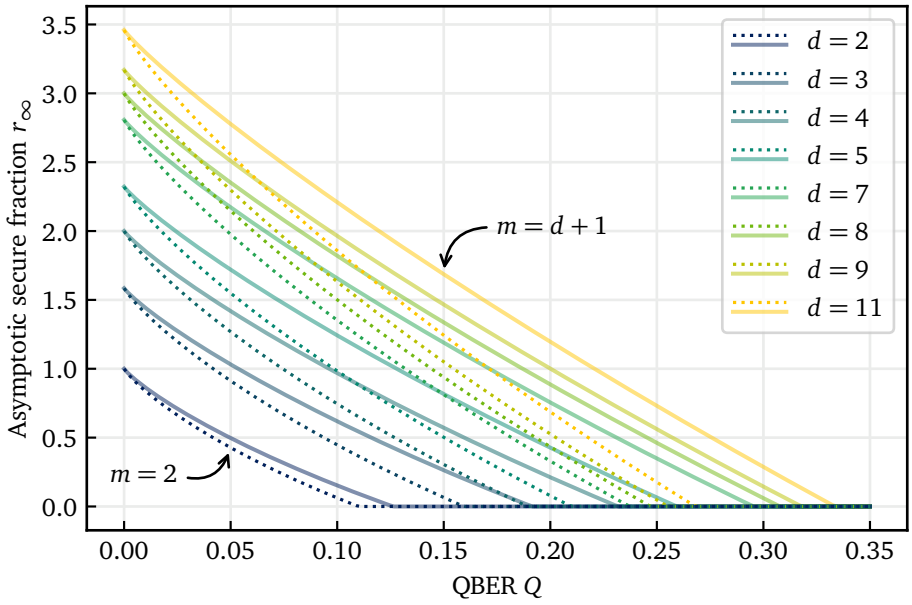

Figure 1.9: Asymptotic secure key r_∞ as a function of the QBER Q for the two-basis protocol (dotted lines, eq. (1.4.9)) and the $(d+1)$-basis protocol (solid lines, eq. (1.4.10)) in different dimensions d. Although this rigorous analysis yields a generally lower secret key fraction than the probabilistic intercept-resend case (notice the different QBER scale with respect to Figure 1.7), the high-dimensional advantage at low errors remains unchanged, yielding $r_\infty = \log_2 d$ for $Q = 0$. The error tolerance derived from using the complete set of $m = d + 1$ bases is greatly reduced in this case, because Eve can perform optimal measurements to minimize her disadvantage.

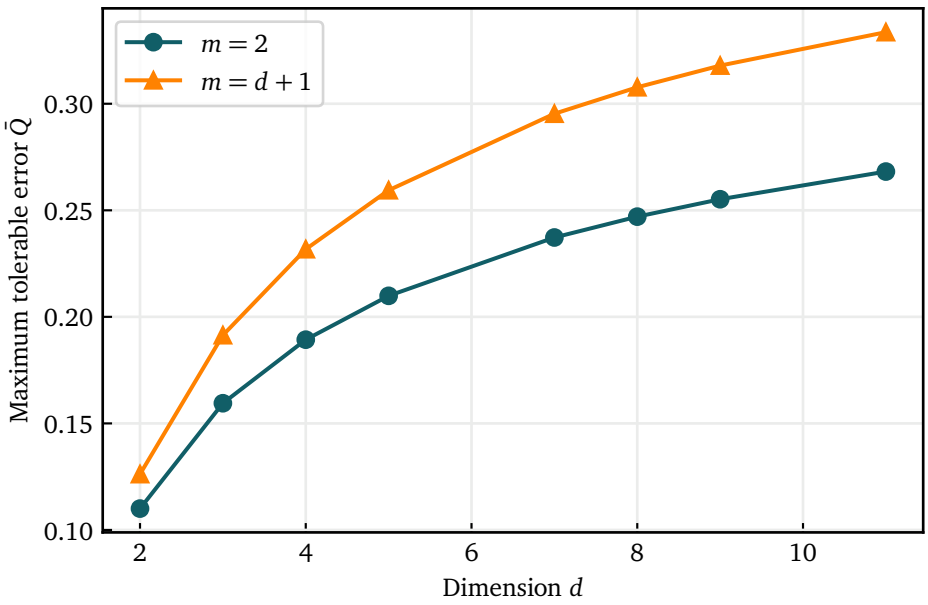

Figure 1.10: Maximum tolerable error as a function of the dimension d for the two-basis protocol (blue) and the $(d+1)$-basis protocol (orange). These values are obtained from eq. (1.4.9) and eq. (1.4.10), respectively, and match the values tabled in [4, 5]. The lowest value corresponds to the well-known error threshold of 11% in BB84. This threshold can be doubled by a two-basis protocol in $d = 5$, and tripled by a $(d+1)$-basis protocol in $d = 8$ dimensions.

Finite key analysis and experimental considerations

The values of $\bar{Q}$, while useful, do not constitute the final results of the security proof for HD-QKD. In [37], the authors also perform the so-called *finite key analysis*, which accounts for the fact that, in any practical QKD implementation, the number of rounds N must be finite. This implies that, unlike in the asymptotic regime, only a finite amount of information can be used for parameter estimation, making the statistical error on estimated parameters (such as the QBER Q) quite relevant. In turn, this leads to uncertainty in the estimate of Eve's knowledge; due to the restraints of secure communication, Alice and Bob must take the upper bound of this estimate—typically, a pessimistic choice that results in more discarded key bits.

Another important point, which we have so far overlooked, is that Bob, just like Eve, is less likely to choose the correct basis as m increases. To mitigate the resulting factor $1/m$ in front of the key rate, Alice and Bob can agree to use the same basis (called *key basis*) for the majority of the rounds, and use the remaining $m-1$ *test bases* for parameter estimation. In the asymptotic limit $N \to \infty$, the fraction of key bits lost due to sifting will vanish, as will the number of bits discarded to estimate the QBER. However, this is no longer true in the finite-key regime, where the fraction of measurements in the test basis must be appropriately increased to maintain statistical significance.

The finite number of rounds also affects the error correction and privacy amplification algorithms, reducing their efficiency. Overall, these effects will result in a shorter final key, whose length is quantified by the finite-key analysis. In [40], one can find a clear and intuitive term-by-term explanation finite-key analysis for binary QKD, whose meaning can easily be generalized to a larger-dimensional space.

The considerations made so far are based solely on theoretical models. In an experimental setting, one must also account for the repetition rate f at which the protocol rounds are performed. The key fraction r and the repetition rate combine in the *secret key rate* $R = r \cdot f$, which describes the number of secure bits transmitted per second. In any practical implementation of QKD, increasing the repetition rate is therefore as critical as improving the key fraction. This implies that, for experimental designs that present a trade-off between repetition rate and QBER, these two quantities must be carefully balanced. A typical example is the application of filtering to improve the QBER, which inevitably discards more signal and thus reduces the effective repetition rate.

Finally, any practical realization of QKD will come with its own loopholes, which must be countered and accounted for in the final key rate estimation. One notorious example is the *photon-number-splitting* attack: due to easier technical accessibility, prepare-and-measure protocols typically use attenuated coherent pulses instead of true single photons. As a result, in some rounds Alice will send

more than one photon (i.e., at least two identical qudits), giving Eve the chance to measure only one photon and remain undetected. This attack can be countered with the *decoy states* technique, which consists in picking a different predefined mean-photon-number in each round [41]. In the classical post-processing phase, these values can be compared to the detection probability to verify whether a photon-number-splitting attack was carried out—clearly, at the cost of more discarded key bits.

1.4.4 Entanglement-based HD-QKD

In this section, we have explored a high-dimensional prepare-and-measure protocol, similar in structure to the original BB84. However, any such protocol can be mapped to an equivalent entanglement-based scheme, where Alice prepares an entangled state, measures her subsystem in one of the m bases, and sends the remaining qudit to Bob [17]. Security proofs are typically derived for entanglement-based schemes and then translated to their prepare-and-measure equivalent, as this approach often simplifies the analysis.

Despite their equivalence in security proofs, these two types of protocols differ significantly in practical implementations. For instance, entanglement-based QKD is inherently resilient to the photon-number-splitting attack: even if two photons were sent to Bob in the same round, they would not necessarily be in the same quantum state, therefore Eve would get no useful information by measuring one of them (although this same effect may slightly increase the QBER). Moreover, since the security proof of entanglement-based protocols relies on the violation of Bell inequalities, the entanglement source could even be directly handed over to Eve without compromising security—hence the term *device-independent* QKD used to describe this type of schemes. However, this robustness comes at a cost: despite these advantages, entanglement-based QKD is significantly more challenging to implement experimentally. As a result, both protocols continue to be actively studied and tested still today.

1.5 Chapter conclusion

This concludes the first part of the theoretical introduction to this thesis, which focused on qudits in quantum communication. In this chapter, we started from the fundamentals of classical information theory, exploring the meaning of information itself and its link to the Shannon entropy, and extended these concepts to quantum mechanics, where the unique properties of qubits enable new communication protocols. Then, we expanded our Hilbert space, introducing qudits as the generalization of qubits to high-dimensional systems, and analyzed how this led to new interesting properties for quantum information and communication. Finally, we explored an HD-QKD protocol, from its step-by-step implementa-

tion to its secret key estimation after eavesdropping attacks, highlighting the advantages of encoding in high dimensions and more bases.

The major challenge of HD-QKD is arguably its experimental realization. To move from theory to practice, we need three key components: a robust high-dimensional alphabet to encode the qudits, a high-dimensional entanglement source capable of generating the required quantum states, and, most critically, a versatile high-dimensional decoder. Such a decoder must be able to perform simultaneous, high-fidelity single-shot projective measurements onto all elements of an arbitrary d-dimensional basis, a capability that represents a significant experimental bottleneck. The remainder of this thesis is therefore dedicated to the design, implementation, and characterization of the devices that solve these challenges, thereby translating the theoretical advantages discussed here into practical, real-world applications.

2

Time-frequency qudits and integrated nonlinear processes

In the previous chapter, we established the significant theoretical advantages of high-dimensional quantum states for communication. The time-frequency domain of photons offers a particularly robust and scalable platform for such encodings. Realizing this potential, however, requires experimental tools capable of generating and decoding qudits with high fidelity, versatility, and scalability. While specialized devices have been developed in both state generation [42–47] and detection [48–52], the field has lacked a flexible framework adaptable to different dimensionalities, bases, encoding schemes, and applications.

This thesis develops and demonstrates such a versatile framework based on time-frequency qudits, which for the first time enables precise, programmable control over their generation and decoding. At the core of this framework are the two key components that were previously missing: a programmable source of high-dimensional entanglement and a reconfigurable high-dimensional decoder for time-frequency qudits. We realized these devices through the careful engineering of integrated nonlinear processes, which required a deep understanding of their underlying physical principles. Before presenting the experimental implementation of our system, it is therefore essential to establish these fundamentals, as they provide the necessary foundation to understand not only the operation of our devices but also the specific choices made to optimize their performance.

In this chapter, we build this essential toolkit for the experimental work central to this thesis. We begin by identifying the time-frequency degree of freedom of photons as the ideal information encoding platform for high-dimensional quantum communication, and we explore possible high-dimensional alphabets in this domain. Then, we focus on nonlinear integrated processes, namely parametric down-conversion and sum-frequency generation, as the means to generate and detect time-frequency qudits. Finally, we investigate techniques to tailor these processes through dispersion engineering and spectral shaping, essential to adapt these methods to a wide range of applications, while also providing a foundation that enables future expansions of this framework.

2.1 Time-frequency qudits

In any physical implementation of a qudit, the basis states $|0\rangle, \ldots, |d-1\rangle$ represent mutually exclusive properties of the quantum particle that encodes the information. Common examples for qubit encoding are the spin state of an electron, the energy of a two-level atomic system or the polarization of a photon. However, for qudits we need a high-dimensional encoding alphabet. This can be realized in a quantum system with many possible states, such as multiple energy levels of an atom, the spatial distribution of a photon, or the discretized time or frequency regions it can occupy. In order to build a quantum information framework from these systems, and thus implement high-dimensional quantum communication, we need tools to prepare, manipulate, and measure the quantum states that encode information [16].

For quantum communication, photons are the natural choice of information carriers: they travel at the speed of light and do not interact with other radiation, which helps preserve quantum states over long distances. Transmitting information over long distances is crucial for communication, but is often challenging due to optical loss. In practice, photons are typically distributed through free space or low-loss optical fibers, depending on the environment; therefore, our choice of encoding alphabet must be compatible with these infrastructures and resilient in transmission.

2.1.1 Photonic degrees of freedom

In order to encode quantum information into photons, we first need to identify the physical properties that we can use to build an encoding alphabet. To understand this, we start by describing the quantum electric field. The field

operator at position $\mathbf{r}$ and time t can be written as a sum of its positive- and negative-frequency[1] components [53]:

$$\hat{\mathbf{E}}(\mathbf{r},t) = \hat{\mathbf{E}}^{+}(\mathbf{r},t) + \hat{\mathbf{E}}^{-}(\mathbf{r},t), \tag{2.1.1}$$

where $\hat{\mathbf{E}}^{+}(\mathbf{r},t)$ is the annihilation operator of the electric field, and $\hat{\mathbf{E}}^{-}(\mathbf{r},t) = (\hat{\mathbf{E}}^{+}(\mathbf{r},t))^{\dagger}$ is the creation operator. In a limited volume V, such as in a cavity, photons can only exist in specific *modes* (or superpositions of modes) corresponding to the standing-wave solutions of the field equation, defined by discrete frequencies ω_l and wavevectors $\mathbf{k}_l$.

The expression for $\hat{\mathbf{E}}^{+}(\mathbf{r},t)$ in free space can be derived from the quantization of the classical complex field and expressed as the sum of monochromatic plane wave modes [54]:

$$\hat{\mathbf{E}}^{+}(\mathbf{r},t) = i\sum_{l} \mathcal{E}_l \hat{a}_l \boldsymbol{\epsilon}_l e^{i(\mathbf{k}_l\mathbf{r}-\omega_l t)}, \quad \mathcal{E}_l = \sqrt{\frac{\hbar\omega_l}{2\varepsilon_0 V}}. \tag{2.1.2}$$

Here, $\mathcal{E}_l$ is the single-photon electric field, $\hat{a}_l$ is the annihilation operator for plane-wave mode l, and ϵ_l is the polarization vector.

The different eigenmodes derived from the same field equation are orthogonal[2], therefore, we could build an encoding basis from monochromatic plane wave modes. However, this is not the most practical alphabet to operate with, for two fundamental reasons. Spatially, plane waves are infinitely large and thus cannot be confined to a practical transmission medium like an optical fiber. More critically, monochromatic waves have an infinite time duration, which makes them unsuitable for any communication protocol that relies on sending distinct symbols over time.

In order to identify other possible encoding alphabets for photons, it is convenient to reformulate expression (2.1.2) to separate the different degrees of freedom. This can be done by making some reasonable approximations focused on quantum communication applications, i.e., on the goal of transmitting quantum information. First, we assume a fixed propagation direction along the z-axis, which defines the direction along which we transmit the photons. Under this assumption, the field becomes approximately collinear (paraxial approximation, $|\mathbf{k}_l| \approx k_{z,l}$) and the polarization direction is transverse, confined to the xy-plane.

Then, under the assumption of long-distance propagation, we extend the cavity along the z-direction indefinitely. Mathematically, this is done by factorizing the system volume into $V = AL$, and extending its length $L \to +\infty$ while keeping

[1] We follow the convention in [53, 54] and label "positive" ("negative") the part of the electric field associated to the clockwise (counterclockwise) rotation of the field in the complex plane as t increases. The opposite notation is also commonly used.

[2] Note that any solution of the field equation is still a *mode*; this includes superpositions of the eigenmodes, which are not orthogonal to the eigenmodes themselves.

the area A in the xy-plane limited. This extension to an infinitely long cavity reduces the separation between the discrete parameters ω_l and $k_{z,l}$, converting them into the continuous variables ω and $k_z(\omega) \approx \omega/c$, respectively. The (small) transverse components of the wavevector $k_x, k_y \ll k_z$ remain quantized due to the constrained area A.

Due to ω becoming continuous, the sum over all possible values of ω_l becomes an integral over all positive frequencies. Since real-world communication is typically limited to a finite bandwidth $\Delta\omega \ll \omega_0$ around a central frequency ω_0, we can safely extend the integral range to infinity without expecting divergence. Under all these assumptions, we can finally rewrite the electric field as [53]

$$\hat{\mathbf{E}}^+(\mathbf{r},t) = i\mathcal{E}\sum_{j,l}\boldsymbol{\epsilon}_j e^{i(k_{l,x}x+k_{l,y}y)}\int \mathrm{d}\omega\, \hat{a}_{j,l}(\omega)e^{i(k_z(\omega)z-\omega t)}, \quad \mathcal{E} = \sqrt{\frac{\hbar\omega_0}{4\pi\varepsilon_0 cA}}. \tag{2.1.3}$$

This expression explicitly reveals the different degrees of freedom of photons: *polarization*, determined by the vector $\boldsymbol{\epsilon}_j$, *space*, given by the combination of wavevectors and coordinates in the xy-plane, and *frequency*, described by the terms in the $\mathrm{d}\omega$ frequency integral. These degrees of freedom are associated to their respective modes, which identify possible encoding alphabets for quantum information. In this thesis, we will refer to the modes in the temporal degree of freedom as "time-frequency" modes, as we will consider both their spectral and temporal properties.

While the polarization degree of freedom is the most common platform for quantum communication, it is not suitable for qudits as it is intrinsically limited to two dimensions. In contrast, both the spatial and time-frequency degrees of freedom can provide high-dimensional bases, and both have been used for various quantum communication demonstrations [14, 49, 51, 55–59]. However, the latter arguably offers the most advantages for qudit-based communication, as time-frequency modes are compatible with the existing spatially single-mode optical fiber infrastructure and are resilient in transmission, because they maintain orthogonality even through slowly-varying perturbations (e.g., linear dispersion) [16]. For this reason, this thesis will focus on the time-frequency degree of freedom of photons as an encoding platform for high-dimensional quantum communication.

2.1.2 Temporal modes

Let us consider the quantum electric field in eq. (2.1.3) to be in a single spatial and polarization mode. This leaves the field to be characterized only by the frequency integral, which contains all possible monochromatic modes. However, in quantum communication, it is common to use light pulses, because they allow information to be transmitted in discrete shots. Describing them using

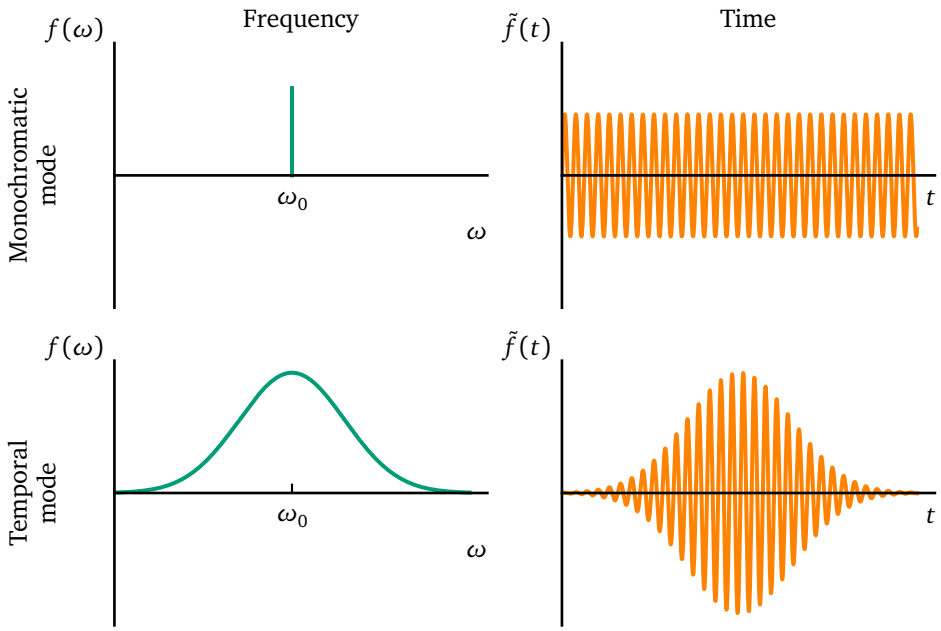

Figure 2.1: Illustration of the envelope function of a monochromatic mode **(top)** and Gaussian-shaped temporal mode **(bottom)** in frequency and time, where the two descriptions are linked by a Fourier transform. The oscillations in time derive from the carrier frequency ω_0.

monochromatic modes is inconvenient, as pulses inherently contain infinitely many frequency components.

To address this, we define a temporal mode (TM) $f(\omega)$ as a wavepacket mode that can be expressed as a coherent superposition of monochromatic modes [16, 59]. While the mode itself is a classical function which describes the complex spectral amplitude profile of the pulse as a function of frequency, it can be used to define a creation operator $\hat{A}^\dagger$ which, when applied to the vacuum state $|\text{vac}\rangle$, generates a single-photon state in this specific TM:

$$|A\rangle = \hat{A}^\dagger |\text{vac}\rangle := \int \frac{\mathrm{d}\omega}{2\pi} f(\omega)\, \hat{a}^\dagger(\omega) |\text{vac}\rangle \,, \tag{2.1.4}$$

where $\hat{a}^\dagger(\omega)$ is the monochromatic creation operator at frequency ω. The term "coherent" is crucial, as it implies that there is a fixed phase relationship between the different frequency components.

Throughout this thesis, we will mainly consider single-photon states. For the sake of simplicity, we will therefore often refer to the single-photon state $|A\rangle$ and its underlying TM $f(\omega)$ interchangeably, and we will typically indicate the mode simply as A. However, it is important to remember this shorthand is not valid for multi-photon states, where the distinction between mode and state is essential.

Labeling these states "temporal" modes while describing them in terms of frequency might appear counterintuitive. However, time and frequency are inherently related by the nature of a monochromatic wave, which oscillates in time at a certain frequency. As a consequence, these two variables are Fourier conjugates, and the time and frequency descriptions of temporal modes are equivalent (see Figure 2.1).

We can use a Fourier transform to reformulate (2.1.4) in terms of time. Following standard convention, we indicate with $\mathcal{F}$ the Fourier transform and with $\tilde{\mathcal{F}}$ its inverse, which differs only by a sign and normalization factor. We can calculate the time-dependent envelope function $\tilde{f}(t)$ and the creation operator $\hat{\tilde{a}}^\dagger(t)$ which creates a photon at time t:

$$\tilde{f}(t) \equiv \tilde{\mathcal{F}}\{f(\omega)\} = \int \frac{\mathrm{d}\omega}{2\pi} e^{i\omega t} f(\omega) \iff f(\omega) = \mathcal{F}\{\tilde{f}(t)\} = \int \mathrm{d}t\ \tilde{f}(t) e^{-i\omega t}\,, \tag{2.1.5}$$

$$\hat{\tilde{a}}^\dagger(t) \equiv \tilde{\mathcal{F}}\{\hat{a}(\omega)\}^\dagger = \int \frac{\mathrm{d}\omega}{2\pi} e^{-i\omega t}\, \hat{a}^\dagger(\omega) \iff \hat{a}^\dagger(\omega) = \mathcal{F}\{\hat{\tilde{a}}(t)\}^\dagger = \int \mathrm{d}t\ e^{i\omega t}\, \hat{\tilde{a}}^\dagger(t)\,. \tag{2.1.6}$$

Substituting these terms into eq. (2.1.4) gives

$$\begin{aligned} |A\rangle &= \int \frac{\mathrm{d}\omega}{2\pi} f(\omega)\, \hat{a}^\dagger(\omega)\, |\mathrm{vac}\rangle = \int \frac{\mathrm{d}\omega}{2\pi} \left(\int \mathrm{d}t\ \tilde{f}(t) e^{-i\omega t} \right) \hat{a}^\dagger(\omega)\, |\mathrm{vac}\rangle \\ &= \int \mathrm{d}t\ \tilde{f}(t) \left(\int \frac{\mathrm{d}\omega}{2\pi}\, \hat{a}^\dagger(\omega) e^{-i\omega t} \right) |\mathrm{vac}\rangle = \int \mathrm{d}t\ \tilde{f}(t)\, \hat{\tilde{a}}^\dagger(t)\, |\mathrm{vac}\rangle\,. \end{aligned} \tag{2.1.7}$$

This expression explicitly tells us how we can equivalently describe the single-photon TM $|A\rangle$ either in terms of time or frequency, while indicating the same exact state.[3]

2.1.3 A temporal mode basis

Each TM represents a quantum state that photons can occupy. In the case of single photons, we can identify the TM envelope function $f_i(\omega)$ with the single-

[3] Technically, in this passage we switched between the notations generally associated with first quantization ($|A\rangle$) and second quantization (using operators like $a^\dagger(\omega)$ applied to the vacuum state $|\mathrm{vac}\rangle$). The notation of the first quantization typically describes which mode a particle is in, which is useful when dealing with a small fixed number of particles, whereas the notation of the second quantization focuses on how many particles are in each mode, which is more helpful for many identical particles and for processes like creating or destroying particles. Although they derive from two different concepts (quantizing particles versus quantizing fields), here we use them as equivalent ways to describe the same physics, changing notation for convenience in different contexts.

photon state $|A_i\rangle$. We can use these states to define the fundamental basis of a high-dimensional Hilbert space. To form a basis for quantum information, the quantum states must be orthonormal, that is, they must be normalized and their overlap (scalar product) must be zero. The overlap between two TMs $|A_i\rangle$ and $|A_j\rangle$ is

$$\begin{aligned}\langle A_i|A_j\rangle &= \langle \text{vac}| \int \frac{d\omega}{2\pi} f_i^*(\omega)\hat{a}(\omega) \int \frac{d\omega'}{2\pi} f_j(\omega')\hat{a}^\dagger(\omega')\,|\text{vac}\rangle \\ &= \int \frac{d\omega}{2\pi} f_i^*(\omega) \int \frac{d\omega'}{2\pi} f_j(\omega')\delta(\omega,\omega') \\ &= \int \frac{d\omega}{4\pi^2} f_i^*(\omega) f_j(\omega)\,. \end{aligned} \tag{2.1.8}$$

The orthonormality condition is then

$$\langle A_i|A_j\rangle = \delta_{ij} \quad \Leftrightarrow \quad \int \frac{d\omega}{4\pi^2} f_i^*(\omega) f_j(\omega) = \delta_{ij}\,. \tag{2.1.9}$$

meaning that the complex spectral overlap of the envelopes of two orthogonal TMs is zero.

Constructing a d-dimensional TM basis thus requires choosing a proper set of functions $\{f_i(\omega)\}_{i=0,\dots,d-1}$ with zero mutual overlap. Although there are infinite ways to define such a basis, the most common choices are frequency bins, time bins and pulse modes. While historically treated as distinct encodings, in this thesis we group these in the family of temporal modes, as they are all fundamentally described by complex functions of time and frequency [60]. Since the envelopes of these modes are generally complex, they cannot be fully represented in the real plane as the particular examples in Figure 2.1, but instead require the explicit representation of their amplitude and phase shown in Figure 2.2. In Appendix B.2, we explicitly report the expression for the complex spectral envelope of the main encodings used throughout this thesis.

The fundamental basis of pulsed frequency bins consists in a set of finite envelope functions, generally Gaussian-shaped, centered at different frequencies and sufficiently separated to be effectively intensity-orthogonal according to eq. (2.1.9). In the time description, Gaussian frequency bins are mapped to Gaussian functions that overlap in time, but have different linear phases. MUBs in this encoding are constructed as superpositions of bins from the fundamental basis with appropriate phases, given by the MUB coefficients. In the time domain, these superpositions give rise to oscillations.

Analogously, the fundamental basis of time bins contains a set of finite envelope functions with different delays, with a separation larger than their time duration.

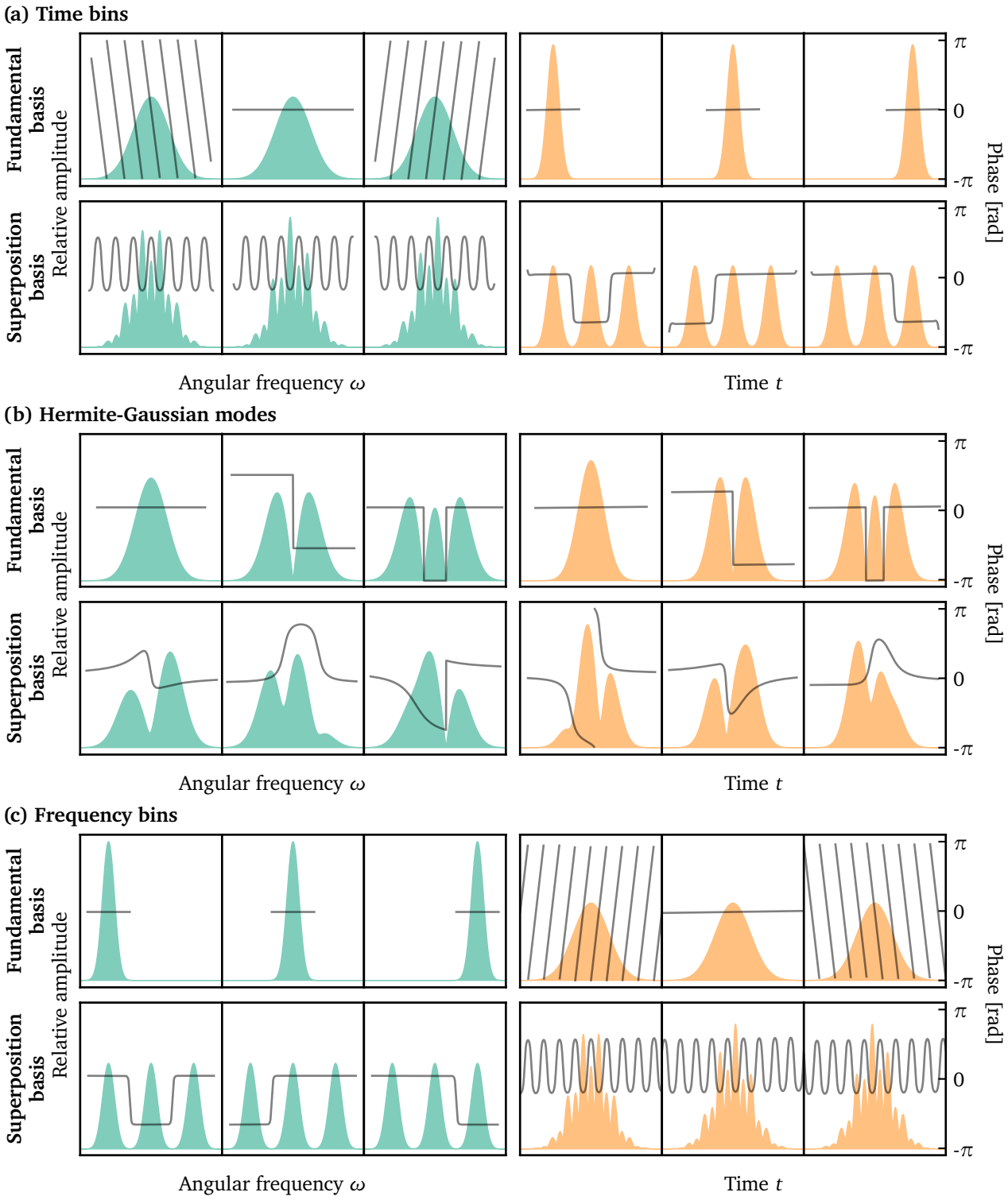

Figure 2.2: Spectral amplitude (filled area) and phase (gray line) of the fundamental basis **(top)** and one MUB **(bottom)** of different TM encoding alphabets in dimension $d = 3$: **(a)** time bins, **(b)** Hermite-Gaussian modes, and **(c)** frequency bins.

In frequency space, different time bins are described by the same envelope function with different linear spectral phases. Similarly to the previous case, MUBs are formed as a superposition of time bins with appropriate phase coefficients, which correspond to oscillations in frequency.

In contrast, the intensity profile of pulse modes overlaps in both time and frequency. Different pulse modes are field-orthogonal (hence satisfy eq. (2.1.9)) due to the phase relations of their respective envelope functions, which have zero overlap with each other. Hermite-Gaussian (HG) modes are a common example of this type of encoding alphabet; due to the properties of HG functions in Fourier transforms, these modes retain the same envelope shape in time and frequency. MUBs are formed by superimposing the fundamental HG modes with phases given by MUB coefficients, which results in different envelope shapes.

2.2 Integrated nonlinear processes

After constructing a high-dimensional Hilbert space based on TMs, we need to implement operations such as the generation of entangled qudits or projective measurements, which form the building blocks of quantum communication protocols. However, we are faced with a challenge: photons do not directly interact with each other! In fact, their bosonic nature allows them to overlap in space and time without influencing one another—an advantage for low-loss communication, but a problem when we want to induce interactions between quantum states. To overcome this, we can exploit light-matter interactions: different electric fields can interact with the same dielectric material, directly influencing each other in the process.

2.2.1 Three-wave mixing in waveguides

Dielectric materials respond to an applied electric field by becoming polarized. This response can be described quantum mechanically[4] by expanding the induced polarization operator as

$$\hat{\mathbf{P}} = \hat{\mathbf{P}}_{\mathrm{L}} + \hat{\mathbf{P}}_{\mathrm{NL}} = \epsilon_0 \left(\chi^{(1)} \hat{\mathbf{E}} + \chi^{(2)} \hat{\mathbf{E}}\hat{\mathbf{E}} + \chi^{(3)} \hat{\mathbf{E}}\hat{\mathbf{E}}\hat{\mathbf{E}} + \dots \right), \tag{2.2.1}$$

which we have separated into its linear $\hat{\mathbf{P}}_{\mathrm{L}} = \epsilon_0 \chi^{(1)} \hat{\mathbf{E}}$ and nonlinear $\hat{\mathbf{P}}_{\mathrm{NL}} = \epsilon_0 \left(\chi^{(2)} \hat{\mathbf{E}}\hat{\mathbf{E}} + \chi^{(3)} \hat{\mathbf{E}}\hat{\mathbf{E}}\hat{\mathbf{E}} + \dots \right)$ terms. Here, $\hat{\mathbf{E}}$ is the quantized electric field in (2.1.1), and $\chi^{(i)}$ are the ith-order susceptibility tensors. The linear term accounts for effects such as refraction, dispersion, and absorption. To enable photon-photon interaction, we rely on the nonlinear term, particularly on the second-order nonlinearity $\chi^{(2)}$. This coefficient is nonzero only in non-centrosymmetric

[4] Three-wave mixing is typically introduced in the framework of classical nonlinear optics [48, 61, 62], and only then extended to the quantum domain. For conciseness, and in line with the focus of this thesis, here we present the quantum picture directly.

materials like lithium niobate ($LiNbO_3$) or potassium titanyl phosphate (KTP), where $\chi^{(2)}$ processes are dominant compared to third-order effects. Therefore, we approximate the nonlinear polarization as

$$\hat{\mathbf{P}}_{\mathrm{NL}} \approx \epsilon_0 \chi^{(2)} \hat{\mathbf{E}}\hat{\mathbf{E}}. \tag{2.2.2}$$

This term gives rise to a process known as *three-wave mixing*, where two electric fields induce a polarization that, in turn, radiates a third electric field.

To enhance nonlinear interactions, we typically work in an integrated platform using waveguides. Waveguides offer two main advantages: they confine the light to a small cross-sectional area, thereby improving the spatial overlap between interacting fields, and maintain this strong overlap over longer interaction lengths than bulk crystals, where beam spreading reduces the interaction efficiency. In this thesis, we focus on *weakly guiding* waveguides, characterized by a low refractive index contrast between the core and substrate. This is the case, for example, in titanium in-diffused $LiNbO_3$ waveguides or rubidium-exchanged KTP waveguides. The description of three-wave mixing in weakly guiding waveguides has been derived rigorously in *Engineering ultrafast quantum frequency conversion* by B. Brecht [63]. In this section, we will summarize the key concepts of this derivation.

In weakly guiding waveguides, the confinement in the transverse xy-plane leads to discrete spatial modes denoted by $\zeta_k(x,y)$. Each spatial mode, combined with the field's polarization, has an *effective refractive index* $n_k(\omega)$ which typically differs slightly from the bulk value, leading to an *effective wavevector* $\boldsymbol{\beta}_k$ of magnitude

$$\beta_k = n_k(\omega)\frac{\omega}{c}, \tag{2.2.3}$$

also called the *propagation constant*. The positive-frequency component of the electric field becomes

$$\hat{\mathbf{E}}^{+}(\mathbf{r},t) = i2\pi \sum_k \boldsymbol{\epsilon}_k \zeta_k(x,y) \int \mathrm{d}\omega \sqrt{\frac{\hbar\omega}{4\pi\varepsilon_0 c n_k(\omega)}}\, \hat{a}_{j,l}(\omega) e^{i(\beta_k(\omega)z-\omega t)}. \tag{2.2.4}$$

2.2.2 Nonlinear interaction Hamiltonian

To understand how this field is affected by the polarizability, we start by considering the general time evolution of a quantum state $|\psi(t)\rangle$ from $t=0$ to $t=T$:

$$|\psi(T)\rangle = \exp\left\{-\frac{i}{\hbar}\int_0^T \hat{\mathcal{H}}(t)\,\mathrm{d}t\right\}|\psi(0)\rangle\,, \tag{2.2.5}$$

where we neglected the time-ordering operator[5]. The Hamiltonian $\hat{\mathcal{H}}(t)$ is related to the energy of the quantum system, and for three-wave mixing it is

$$\hat{\mathcal{H}} \propto \int_V \hat{\mathbf{P}}_{\mathrm{NL}} \hat{\mathbf{E}} \, \mathrm{d}V = \int_V \chi^{(2)} \hat{\mathbf{E}} \hat{\mathbf{E}} \hat{\mathbf{E}} \, \mathrm{d}V \,, \tag{2.2.6}$$

where the integral is taken over the total interaction volume. We use the proportionality symbol ($\propto$) to emphasize that, in the context of this thesis, we are mainly interested in how the nonlinear Hamiltonian depends on the relevant physical quantities—such as the electric field amplitudes, the nonlinear susceptibility, and the spatial mode overlap—rather than in its exact numerical value. Determining the absolute prefactor is nontrivial: different derivations [63, 65] yield slightly different coefficients, which are difficult to verify experimentally. Therefore, we will focus on the functional dependencies that govern the nonlinear interaction, while absorbing all constant factors into a global parameter that characterizes its overall gain.

Let us consider an electric field $\hat{\mathbf{E}}$ that contains three components, each in a particular polarization and spatial mode (that is, $k \in \{1,2,3\}$ in eq. (2.2.4)):

$$\hat{\mathbf{E}} = \hat{\mathbf{E}}_1 + \hat{\mathbf{E}}_2 + \hat{\mathbf{E}}_3 \,. \tag{2.2.7}$$

By separating each field into its positive and negative frequency parts, we can expand the triple product in eq. (2.2.6) into the sum of all possible combinations of the three fields:

$$\hat{\mathcal{H}} \propto \sum_{i,j,k} \int_V \chi^{(2)}_{i,j,k} \hat{\mathbf{E}}_i^{\pm} \hat{\mathbf{E}}_j^{\pm} \hat{\mathbf{E}}_k^{\pm} \, \mathrm{d}V + \mathrm{h.c.}, \quad i,j,k \in \{1,2,3\} \tag{2.2.8}$$

where the three indexes i, j, k can also be degenerate.

Since the only time-dependent part of the electric field is in its exponent $e^{i\omega t}$, taking the time integral in eq. (2.2.5) leads to a term in the form

$$\int e^{i(\pm\omega_i \pm \omega_j \pm \omega_k)t} \, \mathrm{d}t = \delta(\pm\omega_i \pm \omega_j \pm \omega_k), \quad i,j,k \in \{1,2,3\}, \tag{2.2.9}$$

[5]The rigorous expression for the time evolution of a quantum state is $|\psi(T)\rangle = \hat{\mathcal{T}} \exp\left\{-\frac{i}{\hbar}\int_0^T \hat{\mathcal{H}}(t)\,\mathrm{d}t\right\}|\psi(0)\rangle$, where $\hat{\mathcal{T}}$ is the *time-ordering operator*, which rearranges time-dependent operators according to the time instant on which they act. This is mathematically required because the Hamiltonian does not commute at different points in time. Essentially, the time-ordering operator ensures that the interactions are accounted for in the correct sequence. In this context, it means that the electric fields are modified as they propagate through the waveguide, affecting the nonlinear interactions at subsequent times. A detailed analysis of time-ordering effects in some nonlinear processes was performed by Christ et al. [64], showing that its effects become more visible in the high-gain regime, i.e., for high interaction strengths. In this thesis, however, we will consider the low-gain regime, in which time-ordering effects are negligible.

which contains all possible combinations of signs. This expression assumes non-zero values only when

$$\pm\omega_i \pm \omega_j \pm \omega_k = 0\,, \tag{2.2.10}$$

which defines the energy conservation condition of three-wave mixing, excluding unphysical processes such as the simultaneous creation or annihilation of three photons.

Many sets of frequencies satisfy this condition, leading to all possible three-wave mixing processes [63]. Here, we will focus on a set of frequencies related by

$$\omega_3 = \omega_1 + \omega_2\,, \tag{2.2.11}$$

which lead to the simplified Hamiltonian

$$\hat{\mathcal{H}} \propto \int_V \chi^{(2)} \hat{\mathbf{E}}_1^+ \hat{\mathbf{E}}_2^+ \hat{\mathbf{E}}_3^- \,\mathrm{d}V + \int_V \chi^{(2)} \hat{\mathbf{E}}_1^- \hat{\mathbf{E}}_2^- \hat{\mathbf{E}}_3^+ \,\mathrm{d}V\,. \tag{2.2.12}$$

In this expression, the first term describes the annihilation of two photons at frequencies ω_1 and ω_2 and the creation of a higher-energy photon at frequency ω_3, while the second term describes the annihilation of a photon at frequency ω_3 and the creation of two lower-energy photons at frequencies ω_1 and ω_2.

In the quantum regime, these processes have exceedingly low probability unless one of the fields is replaced by a strong (classical) *pump* field. By doing so, the *pump function* $\alpha(\omega_\mathrm{p})$, which describes the complex spectral amplitude of the pump, imposes energy conservation by linking the other two frequencies: the nonlinear process can only happen where the pump spectrum "activates" it. If the pump replaces one of the low-energy fields $\hat{\mathbf{E}}_1$ or $\hat{\mathbf{E}}_2$, then we obtain sum-frequency generation (SFG), a process in which two photons are annihilated to create a photon with the sum of their frequencies. On the other hand, if the pump replaces the higher-energy field $\hat{\mathbf{E}}_3$, then we have parametric down-conversion (PDC), a purely quantum process in which a photon in a nonlinear medium decays into two lower-energy photons. We can rewrite the pump wavelength in terms of the other two wavelengths, which we relabel *input* and *output* for SFG ($\omega_\mathrm{p} = \omega_\mathrm{out} - \omega_\mathrm{in}$), and *signal* and *idler* for PDC ($\omega_\mathrm{p} = \omega_\mathrm{s} + \omega_\mathrm{i}$).

The next step to study this process is to perform the volume integral in eq. (2.2.12), which can be split into a transverse integral in the xy-plane and a longitudinal integral along the propagation direction z. The transverse integration yields an overlap factor between the spatial modes, which influences the strength of the conversion process. The longitudinal integration along the waveguide length L results in the *phase-matching* function:

$$\Phi(\Delta\beta) = \int_0^L e^{i\Delta\beta z}\,\mathrm{d}z = L\,\mathrm{sinc}\left(\frac{\Delta\beta L}{2}\right) e^{i\frac{\Delta\beta L}{2}} \tag{2.2.13}$$

where we have defined the *phase mismatch*

$$\Delta\beta(\omega_1,\omega_2,\omega_3) = \pm\beta_1(\omega_1) \pm \beta_2(\omega_2) \mp \beta_3(\omega_3)\,, \tag{2.2.14}$$

with the signs chosen according to whether we are taking the positive- or negative-frequency component in eq. (2.2.12). The phase-matching function defines the momentum conservation condition of the nonlinear process, and is maximized when $\Delta\beta(\omega_1,\omega_2,\omega_3) = 0$; the frequencies that satisfy this condition are said to be phase-matched. Through eq. (2.2.14), we can express the phase-matching function explicitly in terms of frequencies: $\Phi(\omega_1,\omega_2,\omega_3) \equiv \Phi(\Delta\beta(\omega_1,\omega_2,\omega_3))$, so that Φ will be maximized when $\omega_1,\omega_2,\omega_3$ are phase-matched. We note that, if working with monochromatic light, one could directly choose to use a set of perfectly phase-matched frequencies; however, with broadband pulses, we must take into account how the phase mismatch changes for their different frequency components.

We can substitute the complete expression of the fields in eq. (2.2.12) and separate the time-integrated Hamiltonians for the two processes [63]. We make use of the energy conservation condition to implicitly rewrite the pump frequency as a function of the other two, in order to express the phase-matching function and the pump function only in terms of two variables. For SFG, we find

$$\begin{aligned}\int \hat{\mathcal{H}}_{\mathrm{SFG}}(t)\,\mathrm{d}t &\propto \iint \mathrm{d}\omega_{\mathrm{in}}\,\mathrm{d}\omega_{\mathrm{out}}\;\Phi(\omega_{\mathrm{in}},\omega_{\mathrm{out}})\,\alpha(\omega_{\mathrm{out}}-\omega_{\mathrm{in}})\,\hat{a}(\omega_{\mathrm{in}})\,\hat{c}^\dagger(\omega_{\mathrm{out}}) + \mathrm{h.c.}\\ &\equiv \iint \mathrm{d}\omega_{\mathrm{in}}\,\mathrm{d}\omega_{\mathrm{out}}\;\mathrm{G}(\omega_{\mathrm{in}},\omega_{\mathrm{out}})\,\hat{a}(\omega_{\mathrm{in}})\,\hat{c}^\dagger(\omega_{\mathrm{out}}) + \mathrm{h.c.}\,,\end{aligned} \tag{2.2.15}$$

where we defined the *transfer function*

$$\mathrm{G}(\omega_{\mathrm{in}},\omega_{\mathrm{out}}) := \Phi(\omega_{\mathrm{in}},\omega_{\mathrm{out}})\cdot\alpha(\omega_{\mathrm{out}}-\omega_{\mathrm{in}})\,. \tag{2.2.16}$$

For PDC instead we have

$$\begin{aligned}\int \hat{\mathcal{H}}_{\mathrm{PDC}}(t)\,\mathrm{d}t &\propto \iint \mathrm{d}\omega_{\mathrm{s}}\,\mathrm{d}\omega_{\mathrm{i}}\;\Phi(\omega_{\mathrm{s}},\omega_{\mathrm{i}})\,\alpha(\omega_{\mathrm{s}}+\omega_{\mathrm{i}})\,\hat{a}^\dagger(\omega_{\mathrm{s}})\,\hat{b}^\dagger(\omega_{\mathrm{i}}) + \mathrm{h.c.}\\ &\equiv \iint \mathrm{d}\omega_{\mathrm{s}}\,\mathrm{d}\omega_{\mathrm{i}}\;F(\omega_{\mathrm{s}},\omega_{\mathrm{i}})\,\hat{a}^\dagger(\omega_{\mathrm{s}})\,\hat{b}^\dagger(\omega_{\mathrm{i}}) + \mathrm{h.c.}\,,\end{aligned} \tag{2.2.17}$$

where the joint spectral amplitude (JSA) is defined as

$$F(\omega_{\mathrm{s}},\omega_{\mathrm{i}}) := \Phi(\omega_{\mathrm{s}},\omega_{\mathrm{i}})\cdot\alpha(\omega_{\mathrm{s}}+\omega_{\mathrm{i}})\,. \tag{2.2.18}$$

The JSA and the transfer function share a similar mathematical structure, deriving from the product of the pump and phase-matching functions: in order for a process to happen, it needs to simultaneously satisfy the energy and momentum conservation conditions. However, these two functions have a deeply different meaning: the transfer function describes a process in which a quantum input state is converted to an output state, whereas the JSA describes the spectral structure of a (typically entangled) quantum state.

2.2.3 Frequency-space picture and Schmidt decomposition

The frequency-space representation fully describes the three-wave mixing process in the time-frequency degree of freedom. For PDC (Figure 2.3), the JSA correlates the possible frequencies of signal and idler phiotons both in amplitude and in phase. In SFG (Figure 2.4), the transfer function maps input frequency components to output frequencies. The immediate noticeable difference between these two processes is the direction of the pump function, which is angled at 45° for SFG and −45° for PDC because of the different form of the energy conservation condition. Beyond this, the underlying mathematical structure of the two processes is analogous, making it possible to apply the same analysis method and process engineering to both functions.

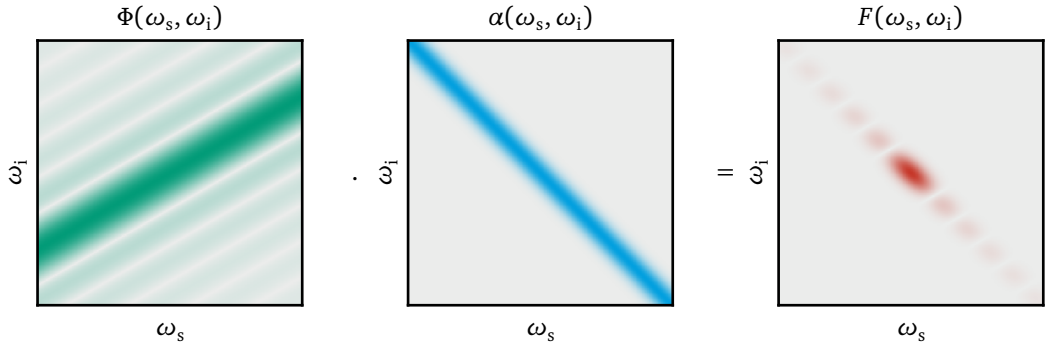

Figure 2.3: Representation of a PDC process in frequency space, as a function of the signal and idler frequencies, ω_s and ω_i. The product of the phase-matching function $\Phi(\omega_s, \omega_i)$ and pump function $\alpha(\omega_s, \omega_i)$ yields the JSA $F(\omega_s, \omega_i)$, which describes the correlations between signal and idler frequencies. Only the amplitude of these two-dimensional functions is represented.

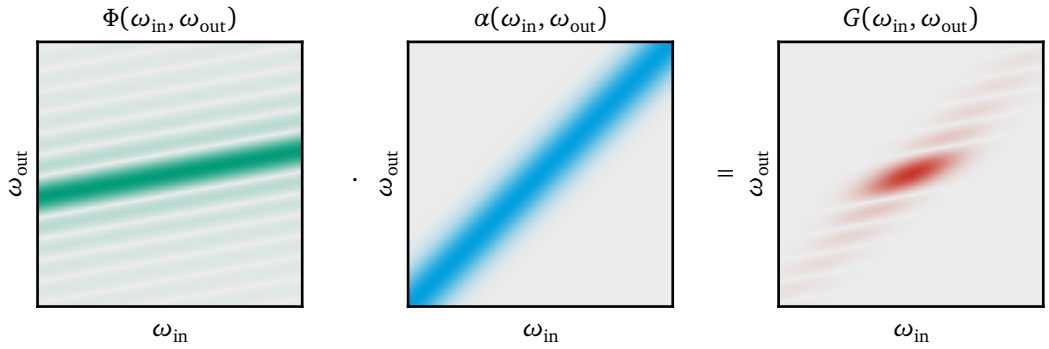

Figure 2.4: Representation of an SFG process in frequency space, as a function of the input and output frequencies, ω_{in} and ω_{out}. The product of the phase-matching function $\Phi(\omega_{in}, \omega_{out})$ and pump function $\alpha(\omega_{in}, \omega_{out})$ yields the transfer function $G(\omega_{in}, \omega_{out})$, which maps input frequency components to output frequencies. Only the amplitude of these two-dimensional functions is represented.

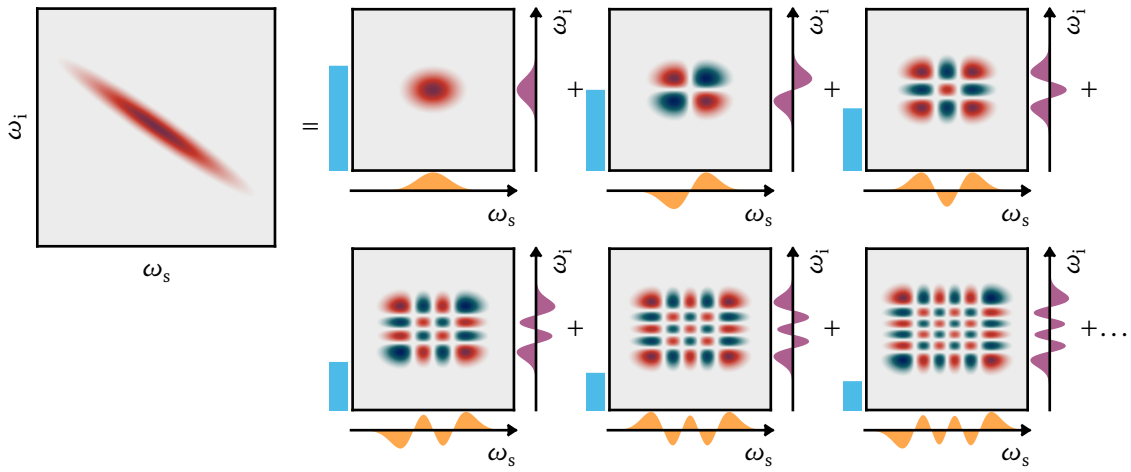

Figure 2.5: Illustration of the Schmidt decomposition for a PDC process in eq. (2.2.19). The JSA $F(\omega_s, \omega_i)$, shown on the left, can be decomposed into pairwise correlated Schmidt modes $f_k(\omega_s)$ (orange) and $g_k(\omega_i)$ (purple), representing the correlated TM envelopes of signal and idler, respectively. The blue bar next to each component represents the corresponding Schmidt coefficient $\sqrt{\lambda_k}$.

In particular, to better analyze both PDC and SFG in terms of TMs rather than just frequencies, we can perform a *Schmidt decomposition* [66–68]. This method rewrites a two-dimensional function (such as the JSA or the transfer function) as a sum of pair-wise products of functions from two basis sets, each depending on only one variable.

For PDC, the Schmidt decomposition reads:

$$F(\omega_s, \omega_i) = \sum_k \sqrt{\lambda_k} f_k(\omega_s) g_k(\omega_i), \tag{2.2.19}$$

where $\sqrt{\lambda_k}$ are the *Schmidt coefficients*, and $\{f_k\}$ and $\{g_k\}$ are orthonormal sets of functions, called *Schmidt modes*, describing the spectral profiles of correlated signal and idler TMs [69]. If the JSA is normalized, i.e., $\iint |F(\omega_s, \omega_i)|^2 \, \mathrm{d}\omega_s \, \mathrm{d}\omega_i = 1$, then the Schmidt coefficients satisfy the normalization condition $\sum_k \lambda_k = 1$. In the remainder of this thesis, we assume a normalized JSA and absorb any scaling factor into the process gain.

We define the creation operators corresponding to the Schmidt modes as

$$\hat{A}_k^\dagger = \int \mathrm{d}\omega_s \, f_k(\omega_s) \hat{a}^\dagger(\omega_s), \quad \hat{B}_k^\dagger = \int \mathrm{d}\omega_i \, g_k(\omega_i) \hat{b}^\dagger(\omega_i), \tag{2.2.20}$$

neglecting the $1/2\pi$ factor from eq. (2.1.4). Substituting this decomposition into the PDC Hamiltonian (2.2.17) leads to

$$\iint \mathrm{d}\omega_s \, \mathrm{d}\omega_i \, F(\omega_s, \omega_i) \, \hat{a}^\dagger(\omega_s) \, \hat{b}^\dagger(\omega_i) = \sum_k \sqrt{\lambda_k} \hat{A}_k^\dagger \hat{B}_k^\dagger. \tag{2.2.21}$$

The time evolution in eq. (2.2.5), then, gives the PDC state

$$|\Psi\rangle_{\mathrm{PDC}} = \prod_k \exp\left\{\mathcal{B}_k \hat{A}_k^\dagger \hat{B}_k^\dagger + \mathrm{h.c.}\right\} |\mathrm{vac}\rangle \,, \tag{2.2.22}$$

where the coupling constant $\mathcal{B}_k$ incorporates the Schmidt coefficient and all the conversion efficiency factors. In the low-gain regime, where the coupling constant is small, we can approximate the PDC state as

$$|\Psi\rangle_{\mathrm{PDC}} \approx \sum_k \mathcal{B}_k \hat{A}_k^\dagger \hat{B}_k^\dagger |\mathrm{vac}\rangle \approx \sum_k \mathcal{B}_k |A_k\rangle |B_k\rangle \,, \tag{2.2.23}$$

where we neglected the vacuum term in the final expression because in experiments we will typically post-select on "clicks", i.e., we will only consider measurements in which we detected at least one photon. Eq. (2.2.23) expresses the PDC state as a superposition of bi-photon temporal modes—the high-dimensional entangled state introduced in Chapter 1. This process is the foundation for the source of high-dimensional entangled states that we demonstrate in Chapter 3, which we realize by tailoring the spectral properties of the entanglement to achieve a controlled modal structure.

Figure 2.5 illustrates an example of Schmidt decomposition of a JSA generated by the product of a Gaussian-shaped pump and a Gaussian-shaped phase-matching function, for simplicity. In this example, the Schmidt decomposition yields an infinite number of Schmidt modes, with exponentially lower coefficients. The TMs associated with signal and idler in this case take the form of HG functions. In principle, the TMs resulting from the Schmidt decomposition can take any form, depending on the shape of the JSA. While all functions shown in this example are real (allowing us to represent them simply by showing their positive and negative parts), in general they could have any arbitrary phase profile.

For SFG, we can perform an analogous Schmidt decomposition to rewrite the transfer function as a set of independent, single-mode conversion processes:

$$\mathrm{G}(\omega_{\mathrm{in}}, \omega_{\mathrm{out}}) = \sum_k \sqrt{\lambda_k}\, f_k^*(\omega_{\mathrm{in}})\, g_k(\omega_{\mathrm{out}}) \,, \tag{2.2.24}$$

where $\{f_k(\omega_{\mathrm{in}})\}$ and $\{g_k(\omega_{\mathrm{out}})\}$ are sets of orthonormal functions describing the complex envelope of the input and output TMs, respectively. For the input envelope, we consider the complex conjugate as we associate it with the annihilation operator

$$\hat{A}_k = \int \mathrm{d}\omega_{\mathrm{in}}\, f_k^*(\omega_{\mathrm{in}})\, \hat{a}(\omega_{\mathrm{in}}) \,, \tag{2.2.25}$$

whereas the creation operator associated to the output is

$$\hat{C}_k^\dagger = \int \mathrm{d}\omega_{\mathrm{out}}\, g_k(\omega_{\mathrm{out}})\, \hat{c}^\dagger(\omega_{\mathrm{out}}) \,. \tag{2.2.26}$$

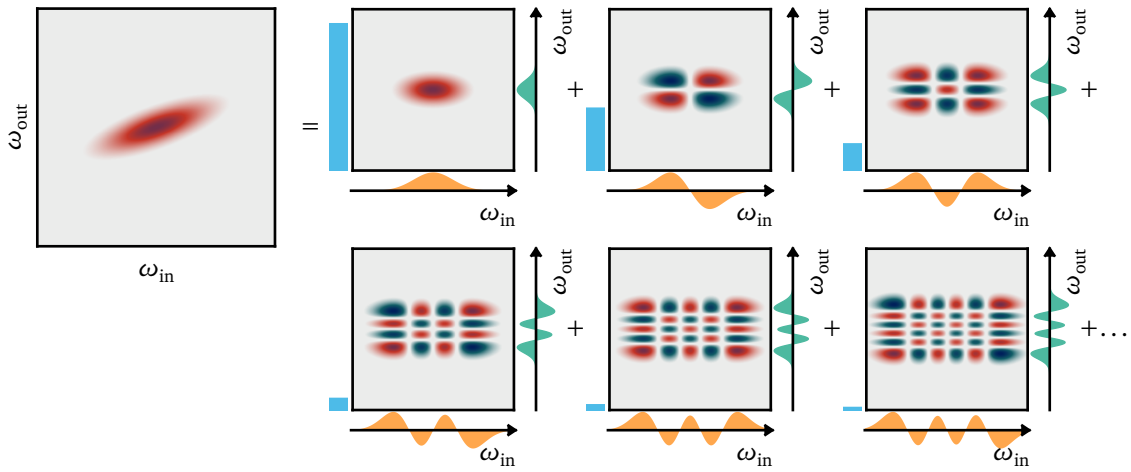

Figure 2.6: Illustration of the Schmidt decomposition for an SFG process in eq. (2.2.24). The transfer function $G(\omega_{in}, \omega_{out})$, shown on the left, can be decomposed into pairwise correlated basis functions $f_k^*(\omega_{in})$ (orange) and $g_k(\omega_{out})$ (green). Each pairwise product of Schmidt modes represents a quantum beam splitter in which an input TM with envelope $f_k(\omega_{in})$ is converted into an output TM with envelope $g_k(\omega_{out})$. The blue bar next to each component represents the corresponding Schmidt coefficient $\sqrt{\lambda_k}$.

Using these definitions, the time-integrated SFG Hamiltonian can be rewritten as

$$\iint \mathrm{d}\omega_{in}\,\mathrm{d}\omega_{out}\; G(\omega_{in},\omega_{out})\,\hat{a}(\omega_{in})\,\hat{c}^{\dagger}(\omega_{out}) + \mathrm{h.c.} = \sum_k \mathcal{C}_k \hat{A}_k \hat{C}_k^{\dagger} + \mathrm{h.c.}\,. \quad (2.2.27)$$

This expression indicates that the frequency conversion process can be understood as a set of parallel, independent single-mode conversion processes, each with a coupling constant $\mathcal{C}_k$ which incorporates the corresponding Schmidt coefficient. Each term of this Hamiltonian is mathematically equivalent to a beamsplitter operation between the input TM associated to $\hat{A}_k$ and the output TM associated with $\hat{C}_k^{\dagger}$, with a splitting ratio determined by $\mathcal{C}_k$. Therefore, the Schmidt decomposition lets us study the SFG process as a tensor product of independent beamsplitters for TMs. This beamsplitter model forms the conceptual basis for our high-dimensional TM decoder; in the next section, we introduce the techniques required to build and tailor this process to design the device we demonstrate in Chapter 4.

2.3 Tailoring nonlinear processes

In the previous section, we introduced the two nonlinear processes that are central to our work with time-frequency qudits: PDC for generating entangled TM states, and SFG as a TM beamsplitter for detection. For the quantum communication protocols that we will demonstrate in this thesis, however, it is not enough to

simply use this processes as they are; we must be able to precisely control and engineer them to meet our specific objectives.

For PDC, our primary goal is to gain full control over the modal structure of the generated entanglement. This involves shaping the JSA to precisely define the number of entangled modes and their relative weights, which are governed by the Schmidt coefficients $\sqrt{\lambda_k}$. Specifically, we aim to generate so-called maximally entangled states, which are characterized by a set of equally weighted Schmidt coefficients. Furthermore, we seek to programmatically control the number of these modes to define the dimensionality of the entanglement.

For SFG, our objective is to build a high-dimensional state decoder. While a standard SFG process (such as the one shown in figure 2.6) is typically multi-mode, it maps a basis of overlapping input TMs to a set of output modes that still overlap both in time and frequency, which does not solve the fundamental detection challenge. A practical decoder must instead *demultiplex* these modes by mapping each orthogonal input to an unambiguously distinguishable output. An effective method to achieve this is to convert each input mode to a distinct, non-overlapping output frequency. This requires engineering a transfer function with multiple, independent conversion processes, each centered at a different output frequency. This multi-channel operation is the working principle of the high-dimensional decoder detailed in Chapter 4, and the key to its realization is a phase-matching function with multiple, well-separated peaks.

We achieve the control required for both of these objectives by tailoring their characteristic two-dimensional spectral functions: the JSA and the transfer function. As their structure in eqs. (2.2.18) and (2.2.16) reveals, this can be accomplished in two ways: by engineering the phase-matching function to control momentum conservation, and by shaping the pump spectrum to control energy conservation. In the this section, we provide an overview of methods for both dispersion engineering and pump shaping, focusing particularly on the periodic poling modulation and 4-f waveshapers central to our experiments. Given the relevance of these methods for our work, this section will present a more technical and detailed discussion than those preceding it.

2.3.1 Dispersion engineering

To understand how we can tailor nonlinear processes, we must first analyze the behavior of the phase-matching function $\Phi(\Delta\beta)$ in frequency space. Since the frequency dependence of this function is determined by the phase mismatch $\Delta\beta(\omega_1, \omega_2, \omega_3)$ through $\Phi(\omega_1, \omega_2, \omega_3) := \Phi(\Delta\beta(\omega_1, \omega_2, \omega_3))$, we have two distinct approaches to control this function: either by changing how Φ depends on $\Delta\beta$, or by modifying how $\Delta\beta$ depends on the interacting frequencies themselves. We begin with this latter approach, which is known as dispersion engineering.

We begin by analyzing the origin of the frequency dependence of the phase mismatch. From the definition of the propagation constant in eq. (2.2.3), $\beta_k = n_k(\omega)\,\omega/c$, we see that this dependence is both direct through the ω factor and indirect through the effective refractive index $n_k(\omega_k)$. The refractive index is, in turn, determined by the waveguide material and geometry, as well as the spatial and polarization modes of each field k [70, 71].

Parametric down-conversion

Let us study the PDC process first. For this process, the phase mismatch is

$$\Delta\beta_{\mathrm{PDC}}(\omega_\mathrm{p},\omega_\mathrm{s},\omega_\mathrm{i}) = \beta_\mathrm{p}(\omega_\mathrm{p}) - \beta_\mathrm{s}(\omega_\mathrm{s}) - \beta_\mathrm{i}(\omega_\mathrm{i})\,. \tag{2.3.1}$$

Generally, we will focus on a particular region of interest around the phase-matched central frequencies $(\bar{\omega}_\mathrm{s},\bar{\omega}_\mathrm{i},\bar{\omega}_\mathrm{p})$, with $\bar{\omega}_\mathrm{p} = \bar{\omega}_\mathrm{s} + \bar{\omega}_\mathrm{i}$. Defining the frequency detunings as

$$\Delta\omega_\mathrm{s} = \omega_\mathrm{s} - \bar{\omega}_\mathrm{s}\,, \quad \Delta\omega_\mathrm{i} = \omega_\mathrm{i} - \bar{\omega}_\mathrm{i}\,, \quad \Delta\omega_\mathrm{p} = \Delta\omega_\mathrm{s} + \Delta\omega_\mathrm{i}\,, \tag{2.3.2}$$

we can perform a Taylor expansion of $\Delta\beta_{\mathrm{PDC}}$ around the central frequencies:

$$\begin{aligned}\Delta\beta_{\mathrm{PDC}}(\Delta\omega_\mathrm{s},\Delta\omega_\mathrm{i}) \approx{}& \beta_\mathrm{p}(\bar{\omega}_\mathrm{p}) - \beta_\mathrm{s}(\bar{\omega}_\mathrm{s}) - \beta_\mathrm{i}(\bar{\omega}_\mathrm{i}) \\ &+ \Big[\beta_\mathrm{p}'(\bar{\omega}_\mathrm{p}) - \beta_\mathrm{s}'(\bar{\omega}_\mathrm{s})\Big]\Delta\omega_\mathrm{s} + \Big[\beta_\mathrm{p}'(\bar{\omega}_\mathrm{p}) - \beta_\mathrm{i}'(\bar{\omega}_\mathrm{i})\Big]\Delta\omega_\mathrm{i} \\ &+ \frac{1}{2}\Big[\Big(\beta_\mathrm{p}''(\bar{\omega}_\mathrm{p}) - \beta_\mathrm{s}''(\bar{\omega}_\mathrm{s})\Big)\Delta\omega_\mathrm{s}^2 + \Big(\beta_\mathrm{p}''(\bar{\omega}_\mathrm{p}) - \beta_\mathrm{i}''(\bar{\omega}_\mathrm{i})\Big)\Delta\omega_\mathrm{i}^2 + 2\beta_\mathrm{p}''(\bar{\omega}_\mathrm{p})\Delta\omega_\mathrm{s}\Delta\omega_\mathrm{i}\Big] \\ &+ \mathcal{O}(\Delta\omega^3)\,,\end{aligned} \tag{2.3.3}$$

where we have defined the first and second derivatives of the propagation constant as

$$\beta_k'(\bar{\omega}_k) = \left.\frac{d\beta_k}{d\omega_k}\right|_{\omega_k=\bar{\omega}_k} = \frac{1}{v_{\mathrm{g},k}(\bar{\omega}_k)}\,, \tag{2.3.4}$$

$$\beta_k''(\bar{\omega}_k) = \left.\frac{d^2\beta_k}{d\omega_k^2}\right|_{\omega_k=\bar{\omega}_k} = \left.\frac{d}{d\omega_k}\left(\frac{1}{v_{\mathrm{g},k}(\omega_k)}\right)\right|_{\omega_k=\bar{\omega}_k} = \mathrm{GVD}_k(\bar{\omega}_k)\,. \tag{2.3.5}$$

Here, $v_{\mathrm{g},k}(\omega_k)$ denotes the group velocity and $\mathrm{GVD}_k(\omega_k)$ the group-velocity dispersion for each field.

Substituting the expansion in eq. (2.3.3) into the phase-matching function $\Phi(\Delta\beta)$ reveals its explicit dependence on ω_s and ω_i. For instance, let us consider the sinc-shaped phase-matching peak in eq. (2.2.13). This function is maximized when $\Delta\beta = 0$; this will always happen at $(\bar{\omega}_\mathrm{s},\bar{\omega}_\mathrm{i})$, because the first line in eq. (2.3.3) vanishes if the central frequencies are perfectly phase-matched. For small frequency detunings, i.e., in the linear regime, the phase-matching function is maximized when

$$\Big[\beta_\mathrm{p}'(\bar{\omega}_\mathrm{p}) - \beta_\mathrm{s}'(\bar{\omega}_\mathrm{s})\Big]\Delta\omega_\mathrm{s} + \Big[\beta_\mathrm{p}'(\bar{\omega}_\mathrm{p}) - \beta_\mathrm{i}'(\bar{\omega}_\mathrm{i})\Big]\Delta\omega_\mathrm{i} = 0\,. \tag{2.3.6}$$

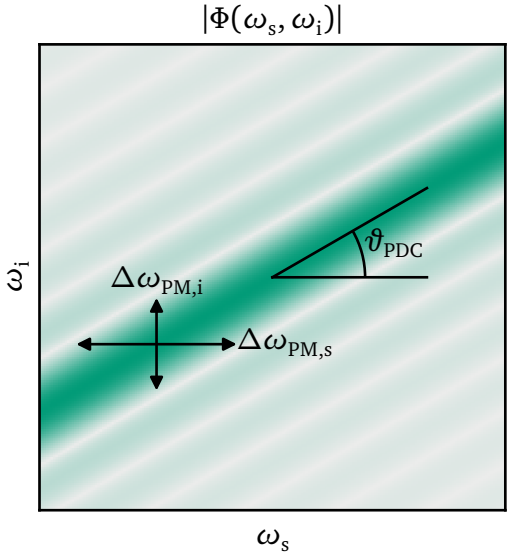

Figure 2.7: Illustration of the phase-matching amplitude $|\Phi(\omega_s, \omega_i)|$ for PDC in frequency space. ϑ_{PDC} is the phase-matching angle from eq. (2.3.7), whereas $\Delta\omega_{PM,s}$ and $\Delta\omega_{PM,i}$ represent the horizontal and vertical phase-matching widths in eq. (2.3.8).

This condition defines a straight line in the signal-idler frequency plane, whose slope is determined by the inverse group velocities of the three fields:

$$\vartheta_{PDC} = -\arctan\left(\frac{\beta_p'(\bar{\omega}_p) - \beta_s'(\bar{\omega}_s)}{\beta_p'(\bar{\omega}_p) - \beta_i'(\bar{\omega}_i)}\right). \tag{2.3.7}$$

This *phase-matching angle* defines all lines of constant $\Delta\beta$ (and hence constant Φ) in the signal-idler frequency plane. The name derives from the fact that, in the linear regime, the phase-matching function looks like a line that passes through $(\bar{\omega}_s, \bar{\omega}_i)$ at an angle ϑ_{PDC} with respect to the horizontal axis (Figure 2.7). In this regime, the phase-matching function also preserves its sinc-function shape in frequency space, as shown in Figure 2.8. When extending the analysis to a broader frequency range, the quadratic terms in eq. (2.3.3) introduce a curvature to the constant-$\Delta\beta$ lines, hence the phase-matching function will curve in frequency space, as shown in Figure 2.9.

Defining a phase-matching width in frequency space is trickier. In terms of $\Delta\beta$, we can define the width of $\Phi(\Delta\beta)$ as the distance $4\pi/L$ between the zeroes[6] of the sinc function in eq. (2.2.13). In the linear regime, any cut of the phase-matching function in the signal-idler frequency plane (provided it is not angled at ϑ_{PDC}) will appear as a sinc function; however, the width of this sinc will depend on the angle of the cut, and the units of this width will only be well-defined along the horizontal or vertical direction. For this reason, the most meaningful definition of phase-matching width in frequency space is obtained by cutting the

[6] A definition based on full width at half maximum (FWHM) is equally valid and corresponds to approximately 44% of the zero-to-zero distance. Here, we prefer the zero-to-zero definition because it remains consistent whether considering the phase-matching amplitude or intensity.

plane parallel to the signal or idler axis, and calculating the distance between the zeroes of the sinc as a function of ω_s or ω_i. This results in

$$\Delta\omega_{PM,s} = \frac{2\pi}{L}\left|\beta_p'(\bar{\omega}_p) - \beta_s'(\bar{\omega}_s)\right|^{-1}, \tag{2.3.8}$$

$$\Delta\omega_{PM,i} = \frac{2\pi}{L}\left|\beta_p'(\bar{\omega}_p) - \beta_i'(\bar{\omega}_i)\right|^{-1}, \tag{2.3.9}$$

along the signal and idler axes, respectively. These quantities are illustrated in Figure 2.7.

Sum-frequency generation

For SFG, the phase mismatch is

$$\Delta\beta_{SFG}(\omega_p, \omega_{in}, \omega_{out}) = \beta_{out}(\omega_{out}) - \beta_{in}(\omega_{in}) - \beta_p(\omega_p). \tag{2.3.10}$$

We can perform a similar expansion as above around the phase-matched frequencies ($\bar{\omega}_{in}, \bar{\omega}_{out}, \bar{\omega}_p = \bar{\omega}_{out} - \bar{\omega}_{in}$), but with two main differences. First, the energy conservation condition changes sign because the pump now replaces one of the lower-energy fields, so that $\Delta\omega_p = \Delta\omega_{out} - \Delta\omega_{in}$. Second, the frequency representation for SFG uses the input-output plane, expressing the explicit dependence on the highest-energy field.

As a consequence, the phase-matching angle with respect to the horizontal (input) axis is expressed by

$$\vartheta_{SFG} = \arctan\left(\frac{\beta_p'(\bar{\omega}_p) - \beta_{in}'(\bar{\omega}_{in})}{\beta_p'(\bar{\omega}_p) - \beta_{out}'(\bar{\omega}_{out})}\right). \tag{2.3.11}$$

The different role of the high- and low-frequency components in SFG and PDC leads to a different phase-matching angle for identical fields. For instance, a phase-matching angle of $\vartheta_{SFG} = 0°$ in SFG corresponds to an angle of $\vartheta_{PDC} = -45°$ in PDC for the same set of fields.

Similarly to the previous case, for SFG we can define the phase-matching width in frequency space as

$$\Delta\omega_{PM,in} = \frac{2\pi}{L}\left|\beta_p'(\bar{\omega}_p) - \beta_{in}'(\bar{\omega}_{in})\right|^{-1}, \tag{2.3.12}$$

$$\Delta\omega_{PM,out} = \frac{2\pi}{L}\left|\beta_p'(\bar{\omega}_p) - \beta_{out}'(\bar{\omega}_{out})\right|^{-1}, \tag{2.3.13}$$

obtained by cutting $\Phi(\omega_{in}, \omega_{out})$ horizontally and vertically, respectively.

From the analysis in this subsection, we see that dispersion engineering provides a powerful means to control the phase-matching shape in frequency space. This can range from straightforward approaches, such as choosing a set of wavelengths

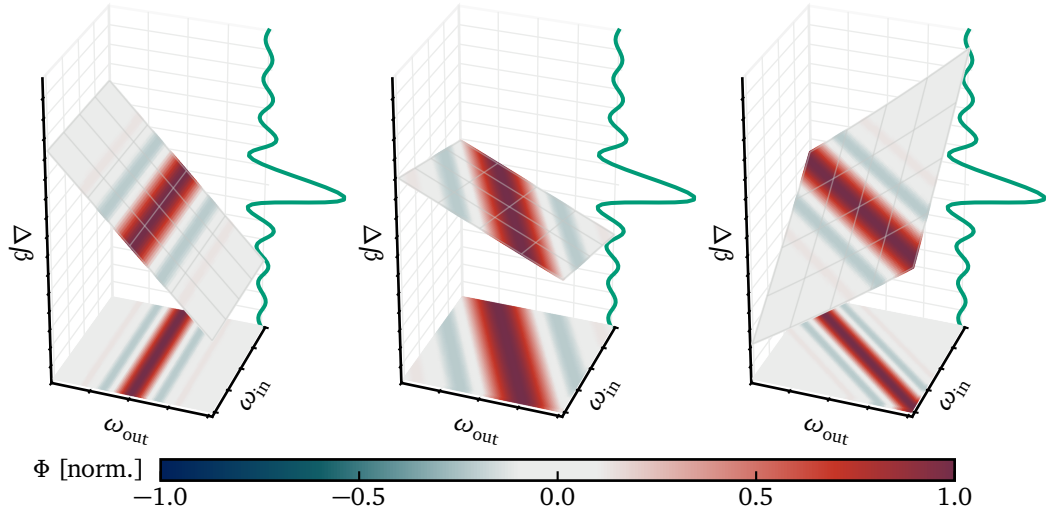

Figure 2.8: Illustration of how the phase mismatch $\Delta\beta$ determines the phase-matching function Φ in frequency space for SFG in the linear regime. In all three examples, the nonlinear waveguide has the same length L, resulting in the same width of $\Phi(\Delta\beta)$ (green line; see eq. (2.2.13)). The phase-matching function $\Phi(\Delta\beta)$ is mapped to $\Phi(\omega_{\text{in}}, \omega_{\text{out}})$ through the 3D plane representing $\Delta\beta(\omega_{\text{in}}, \omega_{\text{out}})$. In the linear regime, this plane is flat, so the phase-matching function retains its sinc shape when it is projected onto the input-output frequency plane. The linear dependence of $\Delta\beta$ on ω_{in} and ω_{out} determines the orientation of the $\Delta\beta$ plane, and thus directly affects both the width and the angle of the phase-matching function in frequency space.

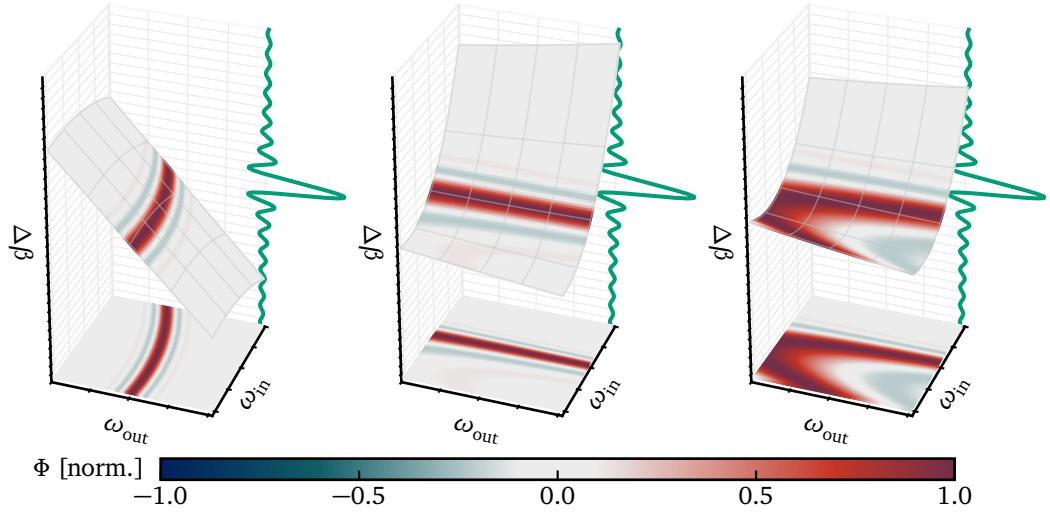

Figure 2.9: Illustration of how the phase mismatch $\Delta\beta$ determines the phase-matching function Φ in frequency space for SFG beyond the linear regime. The represented quantities are the same as in Figure 2.8, but here we are considering a wider frequency range $\Delta\omega$, in which the linear approximation is no longer valid and $\Delta\beta(\omega_{\text{in}}, \omega_{\text{out}})$ becomes a curved surface. In these conditions, the sinc-shaped $\Phi(\Delta\beta)$ is mapped to $\Phi(\omega_{\text{in}}, \omega_{\text{out}})$ which can be curved or distorted, depending on the shape of the $\Delta\beta$ surface.

with specific dispersion properties, to more complex methods like using nanostructures [72, 73] or modifying the geometry of strongly confining waveguides, such as in thin-film lithium niobate platforms [74].

For the weakly guiding waveguides considered in this thesis, however, the waveguide geometry does not significantly affect the dispersion properties. Furthermore, we will operate in a frequency range narrow enough to remain in the linear regime of $\Delta\beta$. Our use of dispersion engineering will therefore consist primarily of selecting the appropriate material, frequencies, and polarizations to achieve a desired phase-matching angle, as detailed in Chapters 3 and 4. Nevertheless, one could in principle develop tailored processes by exploiting the behavior of the phase mismatch beyond the linear approximation to realize unique phase-matching profiles [75].

Now that we have studied how the phase-matching function depends on frequency through $\Delta\beta$, we will proceed to examine methods for modulating $\phi(\Delta\beta)$ directly. The following analysis will be general, applicable to both PDC and SFG, and its conclusions can be mapped to frequency space using the relations introduced here.

2.3.2 Quasi-phase-matching and poling modulation

To tailor the phase-matching function $\Phi(\Delta\beta)$, and thus control which frequencies efficiently interact, we can engineer the spatial dependence of the nonlinear coupling coefficient along the waveguide. In fact, when we defined the phase-matching function in eq. (2.2.13), we implicitly assumed a homogeneous nonlinear susceptibility along the z axis. Relaxing this assumption yields a more general definition:

$$\Phi(\Delta\beta) = \int_0^L d(z)\, e^{i\Delta\beta z}\, \mathrm{d}z\,, \tag{2.3.14}$$

where $d(z) \propto \chi^{(2)}(z)$ describes the spatial dependence of the nonlinear coupling coefficient [61]. This expression resembles a Fourier transform of $d(z)$ from the variable z to $\Delta\beta$, except for the finite integration range corresponding to the finite length of the waveguide. We can express this integration range through the rectangle function Π, defined as

$$\Pi(x) = \begin{cases} 1, & 0 \le x < 1\,, \\ 0, & \text{otherwise}\,. \end{cases} \tag{2.3.15}$$

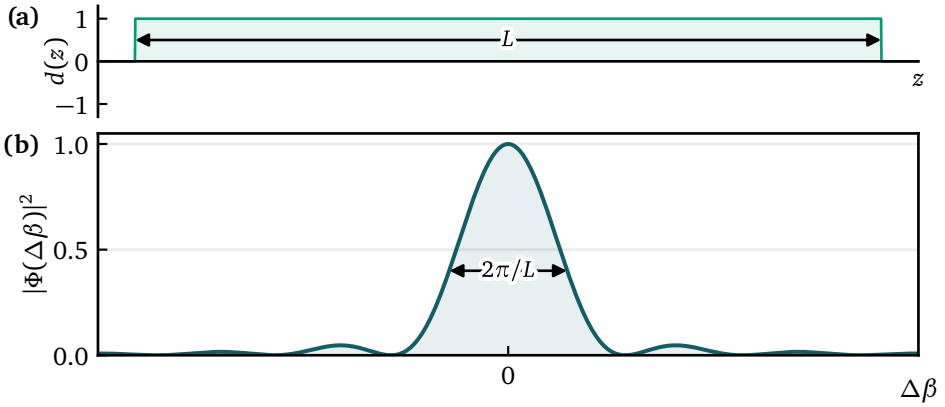

Figure 2.10: (a) Uniform nonlinearity profile $d(z) = 1$ over the waveguide length L for birefringent phase-matching. **(b)** Corresponding phase-matching intensity $|\Phi(\Delta\beta)|^2$, normalized to its peak value, showing the characteristic width determined by the waveguide length L.

This allows us to extend the integration range to infinity and obtain the Fourier transform:

$$\begin{aligned}\Phi(\Delta\beta) &= \int \Pi\left(\frac{z}{L}\right) d(z)\, e^{i\Delta\beta z}\, \mathrm{d}z \\ &= \mathcal{F}\left\{\Pi\left(\frac{z}{L}\right) d(z)\right\} \\ &= L\left[\operatorname{sinc}\left(\frac{\Delta\beta L}{2}\right) e^{i\frac{\Delta\beta L}{2}}\right] * \frac{1}{2\pi}\mathcal{F}\{d(z)\}\,, \end{aligned} \tag{2.3.16}$$

where we have used the convolution theorem (A.1.3) together with the property that the Fourier transform of a rectangle is a sinc function.

This relationship is the key to engineering the phase-matching function. By designing different nonlinearity profiles $d(z)$, we can directly shape its Fourier transform and thus control $\Phi(\Delta\beta)$. We will exploit this principle through a novel technique introduced in this work, super-poling, which generates the multi-peak phase-matching structure that enables our high-dimensional TM decoder discussed in Chapter 4. To build a thorough understanding of this method and its advantages, we will proceed step by step. We begin with the simplest case of a uniform medium (birefringent phase-matching) and then introduce periodic poling (quasi phase-matching) and its phase-reversal modulation. These steps are necessary to fully appreciate the design and advantages of the super-poling method compared to other techniques.

Birefringent phase-matching

If $d(z) = 1$ along the entire length L of the waveguide. the integration in eq. (2.3.16) yields the familiar sinc profile centered at $\Delta\beta = 0$, as given in

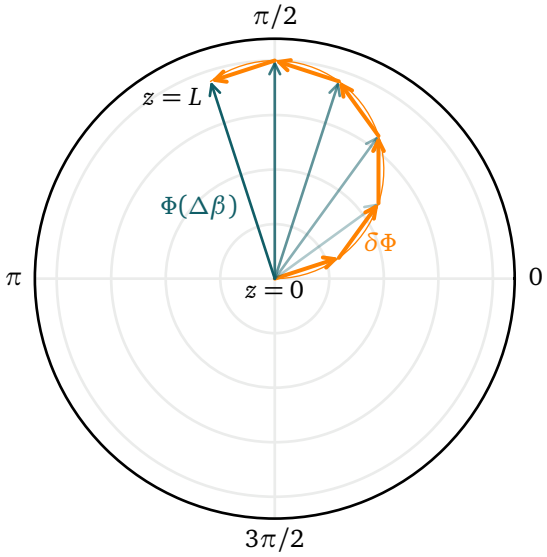

Figure 2.11: Phasor representation of the birefringent phase-matching function $\Phi(\Delta\beta)$ as a function of propagation distance z, for a fixed nonzero phase mismatch $\Delta\beta$ (i.e., for a non-phase-matched set of frequencies). As we move through the nonlinear waveguide, that is, as z increases, the phase-matching function generated in each step (orange arrows) gradually accumulates, moving along a circular trajectory. The blue radial arrows indicate the instantaneous amplitude and phase of $\Phi(\Delta\beta)$ at discrete positions z [62].

eq. (2.2.13) and shown in Figure 2.10. We can gain further insight by analyzing $\Phi(\Delta\beta)$ through its phasor representation, which shows how the amplitude and phase of the phase-matching function evolve along the nonlinear waveguide. This type of analysis was presented in [62], focusing on the generated field; here, however, we study $\Phi(\Delta\beta)$ directly to provide a more general perspective, equally applicable to both SFG and PDC processes.

Figure 2.11 illustrates how such a plot is constructed for a fixed $\Delta\beta \neq 0$ (i.e., for a non-phase-matched set of frequencies). The phase-matching function starts at position $z = 0$ with zero amplitude, in the center of the polar plot. As the position z increases along the waveguide, local contributions to $\Phi(\Delta\beta)$ (orange arrows) are generated with varying phases. These gradually accumulate, resulting in a curved trajectory of the total phase-matching function $\Phi(\Delta\beta)$ (blue radial arrows), which evolves in both amplitude and phase until it reaches its final value at $z = L$. Varying $\Delta\beta$ leads to different phasor trajectories, ultimately determining the overall profile of the phase-matching function.

Figure 2.17 shows phasor plots and the corresponding phase-matching profiles at different points z along the waveguide, which extends from 0 to L. The perfectly phase-matched case, corresponding to $\Delta\beta = 0$, follows a straight line in the phasor diagram, with each local contribution constructively adding in phase. As a result, $\Phi(\Delta\beta = 0)$ increases linearly in amplitude with z. For all other nonzero $\Delta\beta$, as z increases, $\Phi(\Delta\beta)$ moves along a circle of radius proportional to $(\Delta\beta)^{-1}$, determined by the integral of the exponential $e^{i\Delta\beta z}$. Once the trajectory completes a full loop and returns to the zero-amplitude origin, it continues along the same circular path, leading to oscillations in the amplitude of $\Phi(\Delta\beta)$. What this means for the nonlinear process is that as the waveguide length L increases, the conversion efficiency for the perfectly phase-matched frequencies grows quadratically, while the efficiency for neighboring, non-phase-matched

frequencies oscillates. This behavior results in the familiar sinc-shaped profile, which becomes progressively taller and narrower for longer interaction lengths.

Our primary method of dispersion engineering in weakly guiding waveguides, as discussed, consists of selecting a material and a set of operating frequencies and polarizations to achieve a desired phase-matching angle. This approach, however, faces a fundamental constraint: in weakly guiding waveguides, the set of frequencies that satisfy the birefringent phase-matching condition $\Delta\beta = 0$ is essentially determined by the material properties, with little influence from the waveguide geometry. It is highly unlikely that these natural phase-matching frequencies will coincide with the predetermined set we chose for our application. This practical limitation motivates the technique we discuss next, quasi-phase-matching, which provides the flexibility to achieve efficient momentum conservation at arbitrary frequencies.

Quasi-phase-matching

By modifying the nonlinearity profile $d(z)$, it is possible to allow nonlinear interactions for frequency sets that do not naturally satisfy $\Delta\beta = 0$ in the selected material. A widely employed technique is quasi-phase-matching (QPM), which consists in periodically poling the material by inverting the orientation of a crystal axis with a period Λ along the propagation direction [61]. This process creates a structure where the sign of the nonlinear coefficient $d(z)$ alternates between $+1$ (in the natural orientation) and -1 (in the inverted regions) at regular intervals, as shown in Figure 2.12(a). In weakly guiding waveguides and bulk crystals, where dispersion is dominated by material properties, this spatial modulation of the nonlinearity is the most powerful tool available for engineering the phase-matching condition, aside from changing the material itself [76].

Periodic poling shapes $d(z)$ into a square wave $s(z/\Lambda)$, alternating between 1 and -1, which can be expanded as a Fourier series (see Appendix A.1):

$$d(z) = s\left(\frac{z}{\Lambda}\right) = \sum_{n\,\text{odd}} \frac{2}{i\pi n} e^{i\frac{2\pi}{\Lambda}nz}, \tag{2.3.17}$$

with Fourier transform

$$\mathcal{F}\{d(z)\} = 2\pi \sum_{n\,\text{odd}} \frac{2}{i\pi n} \delta\left(\Delta\beta - \frac{2\pi}{\Lambda}n\right). \tag{2.3.18}$$

Substituting this into eq. (2.3.16), we obtain

$$\Phi(\Delta\beta) = L \sum_{n\,\text{odd}} \frac{2}{i\pi n} \operatorname{sinc}\left(\left(\Delta\beta - \frac{2\pi}{\Lambda}n\right)\frac{L}{2}\right) e^{i\left(\Delta\beta - \frac{2\pi}{\Lambda}n\right)\frac{L}{2}}, \tag{2.3.19}$$

which describes a "splitting" of the phase-matching peak into many sinc functions centered at $\Delta\beta = 2\pi n/\Lambda$, as shown in Figure 2.12(b-c). The intensity of each

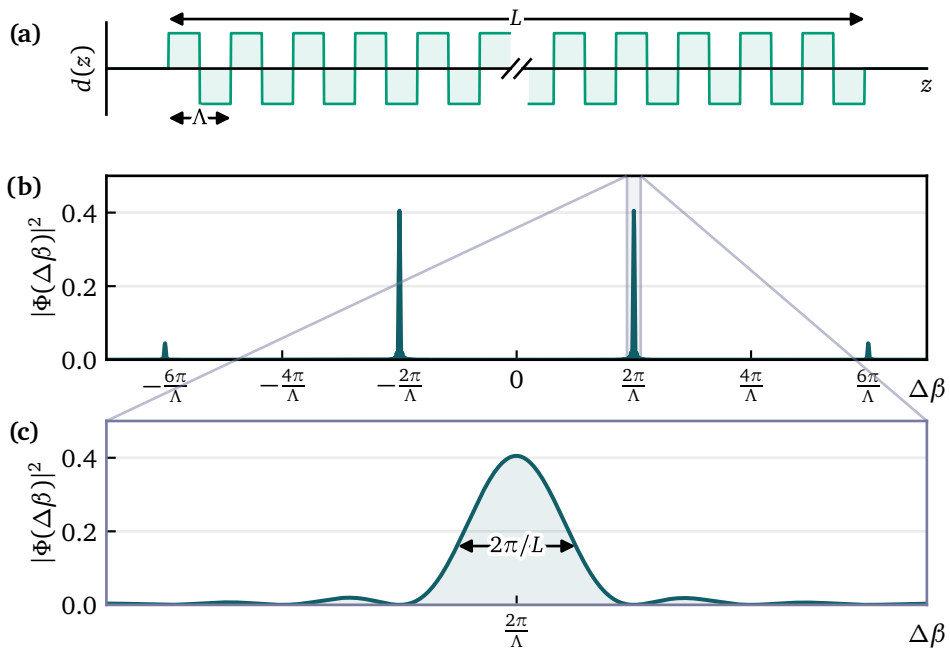

Figure 2.12: **(a)** Periodic nonlinearity profile $d(z)$ for quasi-phase-matching (QPM) with poling period Λ. **(b)** Phase-matching intensity $|\Phi(\Delta\beta)|^2$, showing multiple peaks corresponding to different QPM orders. **(c)** Zoomed-in view of the first-order peak ($n = 1$). The intensity is normalized to the peak of a birefringent process of the same length.

peak is a fraction $\left(\frac{2}{i\pi n}\right)^2$ of the birefringent phase-matching function; therefore, the peaks at $n = \pm 1$ are dominant. The intensities of all peaks sum up to the intensity of the birefringent phase-matching function.

The poling period Λ can be chosen to shift one of these phase-matching peaks to our predefined central frequencies. Typically, one chooses $n = \pm 1$ to obtain the most efficient phase-matching peaks, although this still results in an intensity lower by a factor $4/\pi^2 \approx 0.4$ with respect to the original birefringent process. For simplicity, we consider $n = 1$ and, if Λ is sufficiently small so that the separation between sinc functions is large, we can assume the frequency range of interest contains only one such peak. Defining a shifted phase mismatch

$$\Delta\beta' = \Delta\beta - \frac{2\pi}{\Lambda}, \tag{2.3.20}$$

so that $\Delta\beta'(\bar{\omega}_1, \bar{\omega}_2, \bar{\omega}_1 + \bar{\omega}_2) = 0$, the quasi-phase-matching function can then be approximated by

$$\Phi(\Delta\beta') \approx L \frac{2}{i\pi} \operatorname{sinc}\left(\frac{\Delta\beta' L}{2}\right) e^{i\frac{\Delta\beta' L}{2}}. \tag{2.3.21}$$

This is simply the birefringent phase-matching function in eq. (2.2.13) shifted to the desired central frequencies, with an overall lower efficiency indicated by the pre-factor.

Figure 2.18 shows the amplitude and phase of this function for different $\Delta\beta'$ at various points z along a periodically poled waveguide. The periodic poling inverts the sign of the nonlinearity every time the line at $\Delta\beta' = 0$ (i.e., $\Delta\beta = 2\pi/\Lambda$) would go out of phase, resulting in a series of semi-circles that follow a straight line. The ratio between the effective distance traveled at each semi-circle (i.e., its diameter) and the length of each semicircle is 2π, which corresponds exactly to the amplitude loss experienced with respect to the birefringent process. The overall behavior of the phasor lines at different $\Delta\beta'$ mimics the birefringent case, with the only difference of this semi-circular micro-structure: the phase-matching amplitude at $\Delta\beta' = 0$ constantly increases with z, whereas all other non-quasi-phase-matched trajectories follow a circular orbit that passes through the origin.

By modulating the periodic poling pattern, one can further tailor the phase-matching function beyond just shifting it to different frequencies. This is particularly valuable in weakly guiding waveguides, where, in contrast to strongly confining platforms like thin-film lithium niobate, the waveguide geometry has a negligible effect on dispersion. Since the control is limited to arranging a binary pattern of poled (+1) and unpoled (−1) domains, sophisticated tailoring of $\Phi(\Delta\beta)$ is achieved through more complex modulations of this pattern. For a broad overview of such techniques, we refer to [77, 78]. In the following, we will present two methods that enable the generation of multiple phase-matching peaks. We will first review the established technique of phase reversal, which is primarily used to generate a small number of equal-height peaks. We then introduce the more versatile method of super-poling, which provides an adaptable platform to generate an arbitrary number of peaks and is therefore central to the design of our high-dimensional decoder discussed in Chapter 4.

Poling with phase reversal

One possible method for generating multiple phase-matching peaks is phase-reversal poling [79]. This technique consists of modulating the standard QPM poling pattern by superimposing a second, slower square wave s_D with period Γ and duty cycle $D \in [0, 1]$, which defines the fraction of the period where the modulation is +1. This results in the combined nonlinear profile $d(z)$ shown in Figure 2.13(a).

The resulting phase-matching function is calculated using the Fourier transform method from Section 2.3.2, which involves calculating the Fourier transform of $d(z)$ and substituting it into eq. (2.3.16). The detailed, step-by-step derivation of this process is presented in Appendix A.2. With the same approximations as in the standard QPM case, we obtain the final phase-matching function

$$\Phi(\Delta\beta') \approx L \frac{2}{i\pi} \sum_m c_m(D)\, \mathrm{sinc}\left(\left(\Delta\beta' - \frac{2\pi}{\Gamma} m\right)\frac{L}{2}\right) e^{i\left(\Delta\beta' - \frac{2\pi}{\Gamma} m\right)\frac{L}{2}}, \qquad (2.3.22)$$

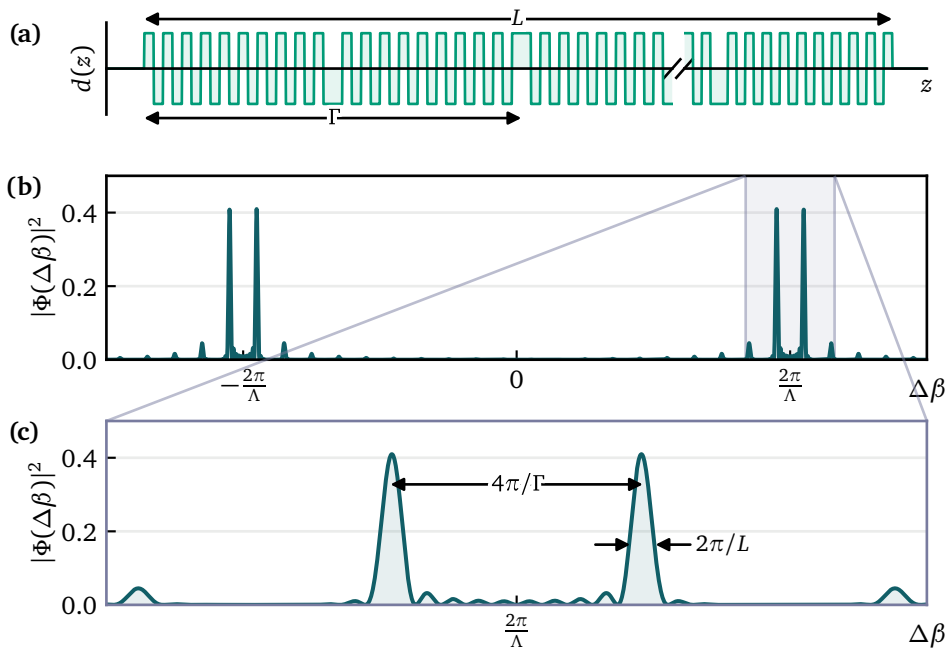

Figure 2.13: **(a)** Modulated nonlinearity profile $d(z)$ for phase-reversal poling with period Γ and duty cycle $D = 0.5$. **(b)** Corresponding phase-matching intensity $|\Phi(\Delta\beta)|^2$. **(c)** Zoomed-in view of the first-order QPM peak, which is now split into two dominant side peaks separated by a distance determined by Γ. The intensity is normalized to the peak of a standard QPM process of the same length.

illustrated in Figure 2.13(b-c). This expression describes a train of sinc-shaped peaks, each identical to a standard QPM peak, but separated in phase mismatch by integer multiples of $2\pi/\Gamma$. The relative amplitude and phase of each peak are determined by a set of complex coefficients $c_m(D)$, given by

$$c_m(D) = \begin{cases} 2D-1, & m = 0\,, \\ -\dfrac{1-e^{-i2\pi mD}}{i\pi m}, & m \neq 0\,. \end{cases} \tag{2.3.23}$$

As shown in Figure 2.14, the duty cycle D controls the relative heights of the peaks. For instance, a symmetric modulation with $D = 0.5$ suppresses the central peak ($m = 0$) and creates the two-peak structure shown in Figure 2.14(a). Another noteworthy case is $D \approx 0.265$, which results in three dominant peaks of equal height, as shown in Figure 2.14(b).

The phasor plot in Figure 2.19 for the $D = 0.5$ case provides further insight. The periodic phase reversal forces the phasor for the central peak ($\Delta\beta' = 0$) to travel back and forth, preventing any net accumulation. Simultaneously, it corrects the phase evolution for the two main side peaks ($\Delta\beta' = \pm 2\pi/\Gamma$) just as they would naturally dephase, ensuring they grow constructively along the entire waveguide length.

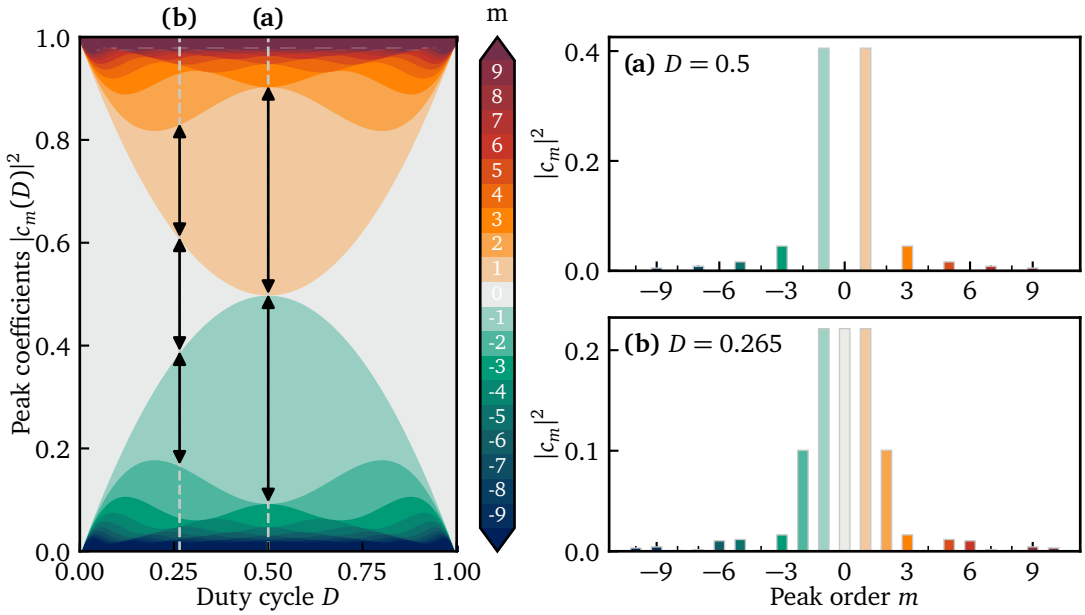

Figure 2.14: Left: illustration showing the stacked heights $|c_m(D)|^2$ of the phase-matching peaks from phase-reversal poling as a function of the duty cycle D, see eq. (2.3.23). For any duty cycle D, the sum of these coefficients for all orders m is always 1, indicating that the total phase-matching efficiency of a nonlinear waveguide with a phase-reversal poled structure is the same as a standard periodically poled waveguide. **(a)** The height of the central peak (gray) vanishes for $D = 0.5$, giving rise to a two-peak phase-matching structure (studied in more details in Figure 2.19). **(b)** For $D \approx 0.265$ we find $|c_{-1}|^2 = |c_0|^2 = |c_1|^2$, giving rise to a three-peak phase-matching structure. At the edges, where $D = 0$ or $D = 1$, we recover a single QPM peak.

However, extending this approach to generate a custom number of identical peaks is nontrivial. While three- and four-peak structures have been demonstrated experimentally [79, 80], creating more sophisticated patterns generally requires numerical optimization of the domain direction [81] or the domain phase [82]. Such methods are more complex and are not guaranteed to converge to the exact desired solution.

Super-poling

To achieve more intuitive and scalable control over the multi-peak structure, we developed a method called *super-poling*. This technique consists in creating a periodic superstructure of poled and unpoled regions, as shown in Figure 2.15(a), in direct analogy to an optical diffraction grating. Each poled segment of length l acts as a "slit", and the interference between segments separated by the super-poling period Γ creates the desired multi-peak structure.

The full mathematical derivation, which follows the Fourier transform method, is presented in Appendix A.3. Conceptually, the Fourier transform of the super-

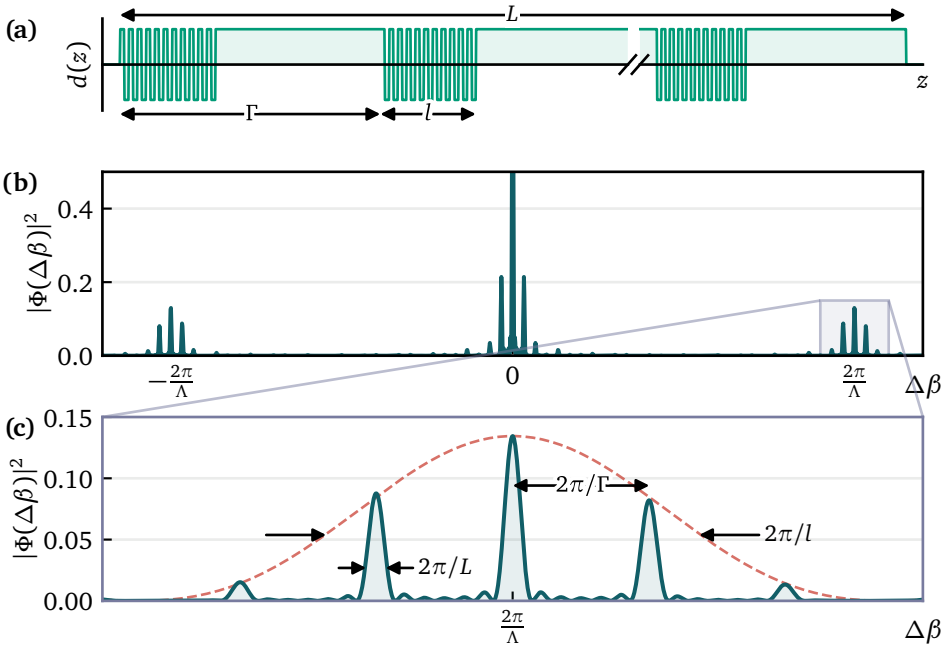

Figure 2.15: **(a)** Super-poled nonlinearity profile $d(z)$, highlighting the unit active length l and the super-poling period Γ. **(b)** Corresponding phase-matching intensity $|\Phi(\Delta\beta)|^2$. **(c)** Zoomed-in view of the first-order QPM peak, now split into a comb of peaks with a separation determined by Γ. The red dashed line shows the modulating sinc-squared envelope, whose width is determined by l.

poling nonlinearity profile $d(z)$ contains three components. The first is a peak at $\Delta\beta = 0$, corresponding to the underlying birefringent phase-matching. The second is a Dirac comb of centered at $\Delta\beta = 0$ that arises from the periodic repetition of the unpoled regions. The final and most important term is another Dirac comb, centered around the original QPM peak ($\Delta\beta' = 0$), which is generated by the interference of the poled regions and gives rise to the desired multi-peak structure.

The resulting phase-matching function in the region near the first-order QPM peak is

$$\begin{aligned}\Phi(\Delta\beta') &\approx L\,\frac{2i}{\pi}\frac{l}{\Gamma}\sum_m c_m\left(\frac{l}{\Gamma}\right)\mathrm{sinc}\left(\left(\Delta\beta' - \frac{2\pi}{\Gamma}m\right)\frac{L}{2}\right)e^{i\left(\Delta\beta' - \frac{2\pi}{\Gamma}m\right)\frac{L}{2}} \\ &\approx L\,\frac{2i}{\pi}\frac{l}{\Gamma}\,\mathrm{sinc}\left(\frac{\Delta\beta' l}{2}\right)e^{i\frac{\Delta\beta' l}{2}}\sum_m \mathrm{sinc}\left(\left(\Delta\beta' - \frac{2\pi}{\Gamma}m\right)\frac{L}{2}\right)e^{i\left(\Delta\beta' - \frac{2\pi}{\Gamma}m\right)\frac{L}{2}},\end{aligned} \tag{2.3.24}$$

where, in the last step, we assumed a slowly-varying envelope ($l \ll L$). As illustrated in Figure 2.15(b-c), this expression describes a comb of sinc-shaped peaks of identical width $2\pi/L$, separated by $2\pi/\Gamma$. The heights of these peaks

are modulated by a broader sinc envelope of width $2\pi/l$. The relative amplitudes of the peaks are given by the coefficients

$$c_m\left(\frac{l}{\Gamma}\right) = \frac{l}{\Gamma}\,\mathrm{sinc}\left(\frac{2\pi m}{\Gamma}\frac{l}{2}\right)e^{i\frac{2\pi m}{\Gamma}\frac{l}{2}}. \tag{2.3.25}$$

The phasor plot in Figure 2.20 provides further physical insight into this process. Within the poled regions, the phase-matching function evolves as in the standard QPM case. In the unpoled regions, however, the evolution is governed by birefringent phase-matching, causing the phasors to trace small circles and thereby accumulate phase without a significant change in amplitude. This periodic "pausing" of the QPM evolution leads to the interference that generates the multiple phase-matching peaks.

This structure provides a highly intuitive design principle, as illustrated in Figure 2.16. The number of significant phase-matching peaks is controlled directly by the poled fraction l/Γ; a smaller fraction creates a wider sinc envelope that encompasses more peaks. For example, a poled fraction of $l/\Gamma = 0.5$ results in three dominant peaks, whereas a smaller fraction of $l/\Gamma = 0.2$ creates a wider envelope that encompasses five significant peaks, as shown in Figures 2.16(a) and (b), respectively. This direct, predictable control makes super-poling a straightforward and powerful technique for engineering multi-channel devices.

Gaussian phase-matching profile

A final note is that, although the sinc function is the natural outcome of a rectangular spatial function, it is sometimes desirable to achieve a Gaussian profile [83]. This can be realized by "softening" the rectangular function, for example, by reducing the efficiency near the edges through adjustments of poling periods [81], duty cycles [84], or domain orientation [85, 86]. In practice, since these profiles may be technically challenging to fabricate, spectral filtering is also often used to suppress sinc side lobes, effectively limiting their effects and bringing the nonlinear process closer to what one would obtain using a Gaussian phase-matching profile. In the experimental demonstrations discussed in the next chapters, we will often make use of the latter approach.

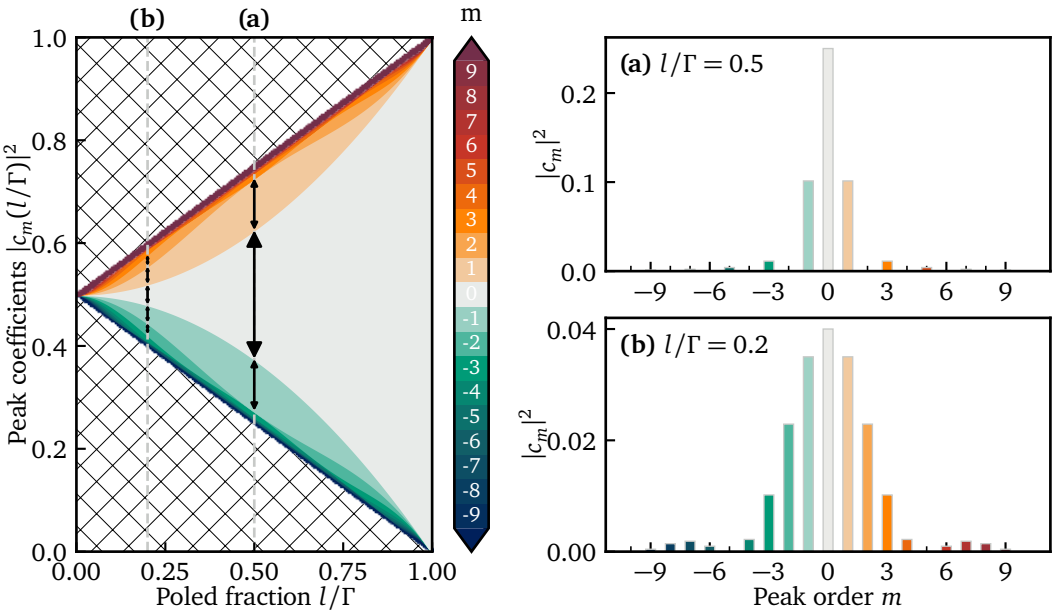

Figure 2.16: Left: illustration showing the stacked heights $|c_m(l/\Gamma)|^2$ of the phase-matching peaks from super-poling as a function of the total poled fraction l/Γ, see eq. (2.3.25). For a fixed poled fraction l/Γ, the total phase-matching efficiency (summed over all peaks) is a fraction l/Γ of that of a fully periodically poled waveguide. The remaining efficiency (cross-hatched area) is "lost" to the birefringent phase-matching due to the unpoled regions. The central peak at $m = 0$ (light gray) is always dominant since it is centered on the sinc envelope. As the poled fraction decreases, the sinc envelope becomes larger and incorporates more peaks: **(a)** for $l/\Gamma = 0.5$, we have dominant peaks at $m = 0, \pm 1$, whereas **(b)** for $l/\Gamma = 0.2$ we find 5 peaks within the FWHM of the sinc envelope. For the edge cases where the poled fraction is 0 or 1, we recover respectively the birefringent phase-matching or QPM.

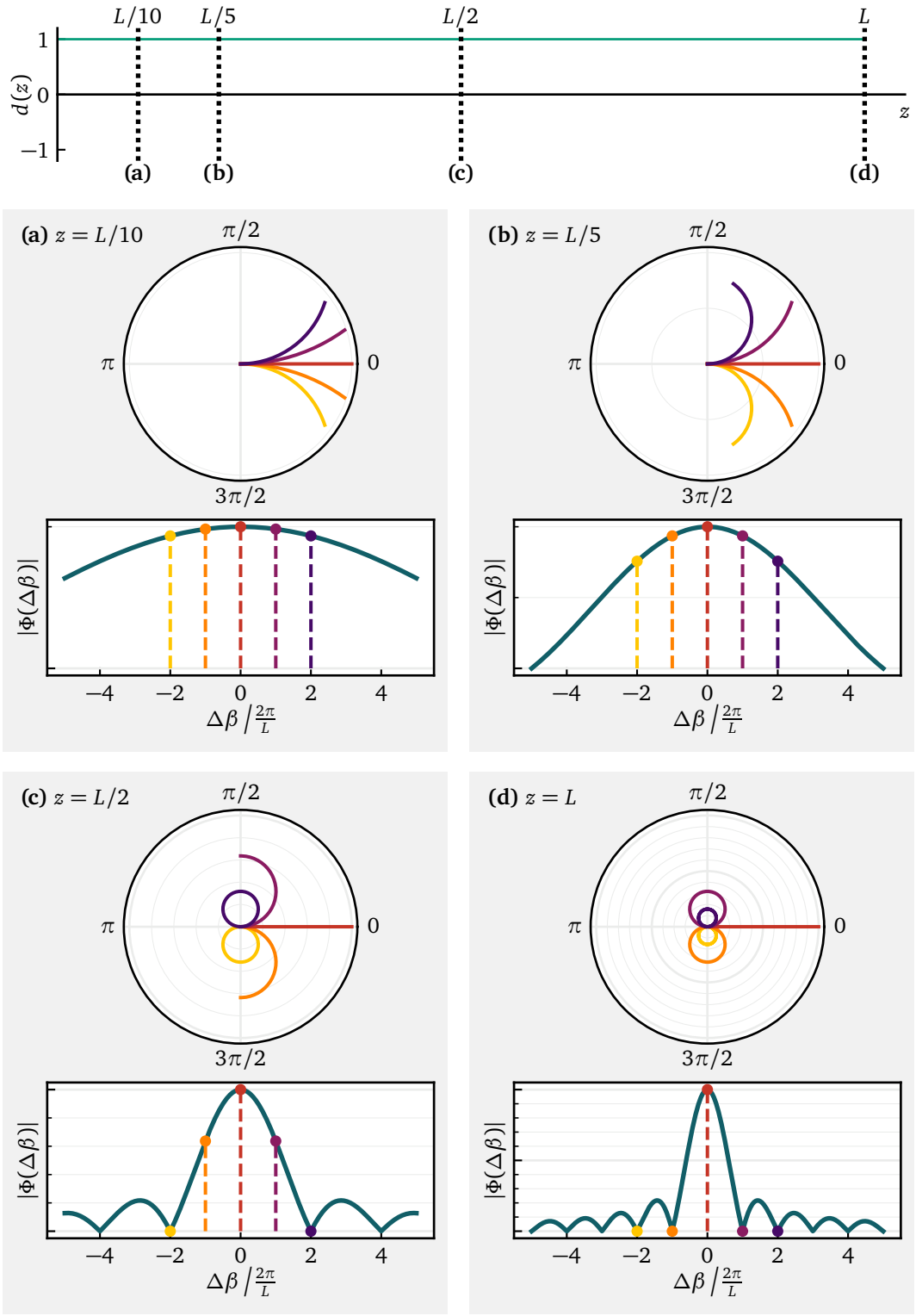

Figure 2.17: Top: Nonlinearity profile $d(z)$ of birefringent phase-matching, with a constant value of 1. **(a-d):** Evolution of the phase-matching function $\Phi(\Delta\beta)$ at different positions z along the waveguide (see eq. (2.2.13)). In each subfigure, the top panel shows a phasor plot representing the amplitude and phase of $\Phi(\Delta\beta)$ for five different values of $\Delta\beta$, while the bottom panel shows the amplitude of $\Phi(\Delta\beta)$ over a continuous range of $\Delta\beta$ (in units of $2\pi/L$). The vertical axis in the lower plot corresponds to the radial coordinate in the phasor plot.

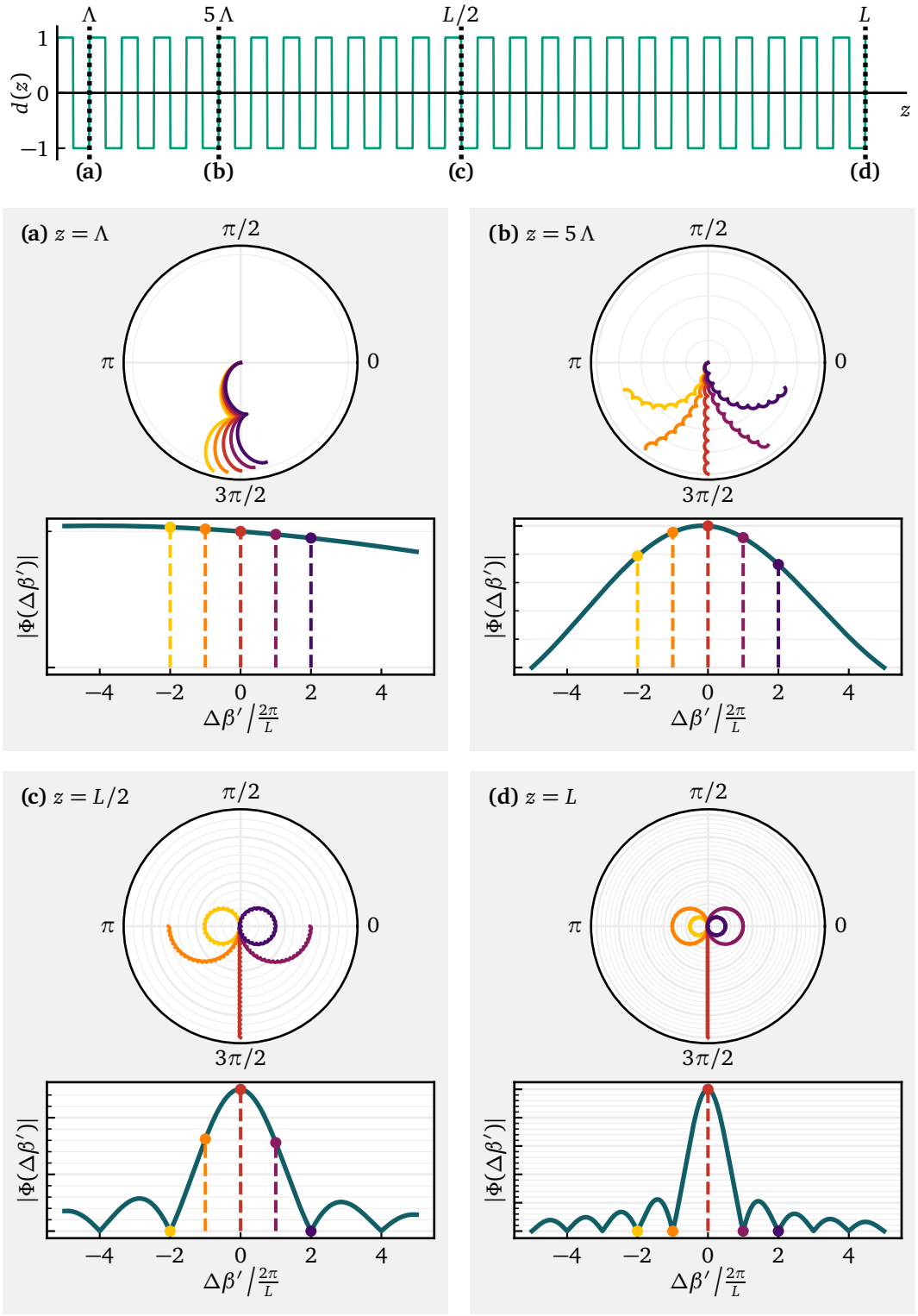

Figure 2.18: Top: Nonlinearity profile $d(z)$ of quasi-phase-matching (QPM). **(a–d):** Evolution of the phase-matching function $\Phi(\Delta\beta')$ at different positions z along the waveguide (see eq. (2.3.19)). In each subfigure, the top panel shows a phasor plot representing the amplitude and phase of $\Phi(\Delta\beta')$ for five different values of $\Delta\beta'$, while the bottom panel displays the amplitude of $\Phi(\Delta\beta')$ over a continuous range of $\Delta\beta'$ (in units of $2\pi/L$). Note that the y-axis in the bottom plot corresponds to the radial axis of the scalar plot. The vertical axis in the lower plot corresponds to the radial coordinate in the phasor plot.

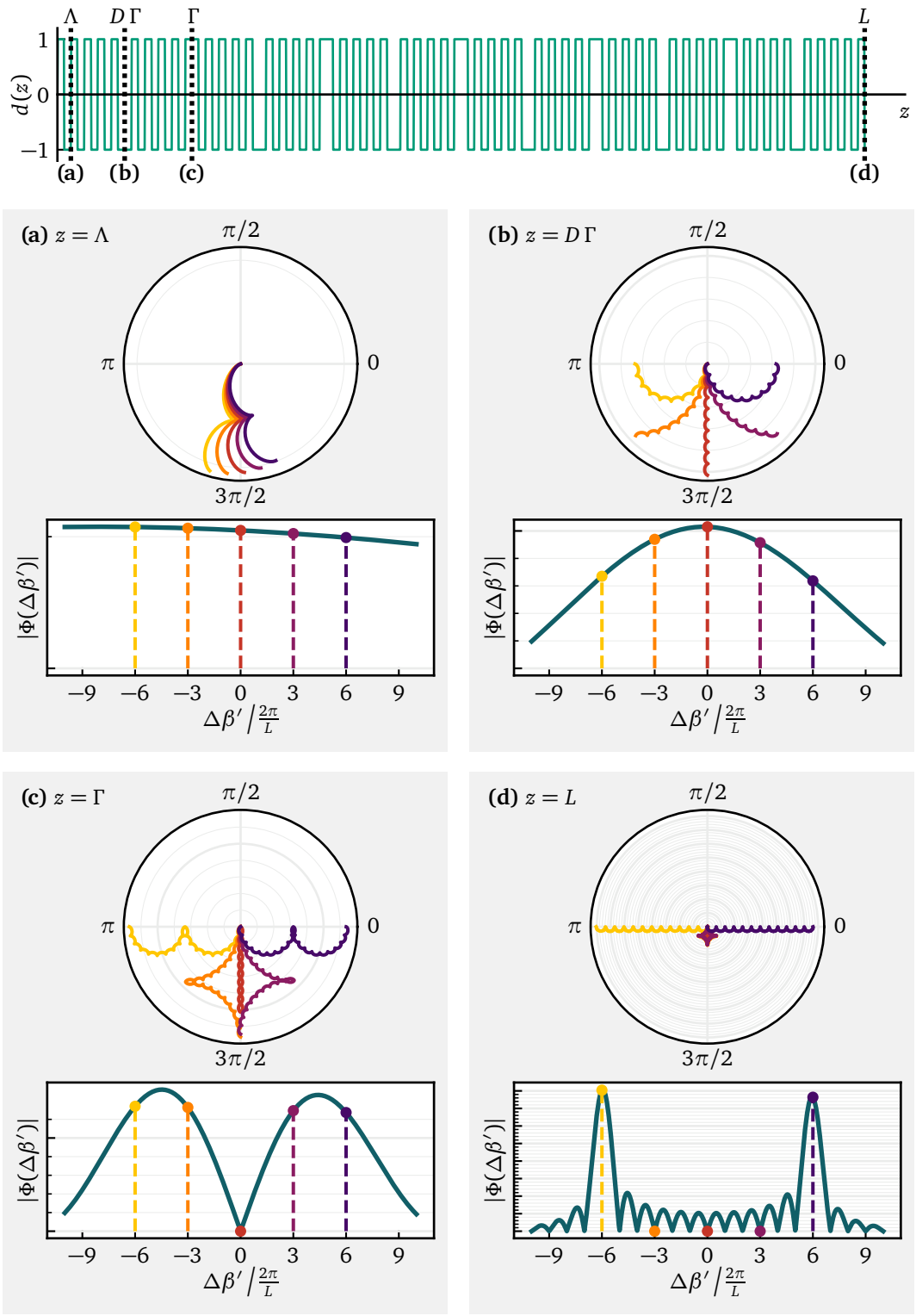

Figure 2.19: Top: Nonlinearity profile $d(z)$ of QPM with a phase-reversal wave of period Γ and duty cycle $D = 0.5$. **(a–d):** Evolution of the phase-matching function $\Phi(\Delta\beta')$ at different positions z along the waveguide (see eq. (2.3.22)). In each subfigure, the top panel shows a phasor plot representing the amplitude and phase of $\Phi(\Delta\beta')$ for five different values of $\Delta\beta'$, while the bottom panel displays the amplitude of $\Phi(\Delta\beta')$ over a continuous range of $\Delta\beta'$ (in units of $2\pi/L$). The vertical axis in the lower plot corresponds to the radial coordinate in the phasor plot.

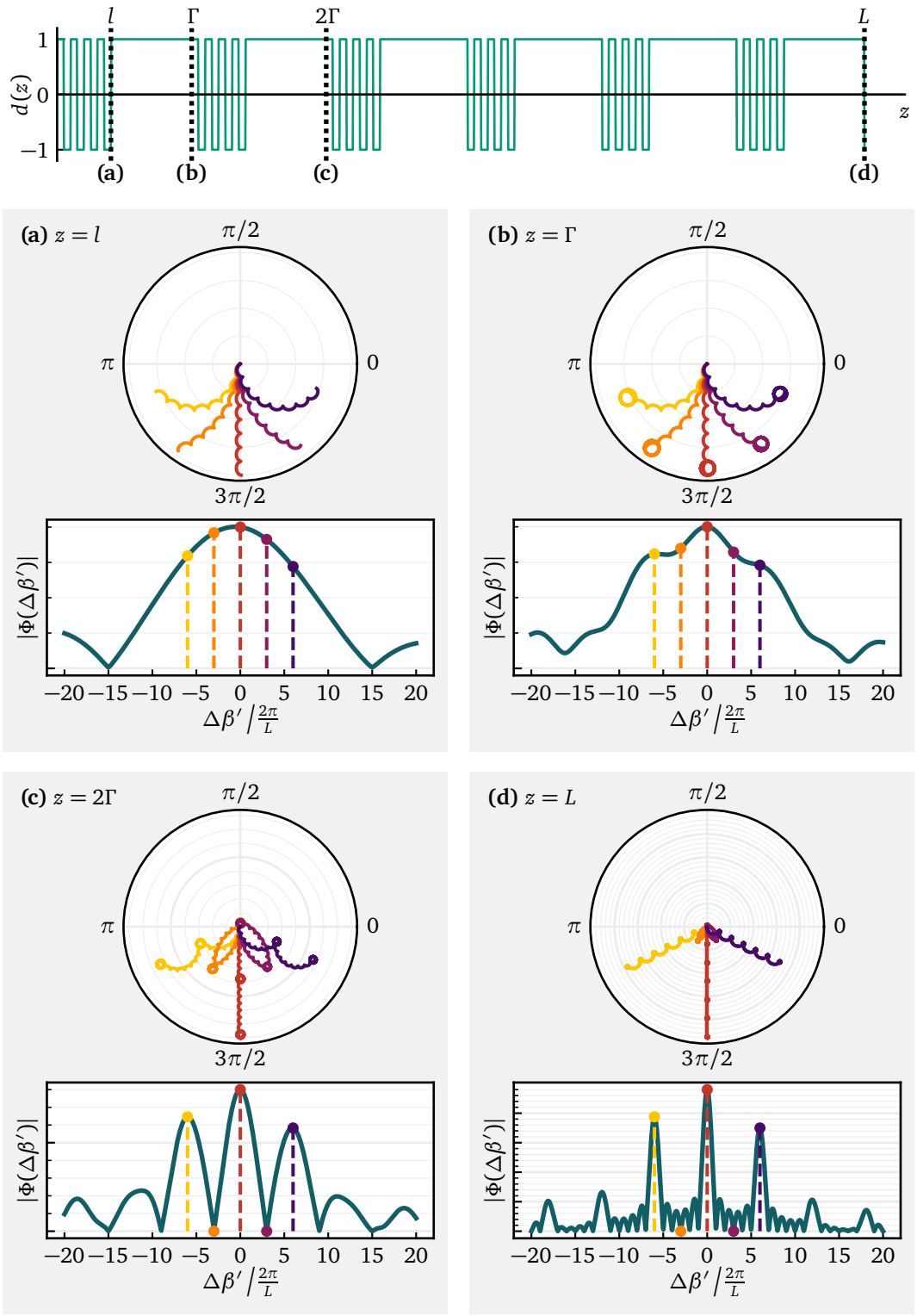

Figure 2.20: Top: Nonlinearity profile $d(z)$ of QPM with super-poling modulation. **(a–d):** Evolution of the phase-matching function $\Phi(\Delta\beta')$ at different positions z along the waveguide (see eq. (2.3.24)). In each subfigure, the top panel shows a phasor plot representing the amplitude and phase of $\Phi(\Delta\beta')$ for five different values of $\Delta\beta'$, while the bottom panel displays the amplitude of $\Phi(\Delta\beta')$ over a continuous range of $\Delta\beta'$ (in units of $2\pi/L$). The vertical axis in the lower plot corresponds to the radial coordinate in the phasor plot.

2.3.3 Spectral shaping of the pump

Shaping the pump spectrum means controlling its frequency-dependent amplitude and phase—that is, its complex spectral profile—thereby modifying the energy conservation condition in the nonlinear process. At first, pump shaping may appear less powerful than dispersion engineering, as the angle of the pump function α in frequency space is fixed by the sign of the energy conservation (Figure 2.21). However, dispersion engineering properties are fixed once the waveguide is fabricated; in contrast, the pump spectrum can be adjusted dynamically, allowing one to modify the generated PDC state or the TM beamsplitter characteristics in real time. Spectral shaping can be implemented via different methods, depending on the pump pulse duration and on the application requirements.

Amplitude-only modulation is typically simpler and can be achieved through spectral filtering. For instance, applying a narrowband tunable filter to a broadband pump spectrum allows one to select specific spectral regions in which the PDC state can be generated (Figure 2.22(a-b)). As a further example, using a bandpass filter to modify the pump bandwidth alters the modal structure of the generated PDC state (Figure 2.22(c)). Some laser sources allow one to achieve these same effects by tuning the pump wavelength or adjusting the pulse duration, which changes the spectral width.

Full spectral shaping, including phase modulation, enables higher levels of control over the nonlinear process. For instance, when combined with a diagonal phase-matching function, the pump shape can directly select the dimensionality of the entangled PDC state (Figure 2.22(d)). This capability will be explored in detail in Chapter 3, where we use it to generate high-dimensional TM-entangled states with arbitrary dimensions. However, this increased flexibility comes with added experimental complexity, requiring more sophisticated setups than those needed for simple filtering.

In the narrowband pulsed regime (nanosecond-scale durations), pump shaping is typically implemented using electro-optic modulators [87, 88]. These devices apply a time-dependent modulation which, through a Fourier transform, maps to amplitude and phase shaping in the frequency domain.

For ultrafast pulses, a diffraction grating combined with a spatial light modulator (SLM) is more appropriate. This type of waveshaper was employed in all experimental demonstrations in the following chapters, using pulse durations as short as 150 fs. We describe its operation in detail below.

SLM-based 4-f waveshaper

A detailed overview of 4-f pulse shapers can be found in [89, 90]. Here, we focus on first-order shaping using a 2D liquid crystal SLM, as detailed in [91, 92].

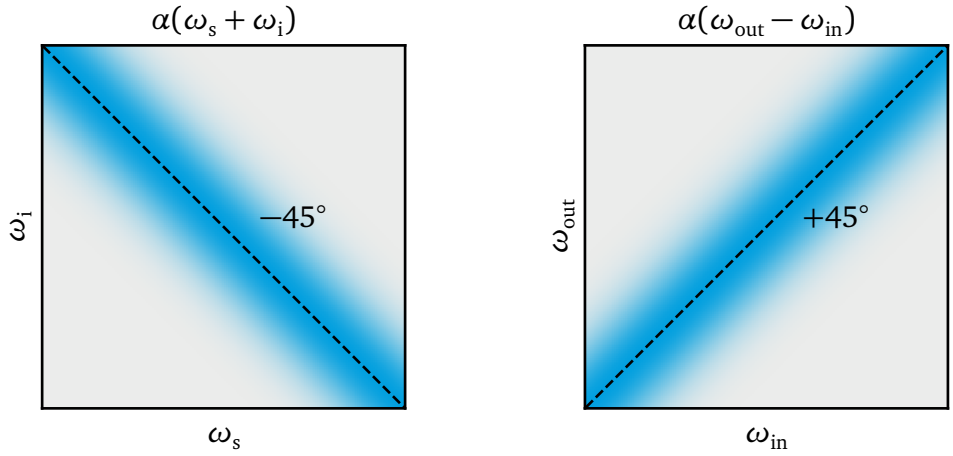

Figure 2.21: Illustration of a Gaussian-shaped pump function for PDC **(left)** and SFG **(right)**. The angle is fixed by the energy conservation condition of the process.

The linear 4-f waveshaper consists of a diffraction grating, a cylindrical lens, a transmissive SLM, and the same mirrored elements for recombination, with all components spaced by the lens focal length f. We use a folded configuration (shown in Figure 2.23) which replaces the lens with a cylindrical mirror and the transmissive SLM with a reflective one. Light is reflected back from the SLM, retracing its path through the mirror and grating. This setup reduces the number of components while maintaining the 4-f geometry.

The basic operating principle of this waveshaper is the following:

1. The diffraction grating spatially separates frequency components of the input pulse by angle:

$$d\,(\sin\theta_i + \sin\theta_d^m(\omega)) = m\lambda = \frac{2\pi mc}{\omega}, \tag{2.3.26}$$

where d is the grating spacing, θ_i the incidence angle, m the diffraction order, and c the speed of light. We use a blazed grating optimized for first-order diffraction ($m = 1$), neglecting higher orders. Thus, each frequency ω is deflected at an angle:

$$\theta_d(\omega) = \arcsin\left(\frac{2\pi c}{\omega d} - \sin\theta_i\right). \tag{2.3.27}$$

2. The cylindrical mirror, placed at a distance f from the grating, performs a Fourier transform along the horizontal axis. It maps angles to positions in the Fourier plane, at distance f:

$$x(\omega) \approx f \cdot \sin\theta_d(\omega) = f \cdot \frac{2\pi c}{\omega d}, \tag{2.3.28}$$

so that frequency components at distance $\delta\omega$ are separated by

$$\delta x(\omega) \approx -f\,\frac{2\pi c}{\omega^2 d}\delta\omega \equiv -K\,\delta\omega, \quad K = \frac{2\pi c}{\omega^2 d}. \tag{2.3.29}$$

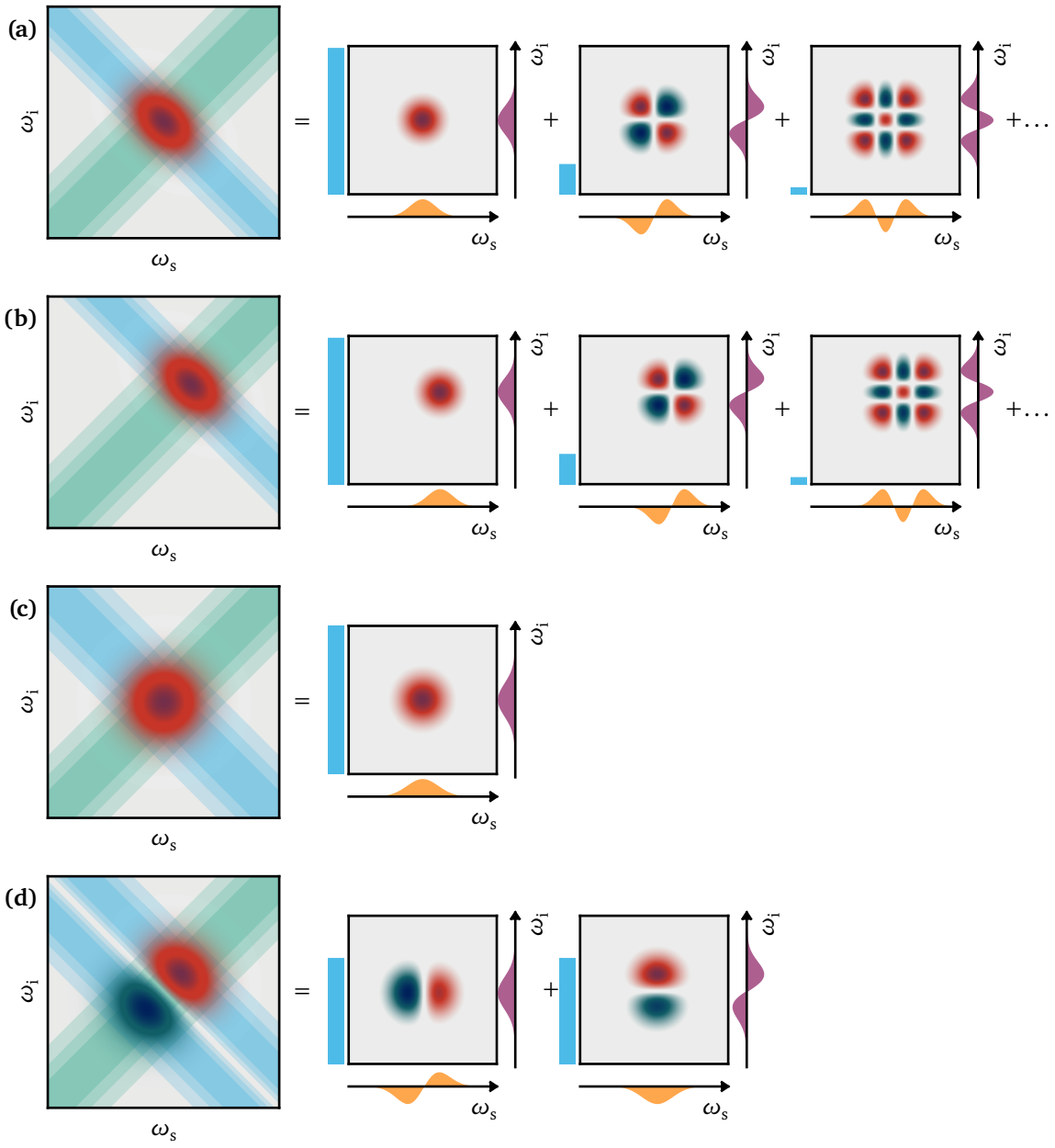

Figure 2.22: Examples of pump spectral shaping combined with a Gaussian-shaped phase-matching function at 45°. The effects of pump shaping on the JSA are shown through a Schmidt decomposition. **(a-b)** Tuning the pump central frequency shifts the signal and idler spectra. **(c)** Changing the pump bandwidth affects the modal structure of the PDC state, e.g., generating single-mode PDC state. **(d)** Shaping the pump as a first-order HG function generates a two-dimensional TM-entangled PDC state.

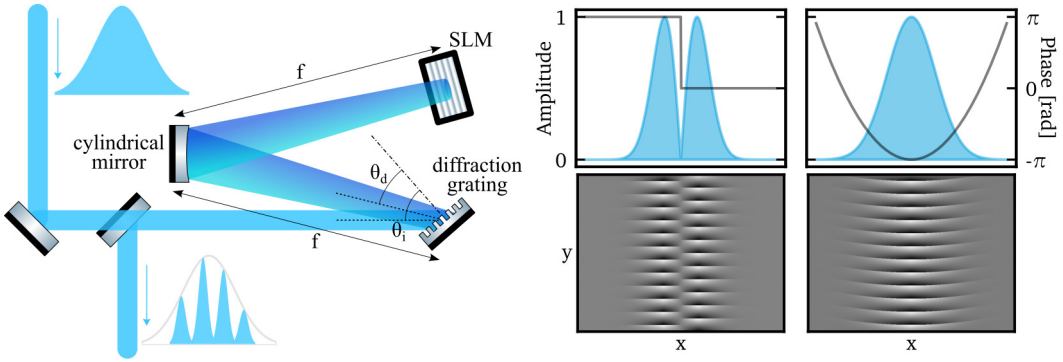

Figure 2.23: Left: 4-f waveshaper in a folded geometry. Right: two examples of amplitude and phase modulation, and corresponding SLM phase mask below (see eq. (2.3.36)). The first example shows how the π phase jump between the two lobes of a first-order HG function is realized by vertically shifting the two parts of the mask relative to each other. The second examples shows a quadratic spectral phase (chirp), applied by gradually shifting the vertical alignment of the phase mask. In both cases, the amplitude modulation vanishes at the edges, where the grating lines are no longer visible.

Simultaneously, the cylindrical mirror also performs a Fourier transform on the spatial distribution of each frequency component. If the input beam has a Gaussian spatial profile with FWHM Δx_{in}, related to the waist w_{in} by $\Delta x_{\text{in}} = \sqrt{2\ln 2}\, w_{in}$, the horizontal spot size (FWHM) of each frequency component in the Fourier plane is

$$\Delta x_0 = 2\ln 2 \frac{\cos\theta_i}{\cos\theta_d(\omega)} \frac{2cf}{\omega \Delta x_{\text{in}}}. \tag{2.3.30}$$

For narrow spectral ranges, we can approximate $\omega \approx \omega_0$ and treat Δx_0 as constant.

3. The SLM, placed in the Fourier plane of the mirror, displays a phase-only mask $\varphi(x, y)$ that modifies the spatial shape of the beam. Due to the frequency-to-space mapping by the 4-f geometry, this also modifies the spectrum. The beam then travels back through the folded setup, where the lens applies an inverse Fourier transform, recombining the different frequency components in the original spatial distribution.

We use a reflective 2D liquid crystal SLM composed of a two-dimensional pixel array. Each pixel acts as an independent waveplate controlled by a voltage which orients the transparent liquid crystal molecules, changing the local refractive index. A reflective coating behind the liquid crystal sends the pulse back through the liquid crystal and out of the SLM. By loading a mask of tailored voltages across the pixel array, the SLM imprints an arbitrary phase shift in each pixel.

Unlike the linear SLMs in [89, 90], a 2D SLM enables amplitude and phase shaping through phase-only spatial modulation. For pulse shaping, we use a phase mask which corresponds to a blazed grating with horizontal lines:

$$\varphi(x,y) = \pi + 2\pi\, a(x) S_P(y + b(x) P), \tag{2.3.31}$$

where S_P is a sawtooth function that increases from $-1/2$ to $1/2$ with period P, $a(x) \in [0,1]$ is the blazing angle coefficient, and $b(x) \in [0,1)$ is a phase shift applied to S_P.

Each column of pixels acts as an independent diffraction grating with a constant diffraction angle determined by the period P. We focus on the first-order diffraction, which is modulated in amplitude and phase by the coefficient [91]

$$H(x) = \mathrm{sinc}[\pi(1-a(x))]\, e^{-i\,2\pi\, b(x)}. \tag{2.3.32}$$

Since frequency ω maps to position $x(\omega)$, the modulation applied to the field becomes:

$$A(\omega) = |H(x(\omega))| \in [0,1], \tag{2.3.33}$$
$$\phi(\omega) = \arg H(x(\omega)) \in [0, 2\pi), \tag{2.3.34}$$

yielding an output field:

$$E(\omega) = E_0(\omega) \cdot A(\omega) e^{i\phi(\omega)}. \tag{2.3.35}$$

We can invert eq. (2.3.32) to compute the phase mask (2.3.31) required for a desired amplitude $A(\omega)$ and phase $\phi(\omega)$ modulation:

$$\varphi(y,\omega) = \pi + 2\pi \left(1 - \frac{\mathrm{sinc}^{-1} A(\omega)}{\pi}\right) S_P\left(y - \phi(\omega)\frac{P}{2\pi}\right). \tag{2.3.36}$$

From this expression, we can see that the amplitude $A(\omega)$ is directly mapped to the efficiency of the blazed grating. If $A(\omega) = 1$, then the grating phase will change by exactly 2π every period, optimizing the blazed grating for the first diffraction order. Contrarily, if $A(\omega) = 0$, the phase will be uniform and the SLM will act as a mirror, so that the amplitude of the first diffraction order will vanish. The phase $\phi(\omega)$ is instead directly mapped to a phase shift of the vertical grating. Additionally, having defined the sawtooth function centered around a mean value of 0 prevents an additional amplitude-dependent phase shift, which would otherwise have to be corrected.

Spectral resolution and limitations

The spectral resolution $\Delta\omega_{\mathrm{res}}$ of the SLM-based waveshaper determines the narrowest spectral feature that can be independently shaped. This resolution

is limited by the smallest spatial feature which can be addressed in the Fourier plane: either the spot size Δx_0 of each frequency component, or the SLM pixel width Δx_{px}.

As shown in Eq. (2.3.28), the spatial position x in the Fourier plane is a function of frequency ω. The relationship between a spatial separation δx and the corresponding frequency separation $\delta\omega$ is given by the inverse of the spatial dispersion K from Eq. (2.3.29): $\delta\omega = \delta x/K$. Using this, we can define the spectral limits imposed by the optical spot size and the pixel size:

$$\Delta\omega_0 = \frac{\Delta x_0}{K} \approx \frac{2\ln 2}{\pi}\frac{\cos\theta_i}{\cos\theta_d(\omega_0)}\frac{d\,\omega_0}{\Delta x_{\mathrm{in}}}, \tag{2.3.37}$$

$$\Delta\omega_{\mathrm{px}} = \frac{\Delta x_{\mathrm{px}}}{K} = \frac{\Delta x_{\mathrm{px}}\,\omega_0^2\,d}{2\pi\,c\,f}. \tag{2.3.38}$$

The effective spectral resolution $\Delta\omega_{\mathrm{res}}$ is then limited by the larger of these two values:

$$\Delta\omega_{\mathrm{res}} = \max\{\Delta\omega_0,\ \Delta\omega_{\mathrm{px}}\}. \tag{2.3.39}$$

The optimal working regime is achieved when $\Delta x_0 \lesssim \Delta x_{\mathrm{px}}$, meaning the spot size of each frequency component in the Fourier plane is comparable to or slightly smaller than the SLM pixel size. If the optical spot size Δx_0 is significantly larger than the pixel size Δx_{px} ($\Delta x_0 \gg \Delta x_{\mathrm{px}}$), the mask applied by individual pixels cannot be fully resolved, and the effective resolution is limited by the larger spot size. Conversely, if the spot size is much smaller than the pixel size ($\Delta x_0 \ll \Delta x_{\mathrm{px}}$), the spectrum is undersampled by the SLM pixels, which can lead to the generation of replica waveforms in the time domain at delays $\pm 2\pi/\Delta\omega_{\mathrm{px}}$ [93].

It is also important to consider the total addressable bandwidth $\Delta\omega_{\mathrm{tot}}$. This is limited by the physical width of the SLM display, Δx_{SLM}:

$$\Delta\omega_{\mathrm{tot}} = \frac{\Delta x_{\mathrm{SLM}}}{K} = \frac{\Delta x_{\mathrm{SLM}}\,\omega_0^2\,d}{2\pi\,c\,f}. \tag{2.3.40}$$

The fact that both the total range $\Delta\omega_{\mathrm{tot}}$ and the pixel resolution $\Delta\omega_{\mathrm{px}}$ scale with the same parameters introduces a trade-off between these two quantities. For a given SLM with a fixed number of pixels $N_{\mathrm{px}} = \Delta x_{\mathrm{SLM}}/\Delta x_{\mathrm{px}}$[7], parameters (like focal length f or grating spacing d) adjusted to improve (decrease) $\Delta\omega_{\mathrm{px}}$ will simultaneously decrease the bandwidth $\Delta\omega_{\mathrm{tot}}$ (since $\Delta\omega_{\mathrm{tot}} = N_{\mathrm{px}} \cdot \Delta\omega_{\mathrm{px}}$). This means one often chooses between resolving very fine spectral details over a narrower range, or shaping coarser features over a broader spectral range. These spectral characteristics directly impact temporal shaping: the smallest temporal feature is $T_{\mathrm{min}} \approx 2\pi/\Delta\omega_{\mathrm{tot}}$, while the maximum temporal shaping window is $T_{\mathrm{max}} \approx 2\pi/\Delta\omega_{\mathrm{res}}$.

[7] Here and in the rest of this section, we neglect the empty space between the SLM pixels.

Table 2.1: Impact of 4-f line parameters on spectral resolution and range.

Parameter	Effects	Limitations	Optimal strategy
Grating spacing d	$d \uparrow \Rightarrow \begin{matrix}\Delta\omega_0 \uparrow \\ \Delta\omega_{\text{px}} \uparrow \\ \Delta\omega_{\text{tot}} \uparrow\end{matrix}$	Limited by ω_0, angles, manufacturing, efficiency.	Smallest practical d (maximize lines/mm).
Input beam width Δx_{in}	$\Delta x_{\text{in}} \uparrow \Rightarrow \Delta\omega_0 \downarrow$	Must fit optics.	Maximize Δx_{in} within practical limits (∼cm).
Focal length f	$f \uparrow \Rightarrow \begin{matrix}\Delta\omega_{\text{px}} \downarrow \\ \Delta\omega_{\text{tot}} \downarrow\end{matrix}$	Setup size $\propto f$; stability.	Largest practical f considering $\Delta\omega_{\text{px}}$ vs $\Delta\omega_{\text{tot}}$.
Grating angle θ_i	$\frac{\cos\theta_i}{\cos\theta_d(\omega_0)} \uparrow \Rightarrow \Delta\omega_0 \uparrow$	Diffraction efficiency (blaze); beam clipping; $\lvert\theta_d(\omega_0)\rvert < 90°$.	Optimize for efficiency; minimize $\cos\theta_i/\cos\theta_d(\omega_0)$.
SLM pixel width Δx_{px}	$\Delta x_{\text{px}} \uparrow \Rightarrow \Delta\omega_{\text{px}} \uparrow$	SLM technology; cost.	Smaller Δx_{px} (and more pixels).
SLM display width Δx_{SLM}	$\Delta x_{\text{SLM}} \uparrow \Rightarrow \Delta\omega_{\text{tot}} \uparrow$	SLM technology; cost.	Larger Δx_{SLM} for wider bandwidth.

The effect of these and more design parameters on the spectral resolution and range are summarized in Table 2.1. A smaller grating spacing d (more lines per mm) generally improves spectral separation by increasing the dispersion K in eq. (2.3.29), but its minimum value is limited (at a fixed ω_0) because the diffraction angle $\theta_d(\omega)$ in eq. (2.3.27) cannot be above 90°. A larger input beam width Δx_{in} reduces the spot size Δx_0, thus improving $\Delta\omega_0$; however, the input beam size is practically limited by the size of the optical components, particularly the height of the SLM and the width of the grating, which is generally strongly tilted. In fact, a larger incidence angle θ_{in} can provide an additional benefit to $\Delta\omega_0$ through the cosine ratio term $\cos\theta_i/\cos\theta_d(\omega_0)$, effectively magnifying the beam horizontally before the Fourier transform if $\cos\theta_i > \cos\theta_d(\omega_0)$. A larger focal length f significantly improves the pixelation limit $\Delta\omega_{\text{px}}$ by spreading the spectrum over more pixels, but it also decreases the total addressable bandwidth $\Delta\omega_{\text{tot}}$ and requires a longer physical setup, which leads to decreased stability.

Amplitude and phase compensation

Even with ideal resolution, achieving the desired spectral shape requires accounting for the initial spectral characteristics of the input pulse: if the input pulse has a

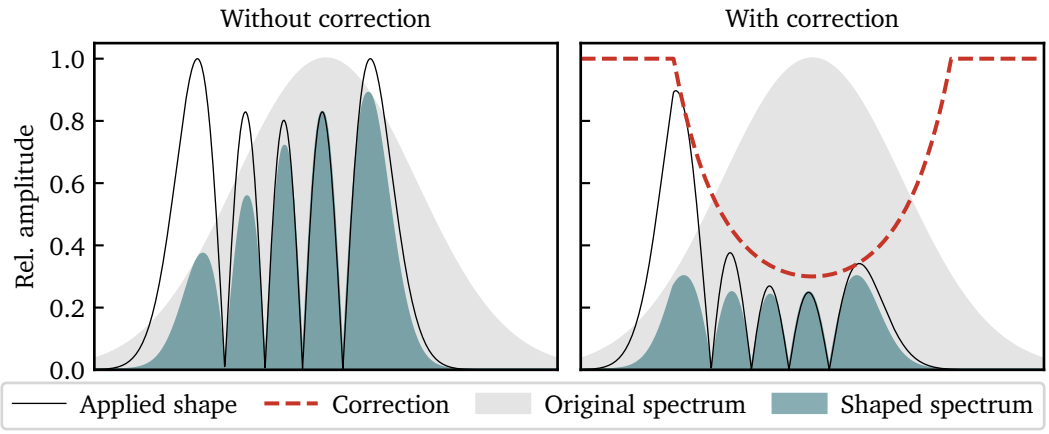

Figure 2.24: Example of amplitude shaping by directly applying the desired amplitude profile **(left)** and by pre-compensating for the original spectral shape **(right)**.

non-uniform intrinsic spectral amplitude and phase profile $E_0(\omega) = A_0(\omega)e^{i\phi_0(\omega)}$, this must be compensated for with the shaping mask.

The initial spectrum $A_0(\omega)$ can be easily measured with a spectrometer and compensated for by applying amplitude shaping as $A(\omega) \propto A_{\text{target}}(\omega)/A_0(\omega)$ (Figure 2.24). Since the SLM can only attenuate the field, not amplify it, for each frequency we are limited to $A(\omega) \leq 1 \Leftrightarrow A_{\text{target}}(\omega) \leq A_0(\omega)$. This means that we must choose the proportionality constant appropriately, because the stronger parts of the field will generally be attenuated to match the weaker parts. In practice, to avoid excessively attenuating the field, it can be useful to define a cutoff amplitude below which the input amplitude will not be compensated for. This type of correction can then be tailored on a case-by-case basis, e.g., by renormalizing the applied modulation.

Similarly, after characterizing the initial phase $\phi_0(\omega)$, the desired shaping phase $\phi_{\text{target}}(\omega)$ would be obtained by applying a shaping phase $\phi(\omega) = \phi_{\text{target}}(\omega) - \phi_0(\omega)$. However, phase characterization can be significantly more challenging than amplitude measurements, often requiring sophisticated devices (see Chapter 7). For this reason, depending on the application, it is often more practical to assume a polynomial spectral phase (up to the second or third order) and attempt to compensate for it by iteratively changing the applied phase coefficients and observing their effects. Indeed, a linear or quadratic spectral phase often has a predictable impact on the experiment: the Fourier relation between time and frequency implies that a linear spectral phase $\phi(\omega) = \alpha\omega$ corresponds to a simple time shift of the pulse by α, whereas a quadratic spectral phase $\phi(\omega) = \beta\omega^2$ corresponds to a temporal chirp, where different frequency components arrive at different times, stretching or compressing the pulse. Higher-order phase terms lead to more complex temporal effects along the same lines.

Ultimately, achieving both high shaping resolution and a wide frequency bandwidth demands a well-designed 4-f waveshaper with state-of-the art components. This typically involves a high-definition SLM and an optical setup with long focal lengths to spread the spectrum effectively. The practical implementation of such a system requires precise optical alignment and robust stability of all components. Consequently, the pulse shaping system is often one of the most complex and critical elements to optimize and maintain in ultrafast quantum experiments.

2.4 Chapter conclusion

This chapter has provided an overview of some techniques for the practical implementation of high-dimensional quantum communication protocols, encoding information in the time-frequency domain of photons. We have discussed high-dimensional TM bases, and we have explored integrated nonlinear processes, SFG and PDC, that serve as the key building blocks for a quantum information framework built on time-frequency qudits. We have studied how dispersion engineering and pump spectral shaping allow for precise control of these nonlinear interactions, enabling the generation of tailored high-dimensional entangled states and the implementation of specific operations. In the remainder of the thesis, we will make use of the principles and tools detailed in this chapter to design, implement, and demonstrate devices for the generation and detection of TM qudits.

3

Generating time-frequency qudits

Entanglement is a uniquely quantum phenomenon, creating correlations between systems stronger than any classical equivalent. For quantum communication and information processing, sources of entangled photons are indispensable. The previous chapter established the techniques needed to control nonlinear optical processes. We now apply those principles to address the first major experimental component of our framework: the development of a source that, for the first time, can generate high-dimensional entangled states with programmable control over the modal structure of their entanglement in the time-frequency domain. In this chapter, we present the realization of such a source, which is a critical step in building a versatile framework for time-frequency qudits.

The experimental results and methodologies presented in this chapter are based on the following publication:

[Optica Quantum 2(5), 339–345 (2024)] L. Serino[†], W. Ridder[†], A. Bhattacharjee, J. Gil-Lopez, B. Brecht, and C. Silberhorn, "Orchestrating time and color: a programmable source of high-dimensional entanglement", *Optica Quantum* **2**(5), 339–345 (2024). DOI: 10.1364/opticaq.532334

[†] These authors contributed equally to the work.

3.1 High-dimensional entanglement with temporal modes

As we have established in previous chapters, the practical implementation of a quantum communication framework based on TMs requires tools to generate, manipulate, and detect high-dimensional TM states [16]. While significant progress has been made in manipulating and detecting single-photon TMs [48, 50, 94–97], the realization of an optimal source of high-dimensional entangled states has remained an open challenge.

An ideal source must satisfy two main criteria: it must generate bi-photon states with a well-defined dimensionality, and it must allow this dimensionality to be programmatically reconfigured [16]. The first ensures that the states live in a finite Hilbert space, while the second provides the flexibility to adapt to different protocols and receivers, such as in high-dimensional device-independent quantum key distribution [5]. However, previous implementations of high-dimensional TM sources typically met only one of these requirements. For instance, sources based on dispersion-engineered PDC could produce high-dimensional entangled states, but their modal structure was permanently fixed during fabrication [45, 98, 99]. While some tunable sources using materials like gas-filled photonic crystal fibers offered dimensionality control, they lacked the precision to guarantee a well-defined modal structure [100]. Other reconfigurable schemes based on post-generation spectral filtering of broadband entanglement using pulse shapers [44, 101], Hong-Ou-Mandel interference [46], or Fabry-Pérot cavities [42, 43, 47, 102] could be scaled to higher dimensions, but the resulting states were often not maximally entangled due to residual frequency correlations or uneven mode populations [103]. Furthermore, this filtering approach would significantly limit the heralding efficiency, which is critical for many practical applications [104, 105].

The work presented in this chapter overcomes these trade-offs by demonstrating a programmable source of high-dimensional, maximally entangled TM states. Our approach uses a spectrally shaped pump pulse to drive an initially decorrelated PDC process. We show that this method allows us to programmatically select the dimensionality of the generated state, from a fully decorrelated state up to a 20-dimensional entangled state, while maintaining maximal entanglement. This source represents the first cornerstone of our work, providing an essential resource for a high-dimensional quantum communication framework based on time-frequency qudits.

3.1.1 Process engineering

In the experiment presented here, we generate entangled photon pairs via PDC, tailored using the dispersion engineering and pump shaping techniques described

in the previous chapter. Specifically, we use a type-II PDC process, in which the signal and idler photons are generated with orthogonal polarizations, in a periodically poled KTP (ppKTP) waveguide. We choose this material because it offers symmetric group-velocity matching at telecom wavelengths, meaning that the group velocities of signal and idler are symmetrically displaced around the pump velocity, leading to a phase-matching angle $\vartheta_{\mathrm{PDC}} = 45^\circ$ from eq. (2.3.7). We choose a poled length that yields a phase-matching function slightly narrower than the total pump bandwidth. The pump width can then be fine-tuned to exactly match the phase-matching width. This is the starting point of the experiment: if the pump is Gaussian-shaped and we filter out the side lobes of the phase-matching function, we obtain a decorrelated JSA corresponding to $d = 1$.

The key to achieving *programmable* entanglement lies in controlling the spectral shape of the pump pulse using an SLM-based 4-f pulse shaper, which we have addressed in Section 2.3.3. The SLM display can be updated in approximately 200 ms, allowing one to change the JSA "on the fly" and arbitrarily. By preparing the pump spectrum in specific shapes, the so-called cosine-kernel (CK) functions, we can selectively populate and control the weight of different Schmidt modes in the two-photon JSA, thereby dictating the dimensionality of the entanglement.

CK functions are Gaussian spectra modulated by a sum of cosine functions, which in the time domain corresponds to a sequence of ultrafast, equally-spaced Gaussian time bins. By shaping the pump into an nth-order CK function, we generate a bi-photon PDC state entangled in $n + 1$ of these time bins. However, since the bins are separated by only picoseconds, they are indistinguishable in time by conventional single-photon detectors. A significant advantage of this method is that higher-order CK modes are contained within the same spectral bandwidth, meaning the dimensionality can be increased without requiring a broader pump spectrum. However, higher-order modes exhibit progressively finer spectral features, which require higher resolution from the pulse shaper. This shaping resolution is ultimately the main experimental limitation on the maximum achievable dimensionality of the entangled state.

3.1.2 Quantifying entanglement dimensionality

Creating high-dimensional entangled states is only one part of the task; verifying and quantifying the dimensionality of this entanglement is equally crucial. This ensures that our source performs as intended and that the generated states are suitable for their targeted applications. To confirm that our source produces entanglement of the intended dimensionality, we employ two primary characterization methods.

Schmidt decomposition

As we have seen in section 2.2.3, the modal structure of the two-photon state generated by PDC can be studied by performing a Schmidt decomposition on its JSA $F(\omega_s, \omega_i)$ [69]. This decomposition expresses the JSA in the form

$$F(\omega_s, \omega_i) = \sum_k \sqrt{\lambda_k} f_k(\omega_s) g_k(\omega_i),$$

as seen in eq. (2.2.19). Here, the Schmidt coefficients $\sqrt{\lambda_k}$ determine the weight λ_k of each Schmidt mode, which is formed by the pairwise product of the orthonormal signal and idler basis functions $\{f_k(\omega_s)\}$ and $\{g_k(\omega_i)\}$, respectively.

A straightforward approach to quantifying the dimensionality of this entangled state might be to simply "count" modes through the number of non-zero Schmidt coefficients, also known as the *Schmidt rank*. However, for typical PDC processes, the Schmidt coefficient distribution exhibits an infinite tail of very small, yet non-zero, λ_k values (see, e.g., Figure 2.5). In such cases, the Schmidt rank is infinite, making it neither a practical nor insightful measure of entanglement.

A more informative metric for the dimensionality of an entangled state is the Schmidt number K, given by

$$K = \frac{1}{\sum_k \lambda_k^2}, \tag{3.1.1}$$

which measures the *effective* number of modes that contribute to the entanglement. The minimum possible Schmidt number is $K = 1$, which indicates a decorrelated two-photon state. If the Schmidt coefficient distribution is uniform (i.e., a finite number of λ_k are equal, and all others are zero), then K equals the Schmidt rank, and the state is considered maximally entangled in that dimension. In particular, an infinite number of equally weighted coefficients will lead to $K \to \infty$.

Beyond dimensionality, the full Schmidt decomposition reveals the entire modal structure of the entanglement, including the spectral shapes $f_k(\omega_s)$ and $g_k(\omega_i)$. However, experimentally obtaining this complete information is challenging as it requires reconstructing the full complex JSA, including its spectral phase, which can be significantly resource-demanding.

In Optica Quantum 2(5), 339–345 (2024), we adopted a practical approach to gain insight into the modal structure without a direct phase measurement of the two-photon state itself. We measured the joint spectral intensity (JSI), $|F(\omega_s, \omega_i)|^2$, using time-of-flight spectrographs. To reconstruct an effective JSA, we made the assumption that the spectral phase of the pump field, as programmed by the pulse shaper, is coherently transferred to the JSA via energy conservation ($\omega_p = \omega_s + \omega_i$). Therefore, in post-processing, we combined the square root of the measured JSI with the *programmed* pump phase to approximate the complex JSA, which we then used for the Schmidt decomposition. While this method offers an accessible way to verify the programmability of our source, it is not rigorous

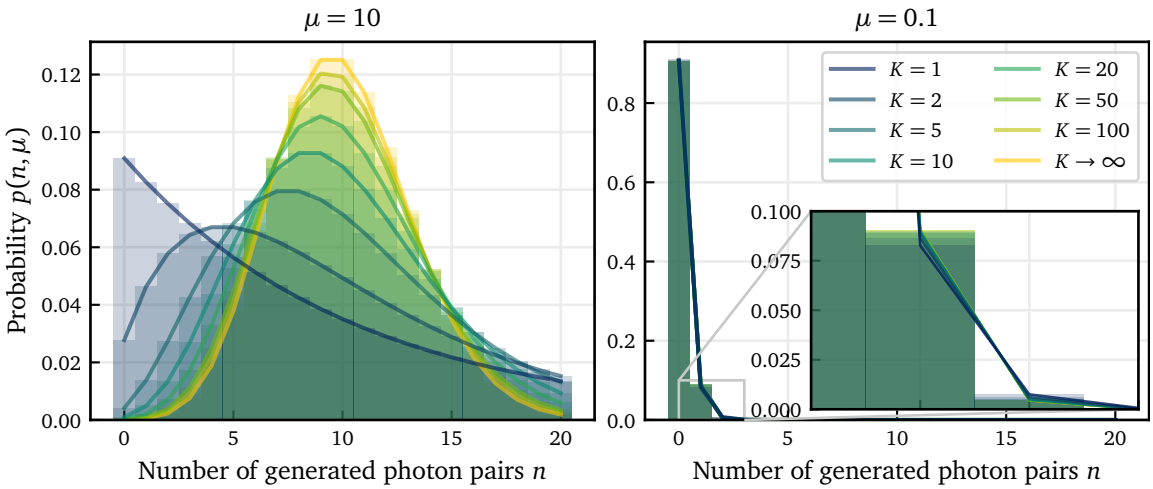

Figure 3.1: Photon number distributions $p(n, \mu)$ from eq. (3.1.4) for a mean photon number $\mu = 10$ (left) and $\mu = 0.1$ (right). As the Schmidt number K increases, the distribution shifts from thermal ($K = 1$) to Poissonian ($K \to \infty$). At low mean photon numbers, this shift results in a slight change of the heights of $p(1)$ and $p(2)$.

because it neglects potential phase distortions, hence it must be complemented with a more direct quantification of the entanglement dimensionality.

Second-order correlation function $g^{(2)}$ measurements

Another method to probe the dimensionality of our PDC source involves measuring the second-order correlation function, $g^{(2)}(0)$. For ultrafast pulsed PDC sources, where the pulse duration is much shorter than the detection window, the $g^{(2)}(0)$ measurement effectively integrates over the entire pulse. In this case, its interpretation gives us insight on the modal structure of the PDC state by sampling its photon number statistics.

In the low-gain regime, each Schmidt mode acts as an independent thermal emitter. For a single-mode PDC process ($K = 1$) with mean photon number μ, the probability $p(n, \mu)$ of generating n photon pairs in a pulse is described by a thermal distribution

$$p_{\text{thermal}}(n, \mu) = \frac{1}{\mu + 1} \left(\frac{\mu}{\mu + 1} \right)^n . \tag{3.1.2}$$

In a multi-mode PDC process, the overall photon number distribution is given by the convolution of the distributions from each mode. In particular, according to the central limit theorem, an infinite number of equally weighted modes leads to a Poissonian distribution

$$p_{\text{Poisson}}(n, \mu) = \frac{\mu^n e^{-\mu}}{n!} . \tag{3.1.3}$$

Between these two extremes, with a finite number of modes or unequal Schmidt weights, computing the convolution can be difficult. This computation can be

made easier by probability generating functions (PGFs) [106, 107]: the values of $p(n)$ are the power-series coefficients of the PGF $G(s) = \sum_{n=0}^{\infty} p(n)s^n$; therefore, knowing the PFG, they can be calculated as $p(n) = \frac{1}{n!}\frac{\partial^n}{\partial s^n}G(s)\big|_{s=0}$. The PGF of a thermal distribution is $G_{\text{thermal}}(s) = [1+\mu(1-s)]^{-1}$, whereas that of a Poissonian is $G_{\text{Poisson}}(s) = e^{-\mu(1-s)}$. The convolution of different distributions can then be derived from the product of their PGFs as $p(n) = \frac{1}{n!}\frac{\partial^n}{\partial s^n}\prod_k G_k(s)\big|_{s=0}$.

For instance, for K equally weighted modes, each associated to a thermal distribution with mean photon number μ/K, we obtain

$$p_K(n,\mu) = \binom{n+K-1}{n}\left(\frac{K}{K+\mu}\right)^K\left(\frac{\mu}{K+\mu}\right)^n. \tag{3.1.4}$$

This distribution correctly reduces to eq. (3.1.2) for $K = 1$ and to eq. (3.1.3) for $K \to \infty$ (see Figure 3.1). Thus, the Schmidt number K, and in general the full modal structure, is strictly linked to the photon number statistics.

In particular, if $\mu \ll 1$, generating three or more photon pairs in the same pulse is extremely unlikely, and the photon number distribution can be characterized by comparing the probability to generate one versus two photon pairs[1]. This can be achieved by measuring the $g^{(2)}(0)$ (hereafter labeled $g^{(2)}$) in the signal or idler arm. Experimentally, this is done by splitting that arm with 50/50 probability into two detectors and calculating $g^{(2)} = \frac{N_{12}N_{\text{tot}}}{N_1N_2}$, where N_{12} are coincidence counts, N_1 and N_2 are the single counts in each detector, and N_{tot} is the total number of pump pulses in the time interval of the measurement.

For a single-mode process, the thermal distribution yields $g^{(2)} = 2$, whereas for an infinitely multi-mode PDC state, the Poissonian statistics gives $g^{(2)} = 1$. In general, the $g^{(2)}$ has been shown to be directly related to the Schmidt number K through [108]

$$g^{(2)} = 1 + \frac{1}{K}, \tag{3.1.5}$$

shown in Figure 3.2. Measuring the $g^{(2)}$ of a single PDC arm, therefore, yields the effective number of modes K, hence the (effective) dimensionality of the entangled state. This method has the important advantage to be independent of optical losses (in the absence of noise or saturation effects), making it an extremely useful tool in real experimental setups. However, the $g^{(2)}$ does not give any information on the Schmidt coefficient distribution beyond the Schmidt number. For this reason, to assess whether a state is maximally entangled, we must also perform other measurements, such as the JSA reconstruction described above.

[1] We excluded vacuum contributions, which are tricky to measure since they represent the absence of a click.

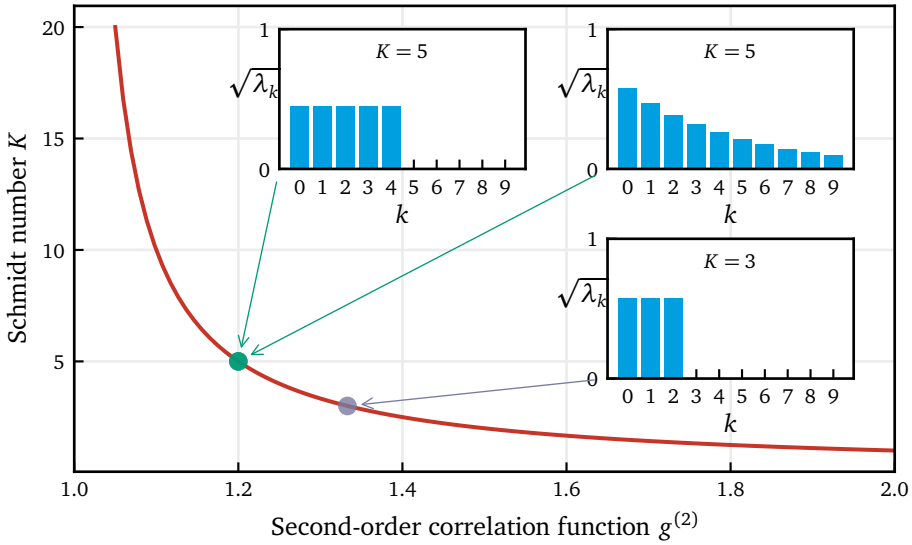

Figure 3.2: Schmidt number K as a function of the second-order correlation function $g^{(2)}$. Note that different Schmidt coefficient distributions characterized by the same K cannot be distinguished by $g^{(2)}$ measurements.

3.1.3 Summary of the experimental results

The following publication, Optica Quantum 2(5), 339–345 (2024), demonstrates the experimental realization of a programmable high-dimensional entangled photon source, based on the principles described above. We showcase the generation of entangled time-frequency qudits with a programmable dimensionality tunable from $d = 1$ (decorrelated state) up to $d = 20$, verified through $g^{(2)}$ measurements. The JSA reconstruction yields a uniform distribution of Schmidt coefficients, indicating the generation of maximally entangled states, which is further supported by the fact that the value of K retrieved from the JSA matches the value obtained from the $g^{(2)}$. This demonstration directly contributes to the overarching goal of this thesis by providing a flexible method for producing the time-frequency entangled qudits that are crucial for the practical realization of high-dimensional quantum communication.

3.1.4 Observing high-dimensional nonlocality

The high-fidelity entangled states generated and characterized in this chapter are not only a valuable resource for quantum communication but also enable fundamental tests of quantum mechanics. We demonstrated this in a collaborative work (not directly included in this thesis) with the groups of J. Leach at Heriot-Watt University and A. Tavakoli at Lund University [109], where the on-demand reconfigurability of our source was fundamental for testing Bell-nonlocality. In this work, we used JSI measurements of our time-frequency entangled states to certify the violation of high-dimensional Bell inequalities.

Specifically, the analysis focused on the Collins-Gisin-Linden-Massar-Popescu (CGLMP) inequality [110], a generalization of the Bell inequality to systems with dimension $d \geq 2$. A crucial experimental challenge in such tests is performing the required multi-outcome measurements in different bases. In [109], we showed that JSI measurements inherently fulfill this requirement: despite relying solely on intensity measurements, the JSI captures the interference arising from the temporal degree of freedom, enabling the certification of high-dimensional quantum nonlocality.

The outcomes of these spectral measurements probe phase-sensitive superpositions of time bins, analogously to the interference pattern observed in a double- or multi-slit experiment, which is precisely the type of measurement needed for high-dimensional Bell tests [110]. Using this technique, we observed violations of the CGLMP inequality up to dimension $d = 8$, demonstrating both the potential of intensity-only measurements to access phase-sensitive superpositions and the deeply non-classical nature of the generated high-dimensional time-frequency entangled states.

Research Article Vol. 2, No. 5 / 25 October 2024 / Optica Quantum 339

OPTICA QUANTUM

Orchestrating time and color: a programmable source of high-dimensional entanglement

Laura Serino,[1,†,*] Werner Ridder,[1,†] Abhinandan Bhattacharjee,[1] Jano Gil-Lopez,[1] Benjamin Brecht,[1] and Christine Silberhorn[1]

Paderborn University, Integrated Quantum Optics, Institute for Photonic Quantum Systems (PhoQS), Warburgerstr. 100, 33098 Paderborn, Germany

[†] *The authors contributed equally to this work.*

[*] *laura.serino@upb.de*

Received 7 June 2024; revised 22 August 2024; accepted 30 August 2024; published 15 October 2024

High-dimensional encodings based on temporal modes (TMs) of photonic quantum states provide the foundations for a highly versatile and efficient quantum information science (QIS) framework. Here, we demonstrate a crucial building block for any QIS applications based on TMs: a programmable source of maximally entangled high-dimensional TM states. Our source is based on a parametric downconversion process driven by a spectrally shaped pump pulse, which facilitates the generation of maximally entangled TM states with a well-defined dimensionality that can be chosen programmatically. We characterize the effective dimensionality of the generated states via measurements of second-order correlation functions and joint spectral intensities, demonstrating the generation of bi-photon TM states with a controlled dimensionality in up to 20 dimensions.

https://doi.org/10.1364/OPTICAQ.532334

1. INTRODUCTION

In recent years, the field of quantum communication has experienced remarkable progress, bringing us closer to the creation of a so-called quantum internet [1] which will exploit the fundamental properties of quantum particles to guarantee secure and efficient transmission of information. High-dimensional entangled states play a key role in these advancements [2]: their higher information capacity allows for significantly more efficient communication, and high-dimensional quantum cryptography protocols offer enhanced security [3]. Photons emerge as a natural information carrier due to their inherent quantum nature and high-dimensional spatial and time-frequency degrees of freedom.

Of the high-dimensional photonic degrees of freedom, the spatial domain is arguably the most explored, due to the possibility to generate and manipulate states using only time-invariant operations [4–6]. However, spatial encoding is incompatible with existing single-mode fiber networks and information is easily degraded by turbulence in free-space transmission [7].

Encoding information in the time-frequency domain of photons overcomes these disadvantages by offering robust transmission both through optical fiber and free space. In this platform, information can be encoded in pulsed temporal modes (TMs) [8], i.e., field-orthogonal wave-packet modes. A practical quantum communication framework based on TMs requires tools to generate, manipulate, and detect high-dimensional TM states. The manipulation and detection of one or many single-photon TMs have been demonstrated through the so-called quantum pulse gate [9–11], interferometric systems [12], or a combination of phase modulators and pulse shapers [13,14]. However, the realization of an optimal source of high-dimensional entangled TM states remains an open challenge.

An ideal source of time-frequency entanglement must generate bi-photon states with a well-defined dimensionality, i.e., states that live in a finite-dimensional Hilbert space [8]. A prime example of this are high-dimensional maximally entangled states, which facilitate entanglement-based quantum communication protocols such as high-dimensional device-independent quantum key distribution [3]. Moreover, the ability to programmatically reconfigure the dimensionality of the generated states can enhance the performance of a wide range of QIS applications, where different protocols and receivers may demand specific dimensionalities for efficient operation. However, current implementations of high-dimensional TM sources typically meet only one of these essential requirements. In dispersion-engineered parametric-downconversion (PDC) sources [15–17], high-dimensional entangled states are generated by precisely tailoring the phase-matching function of nonlinear crystals, preventing the dimensionality of the system from being modified after the fabrication process. Gas-filled photonic crystal fibers are nonlinear materials whose dispersion properties can be altered even after fabrication, allowing for flexible dimensionality control of the generated entangled states [18]; however, in these materials, the dispersion control is not accurate enough to guarantee a well-defined dimensionality.

Alternative reconfigurable schemes rely on spectral manipulation or filtering of broadband frequency-entangled photons applied through pulse shapers [19,20], Hong–Ou–Mandel

340 Vol. 2, No. 5 / 25 October 2024 / *Optica Quantum* Research Article

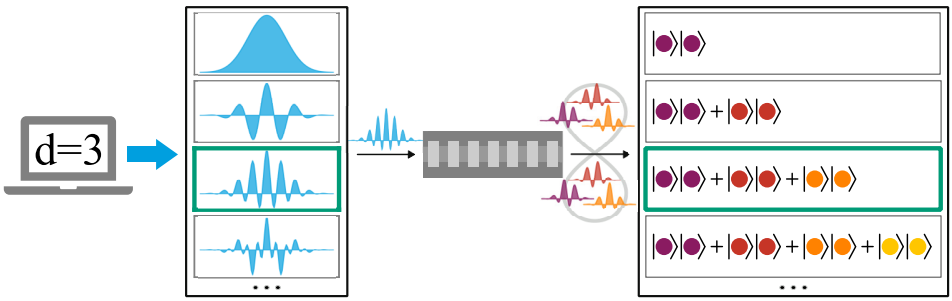

Fig. 1. Working principle of the programmable source of high-dimensional entangled photons: the user-chosen dimensionality defines the pump spectrum for the PDC process, which determines the generated entangled state.

interference [21], or Fabry–Pérot cavities after [22–24] or around [25] the PDC source. These methods generate discrete frequency-bin-entangled states that can be scaled to higher dimensions by increasing the spectral bandwidth of the PDC source; however, these states are not maximally entangled due to the presence of residual frequency anti-correlations [26] or uneven population of the frequency bins. Moreover, filtering an entangled photon pair can limit the maximum achievable heralding efficiency [27,28].

Here, we demonstrate a programmable source of high-dimensional maximally entangled TM states (Fig. 1). Our source is based on a simple setup consisting of an initially spectrally decorrelated PDC process driven by a spectrally shaped pump pulse. Shaping the pump pulse into so-called cosine-kernel functions [29] facilitates the generation of maximally entangled TM states with well-defined dimensionality within a fixed spectral bandwidth. Notably, pulse shaping does not require an overhaul of the experimental setup for accessing different dimensions. The effective dimensionality of the generated states is characterized via measurements of second-order correlation functions $g^{(2)}$, which link photon number statistics and modal properties [30]. The modal structure is additionally analyzed via joint spectral intensities that directly probe the spectral distribution of the generated photon pairs, combined with the *a priori* knowledge of the pump phase. We demonstrate the generation of bi-photon TM states with a controlled dimensionality starting from a fully decorrelated (unentangled) state and scaling up to a 20-dimensional entangled state.

2. THEORETICAL BACKGROUND

PDC is a process in which a *pump* photon is converted into two lower-energy photons labeled *signal* and *idler*. This process must satisfy the requirements of energy conservation, described by the pump function $\alpha(\omega_s + \omega_i)$ in terms of the signal and idler frequencies ω_s and ω_i, respectively, and momentum conservation, given by the phase-matching function $\Phi(\omega_s, \omega_i)$ which is fixed by material properties. The product of these two functions is the joint spectral amplitude (JSA)

$$f(\omega_s, \omega_i) = \alpha(\omega_s + \omega_i)\Phi(\omega_s, \omega_i)\,, \tag{1}$$

which describes the correlations between the signal and idler photons as a function of their frequencies and, therefore, fully characterizes the PDC state [31] (Fig. 2).

The effective dimensionality of the Hilbert space in which the PDC state lives can be determined through a Schmidt decomposition of the corresponding JSA [31]. This process decomposes the JSA into sets of pairwise orthogonal modes

$$f(\omega_s, \omega_i) = \sum_{k=0}^{r-1} \sqrt{\lambda_k}\psi^k(\omega_s)\varphi^k(\omega_i)\,, \tag{2}$$

which are separable into signal ($\psi^k(\omega_s)$) and idler ($\varphi^k(\omega_i)$) complex spectral functions. In the low-gain regime, where one can identify the PDC state with a single photon pair, this expression fully describes the spectral entanglement between the two generated photons [32], and $\{|\psi^k\rangle\}$ and $|\{\varphi^k\rangle\}$ are the TM bases that describe the signal and idler state, respectively (see Supplement 1 for details). The Schmidt coefficients $\sqrt{\lambda_k}$ indicate the relative amplitude of each mode pair and are normalized such that $\sum_k \lambda_k = 1$. The effective dimensionality of the PDC state is quantified by the Schmidt number $K = 1/(\sum_k \lambda_k^2)$, whereas the number of non-zero $\sqrt{\lambda_k}$ coefficients defines the Schmidt rank r. A finite value of r implies that the generated signal and idler photons can be fully described by a finite-dimensional basis. In an experimental setting, this property allows one to fully characterize the PDC state through a finite number of measurements. If $K{=}r$, i.e., the Schmidt coefficients are uniformly distributed, then the photon pair is maximally entangled and can be described as $|\Psi\rangle = \sqrt{\lambda}\sum_{k=0}^{r-1}|\psi^k\rangle|\varphi^k\rangle$.

A Schmidt number of $K{=}1$ indicates a single-mode bi-photon state, i.e., a spectrally decorrelated JSA. This can be realized, for instance, through symmetric group-velocity matching in type-II PDC with a phase-matching function angled at 45° in the signal–idler frequency space [33]. The positively correlated phase-matching function will orthogonally intercept the pump function, which is always oriented at −45° due to energy conservation. If the pump spectrum and phase-matching function are both Gaussian-shaped and have the same bandwidth, then the resulting JSA will be a fully separable circle in frequency space (Fig. 2(a)).

To increase the dimensionality of the entangled state, one needs to modify the distribution of the Schmidt coefficients via appropriately tailoring the JSA. Equation (1) entails that this can be achieved by manipulating either the phase-matching function or the pump spectrum. While both approaches are feasible and have been demonstrated, only the latter allows one to apply these changes "on the fly", i.e., programmatically and without any hardware modifications [34]. For this reason, we focus on complex spectral shaping of the pump pulse [35] as the tool to tailor the PDC state.

We note that this technique fundamentally relies on achieving an initially decorrelated JSA which, in turn, requires an underlying positively correlated phase-matching function. Experimentally, this can be realized in periodically poled

Research Article Vol. 2, No. 5 / 25 October 2024 / Optica Quantum 341

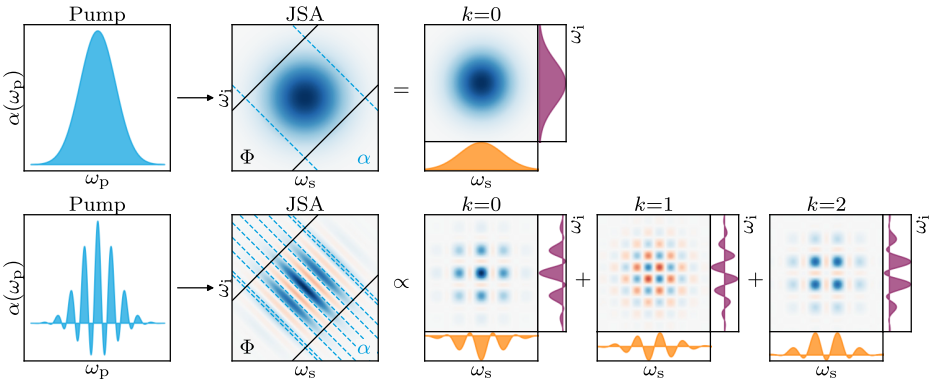

Fig. 2. Visual representation of the Schmidt decomposition of the JSA of a PDC state generated by a pump shaped as a Gaussian (top) and second-order CK (bottom) function. From left to right: pump spectrum $\alpha(\omega_p)$, where ω_p is the pump frequency; JSA, equal to the product of the pump function $\alpha(\omega_s + \omega_i)$ (dashed contour) and phase-matching function $\Phi(\omega_s, \omega_i)$ (solid contour); Schmidt modes and correspondent signal and idler functions. We note that the Schmidt modes in the bottom row have the same Schmidt coefficient $\sqrt{\lambda} = 1/\sqrt{3}$.

potassium titanyl phosphate (ppKTP), which allows one to reach a phase-matching angle of approximately 49° in bulk and 60° in waveguides. The procedure for achieving decorrelation has been detailed in [33,34,36] and, for this work, is described in Supplement 1.

One possibility to generate high-dimensional TM-entangled states is to shape the pump spectrum as Hermite–Gauss functions [10]. However, while this method allows for a well-defined dimensionality of the PDC state, it does not produce maximally entangled states beyond a two-dimensional Bell state [8]. Moreover, the spectral bandwidth spanned by Hermite–Gauss functions grows wider for increasing orders, posing a practical challenge for realistic implementations with a limited available bandwidth.

A notable alternative involves shaping the pump spectrum into the so-called cosine-kernel (CK) modes [29], i.e., Gaussian spectra modulated by a cosine function, which are the frequency-space representation of a superposition of Gaussian time bins. A pump pulse shaped as the nth order CK mode generates an $(n+1)$-dimensional maximally entangled state (Fig. 2). Unlike Hermite–Gauss modes, the spectral bandwidth spanned by CK modes is constant for all mode orders, offering a significant advantage for shaping methods similar to that in this work, in which the pump spectrum is "carved" from an initial pulse with a fixed spectral bandwidth. CK modes present finer spectral features for increasing mode orders; consequently, the highest-order mode that can be realized experimentally, and thereby the highest achievable dimensionality, will then depend solely on the resolution of the shaping system.

To verify the generation of high-dimensional maximally entangled states, one must characterize the modal structure of the PDC process [31]. As mentioned above, this can be done by fully characterizing the JSA and directly performing a Schmidt decomposition to verify that the Schmidt coefficients are uniformly distributed. From the Schmidt coefficients, one can also calculate the Schmidt number K to describe the effective dimensionality of the state. However, existing methods to fully characterize the JSA of PDC states (based on state tomography [34] or spectral shearing interferometry [37]) are extremely resource-expensive, as they require an additional nonlinear process or a complex interferometric setup. Simpler techniques that estimate K based, for instance, on Hong–Ou–Mandel interference of the generated photons [38] are only suitable when the impact of the pump phase on the PDC state is negligible; therefore, they would not be effective in the proposed source, in which the entanglement largely originates from the spectral phase distribution of the pump.

In 2011, A. Christ *et al.* [30] demonstrated a resource-efficient method to probe K using the normalized second-order correlation function $g^{(2)}$ of pulsed quantum light. This approach is suitable for a measurement system in which the detection window is longer than the pulse duration but shorter than the pulse period, which is the typical case in ultrafast quantum optics. In this regime, the value of $g^{(2)}$ indicates the integral of the second-order correlation function over one pulse. In the low-gain regime, the $g^{(2)}$ is connected to the Schmidt number K by the simple relation [30]

$$g^{(2)} \approx 1 + \frac{1}{K}. \tag{3}$$

Although $g^{(2)}$ measurements are an established tool to monitor the effective dimensionality of a PDC state, they are not sufficient to determine whether the state is maximally entangled, as a non-uniform distribution of Schmidt coefficients could also yield an integer value of K. Therefore, we look at $g^{(2)}$ measurements in combination with the joint spectral intensity (JSI) of the state. In contrast to the JSA, the JSI can be straightforwardly measured with a simple spectrometric setup requiring only a dispersive medium and time-resolved detection [39]. The JSI lacks the phase information necessary to correctly estimate the Schmidt coefficients; nevertheless, we can assume that the *a priori* known spectral phase applied to the pump pulse is mapped to the JSA following the energy conservation condition, i.e., antidiagonally in the signal–idler frequency space. We can then apply this phase to the square root of the measured JSI to reconstruct the JSA, and confirm the maximally entangled condition of the PDC state via a Schmidt decomposition. This leads us to an estimate of the dimensionality of the system that we can compare with the effective dimensionality calculated from the $g^{(2)}$ to confirm the generation of a high-dimensional maximally entangled state.

3. EXPERIMENT

A schematic of the experiment is shown in Fig. 3(a). Ultrashort laser pulses with a duration of 150 fs are generated by a Ti:Sapphire laser with a repetition rate of 80 MHz and a

342 Vol. 2, No. 5 / 25 October 2024 / Optica Quantum Research Article

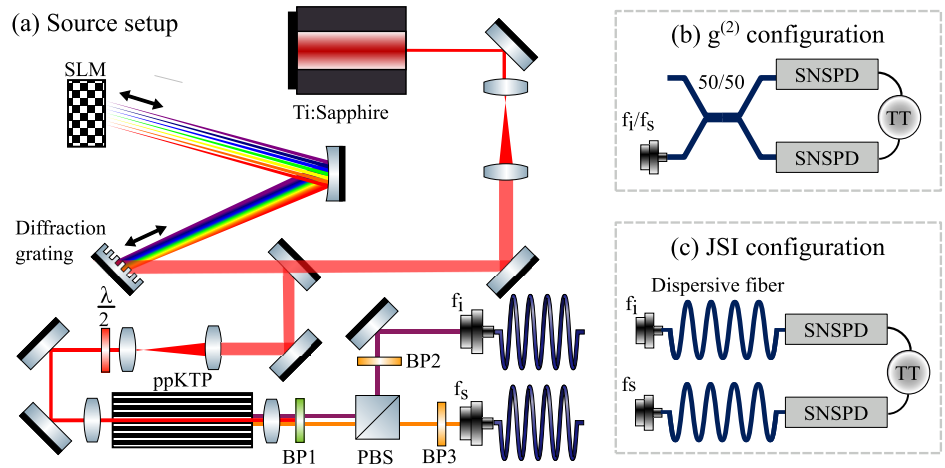

Fig. 3. Schematic of the experimental setup. (a) PDC source. The pump beam (red line) is generated by a Ti:Sapphire laser and is spectrally shaped by a 4-f waveshaper based on a spatial light modulator (SLM). The shaped beam is coupled into a periodically poled potassium titanyl phosphate (ppKTP) waveguide. The photon pair generated by the PDC process in the waveguide is isolated from the remaining pump light by a broad bandpass filter (BP1). The two photons are separated by a polarizing beam splitter (PBS), filtered again by narrowband filters BP2 and BP3, and then coupled into single-mode fibers. (b) $g^{(2)}$-measurement configuration. One arm $f_{i/s}$ of the source setup is connected to a 50/50 fiber beam splitter. The photons in each output of the beam splitter are detected by a combination of superconducting nanowire single-photon detectors (SNSPDs) and a time-tagging unit (TT). (c) Measurement configuration for the time of flight (ToF) spectrograph. The frequencies of signal and idler photons are mapped to delays by dispersive fibers, and arrival-time correlations are detected by single-photon detectors and a time-tagging unit.

spectrum centered at $\lambda_p = 758.7$ nm. The beam is directed to a folded-4-f waveshaper [40] with a resolution of approximately 10 GHz to prepare the pump modes via amplitude and phase shaping. The pump beam is then coupled into an 8-mm-long periodically poled potassium titanyl phosphate (ppKTP) waveguide by AdvR Inc. with a poled length of 1.5 mm and a poling period of 117 µm. The type-II PDC process inside the poled waveguide generates pairs of orthogonally polarized photons with central wavelengths $\lambda_{0,s} = 1511$ nm and $\lambda_{0,i} = 1524$ nm for signal and idler, respectively.

A bandpass filter centered at 1538 nm with an acceptance bandwidth of 82 nm (Semrock FF01-1538/82) filters out the remaining pump light and most of the fluorescence light coming from the waveguide. The photon pair is then separated by a polarizing beam splitter (PBS) into the vertically polarized signal and the horizontally polarized idler. To further filter out fluorescence from the waveguide, both arms contain a narrow bandpass filter with a full-width at half-maximum of 7 nm angle-tuned to match the centers of the signal and idler spectra. The filter bandwidth is very close to the spectral bandwidth of the photons (approximately 7 nm and 5 nm for signal and idler, respectively) as it allows for significantly suppressing fluorescence noise while transmitting most of the PDC photons. After filtering, the photons are coupled into single-mode fibers and detected by two superconducting nanowire single-photon detectors (SNSPDs) with an efficiency of 80%.

We estimate the optical losses of the setup through the Klyshko efficiency [41], defined as $\eta_{s(i)} = p_{coinc}/p_{i(s)}$ for the signal (idler) arm, where p_{coinc} is the probability to detect a coincidence between both arms and $p_{i(s)}$ is the probability to have a click in the idler (signal) arm. Effectively, the Klyshko efficiency measures the probability of detecting one photon from a generated photon pair, given that the other photon has been detected. We measure $\eta_s \approx 25\%$ and $\eta_i \approx 25\%$, where the optical losses are mostly due to the fiber couplings.

For the $g^{(2)}$ measurements, one of the fiber out-couplings is connected to a fiber beam splitter, each output of which is detected by an SNSPD (Fig. 3(b)). Photon arrival times are recorded by a Swabian Instruments time-tagging unit, and time filtering is performed to suppress the fluorescence counts. Using the $g^{(2)}$ value as reference, we optimize the bandwidth and chirp (quadratic phase coefficient) parameters via the waveshaper to obtain the initial decorrelated PDC state from a Gaussian-shaped pump (see Supplement 1 for details).

We measure the JSI using a time-of-flight (ToF) spectrograph [39] (Fig. 3(c)). In this configuration, a dispersive fiber with a chromatic dispersion coefficient of −418 ps/nm is added to each of the PDC output arms to map frequencies to delays. The arrival times of the photons are then measured by two SNSPDs connected to a time-tagging unit. The pulse duration is short enough not to affect this measurement. The correlation between the arrival times of paired signal and idler is used to reconstruct the JSI.

4. RESULTS AND DISCUSSION

Figure 4 shows the measured effective dimensionality K of the PDC states as a function of the programmed CK order n compared with the theoretical values K_{th}. The experimental dimensionality, characterized via $g^{(2)}$ measurements of the signal and idler arms separately, grows linearly with n, confirming that the proposed system can successfully allow the user to programmatically select the effective dimensionality of the PDC state in up to 20 dimensions.

The initial values for the signal and idler arms, $g^{(2)}_{0,s} = 1.93 \pm 0.01$ and $g^{(2)}_{0,i} = 1.88 \pm 0.01$, correspond to a Schmidt number $K_{0,s} = 1.08 \pm 0.01$ and $K_{0,i} = 1.14 \pm 0.01$, respectively. These values are slightly larger than the expected fully decorrelated state value of $K_{0,th} = 1$, primarily due to non-ideal

Research Article Vol. 2, No. 5 / 25 October 2024 / Optica Quantum 343

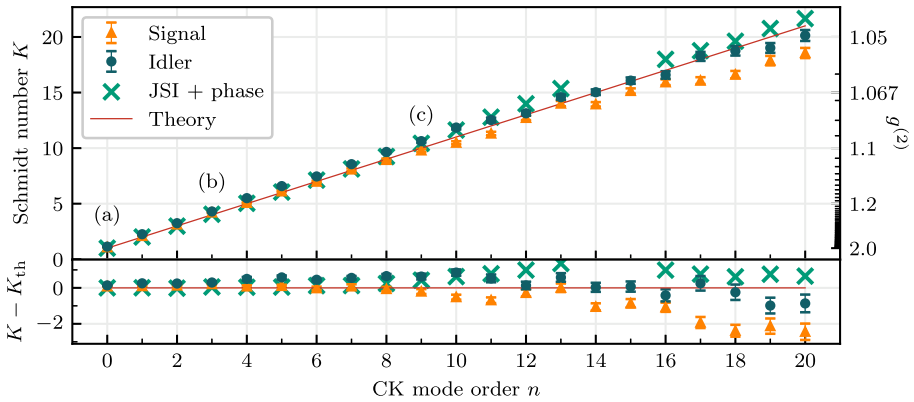

Fig. 4. Experimental Schmidt number K for each CK mode n obtained from $g^{(2)}$ measurements in the signal and idler arms (orange and blue points) and values reconstructed from the deconvolved measured JSI combined with the known pump phase (green cross), compared with the theoretical values K_{th} (red line). The marked points correspond to the CK modes analyzed in Fig. 5.

phase-matching conditions: the phase-matching function of the ppKTP waveguide, shaped as a sinc at an angle of 31° with respect to the signal axis, deviates from the ideal condition of a perfectly diagonal Gaussian phase-matching. This non-ideal configuration leads to unwanted correlations between signal and idler frequencies, introducing a small multi-mode component to the PDC state. While these imperfections could be mitigated with the use of an apodized waveguide with a Gaussian phase-matching spectrum [42,43] engineered to have a perfect positive frequency correlation between signal and idler, their impact in this source is limited and is further reduced by spectral filters, which cut out the side lobes of the sinc-shaped phase-matching function.

Above $K = 18$, one can notice a higher discrepancy between the theoretical and experimental dimensionality. This is a consequence of the limited resolution of the waveshaper, which fails to perfectly shape the narrow features of high-order CK functions. As a matter of fact, the CK function of order $n = 17$ has a main peak with a spectral width of approximately 30 GHz, only three times larger than the resolution of the waveshaper. This issue can be easily addressed by using an improved waveshaper: increasing the resolution by only a factor 2 would allow one to generate CK functions up to order $n = 32$ before reaching the shaping limits.

Figures 5(a)–5(c) show, for three different CK orders, the measured JSI (first row), the JSA reconstructed by applying

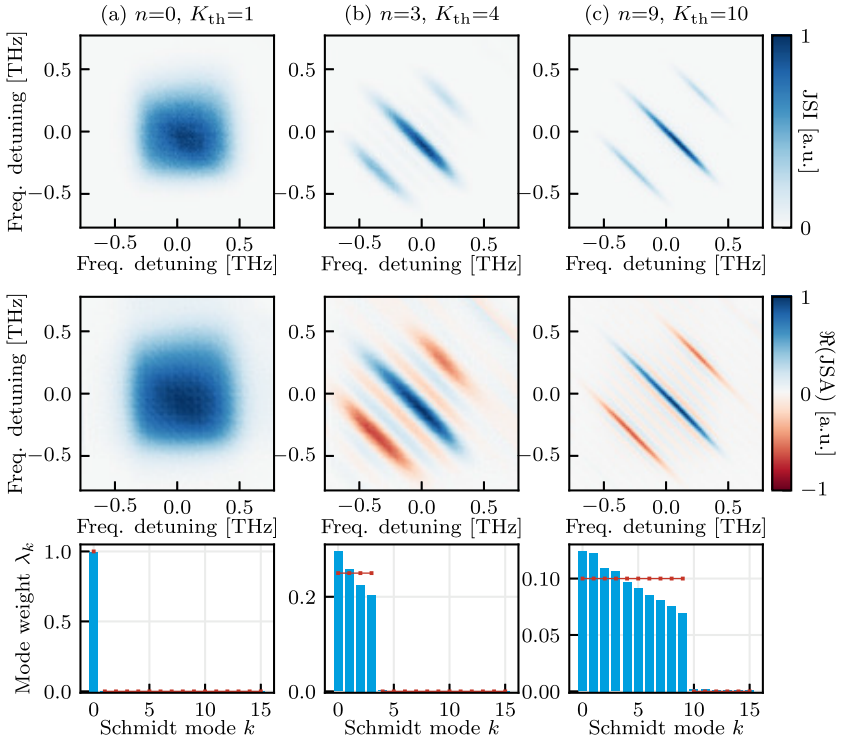

Fig. 5. For three different CK mode orders n: measured JSI (first row), JSA reconstructed from the deconvolved measured JSI combined with the known pump phase (second row), and resulting distribution of the Schmidt weights λ_k (blue bars) for each Schmidt mode k, compared with the expected weights for a maximally entangled state (red line).

the known pump phase to the measured JSI (second row), and the weights λ_k obtained from the Schmidt decomposition of the JSA (last row). We note that the limited resolution of the ToF spectrograph introduced an artificial broadening of the fine spectral features of high-order CK spectra; therefore, to eliminate these artifacts, we performed a deconvolution of the direct JSI measurements using the measured point-spread function of the ToF setup (see Supplement 1 for a detailed explanation).

The resulting Schmidt weights distribution (in blue) presents a clear edge at $k = K_{\text{th}}$, as expected from a maximally entangled state (in red). The zero value of the Schmidt weights beyond K_{th} indicates that the presented source generates states with a finite dimensionality, i.e., containing a finite number of Schmidt modes. The main discrepancy with the theory lies in the uneven value of the coefficients, which we attribute to the spectral distortions induced by the narrowband filters in each arm. As one can observe in the square edges in Fig. 5(a), the filters have a slightly narrower bandwidth than the generated photons and, as a consequence, introduce spectral distortions in the PDC state, which result in uneven additional optical losses for different Schmidt modes. Despite this drawback, narrow filtering is beneficial for $g^{(2)}$ measurements as it limits fluorescence noise, which would otherwise artificially increase the detected single counts and lead to a less accurate assessment of the $g^{(2)}$ value of the source. Contrarily, since JSI measurements are not as significantly affected by fluorescence, the effect of the induced distortions becomes noticeable. This is especially evident in the signal arm, which has a wider spectrum than the idler due to the sub-optimal phase-matching angle. Nevertheless, the unevenness of the Schmidt weights is small enough not to significantly affect K, as indicated by the Schmidt number K calculated from this distribution (the green cross in Fig. 4) being very close to the theoretical value K_{th}. Furthermore, the Schmidt weights can be directly addressed by tailoring the pump spectrum, allowing one to make their distribution more even if necessary.

We refer the reader to Supplement 1 for a more detailed analysis of the causes of experimental imperfections and possible solutions. We note that the highlighted challenges are technical, rather than fundamental limitations, and can be readily addressed, e.g., by employing a dispersion-engineered waveguide, a higher-resolution waveshaper, and spectral filters with an optimally matched bandwidth.

5. CONCLUSION

We demonstrated the generation of time-frequency-entangled photons with a programmable dimensionality ranging from 1 (decorrelated state) up to 20 dimensions, selected via straightforward spectral shaping of the pump pulse. By analyzing the measured joint spectral intensity alongside the *a priori* knowledge of the pump phase, we inferred a Schmidt coefficients distribution compatible with high-dimensional maximally entangled states. While our results and the theoretical predictions strongly suggest maximal time-frequency entanglement, a rigorous proof will necessitate a careful phase-sensitive characterization of the generated PDC states. This can be accomplished through high-dimensional state tomography, facilitated, e.g., by a so-called multi-output quantum pulse gate [11].

The performance of the current system is limited solely by technical constraints, which can be substantially enhanced by incorporating state-of-the-art experimental components. These improvements will facilitate the generation of maximally entangled states in more than 40 dimensions. Beyond dimensional control, manipulating the pump spectrum offers the potential not only to program the state dimensionality, but also to finely adjust the Schmidt weights themselves, thereby achieving an unprecedented degree of entanglement control.

The ongoing development of our source and the integration of cutting-edge components will pave the way for groundbreaking applications in quantum information processing, quantum communication, and quantum metrology, establishing our platform as a promising resource for advancing the capabilities of quantum technologies.

Funding. EU H2020 QuantERA; Deutsche Forschungsgemeinschaft.

Acknowledgment. The authors thank V. Ansari for helpful discussions. This research was supported by the EU H2020 QuantERA ERA-NET Cofund in Quantum Technologies project QuICHE, and by the Deutsche Forschungsgemeinschaft (DFG, German Research Foundation) – SFB-Geschäftszeichen TRR142/3-2022 – Projektnummer 231447078; Project C07.

Disclosures. The authors declare no conflicts of interest.

Data availability. Data underlying the results presented in this paper are not publicly available at this time but may be obtained from the authors upon reasonable request.

Supplemental document. See Supplement 1 for supporting content.

REFERENCES

1. H. J. Kimble, "The quantum internet," Nature **453**, 1023–1030 (2008).
2. Z.-S. Yuan, X.-H. Bao, C.-Y. Lu, *et al.*, "Entangled photons and quantum communication," Phys. Rep. **497**, 1–40 (2010).
3. L. Sheridan and V. Scarani, "Security proof for quantum key distribution using qudit systems," Phys. Rev. A **82**, 030301 (2010).
4. G. C. G. Berkhout, M. P. J. Lavery, J. Courtial, *et al.*, "Efficient sorting of orbital angular momentum states of light," Phys. Rev. Lett. **105**, 153601 (2010).
5. K. Huang, H. Liu, S. Restuccia, *et al.*, "Spiniform phase-encoded metagratings entangling arbitrary rational-order orbital angular momentum," Light: Sci. Appl. **7**, 17156 (2017).
6. M. Mirhosseini, O. S. Maga na-Loaiza, M. N. O'Sullivan, *et al.*, "High-dimensional quantum cryptography with twisted light," New J. Phys. **17**, 033033 (2015).
7. D. Cozzolino, B. Da Lio, D. Bacco, *et al.*, "High-dimensional quantum communication: Benefits, progress, and future challenges," Adv. Quantum Technol. **2**, 1900038 (2019).
8. B. Brecht, D. V. Reddy, C. Silberhorn, *et al.*, "Photon temporal modes: A complete framework for quantum information science," Phys. Rev. X **5**, 041017 (2015).
9. B. Brecht, A. Eckstein, R. Ricken, *et al.*, "Demonstration of coherent time-frequency schmidt mode selection using dispersion-engineered frequency conversion," Phys. Rev. A **90**, 030302 (2014).
10. V. Ansari, E. Roccia, M. Santandrea, *et al.*, "Heralded generation of high-purity ultrashort single photons in programmable temporal shapes," Opt. Express **26**, 2764–2774 (2018).
11. L. Serino, J. Gil-Lopez, M. Stefszky, *et al.*, "Realization of a multi-output quantum pulse gate for decoding high-dimensional temporal modes of single-photon states," PRX Quantum **4**, 020306 (2023).
12. P. C. Humphreys, B. J. Metcalf, J. B. Spring, *et al.*, "Linear optical quantum computing in a single spatial mode," Phys. Rev. Lett. **111**, 150501 (2013).
13. H.-H. Lu, J. M. Lukens, N. A. Peters, *et al.*, "Electro-optic frequency beam splitters and tritters for high-fidelity photonic quantum information processing," Phys. Rev. Lett. **120**, 030502 (2018).
14. H.-H. Lu, J. M. Lukens, N. A. Peters, *et al.*, "Quantum interference and correlation control of frequency-bin qubits," Optica **5**, 1455–1460 (2018).
15. F. Graffitti, P. Barrow, A. Pickston, *et al.*, "Direct generation of tailored pulse-mode entanglement," Phys. Rev. Lett. **124**, 1–6 (2020).

16. C. L. Morrison, F. Graffitti, P. Barrow, *et al.*, "Frequency-bin entanglement from domain-engineered down-conversion," APL Photonics **7**, 066102 (2022).
17. F. Chiriano, J. Ho, C. L. Morrison, *et al.*, "Hyper-entanglement between pulse modes and frequency bins," Opt. Express **31**, 35131–35142 (2023).
18. M. A. Finger, N. Y. Joly, P. S. J. Russell, *et al.*, "Characterization and shaping of the time-frequency Schmidt mode spectrum of bright twin beams generated in gas-filled hollow-core photonic crystal fibers," Phys. Rev. A **95**, 1–10 (2017).
19. C. Bernhard, B. Bessire, T. Feurer, *et al.*, "Shaping frequency-entangled qudits," Phys. Rev. A **88**, 032322 (2013).
20. N. B. Lingaraju, H.-H. Lu, S. Seshadri, *et al.*, "Quantum frequency combs and Hong–Ou–Mandel interferometry: the role of spectral phase coherence," Opt. Express **27**, 38683 (2019).
21. R. B. Jin, R. Shimizu, M. Fujiwara, *et al.*, "Simple method of generating and distributing frequency-entangled qudits," Quantum Sci. Technol. **1**, 015004 (2016).
22. Z. Xie, T. Zhong, S. Shrestha, *et al.*, "Harnessing high-dimensional hyperentanglement through a biphoton frequency comb," Nat. Photonics **9**, 536–542 (2015).
23. G. Maltese, M. I. Amanti, F. Appas, *et al.*, "Generation and symmetry control of quantum frequency combs," npj Quantum Inf **6**, 13 (2020).
24. K.-C. Chang, X. Cheng, M. C. Sarihan, *et al.*, "648 Hilbert-space dimensionality in a biphoton frequency comb: entanglement of formation and Schmidt mode decomposition," npj Quantum Inf **7**, 48 (2021).
25. Z. Y. Ou and Y. J. Lu, "Cavity enhanced spontaneous parametric down-conversion for the prolongation of correlation time between conjugate photons," Phys. Rev. Lett. **83**, 2556–2559 (1999).
26. H.-H. Lu, M. Liscidini, A. L. Gaeta, *et al.*, "Frequency-bin photonic quantum information," Optica **10**, 1655 (2023).
27. A. Christ, C. Lupo, M. Reichelt, *et al.*, "Theory of filtered type-II parametric down-conversion in the continuous-variable domain: Quantifying the impacts of filtering," Phys. Rev. A **90**, 023823 (2014).
28. E. Meyer-Scott, N. Montaut, J. Tiedau, *et al.*, "Limits on the heralding efficiencies and spectral purities of spectrally filtered single photons from photon-pair sources," Phys. Rev. A **95**, 1–8 (2017).
29. G. Patera, C. Navarrete-Benlloch, G. J. de Valcárcel, *et al.*, "Quantum coherent control of highly multipartite continuous-variable entangled states by tailoring parametric interactions," Eur. Phys. J. D **66**, 241 (2012).
30. A. Christ, K. Laiho, A. Eckstein, *et al.*, "Probing multimode squeezing with correlation functions," New J. Phys. **13**, 033027 (2011).
31. C. K. Law, I. A. Walmsley, and J. H. Eberly, "Continuous frequency entanglement: Effective finite hilbert space and entropy control," Phys. Rev. Lett. **84**, 5304–5307 (2000).
32. A. Ekert and P. L. Knight, "Entangled quantum systems and the Schmidt decomposition," Am J. Phys. **63**, 415–423 (1995).
33. G. Harder, V. Ansari, B. Brecht, *et al.*, "An optimized photon pair source for quantum circuits," Opt. Express **21**, 13975–13985 (2013).
34. V. Ansari, J. M. Donohue, M. Allgaier, *et al.*, "Tomography and purification of the temporal-mode structure of quantum light," Phys. Rev. Lett. **120**, 213601 (2018).
35. A. M. Weiner, "Femtosecond pulse shaping using spatial light modulators," Rev. Sci. Instrum. **71**, 1929–1960 (2000).
36. A. Eckstein, A. Christ, P. J. Mosley, *et al.*, "Highly efficient single-pass source of pulsed single-mode twin beams of light," Phys. Rev. Lett. **106**, 1–4 (2011).
37. A. O. C. Davis, V. Thiel, and B. J. Smith, "Measuring the quantum state of a photon pair entangled in frequency and time," Optica **7**, 1317 (2020).
38. M. Barbieri, E. Roccia, L. Mancino, *et al.*, "What Hong-Ou-Mandel interference says on two-photon frequency entanglement," Sci. Rep. **7**, 1–6 (2017).
39. M. Avenhaus, A. Eckstein, P. J. Mosley, *et al.*, "Fiber-assisted single-photon spectrograph," Opt. Lett. **34**, 2873–2875 (2009).
40. A. Monmayrant, S. Weber, and B. Chatel, "Phd tutorial: A newcomer's guide to ultrashort pulse shaping and characterization," J. Phys. B: At. Mol. Opt. Phys. **43**, 1 (2010).
41. D. N. Klyshko, "Use of two-photon light for absolute calibration of photoelectric detectors," Sov. J. Quantum Electron. **10**, 1112–1117 (1980).
42. A. Dosseva, L. Cincio, and A. M. Brańczyk, "Shaping the joint spectrum of down-converted photons through optimized custom poling," Phys. Rev. A **93**, 013801 (2016).
43. F. Graffitti, D. Kundys, D. T. Reid, *et al.*, "Pure down-conversion photons through sub-coherence-length domain engineering," Quantum Sci. Technol. **2**, 035001 (2017).

Supplemental Document

OPTICA QUANTUM

Orchestrating time and color: a programmable source of high-dimensional entanglement: supplement

LAURA SERINO,[1,†,*] WERNER RIDDER,[1,†] ABHINANDAN BHATTACHARJEE,[1] JANO GIL-LOPEZ,[1] BENJAMIN BRECHT,[1] AND CHRISTINE SILBERHORN[1]

Paderborn University, Integrated Quantum Optics, Institute for Photonic Quantum Systems (PhoQS), Warburgerstr. 100, 33098 Paderborn, Germany
[†]*The authors contributed equally to this work.*
[*]*laura.serino@upb.de*

Supplement DOI: https://doi.org/10.6084/m9.figshare.26928925

Parent Article DOI: https://doi.org/10.1364/OPTICAQ.532334

Orchestrating time and color: a programmable source of high-dimensional entanglement: supplemental document

In this supplemental document, we explain the technical details of our work.

1. COSINE-KERNEL FUNCTIONS IN THE FREQUENCY DOMAIN

The cosine-kernel function of order n in the frequency domain (Fig. S1) represents a sequence of $K = n + 1$ Gaussian-shaped time bins centered at time $t = 0$ and separated by Δt, described in terms of frequency ν:

$$\mathrm{CK}_n(\nu) = \sum_{k=0}^{K-1} \frac{1}{\sqrt{K}} \frac{1}{\sqrt{2\pi\sigma^2}} e^{-\frac{(\nu-\nu_0)^2}{2\sigma^2}} e^{i\,2\pi(\nu-\nu_0)\Delta t\,(k-\frac{K-1}{2})}\,, \tag{S1}$$

where ν_0 is the chosen central frequency, and $\sigma = \Delta\nu\,/2\sqrt{2\ln 2}$, with $\Delta\nu$ being the chosen spectral full-width-half-maximum. After some simple calculations, this expression simplifies to

$$\mathrm{CK}_n(\nu) = \frac{1}{\sqrt{K}} \frac{1}{\sqrt{2\pi\sigma^2}} e^{-\frac{(\nu-\nu_0)^2}{2\sigma^2}} \frac{\sin(\pi(\nu-\nu_0)\Delta t\,K)}{\sin(\pi(\nu-\nu_0)\Delta t)}\,, \tag{S2}$$

which describes a Gaussian envelope modulated by an oscillating function. These oscillations result in sharp peaks at frequencies $\nu_m = \nu_0 + m/\Delta t$ with null-to-null bandwidth $\delta\nu = 2/K\Delta t$.

Spectral shaping using CK functions is convenient for the shaping system employed in the current experimental setup: the Gaussian envelope limits the spectral bandwidth equally for all CK orders, and the spectral phase oscillates only between the two constant values 0 and π, which can be shaped more precisely than rapidly varying phases.

Describing CK modes as a sequence of K time bins intuitively explains why a CK-shaped pump generates K-dimensional entangled PDC states. Moreover, one could take this technique one step further and assign different weights λ_k to time bins, effectively tailoring the Schmidt coefficients and gaining full control over the modal structure of the entangled state. Although this approach results in a complex-valued pump spectrum in which the spectral phase can assume any value between 0 and 2π, this can still be generated by the current spectral shaping setup as long as the phase modulations are not excessively steep. This spectrum remains within the same Gaussian envelope, corresponding to the Fourier transform of a single time bin.

2. TEMPORAL MODES FOR SINGLE-PHOTON STATES

For a fixed polarization and transverse field distribution, temporal modes (TMs) form a complete set of quantum states for single photons [1]. Under these conditions, a single-photon quantum state in a specific TM $\left|\psi^k\right\rangle$ can be expressed as

$$\left|\psi^k\right\rangle \equiv \int d\omega\, \psi^k(\omega)\, \hat{a}^\dagger(\omega)\, |0\rangle\,, \tag{S3}$$

which represents the coherent superposition of single-photon monochromatic modes $\hat{a}^\dagger(\omega)$ modulated by the complex spectral amplitude $\psi^k(\omega)$ of the wavepacket.

3. ACHIEVING A DECORRELATED PDC STATE

The first step in the optimization of our source consists in finding the pump spectrum and spectral phase that facilitate the generation of a decorrelated PDC state (i.e., Schmidt number K=1). We expect this optimal pump shape to be a Gaussian spectrum with a bandwidth matching that of the phase-matching function. Additionally, the optical components in the setup will mostly

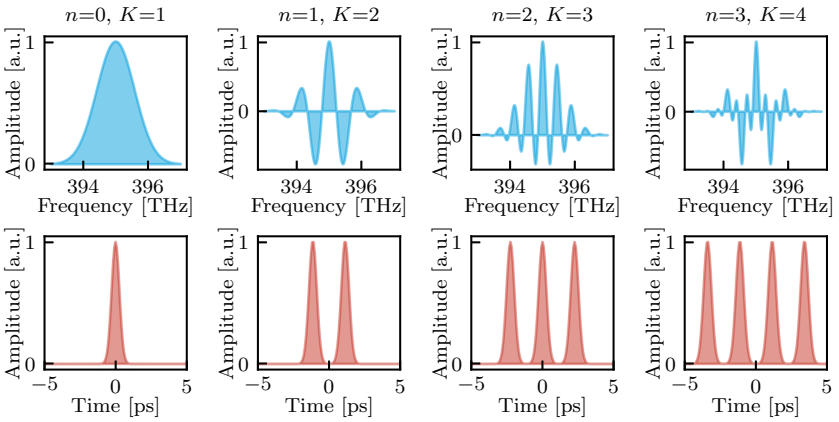

Fig. S1. First four cosine-kernel (CK) functions expressed as a function of frequency (top) and time (bottom).

introduce group-velocity dispersion in the pump, corresponding to a second-order phase coefficient ("chirp") that must be compensated for by the waveshaper to achieve a fully decorrelated state. For this reason, we measure $g^{(2)}$ as a function of different values of the full-width-at-half-maximum (FWHM) and chirp correction, and select the ones that minimize K (i.e., maximize the $g^{(2)}$).

The results of this characterization are shown in Fig. S2. One can notice that, above a FWHM of 2 nm, K saturates because we run into the edges of the narrowband filters in the PDC arms (see Fig. 3 in the main text). We choose a bandwidth of 2.6 nm (1.3 THz) which, after minor optimizations, yields $K = 1.08 \pm 0.01$ ($g^{(2)} = 1.93 \pm 0.01$) in the signal arm. This bandwidth is close to the phase-matching bandwidth of approximately 1 THz, and the discrepancy is to be attributed to the sub-optimal phase-matching angle, which is closer to 29° than to the ideal value of 45°. The optimal chirp correction, of approximately 0.15 ps^2, is a reasonable value to compensate for the chirp introduced by the setup.

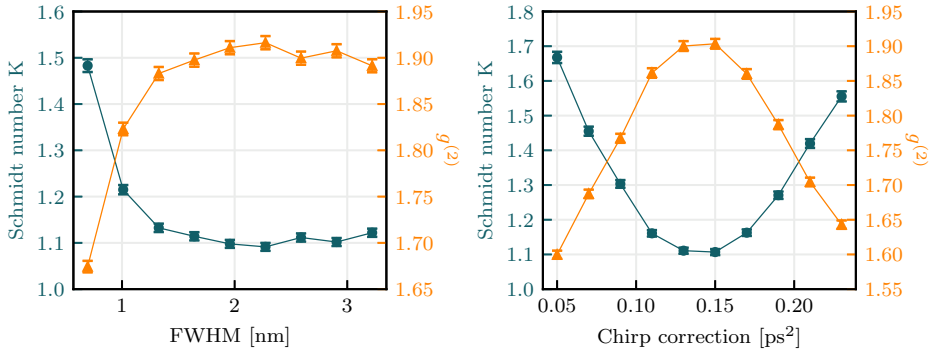

Fig. S2. Schmidt number K (blue circles) and $g^{(2)}$ (orange triangles) measured in the signal arm as a function of the FWHM of the pump spectrum (left) and of the chirp correction (right).

4. JSA RECONSTRUCTION

Fig. S3 illustrates the JSA reconstruction process for three different mode orders. The first row shows the raw JSI measurement which, for high orders, is visibly blurred by the low effective resolution of the time-of-flight (ToF) spectrograph and, therefore, not representative of the real PDC state. To limit this effect, we measure the point-spread function (PSF) of the ToF setup

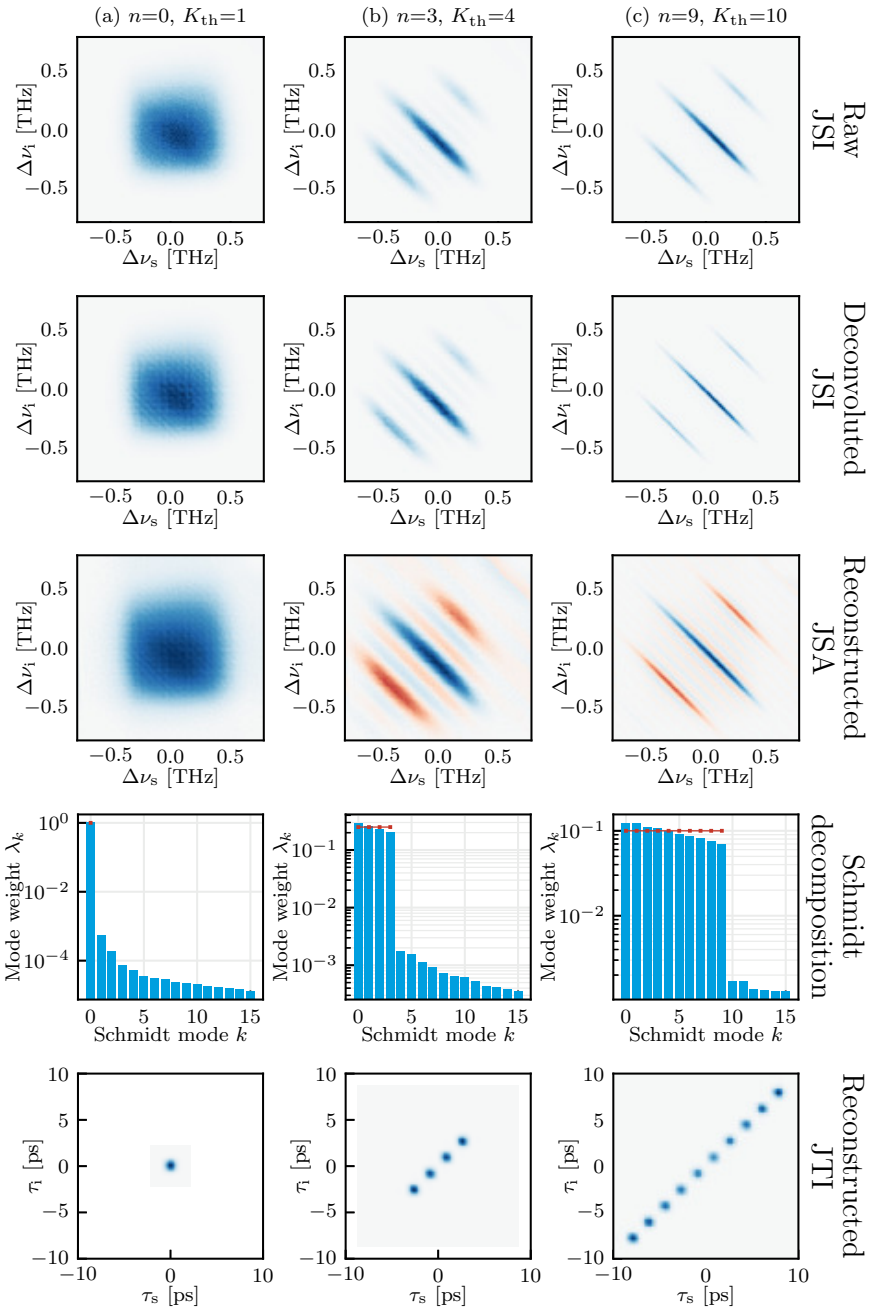

Fig. S3. Reconstruction process of the JSA for three different mode orders. From top to bottom: "raw" JSI measurement, deconvoluted JSI, reconstructed JSA (taking the square root of the JSI and applying the known pump phase), mode weights λ_k resulting from the Schmidt decomposition, reconstructed JTI (as squared modulus of the Fourier transform of the JSA).

and perform a Lucy-Richardson deconvolution [2] to retrieve the higher-resolution JSI shown in the second row. We note that this deconvolution algorithm does not require any information other than the blurred image and the measured PSF. At low CK orders, the deconvoluted JSI is essentially identical to the raw measurement; however, at high orders, the deconvolution brings back the distinctive fine features of the CK modes.

To reconstruct the JSA, we take the square root of the deconvoluted JSI and we apply the known pump phase diagonally (centered on the maximum of the JSI), obtaining the image in the third row. The pump phase consists of a sequence of phase jumps between 0 (blue) and π (red). We note that the phase jumps perfectly match the zero-intensity points in the JSI, confirming that the deconvoluted JSI is close to the real one. Then, we perform a Schmidt decomposition of the reconstructed JSA to retrieve the Schmidt coefficients $\sqrt{\lambda_k}$ which describe the modal structure of the generated PDC state. The distribution of the corresponding mode weights λ_k for the analysed cases is shown in the fourth row. Since the Schmidt number derived this way matches the one calculated from the $g^{(2)}$ measurements, we can assume that the reconstructed JSA is representative of the real one and, therefore, that we can examine the modal structure of the generated PDC state from the calculated mode weights.

One can notice a very clear distinction between the first K_{th} Schmidt weights, corresponding to the modes that compose the maximally entangled state, and the following ones, which are spurious modes arising from spectral imperfections such as shaping defects or too narrow filtering, and artifacts from the grid-like structure of the pixels in the JSA. Although the weight of these spurious modes is orders of magnitude lower than that of the primary modes, their very high number introduces a small component of multi-modedness that slightly increases the value of K. To limit this effect, one could choose spectral filters with a bandwidth still narrow enough to cut off the side lobes of the sinc-shaped phase-matching function and to limit fluorescence, but larger than the spectral bandwidth of the generated photons. This would avoid introducing edge effects in the spectrum and would also lower the optical losses after generation. Moreover, to reach a higher level of accuracy in the generated states, one could implement an iterative optimization method to perfect the spectral shaping of the pump, which would result in a more even distribution of the Schmidt coefficients. If one were able to remove these sources of imperfections in such a way to eliminate the contributions of the spurious modes with $k > K_{\text{th}}$, even keeping the same uneven weights of the main modes, one would obtain the effective dimensionality shown by the "+" symbols in Fig. S4, which follows much more closely the theoretical predictions.

The final row of Fig. S3 shows the reconstructed joint temporal intensity (JTI) calculated as the squared modulus of the Fourier transform of the reconstructed JSA. In the time picture, it becomes intuitive to see that a higher-order CK mode generates higher-dimensional entangled states in the form of correlated time bins whose intensity is determined by the Schmidt coefficients. Notably, due to the extremely short time separation between these correlated "islands" (approximately 2 ps), the time structure of the generated PDC states cannot be resolved by conventional single-photon detectors. For this reason, these states do not fall into the standard definition of time bins but rather correspond to that of temporal modes, which require a more sophisticated detection scheme based, e.g., on a so-called quantum pulse gate [3–5].

REFERENCES

1. B. Brecht, D. V. Reddy, C. Silberhorn, and M. G. Raymer, "Photon temporal modes: A complete framework for quantum information science," Phys. Rev. X **5**, 041017 (2015).
2. W. H. Richardson, "Bayesian-based iterative method of image restoration∗," J. Opt. Soc. Am. **62**, 55–59 (1972).
3. B. Brecht, A. Eckstein, R. Ricken, *et al.*, "Demonstration of coherent time-frequency schmidt mode selection using dispersion-engineered frequency conversion," Phys. Rev. A **90**, 030302(R) (2014).
4. V. Ansari, E. Roccia, M. Santandrea, *et al.*, "Heralded generation of high-purity ultrashort single photons in programmable temporal shapes," Opt. Express **26**, 2764–2774 (2018).
5. L. Serino, J. Gil-Lopez, M. Stefszky, *et al.*, "Realization of a multi-output quantum pulse gate for decoding high-dimensional temporal modes of single-photon states," PRX Quantum **4**, 020306 (2023).

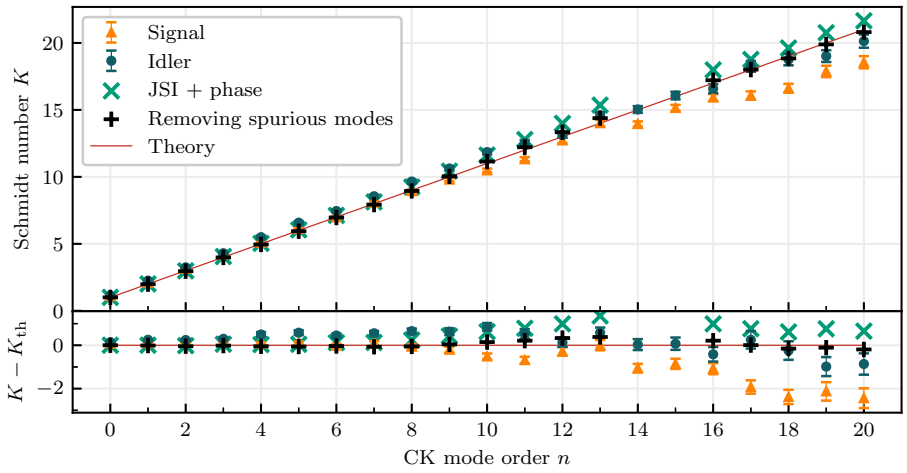

Fig. S4. Experimental Schmidt number K for each CK mode n obtained from $g^{(2)}$ measurements in the signal and idler arms (orange and blue points), values reconstructed from the deconvolved measured JSI combined with the known pump phase (green cross), values obtained by removing the spurious modes in the Schmidt decomposition (black "+"), compared to the theoretical values K_{th} (red line).

4

Decoding time-frequency qudits

After demonstrating a programmable source of high-dimensional entangled states in the previous chapter, we now address the second and arguably more significant experimental challenge: the development of a versatile high-dimensional decoder. A source, no matter how advanced, is of limited use without a corresponding receiver capable of efficiently extracting the information encoded in its states. In this chapter, we present the realization of the multi-output quantum pulse gate, the central technological contribution of this thesis. As we will show, this device solves the long-standing problem of high-dimensional temporal mode detection and serves as the key component for the applications in quantum communication and fundamental quantum mechanics explored in the remainder of this work.

The experimental results and methodologies presented in this chapter are based on the following publications:

[PRX Quantum 4, 020306 (2023)] L. Serino, J. Gil-Lopez, M. Stefszky, R. Ricken, C. Eigner, B. Brecht, and C. Silberhorn, "Realization of a multi-output quantum pulse gate for decoding high-dimensional temporal modes of single-photon states", *PRX Quantum* **4**, 020306 (2023). DOI: 10.1103/PRXQuantum.4.020306

[Opt. Express 33(3), 5577 (2025)] L. Serino, C. Eigner, B. Brecht, and C. Silberhorn, "Programmable time-frequency mode-sorting of single photons with a multi-output quantum pulse gate", *Optics Express* **33**(3), 5577 (2025). DOI: 10.1364/OE.544206

4.1 The challenge of high-dimensional detection

Measuring high-dimensional quantum states encoded in the time-frequency domain presents unique difficulties. Unlike polarization, where waveplates and polarizing beamsplitters suffice for qubit measurements, the time-frequency domain often requires more sophisticated interferometric or frequency-conversion-based approaches, especially for projective measurements onto superposition modes. An ideal decoder must be reconfigurable to different TM bases and capable of distinguishing multiple orthogonal modes simultaneously. This capability is fundamental for realizing the enhanced security and information capacity offered by HD-QKD protocols, such as the d-dimensional BB84 variant discussed in Section 1.4.2, which relies on projective measurements in multiple MUBs. Without high-dimensional decoders, the theoretical advantages of qudits in quantum communication remain largely inaccessible.

This challenge has been addressed by developing dedicated devices tailored to specific encoding alphabets, which led to a fragmented landscape of solutions. For frequency bins, the so-called quantum frequency processor demonstrated mode-sorting in three dimensions using a combination of phase modulators and pulse shapers [50, 52]. For time-bin encoding, interferometric setups achieved decoding for up to four dimensions, although only for two measurement bases [51]. All these specialized solutions generally relied on complex setups that hindered scalability to higher dimensions and lacked the reconfigurability to switch between encodings, creating a significant obstacle for a unified and versatile high-dimensional time-frequency framework.

Our group proposed the quantum pulse gate (QPG), which uses a dispersion-engineered sum-frequency generation process to project an input state onto a single, user-chosen temporal mode [48, 49, 111]. However, while the QPG can operate on high-dimensional inputs, it is fundamentally limited to a single output channel. Although preliminary work towards multi-output frequency conversion was demonstrated [79, 80], these implementations were inherently incompatible with single-photon-level inputs.

To overcome these limitations, we developed the multi-output quantum pulse gate (mQPG). This device is not merely an extension of the QPG, but a distinct technological advance that enables simultaneous, parallel projections onto a complete arbitrary basis of high-dimensional TMs. In this chapter, we will first review the working principles of the single-channel QPG and then detail the design, realization, and characterization of the mQPG, which forms the central component of the versatile framework presented in this thesis.

4.1.1 The quantum pulse gate

The QPG [48, 111–114] is a well-established device for mode-selective measurements in the time-frequency domain. It is based on a quasi-phase-matched SFG process which, as seen in Chapter 2, allows an input photon and a pump photon to be converted to a single photon at their sum frequency. Its working principle, design and behavior are extensively described in [63] and summarized below.

In a QPG, the signal and pump are group-velocity matched ($\nu_{g,in} = \nu_{g,p}$). This is often achieved using type-II SFG, where the signal and pump fields have different polarizations and thus experience different dispersion curves, allowing their group velocities to coincide at different wavelengths. This group-velocity matching makes the phase-matching angle ϑ_{SFG} in eq. (2.3.11) approximately zero. This yields a phase-matching function $\Phi(\omega_{in}, \omega_{out}) \approx \Phi(\omega_{out})$ that is largely independent of ω_{in} over a broad range, making it horizontal in the input-output frequency plane.

If this horizontal phase-matching function is much narrower along ω_{out} than the pump bandwidth, then the output will be confined to a small frequency region around the central frequency $\bar{\omega}_{out}$. Under these conditions, the Schmidt decomposition of the transfer function in eq. (2.2.24) yields a single mode, dictated by the pump shape:

$$G(\omega_{in}, \omega_{out}) \approx \Phi(\omega_{out})\alpha(\bar{\omega}_{out} - \omega_{in}) \approx f_0^*(\omega_{in})\, g_0(\omega_{out})\,. \tag{4.1.1}$$

The output Schmidt mode $g_0(\omega_{out})$ is primarily determined by the phase-matching function $\Phi(\omega_{out})$, whereas the input Schmidt mode $f_0(\omega_{in})$ is the mirrored conjugate of the pump spectrum $\alpha(\bar{\omega}_{out} - \omega_{in})$.

Consequently, the QPG acts as a mode-selective beamsplitter (see eq. (2.2.27)), described by the unitary operator $\hat{U}_{QPG}$ coupling an input TM $|A_0\rangle$ with envelope $f_0(\omega_{in})$ and a target output mode $|C_0\rangle$ with envelope $g_0(\omega_{out})$ [16]:

$$\hat{U}_{QPG} \approx \hat{\mathbb{1}} - (1 - \cos \mathcal{C}_0)(|A_0\rangle\langle A_0| + |C_0\rangle\langle C_0|) + \sin \mathcal{C}_0(|C_0\rangle\langle A_0| - |A_0\rangle\langle C_0|)\,, \tag{4.1.2}$$

where $\mathcal{C}_0$ is the coupling strength. The $\sin \mathcal{C}_0$ term converts $|A_0\rangle$ to $|C_0\rangle$ with efficiency $\eta_0 = \sin^2 \mathcal{C}_0$.

Let us consider an arbitrary single-photon input state $|\psi_{in}\rangle$ with spectral envelope $\xi(\omega_{in})$, sent to a QPG targeting mode $|A_0\rangle$. If we express the input in the pump basis as $|\psi_{in}\rangle = \sum_i c_i |A_i\rangle$, where $c_i = \langle A_i|\psi_{in}\rangle$, we can write the QPG output as

$$|\psi_{out}\rangle = \hat{U}_{QPG}|\psi_{in}\rangle \approx c_0 (\cos \mathcal{C}_0 |A_0\rangle + \sin \mathcal{C}_0 |C_0\rangle) + \sum_{i \neq 0} c_i |A_i\rangle\,, \tag{4.1.3}$$

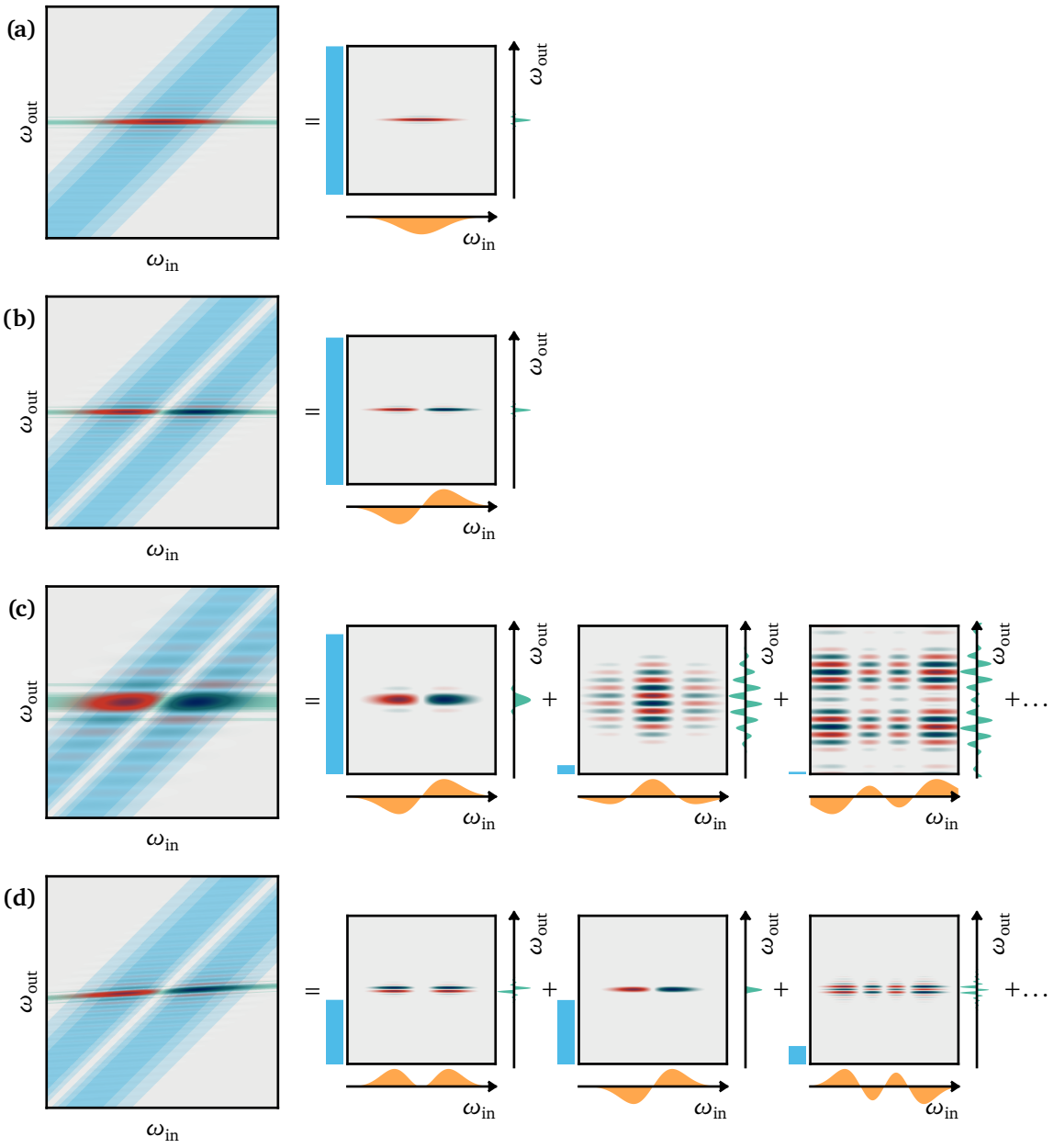

Figure 4.1: Schmidt decomposition of the QPG transfer function $G(\omega_{\text{in}}, \omega_{\text{out}})$. **(a,b)** If the phase-matching function is horizontal and its spectral width along ω_{out} is narrower than the spectral features of the pump, we obtain a single-mode process, i.e., a single beamsplitter, which selectively up-converts the input mode determined by the pump shape. If the phase-matching is too broad **(c)** or not horizontal **(d)**, then the process becomes multi-mode, introducing ambiguity in the measurement.

where only mode $|A_0\rangle$ is converted to $|C_0\rangle$ (assumed to be initially unoccupied), whereas all input modes orthogonal to $|A_0\rangle$ are transmitted unconverted. The probability P^0_{conv} that $|\psi_{\text{in}}\rangle$ is up-converted to $|C_0\rangle$ is:

$$P^0_{\text{conv}} = \sin^2 \mathcal{C}_0 |\langle A_0|\psi_{\text{in}}\rangle|^2 \approx \eta_0 \left| \int \alpha(\bar{\omega}_{\text{out}} - \omega_{\text{in}}) \xi(\omega_{\text{in}}) d\omega_{\text{in}} \right|^2 , \tag{4.1.4}$$

which is maximized when $|\psi_{\text{in}}\rangle$ perfectly matches $|A_0\rangle$. Effectively, the QPG projects the complex spectral amplitude of the signal onto that of the pump, and yields an output with probability proportional to this overlap.

While powerful for single-mode selection, the "legacy" QPG is fundamentally a single-channel device. High-dimensional protocols, however, require simultaneous, projective measurements onto all d elements of a chosen basis. Attempting this with standard QPGs would require a complex and lossy network of d separate devices, making it impractical for scalable systems. This limitation highlights the critical need for a truly multi-channel, reconfigurable decoder integrated into a single device.

4.1.2 Multi-output quantum pulse gate

To overcome this limitation, we developed the mQPG, a single, integrated device capable of performing parallel projective measurements on multiple orthogonal temporal modes. The mQPG achieves this by leveraging the super-poling dispersion engineering technique discussed in Section 2.3.2. Combined with the dispersion engineering conditions of the QPG, namely the group-velocity matching and narrow phase-matching function, this creates multiple phase-matching peaks centered at distinct output frequencies, each enabling an SFG process that can be addressed independently by different spectral regions of the pump. Therefore, through appropriately shaped pump pulses (using the techniques from Section 2.3.3), we realize several QPG operations in parallel within a single device. If the pump modes are mutually orthogonal, the Schmidt decomposition yields an input-output mode pair for each mQPG channel, as shown in Figure 4.2.

For an mQPG with m channels, each channel j projects onto a specific input TM $|A_j\rangle$ and converts it to an output mode $|C_j\rangle$ centered at a distinct output frequency $\bar{\omega}_{\text{out},j}$. If the channels are perfectly independent, the operation for the j-th channel is analogous to eq. (4.1.2), and the overall mQPG operation is

$$\hat{U}_{\text{mQPG}} \approx \hat{\mathbb{I}} + \sum_{j=0}^{m-1} \left[(\cos \mathcal{C}_j - 1)(|A_j\rangle\langle A_j| + |C_j\rangle\langle C_j|) + \sin \mathcal{C}_j (|C_j\rangle\langle A_j| - |A_j\rangle\langle C_j|) \right] \tag{4.1.5}$$

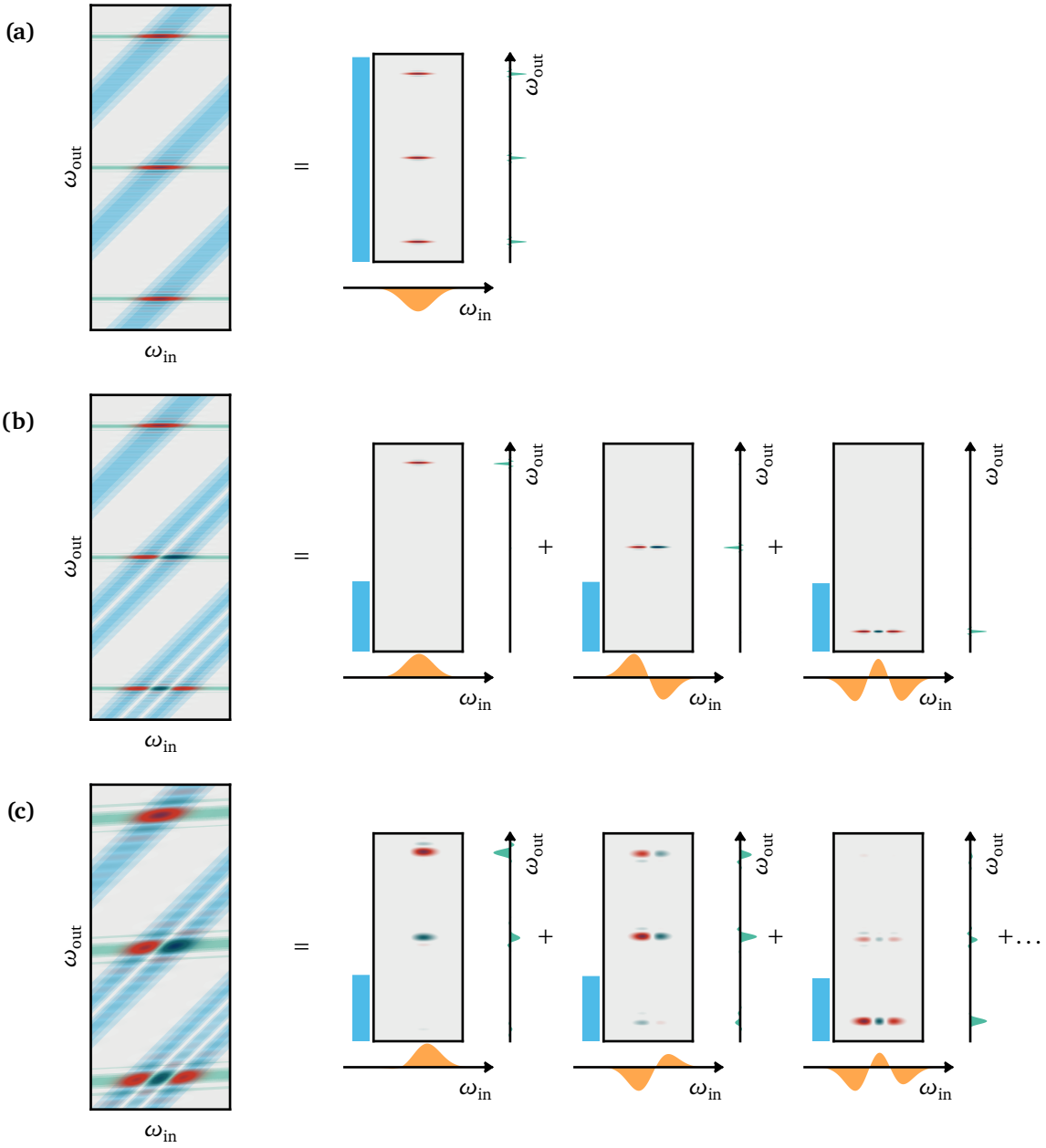

Figure 4.2: Schmidt decomposition of the mQPG transfer function $G(\omega_{in}, \omega_{out})$. The pump is divided in different spectral regions matching the phase-matching peaks. **(a)** If the pump has identical shapes in all three regions, we still have a single-mode conversion process overall. **(b)** If we shape the pump as orthogonal modes, the Schmidt decomposition yields a separate conversion process for each mQPG channel. **(c)** A broad or not horizontal phase-matching function introduces cross-talk between channels.

If the channels target an orthonormal basis $\left\{\left|A_j\right\rangle\right\}_{j=0}^{m-1}$, an input state $|\psi_{\text{in}}\rangle = \sum_i c_i |A_i\rangle$ is transformed to

$$|\psi_{\text{out}}\rangle = \hat{U}_{\text{mQPG}} |\psi_{\text{in}}\rangle \approx \sum_{j=0}^{m-1} c_j \left(\cos \mathcal{C}_j \left|A_j\right\rangle + \sin \mathcal{C}_j \left|C_j\right\rangle\right) + \sum_{i\geq m} c_i |A_i\rangle \ . \tag{4.1.6}$$

The probability of detecting a photon in output channel j therefore is

$$P_{\text{conv}}^{j} = \sin^2 \mathcal{C}_j \left|\left\langle A_j \middle| \psi_{\text{in}} \right\rangle\right|^2 \approx \eta_j \left| \int \alpha_j(\bar{\omega}_{\text{out},j} - \omega_{\text{in}}) \xi(\omega_{\text{in}}) d\omega_{\text{in}} \right|^2 . \tag{4.1.7}$$

Each distinct phase-matching region, addressed by a specific spectral portion of the pump α_j, thus maps an input TM to a photon in a spectrally distinguishable output channel.

4.1.3 Where is the quantum?

A question that naturally arises is: what makes the QPG or mQPG "quantum"? After all, these devices rely on nonlinear frequency conversion, a classical optical process. The mQPG itself does not *create* quantumness in the same way PDC creates entangled photon pairs. Rather, its crucial role in quantum information processing is to *preserve* the quantum nature of the input state during the measurement process. It allows input TMs to be coherently mapped to a superposition of spectrally distinguishable output modes. In our experiments, these output modes are typically directed to single-photon detectors, where the detection process collapses the superposition, yielding a click corresponding to a specific output channel. However, the mQPG output could also be used for more sophisticated quantum applications, e.g., interfacing different parts of a quantum network [115].

4.1.4 Designing an mQPG

To design an mQPG, we combine the principles of dispersion engineering and periodic poling modulation discussed in Section 2.3. The design process, detailed in the appendix of PRX Quantum 4, 020306 (2023), can be summarized as follows:

1. The first step is to choose the operating wavelength of the input field based on the desired application. For our work, we select an input signal in the telecommunication C-band ($\sim 1550\,\text{nm}$).
2. Then, we need to choose the operating wavelength of the pump field. The fundamental requirement for a QPG is a horizontal phase-matching function, which is necessary to achieve mode-selective up-conversion of arbitrary TMs. As discussed in Section 4.1.1, this is achieved through group-velocity

matching between the signal and pump pulses ($\nu_{g,in} = \nu_{g,p}$). We select a pump wavelength around 860 nm, where the material dispersion of our waveguides, realized in titanium in-diffused lithium niobate, allows for this condition to be met by a signal and pump pulses with orthogonal polarizations. Energy conservation then dictates the sum-frequency output center, which in our case will be around 552 nm.

3. Since this set of wavelengths is not naturally phase-matched in our chosen material, we use quasi-phase-matching. We calculate the required poling period Λ to obtain an efficient conversion process centered at our chosen frequencies, which results in $\Lambda = 4.32\,\mu m$.
4. The final and most crucial step of the design is to transform the single-channel quantum pulse gate into a multi-channel device. We achieve this by applying the super-poling technique introduced in Section 2.3.2. This method consists in alternating periodically poled regions of length l to unpoled regions with a period Γ. As described by eq. (2.3.24), this creates a phase-matching function with multiple peaks. The separation between these output channels is proportional to $1/\Gamma$, whereas the effective number of peaks is the inverse of the poled fraction l/Γ.

This entire process is somewhat analogous to designing a diffraction grating: the input signal and pump pulses propagate through the structure, and the generated sum-frequency light from different segments interferes constructively only for specific phase-matching conditions, leading to the separated output channels required for a high-dimensional decoder.

4.1.5 Detector tomography

In the experiments presented in this chapter, we apply single-photon detection at the mQPG output, turning the complete setup into a measurement device that registers "clicks" in a specific output channel when the corresponding TM is detected. We are therefore interested in characterizing the mQPG not just as a process transforming input modes into output modes, but as a complete TM decoder. The operation of such a real-world measurement device, which inherently includes imperfections like optical loss, detector inefficiencies, and potential crosstalk, is described by a set of positive operator-valued measures (POVMs).

A POVM is a set of operators $\{\hat{\pi}^\gamma\}$, where each operator $\hat{\pi}^\gamma$ is associated with a distinct measurement outcome γ (e.g., a click in the γ-th output channel of the mQPG). These operators correspond to positive semi-definite Hermitian matrices, and the probability of obtaining outcome γ when an input state $|\xi\rangle$ is incident on the device is given by $p^{\gamma\xi} = \mathrm{Tr}(|\xi\rangle\langle\xi|\,\hat{\pi}^\gamma) = \langle\xi|\,\hat{\pi}^\gamma\,|\xi\rangle$. Unlike ideal von Neumann projective measurements, where the projectors must be orthogonal and sum to the identity operator, POVM elements are not necessarily orthogonal, and their sum may be less than the identity operator ($\sum_\gamma \hat{\pi}^\gamma \leq \mathbb{1}$). This accounts for the

possibility of an inconclusive outcome, corresponding to $\mathbb{1} - \sum_\gamma \hat{\pi}^\gamma$, where an input photon does not result in a click in any of the m monitored output channels due to, for example, optical losses or imperfect conversion efficiency.

For an mQPG designed to perfectly sort an orthonormal input basis of TMs such that input mode $|\gamma\rangle$ is directed exclusively to output channel γ, the corresponding *ideal* POVM element is

$$\hat{\pi}^\gamma_{\text{ideal}} = \eta_\gamma \, |\gamma\rangle\langle\gamma| \, , \tag{4.1.8}$$

where η_γ represents the combined conversion and detection efficiency for channel γ. In this ideal scenario, the $\{\hat{\pi}^\gamma_{\text{ideal}}\}$ for different γ are orthogonal because the basis states are orthogonal: for instance, if we chose to measure in the basis $\{|A_j\rangle\}_{j=0}^{m-1}$, then the POVM elements would be $\hat{\pi}^j_{\text{ideal}} = \eta_j \, |A_j\rangle\langle A_j|$ in each channel j.

In a *real* mQPG, various imperfections lead to deviations from this ideal. The most typical cause of imperfection is the phase-matching function being too broad with respect to the pump, often due to waveguide defects or temperature inhomogeneities which deform the otherwise sinc-shaped output spectrum, or to constraints on the pump bandwidth. In this case, the assumptions that led to single-mode operation in each channel are no longer valid, and each mQPG channel shows multi-mode behavior. Consequently, a general POVM element $\hat{\pi}^\gamma$ for the γ-th output channel can be expressed in the TM basis $\{|A_i\rangle\}$ as

$$\hat{\pi}^\gamma = \sum_{i,j} (\hat{\pi}^\gamma)_{ij} \, |A_i\rangle\langle A_j| \, . \tag{4.1.9}$$

To experimentally determine these POVM elements $\{\hat{\pi}^\gamma\}$, we employ detector tomography, as detailed in PRX Quantum 4, 020306 (2023), which builds upon standard techniques [116, 117]. This involves:

1. Preparing a set of known input states $\{|\xi\rangle\}$. This set must be informationally complete (or over-complete) for the d-dimensional space in which the input temporal modes reside. In our work, we use all elements of a complete set of MUBs from the d-dimensional Hilbert space.
2. For each input state $|\xi\rangle$, measuring the probability $p^{\gamma\xi}$ of obtaining a click in each output channel of the mQPG, projecting onto state $|\gamma\rangle$. This yields a measurement matrix $P = (p^{\gamma\xi})$. According to the definition of POVMs, $p^{\gamma\xi} = \text{Tr}(|\xi\rangle\langle\xi| \, \hat{\pi}^\gamma) = \langle\xi| \, \hat{\pi}^\gamma \, |\xi\rangle$.
3. Using these measured probabilities $p^{\gamma\xi}$, the POVM elements $\hat{\pi}^\gamma$ are reconstructed via maximum likelihood estimation, subject to the physical constraints of a positive semi-definite Hermitian matrix. The overall efficiency factors η_γ of each channel are typically neglected in this reconstruction.

This characterization provides the POVM elements $\{\hat{\pi}^\gamma\}$, which fully describe the mQPG as a high-dimensionalTMs decoder. Reconstructing the experimental POVMs of the mQPG is essential for understanding its operational capabilities, quantifying projection fidelities, and assessing imperfections such as crosstalk.

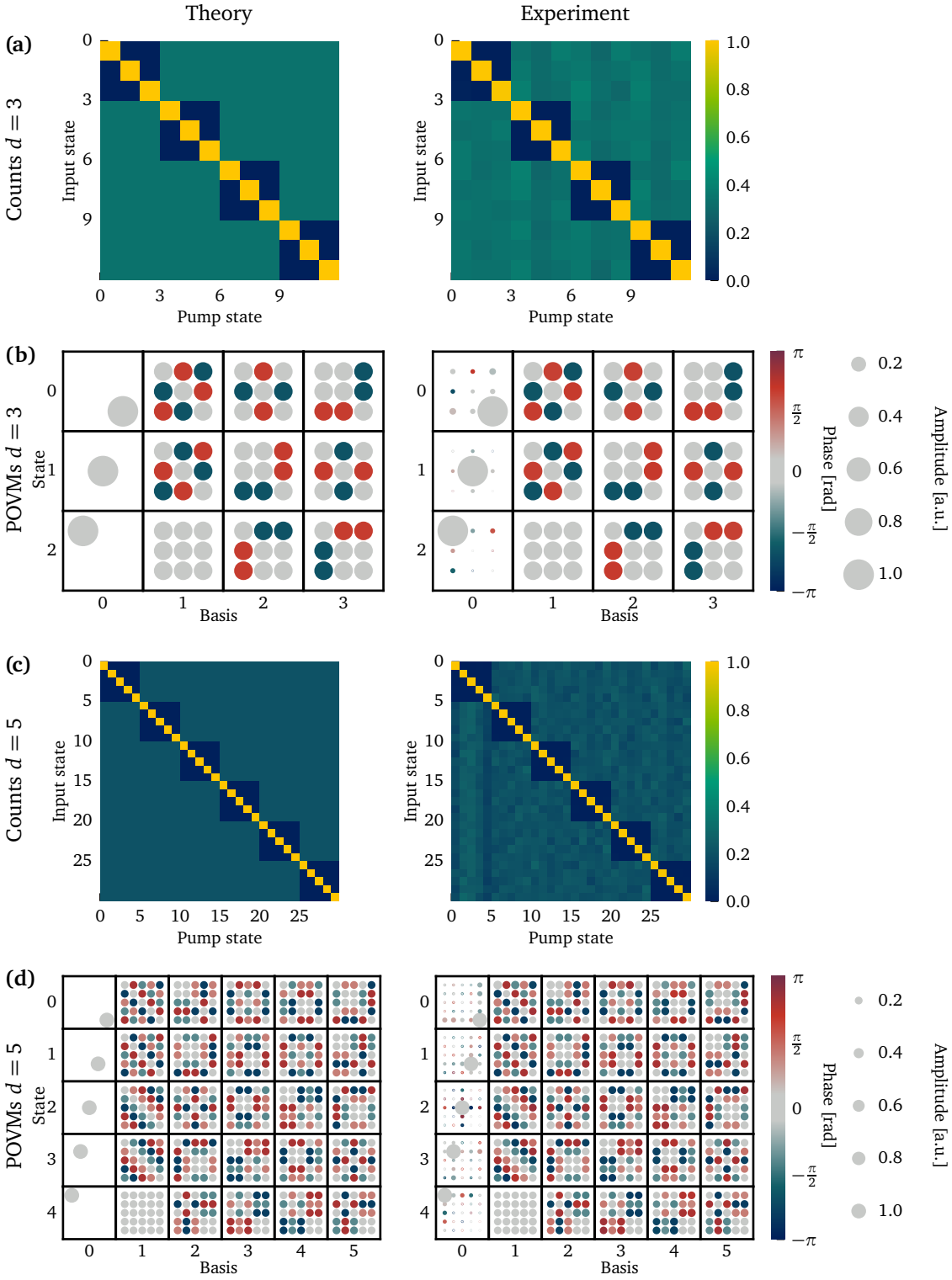

Figure 4.3: Example of detector tomography results using frequency-bin encoding in $d = 3$ and $d = 5$ (data in PRX Quantum 4, 020306 (2023)). **(a,c)** Matrix of the output probabilities $p^{\gamma\xi}$ measured using the ordered set of all eigenstates of the $d+1$ MUBs in dimension d. The probabilities are calculated as relative counts from the simultaneous measurement of the d states in each basis, normalized to the height of the d phase-matching peaks. **(b,d)** Theoretical and reconstructed POVM elements π^{γ} corresponding to each mQPG channel, for each addressed MUB. Each column forms a complete POVM, describing all possible outcomes of a single measurement with the exception of an inconclusive result. The reconstructed POVMs in $d = 3$ and $d = 5$ yielded a fidelity of $(99.7 \pm 0.5)\%$ and $(98.9 \pm 0.5)\%$, respectively.

4.1.6 Beyond Hermite-Gaussian modes

The mQPG is not limited to measuring only a single, fixed basis of temporal modes, nor a single type of encoding. In fact, the reconfigurability of the pump pulses via shaping make it extremely versatile. As long as a set of temporal modes can be addressed by appropriately shaped pump pulses that fulfill the phase-matching conditions for different output channels, the mQPG can measure them. This allows the mQPG to work not only with Hermite-Gaussian modes, but also with the discrete frequency bins and ultrafast time bins discussed in Section 2.1.3. The addressed states are not even required to be orthogonal: at low conversion efficiencies (typical of the experiments presented in this thesis), the up-conversion probability in each channel is largely independent of the others, hence the POVMs will map any non-orthogonality or overlap to the output probabilities.

The main operational limitation is that the spectral features of the pump must be achievable by the spectral resolution of the waveshaper and should ideally be broader than the individual phase-matching peaks of the mQPG to ensure single-mode operation in each channel. While one might consider increasing the pump bandwidth to make its spectral features proportionally larger, the total pump bandwidth is constrained by the initial laser pulse width and by the waveshaper range. This total bandwidth must then be divided among the spectral regions addressing the different output channels of the mQPG. For a large number of channels, this significantly limits the pump bandwidth that can be allocated to each channel and, in turn, constrains the narrowness of the spectral features that can be reliably shaped for the pump, leading to errors.

The “fancy” frequency bin (FFB) decoding scheme, presented in Opt. Express 33(3), 5577 (2025), addresses these bandwidth constraints by leveraging the periodic phase-matching structure of the mQPG to improve its performance. For mode-sorting frequency bins in d dimensions, instead of requiring d^2 independent pump bins, this method uses only $2d-1$ pump bins equally spaced as the phase-matching peaks. Each pump bin overlaps with multiple phase-matching peaks, resulting in effectively broader pump features, improving projection fidelity and reducing cross-talk for a fixed total pump bandwidth. However, this gain in spectral efficiency comes at the cost of reduced programmability. The overlapping structure of the pump bins imposes diagonal correlations among different projections, restricting the set of independently addressable measurement operators. As a result, the FFB scheme cannot implement an arbitrary set of projections in the full d-dimensional Hilbert space. In prime dimensions d, however, this structure still supports d mutually unbiased bases (MUBs), constructed as circulant Hadamard matrices [118] as shown in B.1.

4.2 Summary of the experimental results

In the first experimental demonstration, PRX Quantum 4, 020306 (2023), we implemented for the first time the mQPG and used it to decode single-photon-level input states in a five-dimensional Hilbert space spanned by Hermite-Gaussian TMs and their superpositions. We performed detector tomography in all six MUBs supported by the space, reconstructing the POVM elements associated with each of the five output channels. The average fidelity between the reconstructed and ideal measurement operators was 0.96 ± 0.01, indicating consistent and selective mode-resolved detection across all bases. To further validate the characterization, we prepared random input states and performed quantum state tomography, calibrated using the reconstructed POVMs. The average fidelity between the reconstructed states and the prepared inputs was 0.98 ± 0.02, confirming the suitability of the mQPG for high-dimensional quantum state decoding.

In the second experimental demonstration, Opt. Express 33(3), 5577 (2025), we showcased the versatility of the mQPG as a general decoder for time-frequency encodings by demonstrating its operation with three distinct mode bases: Hermite-Gaussian modes, discrete frequency bins, and ultrafast time bins, with the basis selection achieved solely through spectral reconfiguration of the pump. For each encoding, we performed detector tomography in three- and five-dimensional Hilbert spaces, reconstructing the POVMs corresponding to projections in multiple MUBs. The measured count distribution confirmed high intrinsic projection fidelity, above 90% for all encodings. In addition, we implemented the FFB scheme and demonstrated its ability to perform high-fidelity mode sorting using only $2d-1$ pump bins in dimensions $d = 3$ and $d = 5$.

PRX QUANTUM **4,** 020306 (2023)

Realization of a Multi-Output Quantum Pulse Gate for Decoding High-Dimensional Temporal Modes of Single-Photon States

Laura Serino,* Jano Gil-Lopez, Michael Stefszky, Raimund Ricken, Christof Eigner, Benjamin Brecht, and Christine Silberhorn

Paderborn University, Integrated Quantum Optics, Institute for Photonic Quantum Systems (PhoQS), Warburgerstraße 100, 33098 Paderborn, Germany

(Received 20 September 2022; accepted 15 March 2023; published 12 April 2023)

Temporal modes (TMs) of photons provide an appealing high-dimensional encoding basis for quantum information. While techniques to generate TM states have been established, high-dimensional decoding of single-photon TMs remains an open challenge. In this work, we experimentally demonstrate demultiplexing of five-dimensional TMs of single photons with an average fidelity of 0.96 ± 0.01, characterized via measurement tomography. This is achieved with use of a newly developed device, the multi-output quantum pulse gate (MQPG). We demonstrate a proof-of-principle complete decoder based on the MQPG that operates on any basis from a set of six five-dimensional mutually unbiased bases and is therefore suitable as a receiver for high-dimensional quantum key distribution. Furthermore, we confirm the high-quality operation of the MQPG by performing resource-efficient state tomography with an average fidelity of 0.98 ± 0.02.

DOI: 10.1103/PRXQuantum.4.020306

I. INTRODUCTION

As increasingly more applications for quantum technologies continue to be found, the need to develop a device that enables highly efficient quantum communication (QC) becomes critical [1–3]. Photons are ideally suited for this task due to transmission at the speed of light, intrinsically low decoherence, and their high-dimensional spatial and time-frequency degrees of freedom. These degrees of freedom provide high-dimensional alphabets that allow one to encode more information per photon, leading to important advantages for QC applications, including the higher level of security and efficiency provided by high-dimensional quantum key distribution (HDQKD) with respect to its binary counterpart [4].

Arguably, the most explored high-dimensional photonic degree of freedom is the spatial one, with particular focus on the orbital angular momentum of light. One of the main advantages of this encoding alphabet is the possibility to generate and detect states using time-invariant operations [5–7]. However, this advantage comes with an important drawback, as orbital angular momentum states are inherently incompatible with existing fiber-optic networks and easily degrade in free-space transmission [8].

The time-frequency degree of freedom of photons overcomes this limitation. The standard alphabet based on this degree of freedom is given by time and frequency bins, which can be conveniently generated from an integrated source [9,10]. The manipulation of time-frequency bins and their superpositions is possible with interferometric systems [11] or with a combination of phase modulators and pulse shapers [12,13]. Scaling either of those approaches comes with important challenges, and experimental efforts have been limited to low-dimensional systems [14,15].

To avoid this impediment, we can exploit the time-frequency degree of freedom of light through temporal modes (TMs), i.e., field-orthogonal wave-packet modes. Since TMs span an infinite-dimensional Hilbert space, they can represent any arbitrary time-frequency state of single photons; of particular importance is that they form a natural basis to describe photons generated through ultrafast parametric down-conversion. TMs are characterized by robustness against fiber dispersion and a higher packing density with respect to frequency bins, as they can exploit the full frequency space without the need for guard bands [16,17]. These properties render TMs a valuable resource not only for QC protocols but also for several other applications, from quantum enhanced spectroscopy and metrology [18–20] to quantum memories [21–23] and deterministic photonic quantum gates [24–26].

*laura.serino@upb.de

To fully reap the benefits of high-dimensional encoding, a TM-based QC scheme requires the generation, manipulation, and simultaneous detection of multiple TMs of single photons. Single-photon operation is a requirement as quantum light is used in a wide variety of interfacing and communication protocols. Generation of single photons with a well-defined TM state has been successfully achieved through ultrafast parametric down-conversion [27–29]. Manipulation and detection of single-photon TMs, on the other hand, have been limited to a single TM at a time. These demonstrations were obtained with use of a quantum pulse gate (QPG) [30–32], a TM-selective device based on integrated sum-frequency generation that by design is limited to single-output operation.

In this work, we demonstrate high-dimensional single-photon TM decoding using a multi-output QPG (MQPG). The MQPG is a newly developed device that uses a custom poling structure to project a single-photon-level input signal onto all the elements of a chosen high-dimensional TM alphabet (or their superpositions) and map the results of the projections onto different output frequencies. We then use a single-photon spectrograph to read out the output frequency for each input photon, hence providing the projection result as a "click" in the corresponding output channel. We demonstrate that our device is compatible with single-photon-level input states from a five-dimensional Hilbert space, and characterize its performance by quantum measurement tomography. Thus we showcase a proof-of-principle complete HDQKD decoder based on the MQPG that can work with any basis from a set of six five-dimensional mutually unbiased bases (MUBs). To further confirm the capabilities of our device, we use the reconstructed positive-operator-valued measure (POVM) from the measurement tomography to facilitate a resource-efficient state tomography with an average fidelity of 0.98 ± 0.02. Furthermore, we describe the necessary improvements to scale the decoder scheme to perform high-quality measurements in even higher dimensions.

We note that although preliminary work toward expanding frequency conversion to multi-output operation has been demonstrated [33,34], these implementations were inherently incompatible with single-photon-level input states. Our device allows one to fully exploit the greater information capacity provided by high-dimensional encoding in single photons, granting faster transmission of information and enabling HDQKD protocols [4]. Moreover, the MQPG substantially reduces measurement times for applications that require projections onto a large number of TMs, such as quantum state tomography [31].

II. DEVICE AND PROCESS ENGINEERING

A high-dimensional decoder must allow the user to perform a simultaneous high-quality projection of the input state onto all the elements of a user-chosen basis (Fig. 1). The MQPG achieves this goal through type-II sum-frequency generation (SFG) in periodically poled titanium-in-diffused lithium niobate waveguides. Its operation in frequency space is described by a transfer function G, which maps the input frequencies ν_{in} onto the sum frequencies ν_{out}.

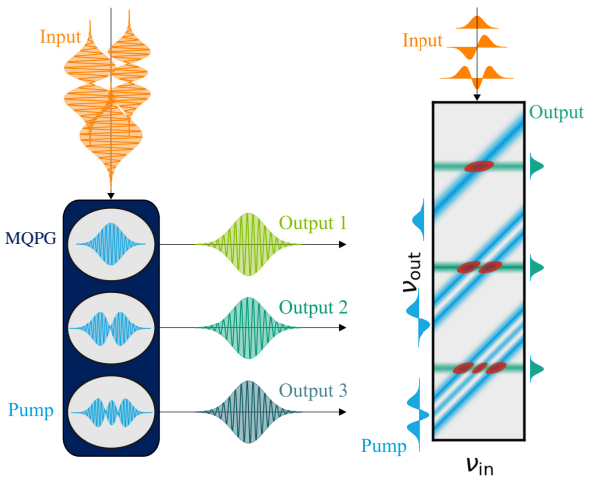

FIG. 1. The working principle of the MQPG (left) and description in frequency space (right): in the MQPG waveguide, the input photons (orange) are demultiplexed to different output frequencies (green) on the basis of their TM. The TMs to be measured are selected by shaping the pump field (blue).

To better understand the nature of the MQPG process, we first describe the simpler single-output process of the QPG [30]. The QPG is a device that selectively up-converts a specific TM component from an input state with an efficiency of up to 87.7%. Such a high conversion efficiency is, in principle, also achievable by the MQPG process.

The transfer function G_0 of the QPG is the product of the pump function α_0, which describes energy conservation, and the phase-matching function Φ_0:

$$G_0(\nu_{\text{in}}, \nu_{\text{out}}) = \alpha_0(\nu_{\text{in}}, \nu_{\text{out}})\Phi_0(\nu_{\text{in}}, \nu_{\text{out}}). \quad (1)$$

The SFG process of the QPG (and the MQPG alike) is dispersion-engineered for group-velocity matching of the pump and input fields, which causes the phase-matching function to be independent of the input frequency [$\Phi_0 \simeq \Phi_0(\nu_{\text{out}})$]. Under the condition that the input and pump bandwidths are significantly broader than the phase-matching bandwidth, the transfer function G_0 becomes separable into a pair of input and output functions [35], meaning that the QPG can perform selective up-conversion of a specific TM. As a consequence, the intensity of the SFG light is proportional to the overlap between the complex spectral amplitudes of the input and pump pulses,

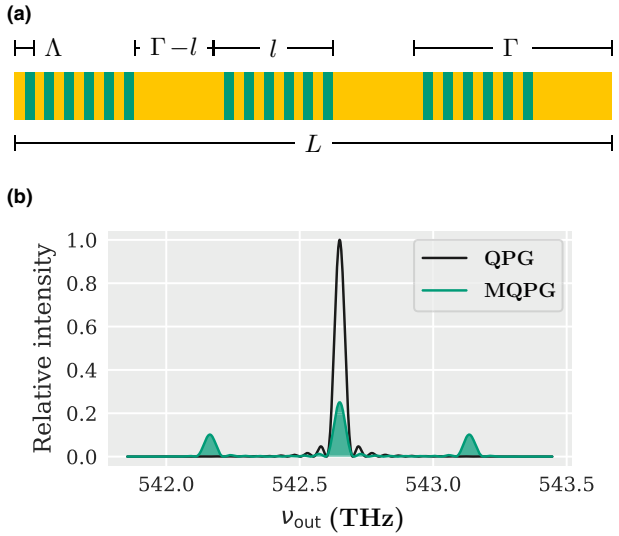

FIG. 2. (a) The superpoling pattern of an MQPG waveguide: regions of length l poled with period Λ are alternating with unpoled regions of length $\Gamma - l$, where Γ is the period of this alternation. The regions corresponding to the standard nonlinearity coefficient of the waveguide are shown in yellow, whereas those corresponding to the reversed nonlinearity coefficient are represented in green. (b) A simulation of the phase-matching intensity spectrum of a MQPG (green) compared with that of a QPG (black). The lower efficiency of a MQPG can be compensated with use of higher pump powers.

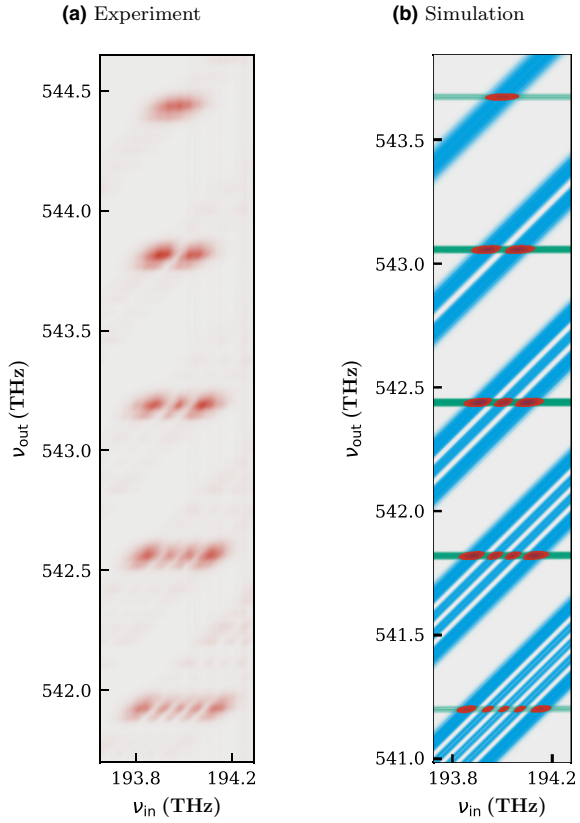

FIG. 3. The experimental (a) and simulated (b) transfer function $G(\nu_{in}, \nu_{out})$ (red) given by the product of a five-peak phase-matching function $\Phi(\nu_{in}, \nu_{out}) \simeq \Phi(\nu_{out})$ (green) and a five-peak shaped pump spectrum $\alpha(\nu_{in}, \nu_{out})$ (blue). The pump peaks are shaped as the first five Hermite-Gaussian modes, and only the intensity of the named quantities is represented. The experimental transfer function resembles well the simulation. On closer inspection, however, it displays a small amount of distortion below the main peaks, which can be attributed to fabrication defects [36]. These imperfections can be removed by applying spectral filtering to each output channel.

but does not depend on their relative phase. The latter influences only the overall phase of the SFG light, which is lost in the phase-insensitive photon-counting detection. The pump pulses can be tailored through spectral shaping, allowing one to select the desired TM, transmitting the orthogonal TM components unperturbed.

The inherent limitation of the QPG to a single output channel limits the detection to a single TM at a time, making this device unsuitable for HDQKD, which requires the detection of any element of the chosen basis at every single shot of the communication. In contrast, the multichannel nature of the MQPG renders it suitable for high-dimensional demultiplexing of many TMs into distinct output channels. Each channel j of the MQPG acts as a distinct QPG with its own transfer function G_j and maps a specific TM into the corresponding output frequency. The multipeak phase-matching function $\Phi = \sum_j \Phi_j$ of the MQPG is generated through the alternation of periodically poled and unpoled regions along the waveguide (Fig. 2). The design framework of the MQPG, illustrated in detail in Appendix A, allows one to freely select the spectral parameters such as the interpeak distance and effective number of peaks. One can then shape a pump spectrum $\alpha = \sum_j \alpha_j$ with as many peaks as Φ in order to create a multi-output transfer function such as the one illustrated in Fig. 3.

For this demonstration, we use a five-peak MQPG waveguide and generate a five-output transfer function to facilitate operation in a five-dimensional space. The experimental transfer function, shown in Fig. 3(a), matches its simulated counterpart [red region in Fig. 3(b)]. The technical specifications of the MQPG waveguide used in this experiment are explained in detail in Appendix A.

III. TOMOGRAPHY THEORY

To quantify the quality of the high-dimensional decoding of the MQPG, we perform quantum measurement tomography [37]. For this purpose, we first introduce the mathematical description of the MQPG operation. We can describe the multi-output decoding as a POVM $\{\pi^\gamma\}$, which corresponds to the complete measurement

basis comprising all the channels of the MQPG. Each individual channel of the MQPG projects the input state onto a user-chosen TM, γ. Consequently, each channel corresponds to a POVM element, i.e., measurement operator, $\pi^\gamma = \sum_{ij} m_{ij}^\gamma |i\rangle\langle j|$ (ideally $|\gamma\rangle\langle\gamma|$), with i and j elements of the fundamental TM basis. We choose to work in a d-dimensional Hilbert space, where d matches the number of channels of the decoder. We select the decoder TMs $\{\gamma\}$ to form a basis for the aforementioned space.

For each MQPG channel, the probability of SFG conversion of a pure input state $\rho^\xi = |\xi\rangle\langle\xi|$ is given by [38]

$$p^{\gamma\xi} = \mathrm{Tr}(\rho^\xi \pi^\gamma). \tag{2}$$

The aim of measurement tomography is to probe the decoder with a full set of input states ρ^ξ so as to reconstruct the full POVM $\{\pi^\gamma\}$. In this work, we use a set of probe states containing all the elements of the $d+1$ MUBs of our d-dimensional Hilbert space, demonstrating the compatibility of the MQPG with quantum communication protocols based on MUBs, including HDQKD.

IV. EXPERIMENT

A schematic of the experimental setup is shown in Fig. 4. We start from ultrashort Ti:sapphire laser pulses with a spectrum centered at $\lambda_{p,0} = 860$ nm (349 THz) and a repetition rate of 80 MHz. A portion of the beam is directed to a homebuilt 4-f line based on a spatial light modulator [39] with resolution $\delta\nu_{\mathrm{shaper},p} = 10$ GHz to shape the amplitude and phase of its complex spectrum so as to prepare the pump states. The pulse is carved into five peaks with centers separated by $\Delta\nu_{\mathrm{sep}} = 0.63$ THz, each shaped as an element of a five-dimensional TM basis. For this experiment, we choose Hermite-Gaussian (HG) modes and their superpositions, as they provide a good approximation of the natural modes of parametric down-conversion processes [40]. The remaining part of the pulse train pumps an optical parametric oscillator that generates pulses centered at $\lambda_{\mathrm{in},0} = 1545$ nm (194 THz). The beam is attenuated to the single photon level with a mean photon number per pulse lower than 0.1 (0.097 ± 0.001 photons per pulse) and is shaped with use of a commercial waveshaper with resolution $\delta\nu_{\mathrm{shaper,in}} = 1$ GHz to prepare the input state. The shaping parameters for the input beam and each pump peak are chosen such that the FWHM of the fundamental HG mode is $\Delta\nu_p = \Delta\nu_{\mathrm{in}} = 0.14$ THz. Both beams are then coupled into the MQPG waveguide, each with a coupling efficiency of approximately 60%. The waveguide is designed to be spatially single mode for telecommunication light, and particular care is taken to ensure the pump field is coupled in the fundamental spatial mode.

The multi-output SFG process of the MQPG generates output fields at multiple frequencies (each defining an output channel) around 552 nm (543 THz) based on the TM

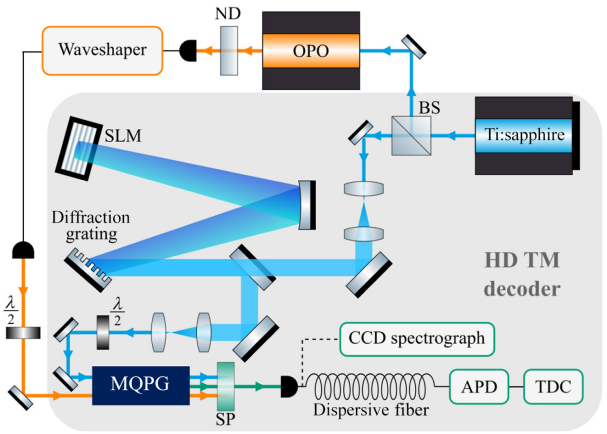

FIG. 4. The experimental setup. A portion of the pump beam (blue line) generated by the Ti:sapphire laser is directed to a 4-f line based on a spatial light modulator (SLM). The shaped beam travels back through the folded configuration at a lower angle than the incoming beam, so as to be picked up by a short mirror and to be coupled into the MQPG waveguide. The remaining part of the Ti:sapphire beam pumps an optical parametric oscillator (OPO) that generates the input beam (orange line) of the experiment at telecommunication wavelengths. The input beam is attenuated to the single-photon level by neutral-density filters (ND) and is shaped with use of a commercial waveshaper, before being coupled into the MQPG waveguide. The output field (green line), isolated by a short-pass filter (SP), is detected either with a commercial CCD spectrograph or with a TOF spectrograph consisting of a dispersive fiber, an avalanche photodiode (APD), and a time-to-digital converter (TDC). The gray area indicates the components of our high-dimensional (HD) TM decoder (for more information, see the main text).

state of the input field. Effectively, the MQPG projects the input TM onto the chosen TM basis and maps the results to the corresponding output frequencies. The internal conversion efficiency is approximately 5%, here limited by the pump pulse energy available in this experiment. The output fields are separated from the residual pump and input fields with use of a dichroic mirror and are then fiber-coupled and measured with a commercial CCD spectrograph (Andor Shamrock 500i) with a resolution of 30 GHz.

To perform the quantum measurement tomography, we probe the decoder with input states from a set comprising all 30 elements of the six MUBs of our Hilbert space. For each measurement we make three acquisitions, each with an integration time of 10 s and an average count rate of 470 Hz. We then calculate the experimental output probabilities for each channel $p^{\gamma\xi}$, and we use them to reconstruct the POVM elements π^γ through a weighted least-squares fit:

$$\min_{\pi^\gamma} \sum_\xi \frac{\left|p^{\gamma\xi} - \mathrm{Tr}(\rho^\xi \pi^\gamma)\right|^2}{p^{\gamma\xi}}, \tag{3}$$

where we constrain π^γ to be Hermitian and positive semidefinite. The first eigenmodes of the reconstructed POVM elements are presented in Fig. 5. One can see that they very closely match the ideal POVMs both in amplitude and in phase.

We quantify the quality of the decoder by calculating the purities of the POVM elements

$$\mathcal{P}^\gamma = \frac{\mathrm{Tr}(\pi^{\gamma 2})}{(\mathrm{Tr}\pi^\gamma)^2} \tag{4}$$

and the fidelities when compared with the ideal operators

$$\mathcal{F}^\gamma = \sqrt{\frac{\langle\gamma|\pi^\gamma|\gamma\rangle}{\mathrm{Tr}\pi^\gamma}}. \tag{5}$$

In an ideal system, both these values are equal to 1. The average experimental results with their respective standard deviations are listed in Table I (left column). The high average fidelity and purity indicate the remarkably good quality of the MQPG measurements.

TABLE I. Average fidelities and purities of the reconstructed POVM elements for $d = 5$ with the corresponding standard deviation.

	CCD spectrograph	TOF spectrograph
Fidelity	0.956 ± 0.014	0.810 ± 0.046
Purity	0.885 ± 0.036	0.552 ± 0.087

V. HDQKD DECODER DEMONSTRATION

To demonstrate a proof-of-principle HDQKD decoder, we need to perform photon counting. For this reason, we replace the CCD spectrograph with a homebuilt time-of-flight (TOF) fiber-assisted single-photon spectrograph [41,42]. This system exploits the chromatic group velocity dispersion of a single-mode fiber to apply various delays to the different frequency components of the pulses, effectively mapping each frequency component to a different arrival time. The arrival times are then measured with

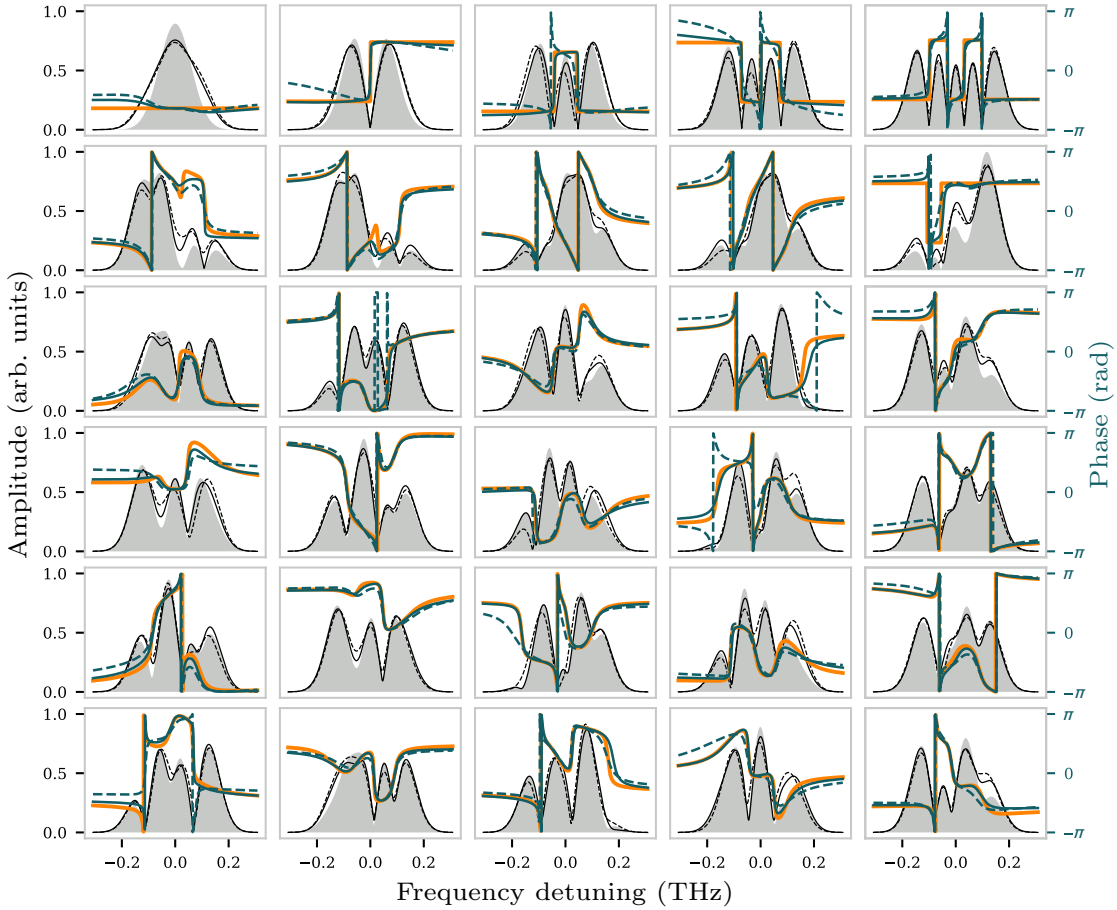

FIG. 5. First eigenmodes of the POVM elements (five for each of the six MUBs). Shaded areas and orange lines show the ideal amplitude and phase; black and blue lines show the same values for experimental data, with solid and dashed lines corresponding to the CCD spectrograph and the TOF spectrograph, respectively.

use of an avalanche photodiode combined with a time-to-digital converter. A calibration of the system then allows one to calculate the frequency corresponding to each arrival time, recovering the information on the detected TM. The simple structure of the TOF spectrograph makes it cost-effective and versatile. The TOF setup used in this experiment has a resolution of 0.3 THz and introduces 20 dB of losses. These values are limited by the availability of low-loss high-group-velocity-dispersion fibers for visible light. The high losses do not pose a fundamental problem for the operation of our decoder; however, they limit the maximum distance at which communication is still possible.

As a first characterization of the complete HDQKD decoder, we perform measurement tomography. For each measurement we make 30 acquisitions, each with an integration time of 10 s and an average count rate of 40 Hz. The characterization results, reported in Table I, show a good average fidelity. The good fidelity is apparent in the agreement between the first eigenmodes of the reconstructed POVMs and the ideal ones (Fig. 5), which show a similarly good quality for all six MUBs. The low average purity of the reconstructed POVMs, however, is an indicator of multimodedness in the decoder, which results in output clicks corresponding to TMs that are not present in the input state. The discrepancy with the high intrinsic purity of the MQPG indicates that the loss of quality can be traced back uniquely to the difference between the TOF spectrograph and the CCD spectrograph. The limited resolution of the TOF spectrograph is not sufficient to completely filter out the phase-matching imperfections of the MQPG [visible in Fig. 3(a)], which then introduce a multimode behavior in the system.

Despite the loss of quality due to the spectrograph, the decoder shows good TM-demultiplexing behavior, which makes it suitable as a proof-of-principle receiver for HDQKD. To demonstrate this, we extract the count rates relative to the projection of each input state onto the corresponding MUB from the same set of experimental data used for the tomography. We then calculate the average selectivity per MUB as the ratio of the number of correct counts to the total number of counts. Our results show an average selectivity per basis ranging from 61% to 78%, which demonstrates a clear mode-selective behavior, but indicates that there is room for improvement. Values in this range are lower than the internal average selectivity of the MQPG $\mathcal{S} = 92\%$ (measured with the CCD spectrograph). The discrepancy is once again explained by the low resolution of the TOF spectrograph used in this experiment, which hinders proper discrimination of the counts. This becomes evident when one compares the relative counts measured by the decoder in one of the six MUBs with the intrinsic performance of the MQPG (Fig. 6). This observation suggests that although the current implementation of the MQPG-based decoder is already up to the task of TM demultiplexing, a high-resolution single-photon-resolving spectrograph will allow one to take full advantage of the high measurement quality provided by the MQPG.

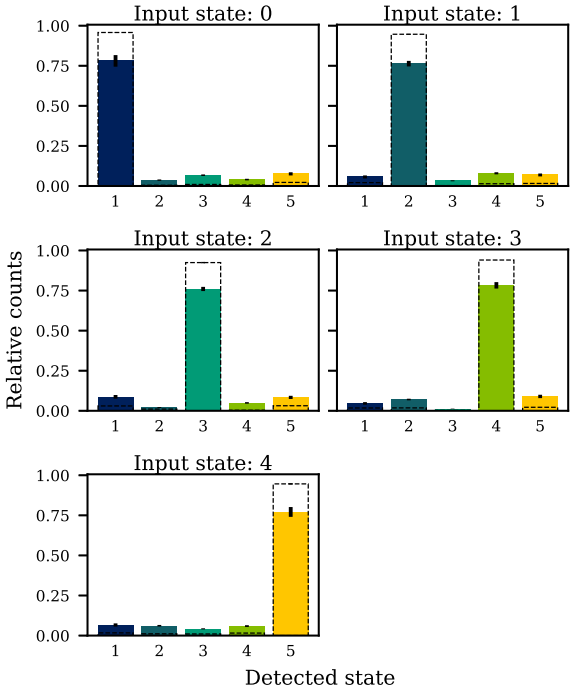

FIG. 6. Relative counts obtained when we project the five elements of one MUB onto the same MUB with the complete decoder (filled bars) and internal performance of the MQPG (dashed lines). The error bars represent the error on the mean relative counts of 30 data acquisitions.

VI. BEYOND QKD: STATE TOMOGRAPHY

In this section, we demonstrate that the measurement tomography of the MQPG allows us to overcome its shortcomings for applications that require measurements that become integrated over time, such as in state tomography. For this purpose, we perform resource-efficient single-photon state tomography with the MQPG and we show the improvement provided by the reconstruction of the experimental POVMs. We prepare 25 random pure input states ρ from our five-dimensional Hilbert space, and measure them using the six MUBs as decoder bases. We perform the frequency-resolved detection with the CCD camera, with three acquisitions for each measurement, each with an integration time of 10 s and an average count rate of 470 Hz. We reconstruct the input states through a weighted least-squares fit:

$$\min_{\rho} \sum_{\xi} |p^{\gamma} - \mathrm{Tr}(\rho\pi^{\gamma})|^2/p^{\gamma}, \tag{6}$$

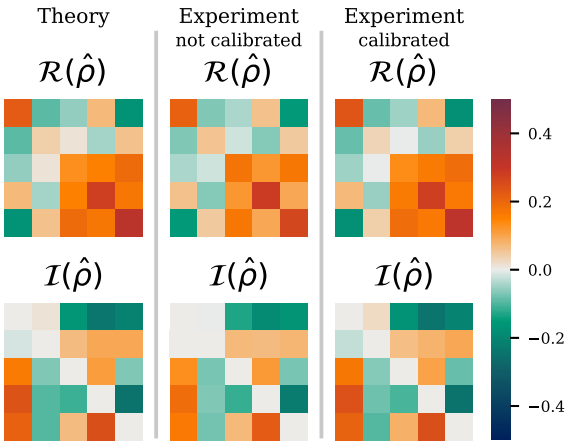

FIG. 7. Example of tomography of a random input state (measured with the CCD spectrograph). The plots correspond to the real (top) and imaginary (bottom) parts of the density matrix of, from left to right, the original input state, the raw reconstructed state, and the state reconstructed with the calibration information obtained from the measurement tomography.

where the p^{γ} are the output probabilities of the different channels and ρ is constrained to be Hermitian and positive semidefinite. We stress that, owing to the high dimensionality of our decoder, it is sufficient to set the pump states to the desired basis to project the input state onto all its elements at the same time within a single measurement. This means that we perform only six measurements to obtain counts on all 30 possible pump states. We highlight that the high number of measurements required constituted the main limitation to dimension scalability for the QPG [38] and that the MQPG overcomes this limitation.

We reconstruct the input state first assuming ideal POVMs $\{|\gamma\rangle\langle\gamma|\}$ ("raw" state tomography), and then considering the measured POVMs $\{\pi^{\gamma}\}$ ("calibrated" state tomography). The results are summarized in Table II, and an example of input-state reconstruction is provided in Fig. 7. The calibrated state tomography significantly increases the fidelity and purity of the reconstructed states. This can be explained considering that the main source of error in our system is the residual crosstalk deriving from the phase-matching imperfections, which cannot be completely eliminated even with the high resolution of the CCD spectrograph. This crosstalk is well characterized through the measurement tomography; therefore, in the calibrated state tomography we exploit this information to correct for the induced errors.

VII. DISCUSSION

The current implementation of the proof-of-principle decoder for HDQKD is limited by available components; however, the issues are of a technical nature and can be overcome rather easily. The main limitation is set by the spectrograph system, which is required to be compatible with photon counting at visible wavelengths. Such a device is not yet commercially available, and the home-built TOF spectrograph used in this work introduced 20 dB of losses and had a limited resolution of 0.3 THz, which decreased the fidelity from the intrinsic value of the MQPG $\mathcal{F} = 0.96 \pm 0.01$ to the resulting decoder fidelity $\mathcal{F}' = 0.81 \pm 0.05$. The loss of fidelity can be prevented with use of state-of-the-art components for the spectrograph system. Indeed, a TOF spectrograph based on a state-of-the-art chirped fiber Bragg grating [43] and a low-jitter superconducting-nanowire single-photon detector [44] would achieve a resolution of 6 GHz for much lower losses, allowing one to fully exploit the high intrinsic fidelity of the MQPG and at the same time increase the efficiency of the decoder.

TABLE II. Average fidelities and purities of the reconstructed input states for $d = 5$ with the corresponding standard deviation.

	Raw	Calibrated
Fidelity	0.941 ± 0.019	0.983 ± 0.016
Purity	0.816 ± 0.062	0.941 ± 0.056

Moreover, the decoding efficiency can be further increased by increasing the internal conversion efficiency of the MQPG waveguide. This can be done through an optimized tailoring of the phase-matching function [34,45,46] and by increasing the pump pulse energy available in the experiment. To achieve a higher pump energy, one can, of course, resort to using a higher-power laser. However, an appealing solution, with the advantage of on-chip integration, would be to generate each pump peak with a separate chip-based mode-locked laser. Indeed, preliminary devices demonstrated a spectral bandwidth of approximately 0.35 THz [47], which matches the ideal bandwidth of each pump peak of the MQPG.

Although the implemented five-channel MQPG has undeniable benefits for QC applications based on single-photon TMs (which until now have been limited to a mere two-dimensional space) one may wish to push the device to even higher dimensions. The methods detailed in Appendix A provide the scheme for generating a MQPG waveguide with the desired number of output channels via straightforward modulation of the poling pattern. The cost of moving to higher dimensions is that each pump peak becomes narrower for a fixed spectral width set by the Ti:sapphire pump pulse. To prevent a loss in measurement quality, one must either increase the available spectral bandwidth or address the difficulties that arise when one is operating with narrower and more densely spaced peaks. This requires an increased spectrograph resolution to fully discriminate the output channels, an increased shaping resolution, and a narrower phase-matching function (e.g.,

through a longer waveguide [48]) to satisfy the single-modedness condition for each channel [35]. In Appendix C, we study how improved technical capabilities can allow high-fidelity operation in higher dimensions. With state-of-the-art components, a MQPG-based decoder could easily achieve operation above 90% selectivity beyond 25 dimensions in all mutually unbiased bases.

VIII. CONCLUSION

We demonstrated five-dimensional temporal-mode demultiplexing of single photons using a newly developed device, the MQPG. We characterized its performance through measurement tomography, obtaining an average fidelity of 0.96 ± 0.01 to the theoretical POVMs. We then demonstrated a complete HDQKD decoder for single photons based on the MQPG, which revealed an average fidelity of 0.81 ± 0.05, solely limited by the currently available spectrograph technology. Finally, we exploited the information obtained from the measurement tomography of the MQPG to demonstrate resource-efficient high-quality state tomography with an average fidelity of 0.98 ± 0.02.

These results show that the demonstrated architecture provides a scalable framework for high-dimensional decoding. The purity and fidelity of the device can be easily increased by limiting the phase-matching imperfections and increasing the resolution of the spectrograph. Doing this will result in a decoder with high-performance operation in more than 25 dimensions, leading to even greater information capacity and security in HDQKD.

Finally, we highlight the versatility of the MQPG, which constitutes one of its main advantages. Because of the fully programmable shaping systems, one can easily work with alternative high-dimensional TM encodings without modifying the experimental setup. This gives one the freedom to explore a wide range of parameters so as to find the optimal solution for different applications. Finally, we emphasize that, independently of the encoding alphabet chosen and of the dimensionality d of the system, the MQPG is always able to work with the full set of $d+1$ MUBs. This makes the MQPG a valuable resource for many QC applications and, furthermore, opens up further opportunities for all TM-based technologies, from quantum spectroscopy and metrology to quantum memories and deterministic photonic quantum gates.

ACKNOWLEDGMENTS

The authors thank M. Santandrea and V. Ansari for helpful discussions. This research was supported by the European Union's Horizon 2020 QuantERA ERA-NET Cofund in Quantum Technologies project QuICHE.

APPENDIX A: MULTI-OUTPUT QUANTUM PULSE GATE

Here we describe the techniques used to obtain a MQPG process for an input signal comprising multiple temporal modes centered at telecommunication wavelengths around 1545 nm (194 THz). We start by finding the optimal parameters for a QPG process, i.e., type-II SFG between two group-velocity-matched fields labeled "pump" and "signal." To achieve group-velocity matching in a nondegenerate process, we exploit the polarization dependency of the group velocity of light in a birefringent crystal. Using this, we are able to find a transverse-magnetic-polarized pump field with different wavelength but same group velocity as the transverse-electric-polarized signal field. Next, we achieve the quasi-phase-matching condition for the chosen fields by applying a periodic poling with period Λ to the waveguide. With this method, we can identify a QPG process tailored for the chosen input wavelength, in our case a telecommunication field.

To obtain the MQPG, we need to expand the QPG process to multiple output channels. We note that, due to the properties of the QPG, each output channel will correspond to one phase-matching peak. Previous work [33,34] demonstrated that multiple phase-matching peaks are attainable through a periodic modulation of the poling pattern. We therefore modify the poling structure of a QPG waveguide by applying a modulation with period Γ ("superpoling period") and an asymmetric duty cycle $\eta \in [0,1]$, obtaining poled regions of length $l = \eta\Gamma$ alternating with unpoled regions of length $(1-\eta)\Gamma$ [Fig. 2(a)]. We can calculate the new phase-matching function analytically to show how this modulation generates multiple output peaks.

The phase-matching function of the SFG process for a waveguide of length L can be described as a function of the birefringent phase mismatch $\Delta\beta_u = \beta_{\text{out}} - \beta_{\text{pump}} - \beta_{\text{in}}$, where β_i is the propagation constant of field i:

$$\phi_{\text{SFG}}(\Delta\beta_u) \propto \int_0^L g(z) e^{i\Delta\beta_u z} dz, \tag{A1}$$

where z is the position on the main waveguide axis and $g(z)$ is the nonlinearity profile along the waveguide, which is fully determined by the modulation of the poling pattern. In the range of output wavelengths allowed by energy conservation of the SFG process, the phase-matching function becomes

$$\phi_{\text{SFG}} \simeq \frac{\Gamma}{L} \frac{e^{i(\Delta\beta_u L/2)}}{e^{i(\Delta\beta_u \Gamma/2)}} \frac{\sin(\Delta\beta_u L/2)}{\sin(\Delta\beta_u \Gamma/2)} \eta \,\text{sinc}\left(\frac{\Delta\beta_p l}{2}\right) e^{i(\Delta\beta_p l/2)}, \tag{A2}$$

where we defined $\Delta\beta_p = \Delta\beta_u - 2\pi/\Lambda$. This expression describes a train of sinc-shaped peaks modulated by a sinc-shaped envelope. A quick analysis reveals that the physical

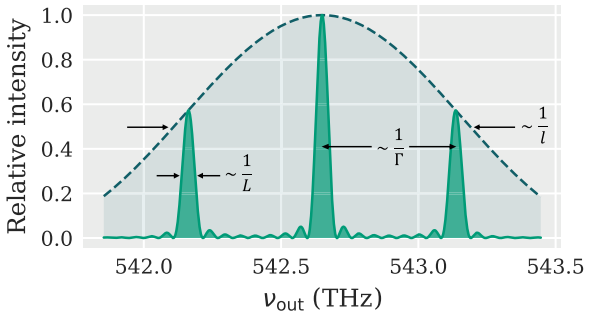

FIG. 8. Simulation of the phase-matching intensity showing how the spectral features are related to the superpoling parameters.

lengths of the waveguide are related to the spectral parameters: the length of the sample L is inversely proportional to the peak width, the superpoling period Γ is inversely proportional to the interpeak distance, and the length of each poled region l is inversely proportional to the envelope width (Fig. 8). In particular, the ratio $\Gamma/l = 1/\eta$ defines the number of peaks within the FWHM of the envelope. Therefore, the framework presented allows one to design a MQPG waveguide with the desired number of phase-matching peaks, i.e., number of output channels.

In the experimental implementation of the MQPG presented in the main text, we used a periodically poled titanium-in-diffused lithium niobate waveguide with poling period $\Lambda = 4.32$ μm operated at a working temperature of 170 °C. The superpoling parameters were set to $l = 397$ μm and $\Gamma = 1590$ μm to obtain five output peaks in a wavelength range that would match the bandwidth of the Ti:sapphire pump $\Delta\nu_{\text{Ti:sa}} = 3$ THz used in the experiment.

APPENDIX B: REAL MQPG PROCESS

In an ideal MQPG process, each channel is characterized by single-mode operation, i.e., it provides an output only if the input signal contains the corresponding TM. This ideal behavior is exhibited only if the width of each phase-matching peak is much narrower than that of the corresponding pump pulse [35]. However, as explored in detail in previous work by our group [36], a real phase-matching function always displays some degree of imperfection [visible, for example, in Fig. 3(a)]. Phase-matching imperfections effectively broaden the width of each peak, causing multimode behavior in each channel of the MQPG process. This multimodedness then results in output clicks corresponding to TMs that are not present in the input state.

To recover single-mode operation in each channel of a real MQPG waveguide, one can exploit the fact that the frequency of the spurious output photons will be slightly offset with respect to the central output frequency of the phase-matching peak. Therefore, one can apply a spectral filter to each output channel so as to discriminate the real counts from the spurious counts arising from the phase-matching imperfections. The method used in this work is to filter in postprocessing the output spectrum acquired by the spectrograph. We define a frequency window around the center of each output peak, and we consider as channel clicks only the counts within this window. The effectiveness of this filtering method is then dependent on the resolution of the spectrograph, which needs to be sufficiently precise to fully distinguish the phase-matching peaks from the surrounding regions.

The definition of resolution for the TOF spectrograph requires careful consideration. Since this type of spectrograph is composed of a highly dispersive fiber combined with an avalanche photodiode and a time tagger, one would intuitively define its resolution as that of the time tagger (1 ps in our case) divided by the total chromatic dispersion of the fiber (217 ps nm^{-1} for our 1 km-long fiber). However, one needs to take into account the timing jitter of the TOF setup (64 ps in FWHM), which introduces uncertainty on the arrival time of each photon, and hence on its frequency. Therefore, the actual resolution of a TOF spectrograph is given by a combination of these two factors, and in our case is dominated by the latter. This results in a much lower frequency resolution of 300 GHz, which is half as large as the separation between the peaks (630 GHz).

The effect of this low resolution is visible in Fig. 9, which shows the fidelity and the purity of the POVM elements of our decoder as a function of the window width, comparing the measurements obtained with the TOF spectrograph with those obtained with the CCD spectrograph (see Table I and Fig. 5 for reference). For the latter, which has a resolution of 30 GHz, one can notice a strong improvement of the measurement quality as the filtering window becomes narrower (from right to left), particularly in the average purity of the POVMs. This is due to the progressive elimination of spurious counts in the regions outside the phase-matching peaks. In the case of the TOF spectrograph, on the other hand, the performance improvement is barely noticeable due to its low resolution. Although it is still possible to apply a filtering window narrower than the actual resolution, we see that below 300 GHz the measurement quality is essentially saturated. The results obtained with the CCD spectrograph are therefore an indication of the high intrinsic quality of our experimental implementation of the MQPG, which could be achieved also for the decoder as a whole by solely increasing the resolution of the TOF spectrograph.

APPENDIX C: EXPANSION TO HIGHER DIMENSIONS

Here we study the maximum dimensionality achievable by a realistic MQPG-based decoder. In the system considered, the dimensionality is defined by the number of basis elements that can be observed at the same time.

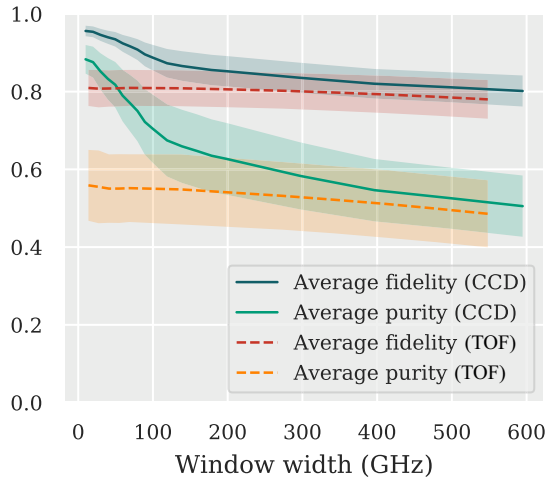

FIG. 9. Average purity and fidelity (with corresponding standard deviations) of the POVMs of our implemented five-dimensional decoder for experimental data acquired with the CCD spectrograph (solid line) and the TOF spectrograph (dashed line) as a function of the spectral window around each central frequency.

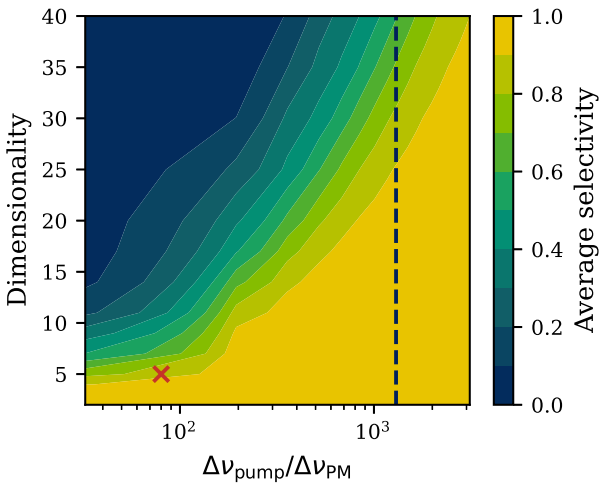

FIG. 10. Average selectivity of a MQPG-based decoder for different dimensionalities as a function of the ratio between the maximum available pump bandwidth ($\Delta\nu_{pump}$) and the bandwidth of the phase-matching function ($\Delta\nu_{PM}$). The cross marks the conditions of the experiment presented in the main text, whereas the dashed line shows what can be achieved with state-of-the-art components (a 10-cm-long sample and a pump laser bandwidth of 13 THz).

When we expand the MQPG system to the dth dimension, therefore, the Hilbert space considered will include HG modes from the zeroth order to the (d-1)th order and their superpositions.

We consider the case in which, as in the experimental demonstration, the pump field that drives the MQPG process is generated by shaping a single broadband pulse. The spectra corresponding to all d elements of the chosen basis ("pump peaks") must be carved within the available spectral bandwidth; therefore, the spectral width allocated for each element is inversely proportional to d. Furthermore, higher-order HG modes span a wider spectral bandwidth; as a consequence, the spectral width of each pump peak must be further reduced to avoid overlaps when one is increasing the dimensionality. This bandwidth constraint constitutes the main limitation to the scalability of the current implementation of the system. Indeed, if each pump peak is not sufficiently broader than the corresponding phase-matching peak, each channel starts displaying multimode behavior, which represents the main source of error in the experiment.

For this reason, we investigate how the ratio between the maximum available pump bandwidth and the bandwidth of the phase-matching function affects the quality of the projections, quantified as the average selectivity over all $d+1$ MUBs of a d-dimensional Hilbert space containing HG states and their superpositions. We simulate a decoder based on a realistic MQPG waveguide in a setup with an ideal shaping resolution and an ideal noiseless spectrograph at the output of the device.

The results of the study are summarized in Fig. 10, which shows the average selectivity for all $d+1$ MUBs of a d-dimensional MQPG-based decoder as a function of the ratio between the maximum available pump bandwidth and the bandwidth of the phase-matching function. The cross marks the conditions of the experiment presented in the main text, whereas the dashed line shows what can be achieved with state-of-the-art components: a 10-cm-long sample and a pump laser bandwidth of 13 THz would allow operation in 25 dimensions (and all 26 MUBs) with a selectivity greater than 90%.

[1] H. J. Kimble, The quantum internet, Nature **453**, 1023 (2008).
[2] J. L. O'Brien, A. Furusawa, and J. Vučković, Photonic quantum technologies, Nat. Photonics **3**, 687 (2009).
[3] J. Wang, F. Sciarrino, A. Laing, and M. G. Thompson, Integrated photonic quantum technologies, Nat. Photonics **14**, 273 (2020).
[4] L. Sheridan and V. Scarani, Security proof for quantum key distribution using qudit systems, Phys. Rev. A **82**, 030301(R) (2010).
[5] G. C. G. Berkhout, M. P. J. Lavery, J. Courtial, M. W. Beijersbergen, and M. J. Padgett, Efficient Sorting of Orbital Angular Momentum States of Light, Phys. Rev. Lett. **105**, 153601 (2010).
[6] K. Huang, H. Liu, S. Restuccia, M. Q. Mehmood, S.-T. Mei, D. Giovannini, A. Danner, M. J. Padgett, J.-H. Teng, and

C.-W. Qiu, Spiniform phase-encoded metagratings entangling arbitrary rational-order orbital angular momentum, Light: Sci. Appl. **7**, 17156 (2018).

[7] M. Mirhosseini, O. S. Magaña-Loaiza, M. N. O'Sullivan, B. Rodenburg, M. Malik, M. P. J. Lavery, M. J. Padgett, D. J. Gauthier, and R. W. Boyd, High-dimensional quantum cryptography with twisted light, New J. Phys. **17**, 033033 (2015).

[8] D. Cozzolino, B. Da Lio, D. Bacco, and L. K. Oxenløwe, High-dimensional quantum communication: Benefits, progress, and future challenges, Adv. Quantum Technol. **2**, 1900038 (2019).

[9] C. Reimer, M. Kues, P. Roztocki, B. Wetzel, F. Grazioso, B. E. Little, S. T. Chu, T. Johnston, Y. Bromberg, L. Caspani, D. J. Moss, and R. Morandotti, Generation of multiphoton entangled quantum states by means of integrated frequency combs, Science **351**, 1176 (2016).

[10] M. Kues, C. Reimer, J. M. Lukens, W. J. Munro, A. M. Weiner, D. J. Moss, and R. Morandotti, Quantum optical microcombs, Nat. Photonics **13**, 170 (2019).

[11] P. C. Humphreys, B. J. Metcalf, J. B. Spring, M. Moore, X.-M. Jin, M. Barbieri, W. S. Kolthammer, and I. A. Walmsley, Linear Optical Quantum Computing in a Single Spatial Mode, Phys. Rev. Lett. **111**, 150501 (2013).

[12] H.-H. Lu, J. M. Lukens, N. A. Peters, O. D. Odele, D. E. Leaird, A. M. Weiner, and P. Lougovski, Electro-optic Frequency Beam Splitters and Tritters for High-Fidelity Photonic Quantum Information Processing, Phys. Rev. Lett. **120**, 030502 (2018).

[13] H.-H. Lu, J. M. Lukens, N. A. Peters, B. P. Williams, A. M. Weiner, and P. Lougovski, Quantum interference and correlation control of frequency-bin qubits, Optica **5**, 1455 (2018).

[14] N. T. Islam, C. C. W. Lim, C. Cahall, J. Kim, and D. J. Gauthier, Provably secure and high-rate quantum key distribution with time-bin qudits, Sci. Adv. **3**, e1701491 (2017).

[15] I. Vagniluca, B. Da Lio, D. Rusca, D. Cozzolino, Y. Ding, H. Zbinden, A. Zavatta, L. K. Oxenløwe, and D. Bacco, Efficient Time-Bin Encoding for Practical High-Dimensional Quantum Key Distribution, Phys. Rev. Appl. **14**, 014051 (2020).

[16] B. Brecht, D. V. Reddy, C. Silberhorn, and M. G. Raymer, Photon Temporal Modes: A Complete Framework for Quantum Information Science, Phys. Rev. X **5**, 041017 (2015).

[17] M. G. Raymer and I. A. Walmsley, Temporal modes in quantum optics: then and now, Phys. Scr. **95**, 064002 (2020).

[18] F. Schlawin, K. E. Dorfman, and S. Mukamel, Pump-probe spectroscopy using quantum light with two-photon coincidence detection, Phys. Rev. A **93**, 023807 (2016).

[19] V. Ansari, B. Brecht, J. Gil-Lopez, J. M. Donohue, J. Řeháček, Z. C. V. Hradil, L. L. Sánchez-Soto, and C. Silberhorn, Achieving the Ultimate Quantum Timing Resolution, PRX Quantum **2**, 010301 (2021).

[20] M. Mazelanik, A. Leszczyński, and M. Parniak, Optical-domain spectral super-resolution via a quantum-memory-based time-frequency processor, Nat. Commun. **13**, 691 (2022).

[21] J. Nunn, I. A. Walmsley, M. G. Raymer, K. Surmacz, F. C. Waldermann, Z. Wang, and D. Jaksch, Mapping broadband single-photon wave packets into an atomic memory, Phys. Rev. A **75**, 011401(R) (2007).

[22] M. Afzelius, C. Simon, H. de Riedmatten, and N. Gisin, Multimode quantum memory based on atomic frequency combs, Phys. Rev. A **79**, 052329 (2009).

[23] Z. Zheng, O. Mishina, N. Treps, and C. Fabre, Atomic quantum memory for multimode frequency combs, Phys. Rev. A **91**, 031802(R) (2015).

[24] G. Harder, V. Ansari, B. Brecht, T. Dirmeier, C. Marquardt, and C. Silberhorn, An optimized photon pair source for quantum circuits, Opt. Express **21**, 13975 (2013).

[25] T. C. Ralph, I. Söllner, S. Mahmoodian, A. G. White, and P. Lodahl, Photon Sorting, Efficient Bell Measurements, and a Deterministic Controlled-Z Gate Using a Passive Two-Level Nonlinearity, Phys. Rev. Lett. **114**, 173603 (2015).

[26] S. Gao, O. Lazo-Arjona, B. Brecht, K. T. Kaczmarek, S. E. Thomas, J. Nunn, P. M. Ledingham, D. J. Saunders, and I. A. Walmsley, Optimal Coherent Filtering for Single Noisy Photons, Phys. Rev. Lett. **123**, 213604 (2019).

[27] V. Ansari, E. Roccia, M. Santandrea, M. Doostdar, C. Eigner, L. Padberg, I. Gianani, M. Sbroscia, J. M. Donohue, and L. Mancino, *et al.*, Heralded generation of high-purity ultrashort single photons in programmable temporal shapes, Opt. Express **26**, 2764 (2018).

[28] X. Shi, A. Valencia, M. Hendrych, and J. P. Torres, Generation of indistinguishable and pure heralded single photons with tunable bandwidth, Opt. Lett. **33**, 875 (2008).

[29] P. J. Mosley, J. S. Lundeen, B. J. Smith, P. Wasylczyk, A. B. U'Ren, C. Silberhorn, and I. A. Walmsley, Heralded Generation of Ultrafast Single Photons in Pure Quantum States, Phys. Rev. Lett. **100**, 133601 (2008).

[30] B. Brecht, A. Eckstein, R. Ricken, V. Quiring, H. Suche, L. Sansoni, and C. Silberhorn, Demonstration of coherent time-frequency Schmidt mode selection using dispersion-engineered frequency conversion, Phys. Rev. A **90**, 030302(R) (2014).

[31] V. Ansari, J. M. Donohue, M. Allgaier, L. Sansoni, B. Brecht, J. Roslund, N. Treps, G. Harder, and C. Silberhorn, Tomography and Purification of the Temporal-Mode Structure of Quantum Light, Phys. Rev. Lett. **120**, 213601 (2018).

[32] D. V. Reddy and M. G. Raymer, High-selectivity quantum pulse gating of photonic temporal modes using all-optical Ramsey interferometry, Optica **5**, 423 (2018).

[33] M. Silver, Y. Huang, C. Langrock, M. Fejer, P. Kumar, and G. Kanter, Three-signal temporal-mode selective upconversion demultiplexing, IEEE Photonics Technol. Lett. **31**, 1749
(2019).

[34] M. H. Chou, K. R. Parameswaran, M. M. Fejer, and I. Brener, Multiple-channel wavelength conversion by use of engineered quasi-phase-matching structures in $LiNbO_3$ waveguides, Opt. Lett. **24**, 1157 (1999).

[35] J. M. Donohue, V. Ansari, J. Řeháček, Z. Hradil, B. Stoklasa, M. Paúr, L. L. Sánchez-Soto, and C. Silberhorn, Quantum-Limited Time-Frequency Estimation through Mode-Selective Photon Measurement, Phys. Rev. Lett. **121**, 090501 (2018).

[36] M. Santandrea, M. Stefszky, V. Ansari, and C. Silberhorn, Fabrication limits of waveguides in nonlinear crystals and their impact on quantum optics applications, New J. Phys. **21**, 033038 (2019).
[37] J. S. Lundeen, A. Feito, H. Coldenstrodt-Ronge, K. L. Pregnell, C. Silberhorn, T. C. Ralph, J. Eisert, M. B. Plenio, and I. A. Walmsley, Tomography of quantum detectors, Nat. Phys. **5**, 27 (2009).
[38] V. Ansari, G. Harder, M. Allgaier, B. Brecht, and C. Silberhorn, Temporal-mode measurement tomography of a quantum pulse gate, Phys. Rev. A **96**, 063817 (2017).
[39] A. Monmayrant, S. Weber, and B. Chatel, A newcomer's guide to ultrashort pulse shaping and characterization, J. Phys. B—At., Mol. Opt. Phys. **43**, 00 (2010).
[40] C. K. Law, I. A. Walmsley, and J. H. Eberly, Continuous Frequency Entanglement: Effective Finite Hilbert Space and Entropy Control, Phys. Rev. Lett. **84**, 5304 (2000).
[41] M. Avenhaus, A. Eckstein, P. J. Mosley, and C. Silberhorn, Fiber-assisted single-photon spectrograph, Opt. Lett. **34**, 2873 (2009).
[42] F. Marsili, V. B. Verma, J. A. Stern, S. Harrington, A. E. Lita, T. Gerrits, I. Vayshenker, B. Baek, M. D. Shaw, R. P. Mirin, and S. W. Nam, Detecting single infrared photons with 93% system efficiency, Nat. Photonics **7**, 210 (2013).
[43] A. O. C. Davis, P. M. Saulnier, M. Karpiński, and B. J. Smith, Pulsed single-photon spectrometer by frequency-to-time mapping using chirped fiber Bragg gratings, Opt. Express **25**, 12804 (2017).
[44] B. Korzh, *et al.*, Demonstration of sub-3 ps temporal resolution with a superconducting nanowire single-photon detector, Nat. Photonics **14**, 250 (2020).
[45] A. M. Brańczyk, A. Fedrizzi, T. M. Stace, T. C. Ralph, and A. G. White, Engineered optical nonlinearity for quantum light sources, Opt. Express **19**, 55 (2011).
[46] D. Zhu, L. Shao, M. Yu, R. Cheng, B. Desiatov, C. J. Xin, Y. Hu, J. Holzgrafe, S. Ghosh, A. Shams-Ansari, E. Puma, N. Sinclair, C. Reimer, M. Zhang, and M. Lončar, Integrated photonics on thin-film lithium niobate, Adv. Opt. Photonics **13**, 242 (2021).
[47] C. Gordón, R. Guzmán, V. Corral, X. Leijtens, and G. Carpintero, On-chip colliding pulse mode-locked laser diode (OCCP-MLLD) using multimode interference reflectors, Opt. Express **23**, 14666 (2015).
[48] J. Gil-Lopez, M. Santandrea, G. Roland, B. Brecht, C. Eigner, R. Ricken, V. Quiring, and C. Silberhorn, Improved non-linear devices for quantum applications, New J. Phys. **23**, 063082 (2021).

Research Article Vol. 33, No. 3 / 10 Feb 2025 / Optics Express 5577
Optics EXPRESS

Programmable time-frequency mode-sorting of single photons with a multi-output quantum pulse gate

L. Serino,[1,2,*] C. Eigner,[2] B. Brecht,[1,2] and C. Silberhorn[1,2]

[1] Paderborn University, Integrated Quantum Optics, Warburgerstr. 100, Paderborn, Germany
[2] Paderborn University, Institute for Photonic Quantum Systems, Warburgerstr. 100, Paderborn, Germany
[*] laura.serino@upb.de

Abstract: We demonstrate a high-dimensional mode-sorter for single photons based on a multi-output quantum pulse gate, which we can program to switch between different temporal-mode encodings including pulse modes, frequency bins, time bins, and their superpositions. This device can facilitate practical realizations of quantum information applications such as high-dimensional quantum key distribution and thus enables secure communication with enhanced information capacity. We characterize the mode-sorter through a detector tomography in 3 and 5 dimensions and find a fidelity up to 0.958 ± 0.030 at the single-photon level.

1. Introduction

Quantum information science based on high-dimensional encodings has the potential to revolutionize computing, communication, and cryptography by harnessing the unique properties of quantum systems [1,2]. High-dimensional encodings allow for increased information capacity of quantum information carriers and noise robustness, thereby improving the security and efficiency of quantum communication protocols such as high-dimensional quantum key distribution (HD-QKD) [3,4]. Photons are a natural choice of information carrier due to their inherent quantum properties and high-dimensional degrees of freedom in both the spatial and time-frequency domain. Although arguably less explored than their spatial counterparts, time-frequency encodings offer significant advantages in quantum information applications: since orthogonal time-frequency modes can share the same spatial distribution, they are resilient in transmission and compatible with existing spatially single-mode telecom fiber infrastructure.

Temporal modes (TMs) provide appealing time-frequency encodings in the form of field-orthogonal wave-packet modes that can be expressed as coherent superpositions of monochromatic modes [5]. These encodings can describe discrete Hilbert spaces with finite high dimensionality, which find applications in many quantum information fields, from quantum cryptography [3] to quantum computing [6,7] and quantum networks [8–10]. TM alphabets used in these applications include frequency bins, time bins, and pulse modes, each offering distinct advantages and posing unique challenges [5,11,12]. Frequency bins and time bins encode information in modes that are, for all practical purposes, intensity-orthogonal in frequency or time, respectively. In contrast, the intensity profiles of pulse modes overlap in time and frequency, and the field-orthogonality condition is determined by their complex spectral profile. Hermite-Gauss (HG) modes are a common example of this type of encoding alphabet.

Despite their different labels, frequency bins, time bins, and pulse modes all belong to the same family: they can be described as complex functions of time or frequency, connected through a Fourier transform and, therefore, they all represent particular realizations of TMs. We note that, since TMs are defined as wave-packet modes, they differ conceptually from the more conventional continuous variable approach which uses time and frequency as conjugate bases containing an

#544206 https://doi.org/10.1364/OE.544206
Journal © 2025 Received 16 Oct 2024; revised 17 Dec 2024; accepted 18 Dec 2024; published 4 Feb 2025

Research Article Vol. 33, No. 3 / 10 Feb 2025 / Optics Express 5578
Optics EXPRESS

infinite number of delta-like bins [13–15]. Instead, TMs include discrete finite bins [12,16] and pulse modes [17] that can be encoded in light pulses. Conjugate bases in this context are constructed as superpositions of states from the fundamental basis with appropriate phases [18].

Establishing a complete TM-based quantum information framework requires the generation, manipulation, and detection of high-dimensional quantum TM states. Engineered parametric down-conversion is a well-known and established tool for generating these states [19–21]. However, simultaneously manipulating or detecting multiple single-photon TMs is challenging because both pulse modes and superpositions of bins overlap in time and frequency. This task is further complicated by the requirements of quantum communication protocols like HD-QKD, which demand a high-dimensional mode sorter capable of operating with single-photon TMs and their superpositions at each individual shot of the communication [3,4].

To date, dedicated devices have been developed and tailored for each application. The so-called quantum frequency processor [22,23], for instance, demonstrated mode-sorting of three-dimensional frequency bins and their superpositions using a combination of phase modulators and pulse shapers. While this approach operates effectively in different superposition bases, scaling it to higher dimensions would require additional components, increasing the setup complexity. Similarly, interferometric setups based on beam splitters [24,25] have been used to decode time bins in up to four dimensions and two conjugate bases, but would necessitate complex cascaded interferometers to access higher dimensions. In contrast, a simpler setup based on group-velocity dispersion [26] has demonstrated time-bin decoding in four dimensions which can be scaled without added complexity. However, this method inherently suffers from higher error rates as dimensionality increases and is limited to operating in a single superposition basis, in addition to the fundamental time-bin basis. The multi-output quantum pulse gate (mQPG) [27] has recently shown simultaneous projections of a single-photon-level input state onto five arbitrary superpositions of pulse modes using a single nonlinear process, which can be scaled to higher dimensions without increasing the number of components. However, no analogous demonstration yet exists for frequency bins and time bins. The need for dedicated infrastructure for each encoding complicates interfacing between devices that work with different alphabets, even though they operate on the same degree of freedom, and necessarily leads to the development of distinct quantum networks that cannot be interconnected without a system capable of handling multiple encodings.

In this work, we demonstrate programmable high-dimensional mode-sorting of different TM-based encoding alphabets at the single-photon-level, achieved through an mQPG. This programmability is enabled through spectral pulse shaping, leveraging the fact that all TM alphabets can be described as complex functions of frequency to change the measurement basis or encoding alphabet without requiring hardware modifications. For each encoding alphabet — pulsed modes, frequency bins and time bins — we demonstrate high-fidelity projections onto multiple superposition bases, namely all possible mutually unbiased bases (MUBs) in 3 and 5 dimensions. The versatility of the mQPG to operate in different high-dimensional encoding alphabets and superposition bases is crucial for interfacing with diverse sources and integrating the unique benefits offered by each encoding alphabet, interconnecting quantum networks and paving the way for practical applications in quantum information science.

2. Multi-output quantum pulse gate

The mQPG serves as a high-dimensional mode-sorter for TM states [27]. Its working principle is based on a dispersion-engineered sum-frequency-generation (SFG) process where an input pulse, driven by a strong pump field, is converted into a particular output pulse based on its TM (Fig. 1). The process takes place in a periodically poled nonlinear waveguide, typically titanium in-diffused lithium niobate [17]. The periodic poling structure of the mQPG waveguide, consisting of alternating poled and unpoled regions (“super-poling”), enables parallel SFG

Research Article Vol. 33, No. 3 / 10 Feb 2025 / Optics Express 5579
Optics EXPRESS

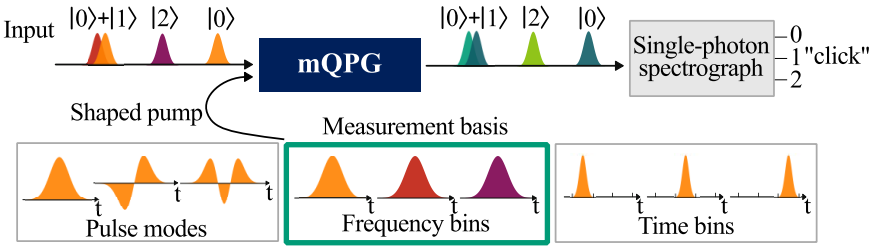

Fig. 1. Working principle of the mQPG-based time-frequency mode sorter: the mQPG process, driven by a pump pulse spectrally shaped to implement the selected measurement basis, up-converts the input photons to a different output frequency based on their temporal mode; the output frequencies, which encode the information in the signal, can be detected with a single-photon spectrograph. We can choose frequency bins, pulse modes, and time bins as encoding alphabet.

processes centered at distinct output frequencies which define the output channels of the device. The SFG process is engineered to achieve group-velocity matching between the input and pump pulses, which is essential for mode-selective operation in each channel [28].

In frequency space, the mQPG operation is described by a transfer function $G(\nu_{\text{in}}, \nu_{\text{out}})$ that relates the input frequencies ν_{in} to the output frequencies ν_{out} (Fig. 2). The transfer function is the product of the pump function α, which describes energy conservation, and the phase-matching function Φ, which is determined by momentum conservation: $G(\nu_{\text{in}}, \nu_{\text{out}}) = \alpha(\nu_{\text{out}} - \nu_{\text{in}}) \cdot \Phi(\nu_{\text{out}})$. The number and spacing of phase-matching peaks depend on the super-poling parameters selected during the fabrication of the mQPG waveguide [27]. The pump function is determined by the complex spectral amplitude of the pump pulse, which can be tailored through spectral shaping. By dividing the pump spectrum into distinct spectral regions, spaced to match the phase-matching peaks, each region can be aligned with a specific phase-matching peak in correspondence of the same input frequencies (as shown in the first three columns of Fig. 2). Each spectral region can then be shaped to implement a different TM in the respective output channel, effectively creating a multi-output transfer function.

If the spectral features of the pump are larger than the bandwidth of each phase-matching peak, the mQPG performs ideal single-mode projections in each channel, meaning that the up-conversion probability in each output channel is proportional to the complex spectral overlap between the corresponding pump mode and the input state [29]. In this optimal regime, each mQPG channel can be described by a von-Neumann projection $\pi^{\gamma} = |\gamma\rangle\langle\gamma|$ onto the assigned TM γ. In this case, the probability of SFG conversion of a pure input state $\rho^{\xi} = |\xi\rangle\langle\xi|$ is given by $p^{\gamma\xi} = \text{Tr}\left\{\rho^{\xi}\pi^{\gamma}\right\}$ [17]. The complete mQPG process, described by the set of projectors $\{\pi^{\gamma}\}$ comprising all channels, effectively sorts the input modes into output frequencies which can be read out using a spectrograph. The modes γ for the projections can be chosen programmatically via pump shaping, which facilitates measurements in different superposition bases without any hardware modifications. Changing the encoding alphabet is equally straightforward, requiring only a change in the shaped pulse from frequency bins to pulse modes or time bins or any of their superpositions.

In a practical experimental setting, however, the mQPG has a non-unity conversion efficiency, which leads to an inconclusive result when the input photons are not up-converted by the device. In this case, the mQPG operation is described by the positive-operator-valued measure (POVM) $\{\pi^{\gamma}\}$, comprising the POVM elements π^{γ} that describe the operation in each channel and an additional POVM element describing the inconclusive result. For simplicity, in the following discussion we will neglect the inconclusive result and consider only the POVM

Research Article Vol. 33, No. 3 / 10 Feb 2025 / Optics Express 5580
Optics EXPRESS

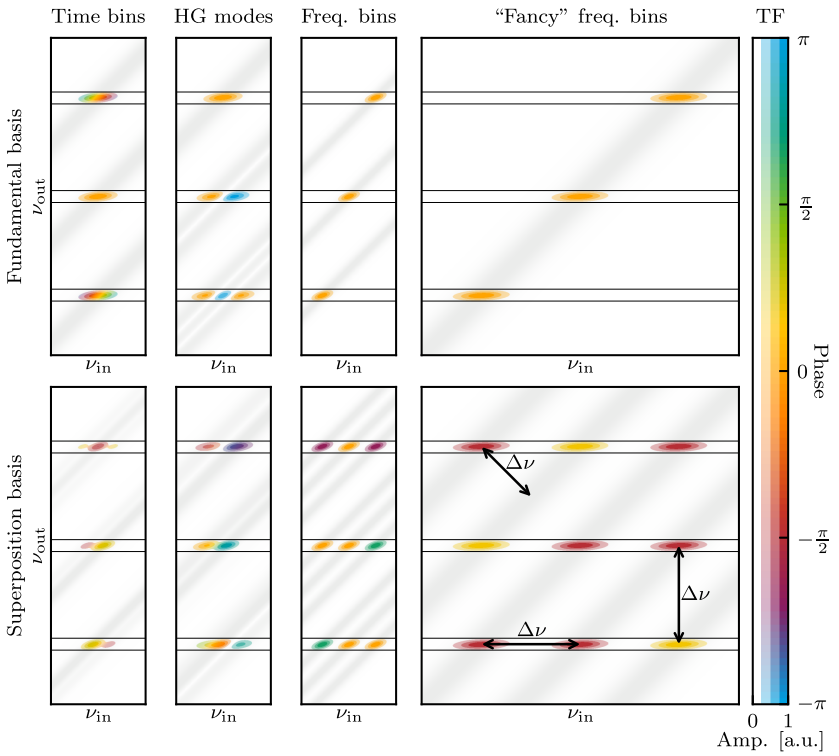

Fig. 2. Frequency-space representation of the transfer functions of the three-dimensional fundamental basis (top) and a superposition basis (bottom) for the three TM alphabets tested in this work: time bins, HG modes, and frequency bins (including the "fancy" frequency bin mode-sorting approach explained in the main text). The horizontal lines indicate the phase-matching function $\Phi(\nu_{out})$, comprising one phase-matching peak for each output channel of the mQPG. The diagonal gray area shows the amplitude of the pump function $\alpha(\nu_{out} - \nu_{in})$. The colored regions indicate the transfer function $G(\nu_{in}, \nu_{out})$, which shows where the SFG process can take place.

elements associated with successful click detection. Experimental constraints can also limit the achievable ratio between the spectral bandwidth of the pump and that of the phase-matching bandwidth, introducing spurious multi-mode processes in each channel that lead to cross-talk in the mode-sorting process [29]. In this case, the POVM elements require the more general description $\pi^{\gamma} = \sum_{ij} m_{ij}^{\gamma} |i\rangle \langle j|$, with i and j elements of the chosen fundamental TM basis [30]. In order to eliminate the induced cross-talk, one must artificially reduce the phase-matching bandwidth through narrowband frequency filtering. However, the resolution of currently available single-photon spectrographs in the mQPG output frequency range (around 550 nm) is insufficient for adequate frequency filtering. This technical limitation significantly constrained previous demonstrations, decreasing the measurement fidelity of the mQPG in five dimensions from the intrinsic value of 92% to 65% [27,31].

To overcome this limitation, we developed an alternative technique for frequency-bin mode-sorting, labeled "fancy" frequency bin (FFB) approach, that leverages the periodic phase-matching structure of the mQPG to improve its performance. Following the energy conservation condition, a single pump bin generally intercepts multiple phase-matching peaks, separated by $\Delta\nu$, in correspondence of input frequencies also separated by $\Delta\nu$ (last column in Fig. 2). This transfer

Research Article Vol. 33, No. 3 / 10 Feb 2025 / Optics Express 5581
Optics EXPRESS

function, generated using only one pump bin, can completely mode-sort discrete frequency bins with separation $\Delta\nu$ in input, which form the fundamental basis of a d-dimensional Hilbert space.

This scheme can be intuitively extended to also mode-sort MUBs containing superpositions of frequency bins by generating pump bins with spacing equal to $\Delta\nu$. In contrast to the standard approach, where each pump bin addresses only one mQPG channel, in the FFB method each pump bin intercepts multiple phase-matching peaks at corresponding input frequencies with an offset of $\Delta\nu$. A total of $2d-1$ pump bins is thus sufficient to generate a complete d×d transfer function, where the mode in each mQPG channel is determined by the relative phase of the pump bins. This approach enables sorting d distinct input modes (frequency bins or their superpositions) starting from only $2d-1$ pump frequency bins, instead of the d^2 bins required by the standard approach. Hence, the FFB method scales linearly with the system dimensionality rather quadratically, effectively reducing the technical demands on the experimental setup. Namely, it allows one to use fewer, broader pump bins within a fixed spectral region, reducing the need for precise spectral shaping while simultaneously increasing the ratio between the spectral features of the pump and the phase-matching width. This generally results in lower cross-talk [29], greatly improving the measurement quality for a fixed available pump bandwidth and reducing reliance on extensive output filtering.

While the FFB approach introduces inter-bin correlations that restrict the full programmability of each channel, it still provides sufficient flexibility for various applications. For instance, in prime dimensions d, this technique allows for measuring in d MUBs [32], only one basis short of the complete set of $d+1$ MUBs. Although this limitation precludes applications such as input state tomography, which require measurements in all MUBs, the FFB method offers significant advantages in HD-QKD, which only requires at least two MUBs and can benefit from additional measurement bases [33–35].

3. Experiment

The schematic of the experimental setup is illustrated in Fig. 3. A mode-locked Ti:sapphire oscillator with a repetition rate of 80 MHz generates pulses centered at 860 nm with a spectral full-width-half-maximum of 3 THz, corresponding to a duration of 150 fs. The pump pulse is generated by shaping the spectral amplitude and phase of the laser pulse through a in-house-built 4-f-line waveshaper based on a spatial light modulator. A portion of the original Ti:sapphire pulse is directed to pump an optical parametric oscillator that generates the input pulse of the experiment centered at 1545 nm, which is shaped by a commercial waveshaper and attenuated to below 0.1 photons per pulse to generate the single-photon-level input states, representing the typical information carrier of a quantum communication scheme such as HD-QKD. For this demonstration, we consider three TM alphabets: time bins, HG modes, and frequency bins. For the latter, we also test the alternative FFB mode-sorting technique explained in the previous section by appropriately shaping the pump pulse. The spectral parameters used for each encoding alphabet are reported in Table 1, and examples of the resulting spectra are shown in the Supplement 1.

The pump and input pulses are coupled into the mQPG, realized as a periodically super-poled titanium-indiffused lithium niobate waveguide [27], with a coupling efficiency of approximately 50% for the pump and 70% for the input. The poling period of 4.32 µm allows for a type-II SFG process in which a horizontally-polarized 1545 nm input photon is up-converted to a horizontally-polarized output photon at 552.5 nm through a vertically-polarized 860 nm pump field, according to the mQPG mode-sorting process. We use a five-output mQPG waveguide of which we use 3 or 5 output channels, depending on the dimensionality of the chosen alphabet. The output channels are centered at frequencies separated by 0.5 THz in the case of FFB in 5 dimensions and 0.63 THz in all other cases.

Research Article Vol. 33, No. 3 / 10 Feb 2025 / Optics Express 5582
Optics EXPRESS

Table 1. Spectral parameters used for each encoding alphabet: full-width-half-maximum (FWHM) of the amplitude profile of each bin, and inter-bin separation.[a]

	d = 3		d = 5	
Encoding	FWHM	Separation	FWHM	Separation
Time bins	1.5 ps	3.5 ps	1.5 ps	5.0 ps
HG modes	210 GHz	-	140 GHz	-
Frequency bins	100 GHz	200 GHz	50 GHz	100 GHz
FFB	300 GHz	630 GHz	150 GHz	500 GHz

[a]In the case of the HG alphabet, the reported FWHM corresponds to the HG0 (Gaussian) mode, and the inter-bin separation is not defined.

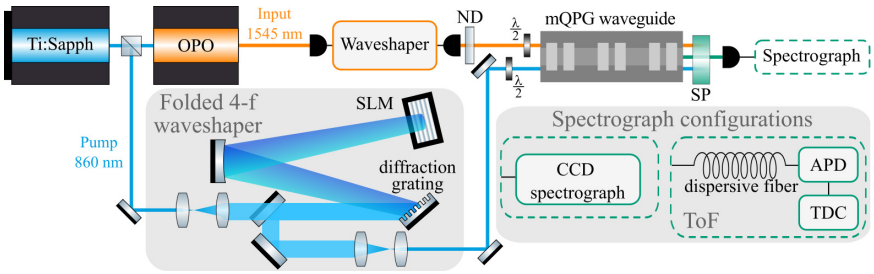

Fig. 3. Schematic of the experimental setup. A system comprising a mode-locked Ti:sapphire laser and an optical parametric oscillator (OPO) generates the initial input and pump pulses centered at 1545 nm and 860 nm, respectively. The input pulse is attenuated to $\langle\hat{n}\rangle<0.1$/ pulse using a neutral density (ND) filter and shaped by a commercial waveshaper to generate the input mode. The pump modes are shaped using a folded 4-f waveshaper [36] comprising a diffraction grating, a cylindrical mirror and a spatial light modulator (SLM). After waveshaping, input and pump pulses are both coupled into the mQPG waveguide. The up-converted output photons are isolated by a short-pass (SP) filter and detected with a CCD spectrograph or a time-of-flight (ToF) spectrograph [37] formed by a dispersive fiber, an avalanche photodiode (APD) and a time-to-digital converter (TDC).

The output field is isolated from the leftover pump and input fields via frequency filtering and detected with an in-house-built time-of-flight (ToF) spectrograph consisting of a dispersive fiber, an avalanche photodiode, and a time-to-digital converter [37]. The ToF spectrograph facilitates shot-to-shot measurements (required, e.g., by HD-QKD protocols) and is cost-effective as it utilizes only one single-photon detector. Nevertheless, the effective resolution of the current implementation is limited to 300 GHz by technical constraints, mainly the timing jitter of the setup and the trade-off between group-velocity dispersion and optical loss in the 550 nm wavelength region [27]. This value is ten times larger than the bandwidth of each phase-matching peak (approximately 30 GHz), negatively affecting the overall quality of the measurements. Therefore, to showcase the quality of the mQPG operation when paired to optimal frequency-resolving measurements in output, we repeat the measurements replacing the ToF spectrograph with a CCD spectrograph (Andor Shamrock 500i) with a resolution of 30 GHz. We note that this device is generally unsuitable for shot-to-shot measurements as it requires a read-out time of the order of ms, incompatible with the 80 MHz repetition rate of the laser.

For each tested encoding alphabet and dimensionality, we quantify the measurement quality of the mQPG through a quantum detector tomography [27,30,38]. This technique aims at reconstructing the POVMs $\{\pi^{\gamma}\}$ by probing the device with an informationally complete set of

Research Article Vol. 33, No. 3 / 10 Feb 2025 / Optics Express 5583
Optics EXPRESS

input states — in this case, all eigenstates of all possible MUBs in the chosen Hilbert space — and counting the output photons in each channel.

To perform the quantum measurement tomography, we first choose the measurement basis that we want to probe, which defines the POVM $\{\pi^\gamma\}$ comprising the POVM elements of each mQPG channel, and we set up the mQPG mode-sorting process by shaping the pump spectrum accordingly. We probe the mQPG with input states from the complete set $\{\rho^\xi\}$ of the $d(d+1)$ elements of all $d+1$ MUBs of the considered d-dimensional Hilbert space.

For each measurement we run 10-20 acquisitions, each with an integration time between 0.5 s and 1 s, chosen based on the measured count rate. The input power is always adjusted to have $\langle\hat{n}\rangle$<0.1/ pulse, whereas the pump power is maximized within the capabilities of the experimental setup, reaching 5 mW to 10 mW. The maximum available pump power, which determines the conversion efficiency and therefore the number of output counts in each measurement, depends on the chosen encoding alphabet and dimensionality, as the waveshaping system needs to "carve" the appropriate spectrum from the original laser pulse.

The conversion efficiency in this experiment lies in the range of 1-10%; however, this is not a fundamental limitation for the mQPG process, as similar devices have demonstrated an efficiency of up to 87.7% [17,39]. Beyond the non-optimized conversion efficiency, the primary source of optical loss in the experimental setup is the ToF spectrograph: the dispersive fiber introduces 20 dB of loss, and the avalanche photodiode has a detection efficiency below 35%. Although the high losses do not pose a fundamental problem for the mQPG mode-sorting operation, they restrict the maximum achievable communication distance in QKD. In principle, the overall conversion and detection efficiencies could be improved with higher pump powers and an optimized spectrograph; nevertheless, these optimizations lie outside the scope of this work, which focuses on a proof-of-principle demonstration. Notably, the relatively low detection efficiency does not degrade the signal-to-noise ratio in the mQPG detection. In fact, the background noise in the measured data is negligible, as the large wavelength difference between pump and signal pulses prevents Raman scattering from the pump from introducing noise in the frequency conversion process.

We normalize the measured counts to obtain the experimental output probabilities for each channel $p^{\gamma\xi}$. From these values, we reconstruct the POVM elements π^γ through a weighted least-squares fit by minimizing the quantity $\sum_\xi \left|p^{\gamma\xi} - \mathrm{Tr}\left\{\rho^\xi \pi^\gamma\right\}\right|^2 / p^{\gamma\xi}$, where we constrain π^γ to be Hermitian and positive semidefinite. We then compare the reconstructed POVM elements to the theoretical projectors $|\gamma\rangle\langle\gamma|$ by calculating the fidelity $\mathcal{F} = \langle\gamma|\pi^\gamma|\gamma\rangle / \mathrm{Tr}(\pi^\gamma)$.

4. Results and discussion

Through the detector tomography, we reconstruct the POVMs that describe the mQPG operation when projecting an input state into the selected MUB. For each encoding alphabet, we test all $d+1$ MUBs in $d = 3$ and $d = 5$, with the exception of the FFB scheme, which is limited to d MUBs. Figure 4 shows the reconstructed POVMs compared to the theoretical ones for the FFB scheme in $d = 3$, corresponding to a measurement at the single-photon level acquired with the ToF spectrograph. We highlight that each row corresponds to 3 POVM elements that are measured simultaneously and, therefore, form the POVM that describes the mode-sorting operation of the mQPG for the respective basis.

Figure 5 shows the average fidelity of the reconstructed POVMs to the ideal operators for all tested TM alphabets in 3 and 5 dimensions. The fidelity measured with the CCD spectrograph (blue bars) is always above 90% and, for frequency bins, reaches (99.7±0.5)% in $d = 3$ and (98.9±0.5)% in $d = 5$, confirming the high intrinsic quality of the mQPG projections. This value is generally higher than the fidelity measured with the ToF spectrograph (orange bars), showing the benefits of optimal filtering in the output of the mQPG to enhance the quality of the

Research Article Vol. 33, No. 3 / 10 Feb 2025 / Optics Express 5584
Optics EXPRESS

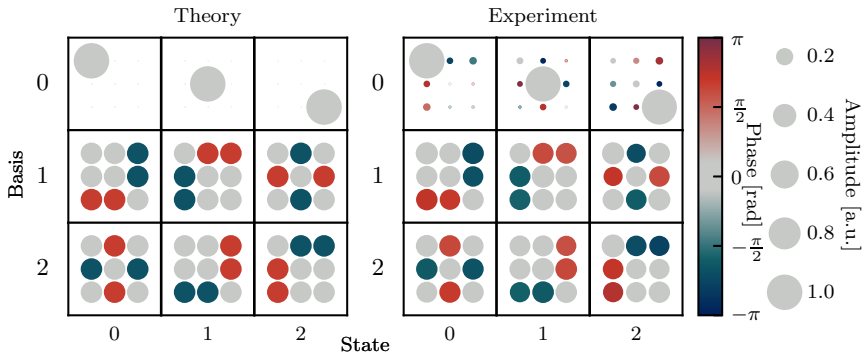

Fig. 4. Theoretical (left) and experimentally characterized (right) POVMs for three-dimensional operation in the frequency-bin alphabet (FFB scheme) at the single-photon level ($\langle\hat{n}\rangle$<0.1/ pulse).

mode-sorting process. This effect is more noticeable in functions with narrow spectral features, such as superpositions of time bins or HG modes (shown in the Supplement 1), especially at higher orders, which benefit more from spectral filtering to reduce cross-talk. Additionally, HG modes and frequency bins in $d = 5$ need to be rescaled to fit within the same spectral bandwidth, as higher-order modes become spectrally broader.

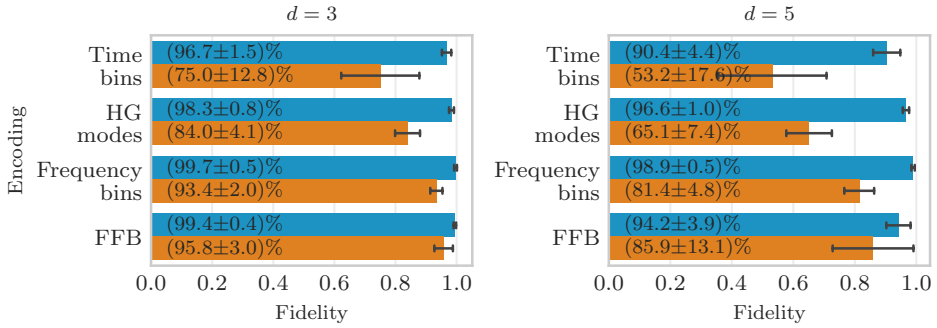

Fig. 5. Average fidelity of the measured POVMs to the ideal operators for each encoding alphabet in $d = 3$ (left) and $d = 5$ (right): time bins, HG modes, and frequency bins both with the standard and FFB approach detailed at the end of section 2. The blue bars represent the results of the measurements performed with the CCD spectrograph in output, corresponding to ideal filtering conditions, whereas the orange bars show the results of the ToF detection at the single-photon level ($\langle\hat{n}\rangle \leq 0.1$/pulse). The error bars indicate the standard deviation of the fidelity for different POVMs.

Frequency bins, however, maintain the same spectral features when building MUBs, and only change the relative phase between the different bins. This results in generally higher fidelity in all bases, visible in the high mean value and narrow spread in Fig. 5. The FFB approach increases the spectral bandwidth available for each mode, reducing measurement imperfections and, consequently, enhancing resilience to the low-resolution ToF spectrograph in output.

Nevertheless, the spectrograph must resolve the output frequencies corresponding to the different channels of the mQPG, separated by 0.5 THz or 0.63 THz in this work. If the spectrograph resolution is not significantly larger than this value, the readout system introduces cross-talk into the measurement. In fact, this additional cross-talk is the main source of error

Research Article | Vol. 33, No. 3 / 10 Feb 2025 / Optics Express 5585
Optics EXPRESS

for the highest-fidelity mode-sorting in $d = 5$ presented in this work, obtained with the FFB approach. Moreover, the larger spectral bandwidth achieved with this technique leads to narrower time durations, which necessitate precise synchronization of the pump and input in time and compensation for delay drifts caused, e.g., by temperature fluctuations. Namely, the FFB input states in $d = 5$ span a frequency range of 2 THz, requiring the time difference between the two pulses to be kept below 200 fs for optimal operation. Correcting the delay of the pulses and improving the spectrographic detection will increase stability and reduce errors, facilitating the scalability of the mQPG mode-sorter to even higher dimensions. Optimizing the spectral parameters for each encoding and dimensionality will further enhance the measurement fidelity, enabling high-quality programmable mode-sorting in a large number of high-dimensional bases.

5. Conclusion

We demonstrated a high-dimensional mode-sorter at the single-photon level based on an mQPG that can programmatically switch encoding alphabet between pulse modes, time bins and frequency bins. Our experimental results show an average measurement fidelity at the single-photon level of up to 0.958 ± 0.030 in $d = 3$ for three MUBs and 0.859 ± 0.131 in $d = 5$ for five MUBs, overcoming the previous dependence of the mQPG on strong output filtering. The mQPG-based mode sorter not only facilitates the practical realization of HD-QKD across various encoding alphabets, but also has the potential to function as a Hadamard receiver [8,9], enabling quantum communication protocols that go beyond QKD. By addressing technical challenges such as spectral bandwidth, synchronization, and spectrographic resolution, the measurement fidelity of the system can be improved to scale the mode-sorter to even higher dimensions. The presented results show that the mQPG provides an ideal platform for unlocking the benefits of high-dimensional encodings in quantum information science.

Funding. European Union Horizon 2020 Framework Programme; QuantERA (ERA-NET).

Acknowledgment. This research was supported by the EU H2020 QuantERA ERA-NET Cofund in Quantum Technologies project QuICHE. The authors thank A. Bhattacharjee for helpful discussions.

Disclosures. The authors declare no conflicts of interest.

Data availability. Data underlying the results presented in this paper are not publicly available at this time but may be obtained from the authors upon reasonable request.

Supplemental document. See Supplement 1 for supporting content.

References

1. H. J. Kimble, "The quantum internet," Nature **453**(7198), 1023–1030 (2008).
2. J. L. O'Brien, A. Furusawa, and J. Vučković, "Photonic quantum technologies," Nat. Photonics **3**(12), 687–695 (2009).
3. L. Sheridan and V. Scarani, "Security proof for quantum key distribution using qudit systems," Phys. Rev. A **82**(3), 030301 (2010).
4. S. Ecker, F. Bouchard, L. Bulla, *et al.*, "Overcoming Noise in Entanglement Distribution," Phys. Rev. X **9**(4), 041042 (2019).
5. B. Brecht, D. V. Reddy, C. Silberhorn, *et al.*, "Photon temporal modes: A complete framework for quantum information science," Phys. Rev. X **5**(4), 041017 (2015).
6. B. P. Lanyon, M. Barbieri, M. P. Almeida, *et al.*, "Simplifying quantum logic using higher-dimensional Hilbert spaces," Nat. Phys. **5**(2), 134–140 (2009).
7. F. Presutti, L. G. Wright, S. Y. Ma, *et al.*, "Highly multimode visible squeezed light with programmable spectral correlations through broadband up-conversion," (2024).
8. S. Guha, "Structured optical receivers to attain superadditive capacity and the holevo limit," Phys. Rev. Lett. **106**(24), 240502 (2011).
9. M. Rosati, A. Mari, and V. Giovannetti, "Multiphase hadamard receivers for classical communication on lossy bosonic channels," Phys. Rev. A **94**(6), 062325 (2016).
10. P. Folge, M. Stefszky, B. Brecht, *et al.*, "A framework for fully programmable frequency-encoded quantum networks harnessing multioutput quantum pulse gates," PRX Quantum **5**(4), 040329 (2024).
11. M. G. Raymer and I. A. Walmsley, "Temporal modes in quantum optics: then and now," Phys. Scr. **95**(6), 064002 (2020).

Research Article Vol. 33, No. 3 / 10 Feb 2025 / Optics Express 5586
Optics EXPRESS

12. H.-H. Lu, M. Liscidini, A. L. Gaeta, *et al.*, "Frequency-bin photonic quantum information," Optica **10**(12), 1655 (2023).
13. B. Qi, "Single-photon continuous-variable quantum key distribution based on the energy-time uncertainty relation," Opt. Lett. **31**(18), 2795–2797 (2006).
14. J. Mower, Z. Zhang, P. Desjardins, *et al.*, "High-dimensional quantum key distribution using dispersive optics," Phys. Rev. A **87**(6), 062322 (2013).
15. J. Nunn, L. J. Wright, C. Söller, *et al.*, "Large-alphabet time-frequency entangled quantum key distribution by means of time-to-frequency conversion," Opt. Express **21**(13), 15959–15973 (2013).
16. A. Widomski, S. Stopiński, K. Anders, *et al.*, "Precise on-chip spectral and temporal control of single-photon-level optical pulses," J. Lightwave Technol. **41**(19), 6255–6262 (2023).
17. B. Brecht, A. Eckstein, R. Ricken, *et al.*, "Demonstration of coherent time-frequency schmidt mode selection using dispersion-engineered frequency conversion," Phys. Rev. A **90**(3), 030302 (2014).
18. S. Barnett, *Quantum Information* (Oxford University Press, Inc., USA, 2009).
19. C. L. Morrison, F. Graffitti, P. Barrow, *et al.*, "Frequency-bin entanglement from domain-engineered down-conversion," APL Photonics **7**(6), 066102 (2022).
20. F. Chiriano, J. Ho, C. L. Morrison, *et al.*, "Hyper-entanglement between pulse modes and frequency bins," Opt. Express **31**(21), 35131 (2023).
21. L. Serino, W. Ridder, A. Bhattacharjee, *et al.*, "Orchestrating time and color: a programmable source of high-dimensional entanglement," Optica Quantum **2**(5), 339–345 (2024).
22. H.-H. Lu, J. M. Lukens, N. A. Peters, *et al.*, "Electro-optic frequency beam splitters and tritters for high-fidelity photonic quantum information processing," Phys. Rev. Lett. **120**(3), 030502 (2018).
23. H. H. Lu, N. A. Peters, A. M. Weiner, *et al.*, "Characterization of Quantum Frequency Processors," IEEE J. Sel. Top. Quantum Electron. **29**(6: Photonic Signal Processing), 1–12 (2023).
24. N. T. Islam, C. Cahall, A. Aragoneses, *et al.*, "Robust and stable delay interferometers with application to d-dimensional time-frequency quantum key distribution," Phys. Rev. Appl. **7**(4), 044010 (2017).
25. I. Vagniluca, B. Da Lio, D. Rusca, *et al.*, "Efficient time-bin encoding for practical high-dimensional quantum key distribution," Phys. Rev. Appl. **14**(1), 014051 (2020).
26. A. Widomski, M. Ogrodnik, and M. Karpiński, "Efficient detection of multidimensional single-photon time-bin superpositions," Optica **11**(7), 926–931 (2024).
27. L. Serino, J. Gil-Lopez, M. Stefszky, *et al.*, "Realization of a multi-output quantum pulse gate for decoding high-dimensional temporal modes of single-photon states," PRX Quantum **4**(2), 020306 (2023).
28. A. Eckstein, B. Brecht, and C. Silberhorn, "A quantum pulse gate based on spectrally engineered sum frequency generation," Opt. Express **19**(15), 13770–13778 (2011).
29. J. M. Donohue, V. Ansari, J. Řeháček, *et al.*, "Quantum-limited time-frequency estimation through mode-selective photon measurement," Phys. Rev. Lett. **121**(9), 090501 (2018).
30. V. Ansari, G. Harder, M. Allgaier, *et al.*, "Temporal-mode measurement tomography of a quantum pulse gate," Phys. Rev. A **96**(6), 063817 (2017).
31. These values have been adapted to the definition of fidelity used in this work, which differs from the one in [27] by a square root.
32. M. Combescure, "Circulant matrices, gauss sums and mutually unbiased bases, i. the prime number case," CUBO, A Mathematical Journal **11**, 73–86 (2009).
33. H. Bechmann-Pasquinucci and A. Peres, "Quantum cryptography with 3-state systems," Phys. Rev. Lett. **85**(15), 3313–3316 (2000).
34. D. Bruß and C. Macchiavello, "Optimal eavesdropping in cryptography with three-dimensional quantum states," Phys. Rev. Lett. **88**(12), 127901 (2002).
35. N. J. Cerf, M. Bourennane, A. Karlsson, *et al.*, "Security of quantum key distribution using d-level systems," Phys. Rev. Lett. **88**(12), 127902 (2002).
36. A. Monmayrant, S. Weber, and B. Chatel, "Phd tutorial: A newcomer's guide to ultrashort pulse shaping and characterization," Journal of Physics B-atomic Molecular and Optical Physics - J PHYS-B-AT MOL OPT PHYS **43**, (2010).
37. M. Avenhaus, A. Eckstein, P. J. Mosley, *et al.*, "Fiber-assisted single-photon spectrograph," Opt. Lett. **34**(18), 2873–2875 (2009).
38. J. S. Lundeen, A. Feito, H. Coldenstrodt-Ronge, *et al.*, "Tomography of quantum detectors," Nat. Phys. **5**(1), 27–30 (2009).
39. J. Gil-Lopez, M. Santandrea, G. Roland, *et al.*, "Improved non-linear devices for quantum applications," New J. Phys. **23**(6), 063082 (2021).

Supplemental Document

Optics EXPRESS

Programmable time-frequency mode-sorting of single photons with a multi-output quantum pulse gate: supplement

L. SERINO,[1,2,*] C. EIGNER,[2] B. BRECHT,[1,2] AND C. SILBERHORN[1,2]

[1] *Paderborn University, Integrated Quantum Optics, Warburgerstr. 100, Paderborn, Germany*
[2] *Paderborn University, Institute for Photonic Quantum Systems, Warburgerstr. 100, Paderborn, Germany*
[*] *laura.serino@upb.de*

Supplement DOI: https://doi.org/10.6084/m9.figshare.28060115

Parent Article DOI: https://doi.org/10.1364/OE.544206

Programmable time-frequency mode-sorting of single photons with a multi-output quantum pulse gate: supplemental document

In this supplemental document, we illustrate the spectra of the time-frequency modes used in the experiment, and we investigate the dimensional scalability of the "fancy" frequency bin (FFB) mode-sorting technique in a multi-output quantum pulse gate (mQPG).

1. DIMENSIONAL SCALABILITY

Here we investigate the scalability of the FFB mode-sorting method to higher dimensions. In d dimensions, this technique involves sorting d frequency bins and their superpositions into d distinct mQPG channels. In this simulated study, we consider an experimental setup analogous to the one presented in the main text, where a waveshaper "carves" the pump spectral bins from a fixed broadband laser pulse. In this system, the maximum width of each bin is limited by the initial spectral bandwidth $\Delta\nu_{\mathrm{Pump}}$ of the laser pulse and by the chosen dimensionality d.

Since broader frequency bins generally lead to a better performance of the mQPG [1, 2], this bandwidth constraint is a major source of error in the mode-sorting process. The operation of the mQPG is ideal when the spectral features of the pump pulse (i.e., the width of the pump bins) are significantly larger than the width of the phase-matching function $\Delta\nu_{\mathrm{PM}}$. For this reason, we study how the ratio between $\Delta\nu_{\mathrm{Pump}}$ and $\Delta\nu_{\mathrm{PM}}$ affects the average error of the mode-sorting process by simulating the mQPG projections in each possible mutually unbiased basis of a d-dimensional frequency-bin Hilbert space. We set the separation between the frequency bins to approximately 3 times the full-width-half-maximum of each bin. In the simulation, we assume ideal experimental conditions: perfect resolution for both the pump waveshaper and the output spectrograph, negligible second-order dispersion in the mQPG waveguide, and a constant relative delay between input and pump pulses.

The simulation results, shown in Fig. S1, provide an estimate of the performance the mQPG mode-sorter can ultimately achieve if all technological challenges are addressed. In the top left region of the plot, the mQPG requires too many phase-matching peaks within a narrow spectral range, causing the output channels to overlap and introducing additional cross-talk. The red line indicates the bandwidth ratio of the current experimental setup, based on a 4-cm-long lithium niobate mQPG waveguide and a 3-THz laser bandwidth, which could theoretically operate in 30 dimensions with a measurement error of 10%. A more broadband laser or a waveguide with narrower phase-matching peaks (achievable, e.g., by increasing the waveguide length) could enable high-quality mode-sorting in even higher dimensions. Beyond this point, practical limitations arise, such as the fragility of longer waveguides, which currently restrict the commercially available lithium niobate wafers to a maximum length of 10 cm, and group-velocity dispersion, which can limit the optimal frequency region for the mQPG process. These technical challenges could potentially be addressed through the introduction of resonant structures or alternative material platforms. Overall, our simulation demonstrates that the FFB technique can, in principle, enable high-dimensional operation with extremely low error rates, limited primarily by the technical quality of the experimental components, particularly their resolution and stability.

2. SPECTRAL REPRESENTATION OF THE ENCODING ALPHABETS

Figures S2 and S3 show, in frequency space, the input and pump modes from the fundamental encoding alphabet and one of the implemented superposition bases in $d = 3$ and $d = 5$, respectively.

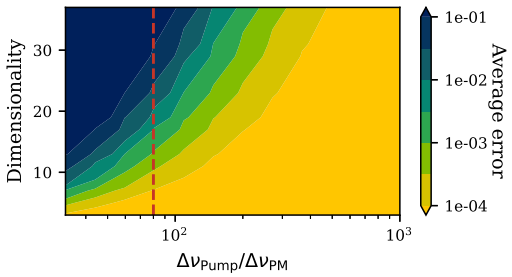

Fig. S1. Simulated error of the FFB technique in different dimensions as a function of the ratio between the available pump bandwidth $\Delta\nu_{\mathrm{Pump}}$ and the phase-matching bandwidth $\Delta\nu_{\mathrm{PM}}$.

REFERENCES

1. J. M. Donohue, V. Ansari, J. Řeháček, *et al.*, "Quantum-limited time-frequency estimation through mode-selective photon measurement," Phys. Rev. Lett. **121**, 090501 (2018).
2. L. Serino, J. Gil-Lopez, M. Stefszky, *et al.*, "Realization of a multi-output quantum pulse gate for decoding high-dimensional temporal modes of single-photon states," PRX Quantum **4**, 020306 (2023).

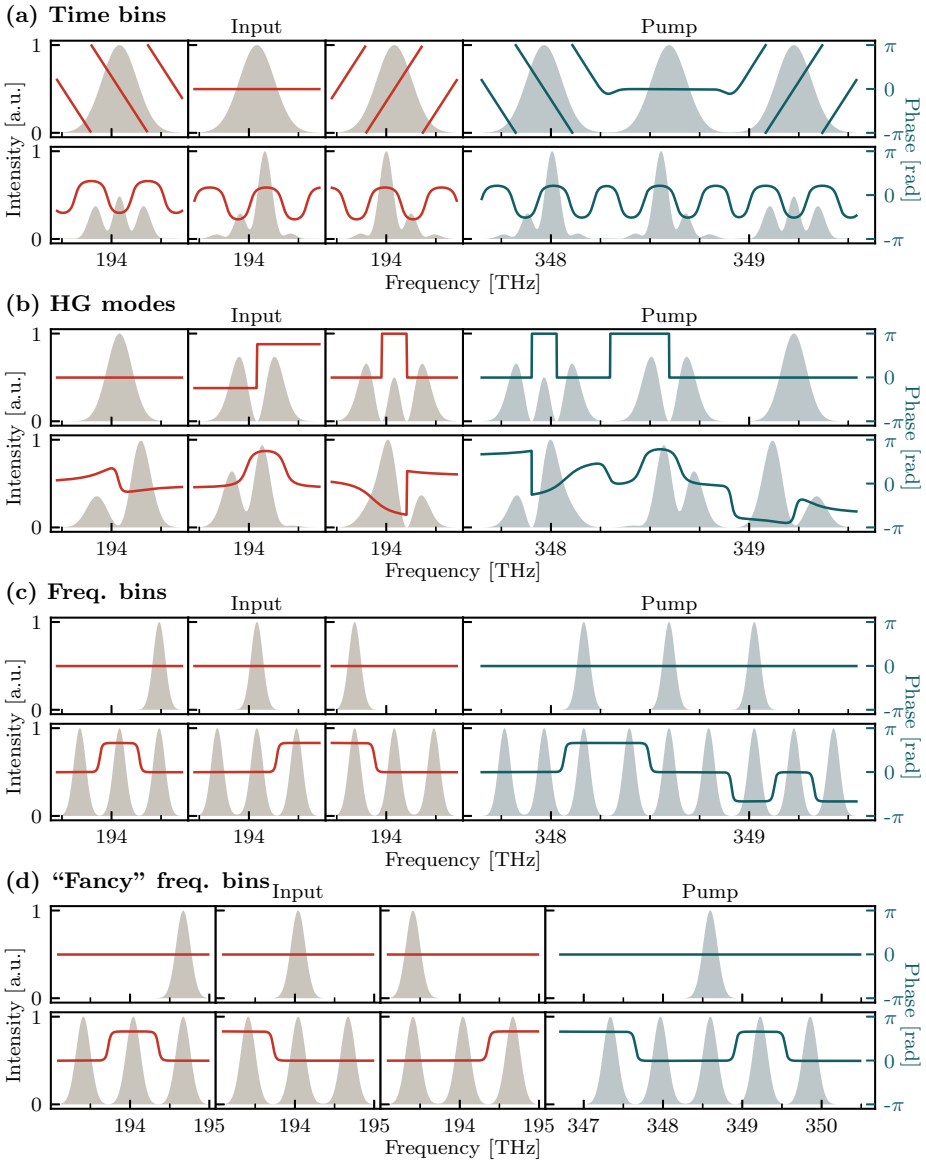

Fig. S2. Spectral intensity and phase of the fundamental basis (top) and one of the implemented superposition bases (bottom) of the different encodings used in $d = 3$: time bins, HG modes, frequency bins, and FFB approach. The red figures show the different possible input modes, whereas the blue figure on the right shows the pump spectrum that facilitates mode-sorting onto the corresponding basis.

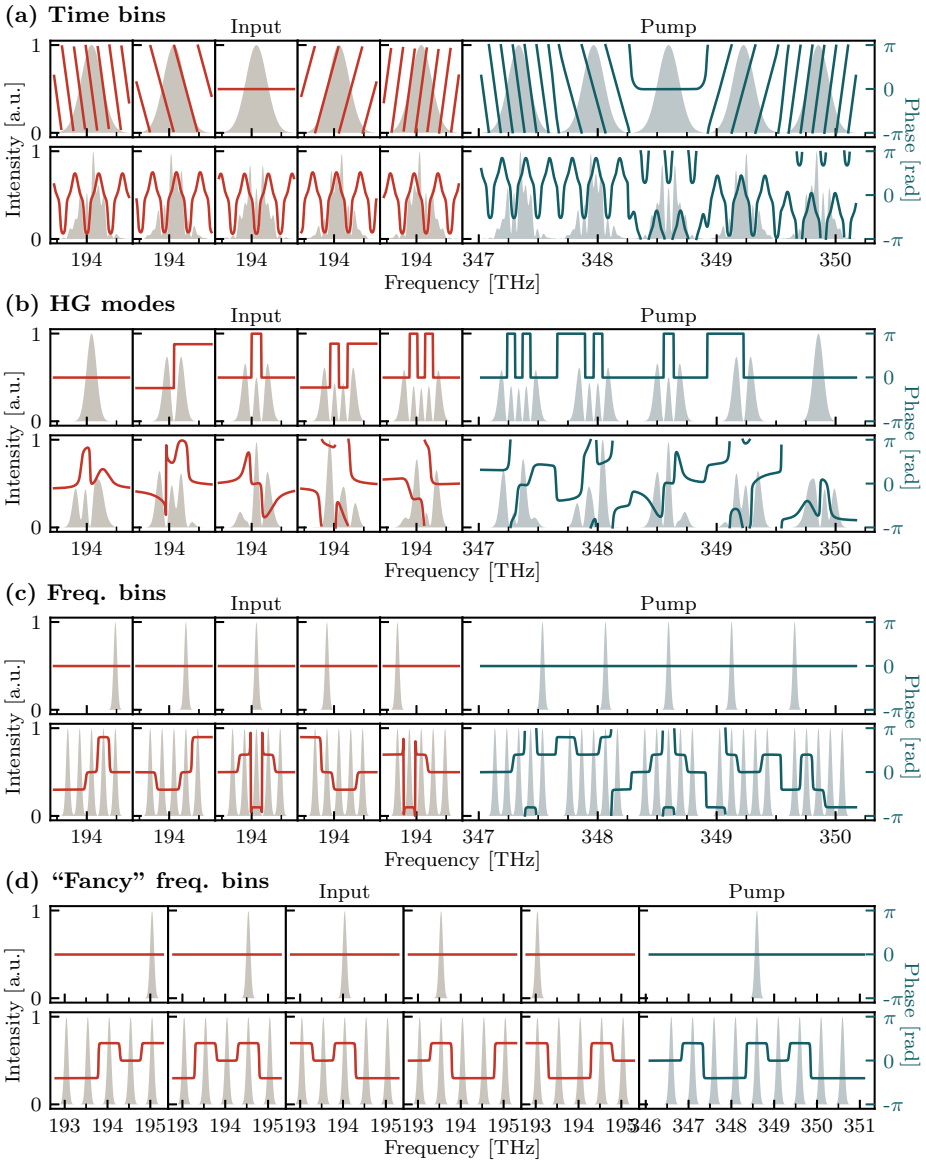

Fig. S3. Spectral intensity and phase of the fundamental basis (top) and one of the implemented superposition bases (bottom) of the different encodings used in $d = 5$: time bins, HG modes, frequency bins, and FFB approach. The red figures show the different possible input modes, whereas the blue figure on the right shows the pump spectrum that facilitates mode-sorting onto the corresponding basis.

5

Experimental HD-QKD

A crucial challenge in realizing the security and efficiency benefits of high-dimensional quantum key distribution [4, 5, 14, 37], as discussed in Chapter 1, is the implementation of a receiver capable of simultaneously projecting a single-photon state onto all elements of an arbitrary d-dimensional encoding basis. The mQPG, introduced in Chapter 4, was designed to be precisely such a high-dimensional quantum receiver.

In this chapter, we move beyond device characterization and integrate the mQPG into a complete quantum communication system. We present the experimental realization of a full proof-of-principle HD-QKD setup in $d = 3$, which incorporates all the necessary components of a functional QKD system, from state preparation to shot-by-shot high-dimensional decoding for key reconstruction. This system achieves an asymptotic key fraction that surpasses the fundamental limit of one bit per photon of qubit systems, showcasing the practical advantage of harnessing a larger Hilbert space. While our demonstration uses two MUBs in $d = 3$, the scheme can be straightforwardly extended to higher dimensions and additional MUBs due to the versatility of the mQPG, as demonstrated in Chapter 4.

5.1 Experimental realization

This demonstration is based on a prepare-and-measure HD-QKD protocol. We implement the three-dimensional extension of BB84 using two MUBs [26, 33, 37], as described in Section 1.4.2. In this protocol, Alice prepares a sequence

of qudits, chosen at random from two MUBs, and sends them to Bob through a quantum channel. Bob then measures the incoming states by projecting them onto one of the two bases, also chosen randomly.

The protocol is realized in $d = 3$ using states encoded as pulsed frequency bins, introduced in Section 2.1.3. The two MUBs are the computational basis Z, used as key-generating basis, and the superposition basis X, which serves as the control basis for error estimation. The Z basis consists of three orthogonal states $\{|Z_0\rangle, |Z_1\rangle, |Z_2\rangle\}$, each corresponding to a distinct Gaussian-shaped frequency bin with a FWHM of 70.7 GHz in intensity, and an inter-bin separation of 250 GHz. The X basis is composed of three states $\{|X_0\rangle, |X_1\rangle, |X_2\rangle\}$ which are equal-amplitude superpositions of the key basis states with different relative phases. The spectral profiles of these six states are shown in Figure 5.1.

The experimental setup is shown in Figure 5.2. On Alice's side, pulses from a mode-locked laser centered at 860 nm pump an optical parametric oscillator (OPO), generating signal pulses in the telecom C-band around 1550 nm. The six required states (from both the Z and X bases) are then prepared by spectrally shaping these telecom pulses using a commercial multi-channel waveshaper (Finisar WaveShaper 16000A). To enable the random shot-by-shot state preparation required by the protocol, the six state-preparation lines are actively switched using a custom-built 6×1 fast optical switch. This switch is composed of six parallel channels, each containing an acousto-optic modulator (AOM, Aerodiode 1550AOM-2) with a rise time of 9 ns. Each AOM, controlled by an arbitrary waveform generator (AWG, Aerodiode TOMBAK) via an RF driver (Aerodiode RFAOM-T-200), acts as a fast gate that opens for a brief window to allow a single pulse to pass. The system is programmed such that only one channel is open at any given time. The outputs of the six AOMs are then combined into a single-mode fiber using a binary tree of fiber couplers. Finally, the prepared pulses are attenuated to 0.25 photons/pulse at the output of Alice's station. A

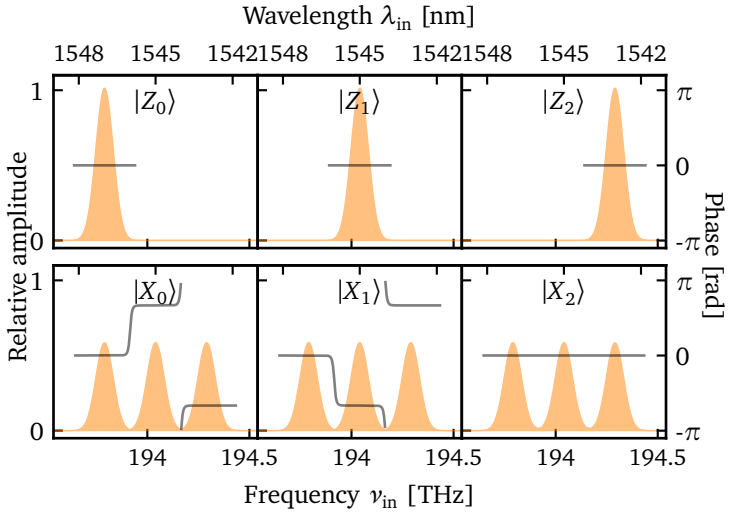

Figure 5.1: Spectra of the prepared states for the $d = 3$ HD-QKD protocol in the key basis $\{|Z_j\rangle\}$ (top) and in the control basis $\{|X_j\rangle\}$ (bottom).

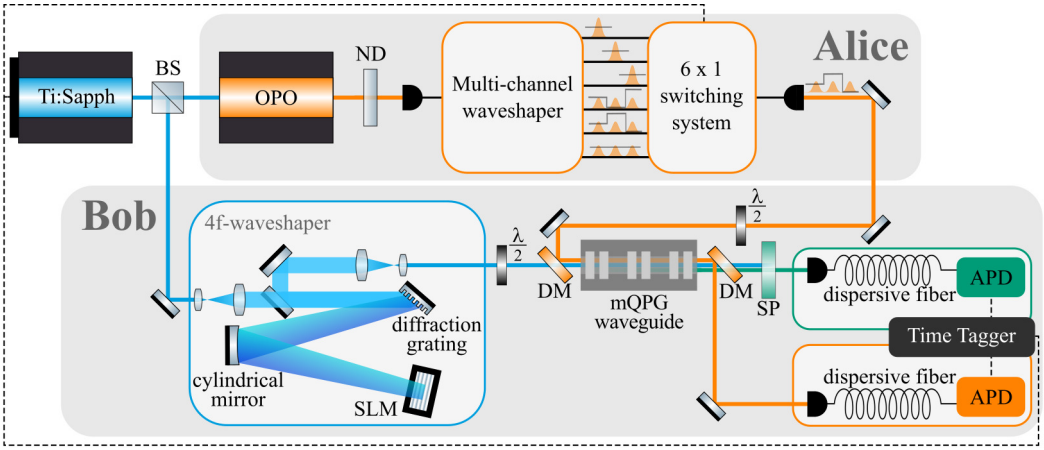

Figure 5.2: Schematic of the experimental setup. Alice prepares one of six possible states using broadband telecom light from an optical parametric oscillator (OPO), attenuated using a neutral density (ND) filter, and a multi-channel waveshaper. A fast optical switch selects the state for each time slot. The states are transmitted to Bob through a single-mode fiber followed by a short free-space link. Bob uses the mQPG and a time-of-flight (ToF) spectrograph to measure in the X basis; unconverted photons are isolated using a dichroic mirror (DM) and measured in the Z basis using another ToF spectrograph. Both ToF spectrographs are connected to the same time tagger, synchronized to the laser pulses.

combination of a half-wave plate (HWP) and a polarizing beamsplitter (PBS) is used to simulate variable channel loss for characterizing the system performance over different distances. The states then travel across a short free-space link to Bob's station.

At Bob's station, the incoming 1550 nm photons are coupled into a three-channel mQPG waveguide with an efficiency of approximately 70%. The mQPG is configured to measure in the X basis by shaping the pump pulses at 860 nm (tapped from the same laser that drives the OPO) into the frequency-bin superposition states to be measured. The shaped pump pulses have a power of 6 mW and are coupled into the mQPG waveguide with 50% efficiency. Input states matching the target $|X_j\rangle$ modes are up-converted to 552 nm photons and resolved by a time-of-flight (ToF) spectrograph for visible wavelengths (introduced in Chapter 4). Thus, a detection event in this spectrograph indicates a successful measurement in the X basis.

Since the conversion efficiency of the mQPG is $\eta \ll 100\%$, most photons are transmitted without conversion. This unconverted light, still at 1550 nm, is then routed to a second ToF spectrograph for telecom wavelengths which measures the frequency of the transmitted photons, effectively performing a projection onto the key basis Z. In this way, Bob's basis choice is implemented passively: a click in the visible ToF spectrograph corresponds to a measurement in basis X,

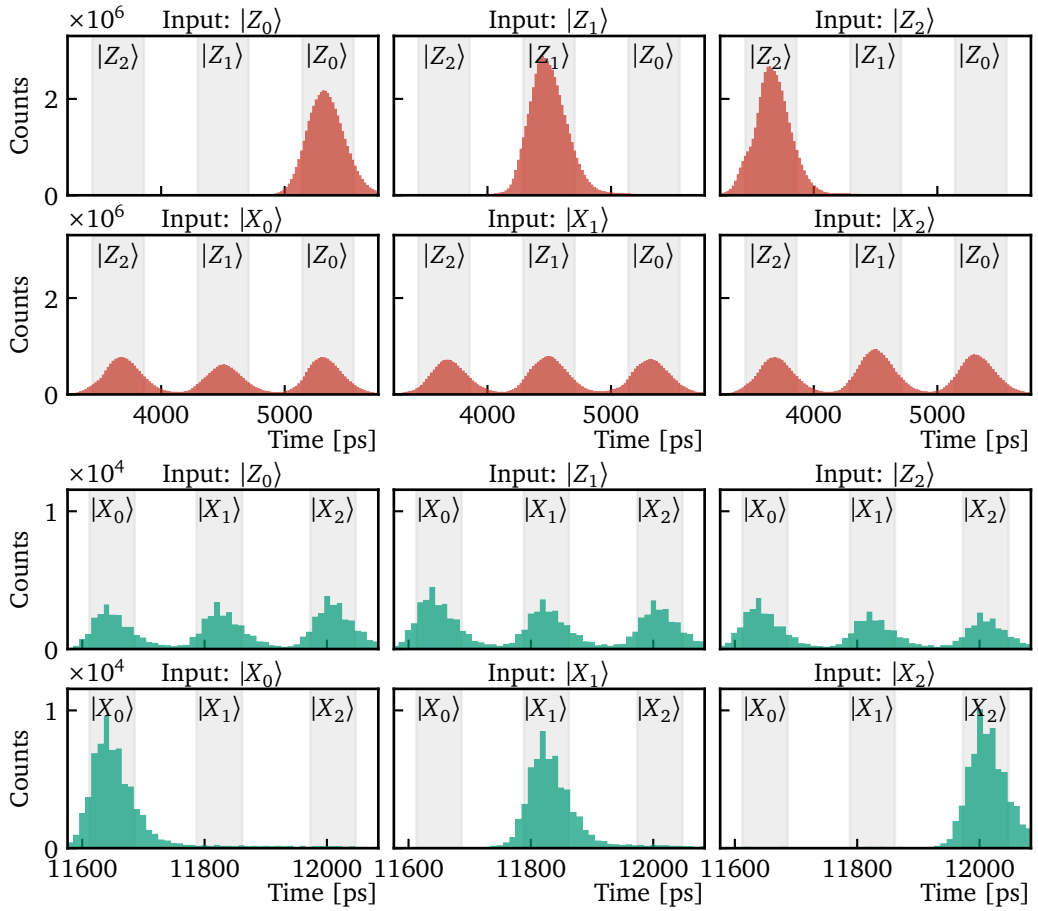

Figure 5.3: Histogram of the experimental sifted time tags from Bob's measurements in the Z (red) and X (green) bases, for all input states prepared by Alice, at a fixed channel loss. The gray areas indicate the timing windows assigned to each detection outcome.

whereas a click in the telecom ToF spectrograph corresponds to a measurement in basis Z.

The laser repetition rate of 80 MHz is downsampled to 40 MHz due to the speed limitations of the switching electronics, resulting in one communication shot every 25 ns. Alice prepares a pseudo-random sequence of 1980 states, repeated every 2000 shots (50 µs). Bob's detection events are recorded with a timetagger (Swabian Time Tagger X) synchronized to the laser clock, allowing us to correlate each detection to the state prepared by Alice. For each attenuation setting, we acquire data until approximately 10^8 total counts are collected in the Z basis, which requires from a few minutes up to 10 hours depending on the loss value.

Figure 5.3 shows the statistical distribution of the time tags measured by both ToF systems. Each measured timing is assigned to a specific detection outcome or discarded based on whether it falls into the assigned detection windows, selected as discussed in the next section.

5.2 Key rate analysis

After a long string of states has been exchanged, Alice and Bob would classically perform sifting, parameter estimation, and privacy amplification. For this proof-of-principle demonstration, we do not perform the full classical post-processing; instead, we acquire the raw detection data, perform sifting in post-processing, and use the measured QBERs to estimate the asymptotic secret key fraction, i.e., the number of secure bits extracted per sifted photon [17].

5.2.1 Asymptotic secret key rate

In the asymptotic limit of an infinitely long key, the secret key fraction r_∞ is given by the difference between the information Alice and Bob share and the maximum information an eavesdropper could have gained (see Section 1.4.3). For a d-dimensional protocol with two MUBs, this can be bounded as [37]:

$$r_\infty \geq \log_2(d) - H_d(Q_Z) - H_d(Q_X) \tag{5.2.1}$$

where $H_d(Q) = -Q\log_2(Q/(d-1)) - (1-Q)\log_2(1-Q)$ is the d-ary entropy function, and Q_Z and Q_X are the QBERs measured in the Z and X bases, respectively. If the errors are symmetric ($Q_Z = Q_X = Q$), this expression simplifies to the form seen previously in eq. (1.4.9) [33].

The performance of our system at different attenuation values is shown in Figure 5.4. At zero channel loss, we measure error rates of $Q_Z = 1.6\%$ and $Q_X = 3.8\%$, with negligible statistical fluctuations, which yield a secret key fraction of $r_\infty \geq 1.18$ bits per sifted photon. With the measured sifted detection rate in the Z basis of 106 kHz, this corresponds to a secure key rate of 125 kbit/s. This value surpasses the fundamental limit of 1 bit per photon for any equivalent qubit-based protocol, clearly demonstrating the practical advantage of using a higher-dimensional alphabet.

The asymptotic key fraction remains positive up to 14 dB of attenuation, equivalent to about 70 km of standard single-mode fiber with 0.2 dB/km loss. However, since real deployed fiber is more sensitive to noise and imperfections than laboratory setups, this distance represents an upper bound to the capabilities of the current implementation.

The observed asymptotic key fraction differs from the ideal value of $\log_2(3) \approx 1.58$ due to experimental imperfections. The dominant sources of error in the system are intrinsic crosstalk in the mQPG (discussed extensively in Chapter 4), delay drifts over the measurement time which affect the spectral phase, and pump-induced fluorescence at telecom wavelengths within the nonlinear waveguide. The latter introduces a loss-dependent error in both bases, as the noise photons may also be up-converted to visible wavelengths by the mQPG process.

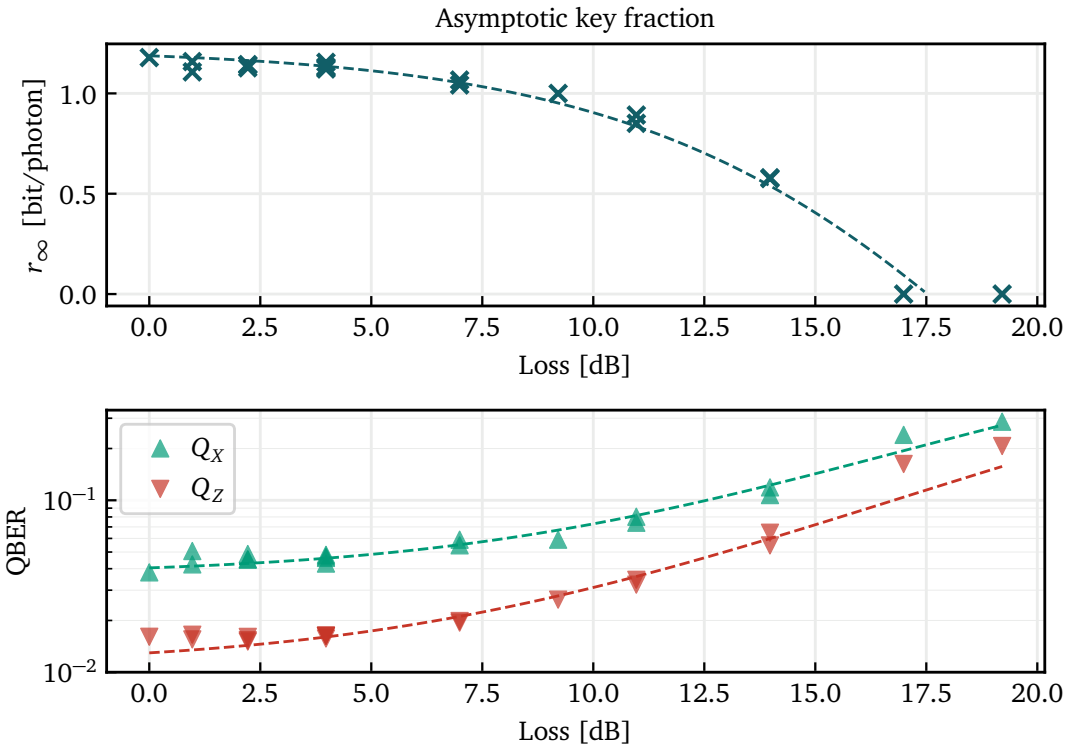

Figure 5.4: Asymptotic secret key fraction (top) and QBER (bottom) as a function of the channel loss. At zero channel loss we achieve $Q_Z = 1.6\%$ and $Q_X = 3.8\%$, yielding $r_\infty \geq 1.18$. The asymptotic key fraction remains positive up to 14 dB of attenuation. The dashed lines in the bottom plot are obtained by fitting the data using a simple model that assumes a constant detection error ratio in addition to a constant background noise. These fit results have been used to estimate the asymptotic key fraction trend (dashed line in the top plot).

5.2.2 Detection window optimization

Reducing the detection window size can mitigate noise, hence lowering the QBER; however, overly narrow windows also reject valid detection events, decreasing the sifted key rate. We studied this trade-off in both bases by varying the window width relative to the separation between detection peaks and observing its effects on the secret key rate, defined as the secret key fraction r_∞ multiplied by the sifted count rate in the Z basis (see Section 1.4.3). The results for two different loss values are shown in Figure 5.5.

The analysis reveals that the optimal parameters can depend on the loss. In the zero-loss case, we can achieve the largest key rate when the Z window is maximized, yielding the highest count rate, and when the X window is minimized, lowering the error. However, in a realistic scenario with a finite key length, decreasing the X window indefinitely would lead to insufficient statistics to estimate the QBER; therefore, we compromise by choosing a window width 40% of the separation between the output centers. In the high-loss case, the Z-basis noise becomes significant, lowering the secret key rate for larger windows.

Hence, we select a Z window half as wide as the channel spacing, sacrificing a few counts at low loss to improve performance at high attenuations. Finally, while we used a fixed detection window for all measurements, one could further optimize the secure key rate by adjusting the window size for each channel loss. However, a thorough security analysis would first be required to ensure that such an adaptive measurement strategy does not introduce new vulnerabilities to the protocol that could be exploited by an eavesdropper.

5.2.3 Beyond the asymptotic limit

While the asymptotic key fraction provides a useful benchmark, real-world QKD protocols are constrained by finite key lengths. In this regime, one must take into account statistical fluctuations, which lead to a reduction in the achievable key rate [37, 40]. A complete finite-key analysis requires precise accounting of the confidence intervals in the estimation of parameters such as the QBERs, which is a complex theoretical task for high-dimensional systems and is beyond the scope of this experimental work.

Another deviation from the ideal protocol in our experimental implementation is the use of weak coherent pulses instead of "true" single photon sources, which makes the system vulnerable to photon-number-splitting attacks. The standard countermeasure is the *decoy-state* method [41], where Alice randomly varies the intensity of her pulses, allowing Bob to detect changes in the photon number statistics. Although we have not implemented decoy states in this work, our fast-switching setup is fully compatible with this technique, which could readily be implemented by programming the AOMs to open only partially to modulate the mean photon number.

5.2.4 Security and future extensions

The physical implementation of a QKD system can introduce security loopholes not present in the theoretical protocol. In our implementation, the two bases are asymmetric due to the different detection setups. This asymmetry could potentially be exploited by an eavesdropper, who could devise states that are preferentially detected in one basis only. A more robust future implementation could address this by replacing the ToF system with a second mQPG dedicated to measurements in the key basis (either the fundamental frequency bin basis or another superposition basis), thereby creating a more symmetric and secure receiver. An even more streamlined approach might employ a single, high-efficiency mQPG with fast pump switching to choose the measurement basis dynamically on a shot-by-shot basis.

For a real-world HD-QKD link over deployed fiber, we must ensure accurate synchronization between the parties, and we must implement chromatic dispersion compensation to preserve the spectral phase over long fiber distances.

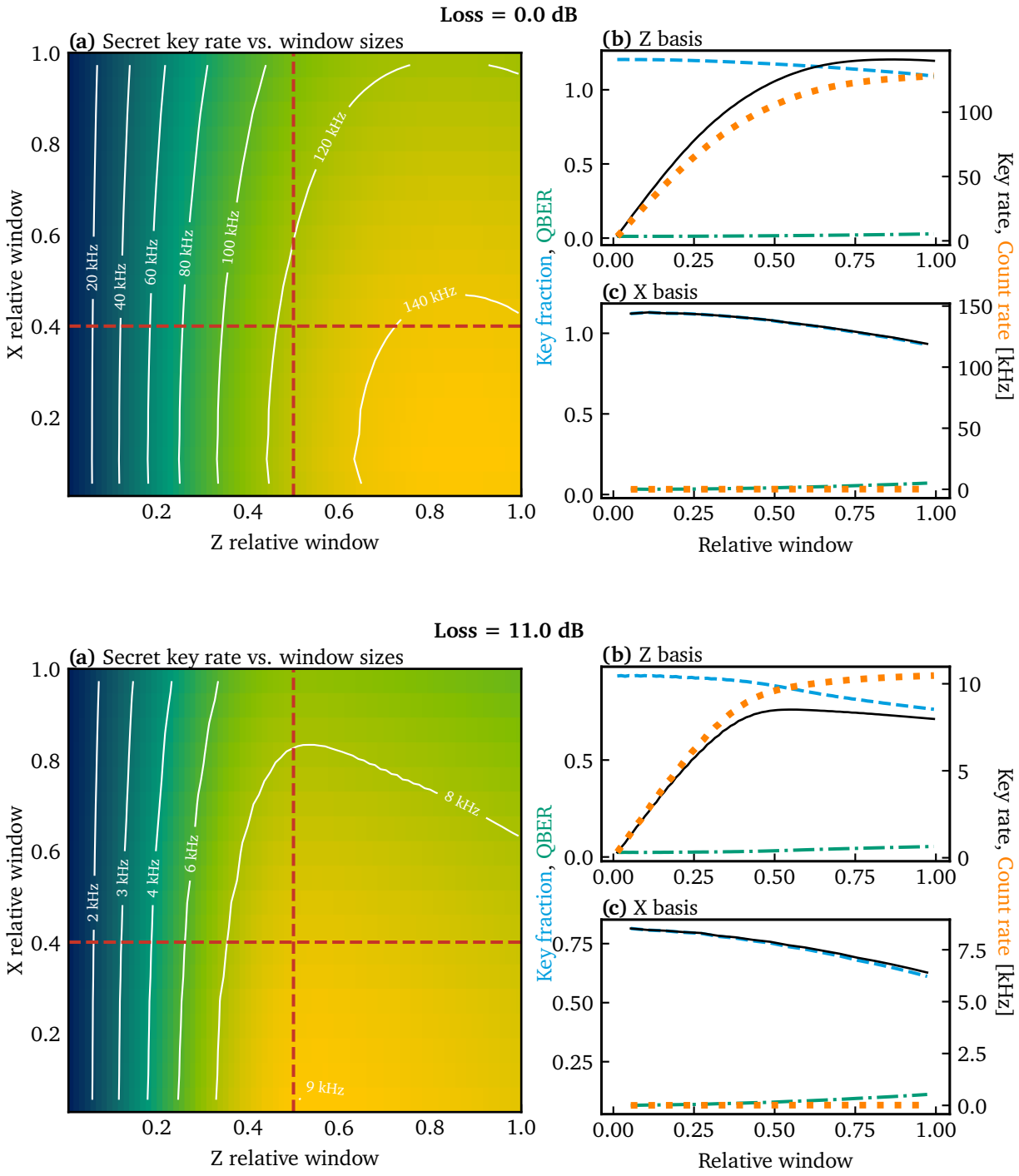

Figure 5.5: Effect of the detection window size on the key rate for 0 dB channel loss (top) and 11 dB channel loss (bottom). In each case, **(a)** shows the secret key rate as a function of the coincidence window; **(b)** shows the key fraction (blue), QBER (green), count rate (orange), and key rate (black) as a function of the Z-basis window, with fixed X window; **(c)** shows the same quantities as a function of the X-basis window, with fixed Z window. The red lines indicate the fixed window values used for the analysis.

Notably, phase stabilization of the channel is not required, since the mQPG is insensitive to global phase fluctuations, which significantly simplifies the stability requirements of a practical implementation.

5.3 Conclusion and outlook

We have successfully demonstrated a complete proof-of-principle HD-QKD system, achieving an asymptotic secret key fraction which surpasses the fundamental limit of qubit-based protocols. This result validates our experimental platform as a viable approach for practical high-dimensional quantum communication.

A key strength of our implementation lies in its flexibility: while this demonstration was performed in $d = 3$ using two bases, the mQPG decoder is fully reconfigurable, as shown in Chapter 4. This enables our system to be straightforwardly extended to higher dimensions and additional MUBs, enhancing the security and noise resilience of HD-QKD. Therefore, this work lays a foundation for future systems that can harness the full potential of high-dimensional quantum communication.

6

Entropic uncertainty relations in high dimensions

The key capability of the mQPG, demonstrated in Chapter 4, is its ability to perform a complete projective measurement on a user-chosen d-dimensional basis in a single shot. This unlocks the ability to experimentally investigate phenomena that require access to the full probability distribution of a measurement outcome in multiple bases. One of the most compelling applications enabled by this device is the direct experimental testing of entropic uncertainty relations in high-dimensional Hilbert spaces.

The experimental results and methodologies presented in this chapter are based on the following publications:

[arXiv:2507.05025 (2025)] L. Serino, G. Chesi, B. Brecht, L. Maccone, C. Macchiavello, and C. Silberhorn, "Experimental entropic uncertainty relations in dimensions three to five", *arXiv:2507.05025* (2025). DOI: 10.48550/arXiv.2507.05025

[Phys. Rev. Research 7, 033152 (2025)] L. Serino, G. Chesi, B. Brecht, L. Maccone, C. Macchiavello, and C. Silberhorn, "Complementarity-based complementarity", *Phys. Rev. Research* **7**, 033152 (2025). DOI: 10.1103/v24q-sl6n

6.1 MUBs and quantum uncertainty

In Chapter 1, we introduced the Shannon entropy as a measure of the information gained from a measurement, and MUBs as sets of measurement choices that are maximally incompatible, or complementary. The Heisenberg uncertainty principle [119] provides a fundamental limit on how precisely we can know the values of two complementary observables. This principle can be elegantly reformulated in the language of information theory, leading to so-called entropic uncertainty relations (EURs), which can be generalized to address two or more observables [120–123]. The total information that can be extracted, quantified by the sum of the individual Shannon entropies, is bounded by an EUR. An EUR provides a lower bound on the total uncertainty—and thus an upper limit on the total information—one can have about a quantum state when measuring it in multiple different MUBs.

These relations are not just a fundamental quantum mechanics curiosity, but have profound implications for the security of quantum cryptography and for quantum communication in general. A particularly interesting challenge is the search for "optimal states", that is, the specific input quantum states that minimize the total measurement uncertainty, thereby saturating the entropic bound [124, 125]. The nature of this challenge changes fundamentally with the number of measurement bases considered, as illustrated in Figure 6.1. When measuring in a single basis, the problem is trivial, as the eigenstates have zero uncertainty. As soon as one considers measurements in more MUBs, the problem transforms into a complex multi-parameter estimation task. For measurements in two MUBs in d dimensions, the Maassen-Uffink bound [124] limits the minimum uncertainty to $\log_2(d)$, but the optimal states that saturate this bound are still the simple eigenstates of either basis. The problem becomes far more complex when considering three or more MUBs simultaneously. In this multi-parameter scenario, the optimal state is no longer guaranteed to be an eigenstate but can be a non-trivial superposition, representing a complex compromise to minimize the total uncertainty across all measurement choices. This search becomes increasingly challenging and less intuitive in high dimensions, where EUR bounds and the corresponding minimum-uncertainty states for more than two MUBs have so far only been found numerically [125].

Experimentally demonstrating these bounds and identifying such states requires the ability to perform simultaneous projections onto all states of a given basis, as well as the reconfigurability to switch between different complete MUBs. This is precisely the capability that the mQPG provides. The first publication presented in this chapter, arXiv:2507.05025 (2025), is a collaborative work with the group of C. Macchiavello and L. Maccone at the University of Pavia dedicated to leveraging the mQPG to perform such measurements, experimentally

verifying EURs in a high-dimensional space and investigating the properties of these minimum-uncertainty states.

6.2 Inequivalent sets of MUBs and their effects on EURs

Beyond verifying established uncertainty relations, our experimental platform allows us to probe deeper, more subtle aspects of quantum complementarity that only arise in higher dimensions. In many high-dimensional spaces, sets of MUBs can exist in so-called *inequivalent* classes, meaning they cannot be transformed into one another by unitary operations [7, 23]. While this is a fascinating mathematical property, demonstrating any physical consequence of this inequivalence has been an outstanding experimental challenge, primarily due to the difficulty of performing the necessary complete projective measurements. Indeed, its first experimental proof for $d = 4$ came only recently [126] and used a method that is not easily scalable to higher dimensions.

In the second publication presented in this chapter, Phys. Rev. Research 7, 033152 (2025), we experimentally investigate a profound physical ramification of this mathematical curiosity, in another joint work with the group of C. Macchiavello and L. Maccone at the University of Pavia. Using the mQPG to measure the total entropic uncertainty for different complete sets of MUBs, we demonstrate that the fundamental uncertainty bound itself depends on *which* inequivalent class of MUBs is chosen for the measurement. This effect reveals that the very nature of quantum complementarity can differ depending on the measurement choices one makes, adding a new layer to our understanding of the uncertainty principle in high dimensions.

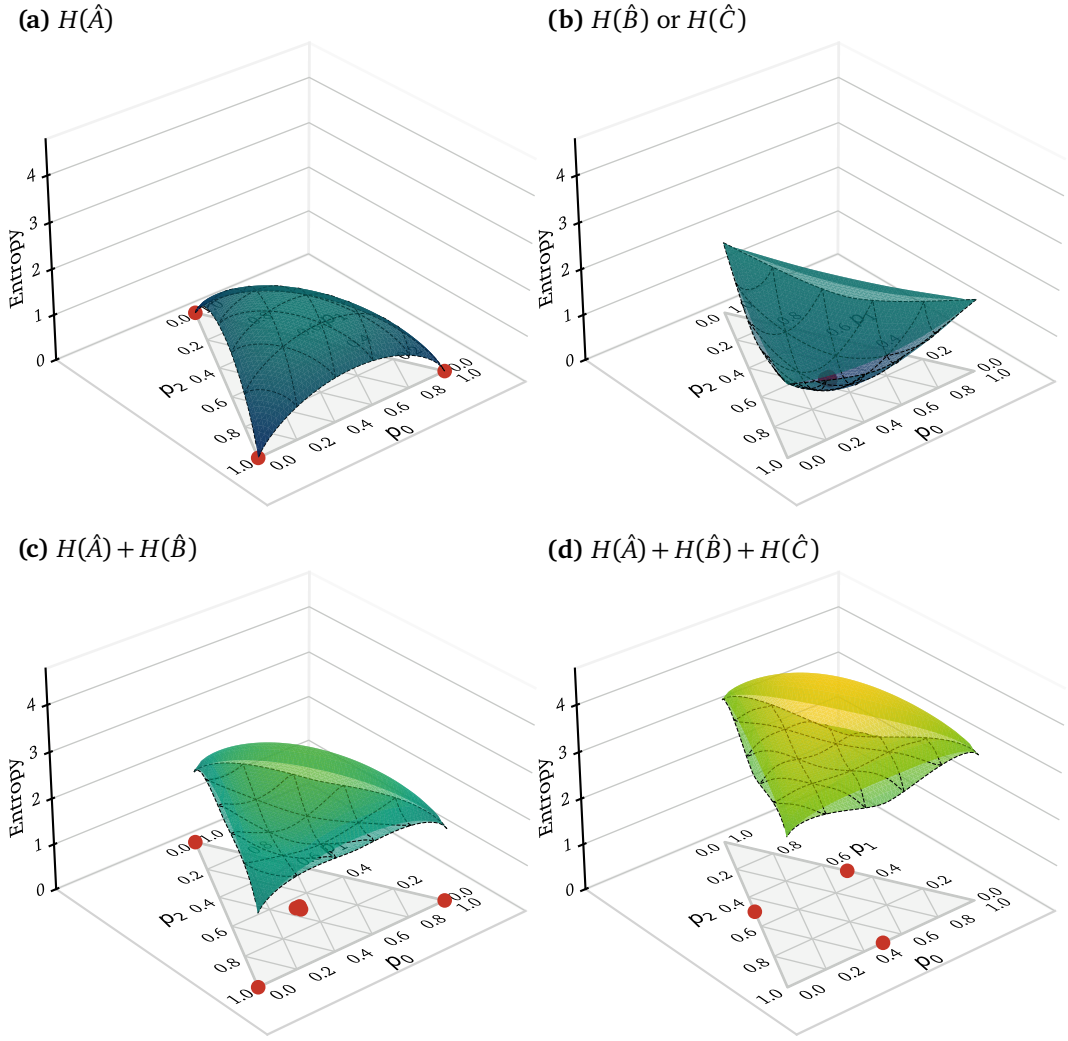

Figure 6.1: Illustration of EURs in different MUBs in $d = 3$. **(a)** When a state $|\psi\rangle = a_0|A_0\rangle + a_1|A_1\rangle + a_2|A_2\rangle$ is measured in the computational basis $\{|A_j\rangle\}_{j=0}^2$, corresponding to observable $\hat{A}$, the probability to obtain outcome j is $p_j = |a_j|^2$, with $p_0 + p_1 + p_2 = 1$. The entropy $H(\hat{A}) = -\sum_j p_j \log_2 p_j$ (eq. (1.1.1)) is minimized ($H(\hat{A}) = 0$) by eigenstates of $\hat{A}$ (red dots). **(b)** Similarly, the entropy in a MUB $\{|B_j\rangle\}_{j=0}^2$ is minimized by its own eigenstates. Since $\hat{A}$ and $\hat{B}$ are complementary, the states that minimize $H(\hat{A})$ maximize $H(\hat{B}) = 0$ and vice versa. **(c)** For measurements in two bases, the total entropy $H(\hat{A}) + H(\hat{B})$ is minimized by the eigenstates of either MUB [124]. **(d)** This changes when measuring in three MUBs: the state that minimize the total uncertainty $H(\hat{A}) + H(\hat{B}) + H(\hat{C})$ are superpositions of two of the three eigenstates from any given basis [125].

Experimental entropic uncertainty relations in dimensions three to five

Laura Serino,[1] Giovanni Chesi,[2] Benjamin Brecht,[1] Lorenzo Maccone,[2] Chiara Macchiavello,[2] and Christine Silberhorn[1]

[1]*Paderborn University, Integrated Quantum Optics, Institute for Photonic Quantum Systems (PhoQS), Warburger Str. 100, 33098 Paderborn, Germany*

[2]*QUIT Group, Physics Department, Univ. Pavia, INFN Sez. Pavia, Via Bassi 6, 27100 Pavia, Italy*

We provide experimental validation of tight entropic uncertainty relations for the Shannon entropies of observables with mutually unbiased eigenstates in high dimensions. In particular, we address the cases of dimensions $d = 3$, 4 and 5 and consider from 2 to $d + 1$ mutually unbiased bases. The experiment is based on pulsed frequency bins measured with a multi-output quantum pulse gate, which can perform projective measurements on a complete high-dimensional basis in the time-frequency domain. Our results fit the theoretical predictions: the bound on the sum of the entropies is never violated and is saturated by the states that minimize the uncertainty relations.

I. INTRODUCTION

The uncertainty principle was originally formulated by Heisenberg [1] to describe the fundamental limit on the precision of quantum measurements in terms of measurement disturbance, namely there exist measurements that irreversibly alter the state of the measured system. It was later generalized by Robertson [2] as a set of relations derived from the postulates of quantum mechanics and expressing measurement incompatibility, which describes sets of measurements that cannot be jointly performed. Notably, these two concepts remained distinct until very recently, when measurement incompatibility was shown to be a sufficient condition for disturbance [3].

The practical relevance of the uncertainty relations has historically evolved and grown with the development of modern quantum technologies. Today, in fact, establishing tight uncertainty bounds and identifying the states that saturate them are crucial for achieving the maximum precision limit in applications such as quantum cryptography, metrology and thermodynamics. Towards this end, uncertainty relations for two observables have been reformulated in terms of the Shannon entropy [4], leading to the so-called entropic uncertainty relations (EURs) [5–10]. Unlike the former Robertson bound, the entropic bounds are state-independent. Moreover, the EURs can be expressed in terms of Rényi entropies [9, 10], which generalize Shannon's entropy, thus providing many different measures of uncertainty.

The most well-known set of EURs is arguably the result by Maassen and Uffink [9], which quantifies the incompatibility between two observables. This bound is tight, meaning it can be saturated, if the two observables correspond to mutually unbiased bases (MUBs) [11, 12]. Extending this bound beyond two MUBs is of both theoretical and practical interest, motivated by the role of high dimensions and multipartite systems in quantum information protocols, as well as by fundamental questions on the complementarity of quantum observables. Since every physical system admits at least three MUBs and, in prime-power dimensions d, $d + 1$ MUBs are known to exist [11–13], the total number of uncertainty relations at a specific dimension can grow very large, amounting to $2(2^d - 1) - d$ in the latter case. Despite many efforts [10, 14–16], the analytic bounds found so far are either not tight or are tight only for specific dimensions and numbers of observables. However, numerical studies have obtained tight EUR bounds for up to $d + 1$ MUBs in dimensions 3, 4 and 5 [17].

Experimentally, the traditional Robertson formulation of the uncertainty principle has been validated in a plethora of different contexts—from position-momentum [18–21] and time-energy [22] relations to less conventional non-commuting observables such as number of Cooper pairs versus wavefunction phase in a superconductor [23]. These uncertainty relations are also implicitly tested every time the ultimate measurement precision bounds [24, 25] are assessed and applied [26–32]. Furthermore, stronger uncertainty relations based on variances have been devised [33, 34] and experimentally confirmed [35–38].

In contrast to the extensively verified Robertson formulation, entropic uncertainty relations have only more recently begun to be experimentally explored. Experiments testing EURs have focused on the later formulation of uncertainty relations in terms of measurement noise and disturbance [39] and entropies conditioned on a quantum memory [40]. These were verified for neutronic spin systems [41–43] and entangled photon pairs [44, 45]. More recently, new uncertainty relations formulated in terms of relative entropy have been devised and experimentally validated [46–48]. However, to date, no experiment has directly tested the high-dimensional entropic bounds predicted in [17]. This gap largely reflects the experimental challenges of operating with discrete high-dimensional Hilbert spaces, which require simultaneous measurements in all elements of a high-dimensional basis [49].

Here, we present the first experimental verification of all the EUR bounds predicted in [17] for dimensions 3, 4, and 5. We achieve this by encoding information in the time-frequency degree of freedom of photons, namely in pulsed frequency bins and their superpositions [50]. For this encoding, we can implement arbitrary projective measurements using a multi-output quantum pulse gate (mQPG) based on sum-frequency generation in a dispersion-engineered waveguide [51]. In particular, to verify the EUR bounds, we simultaneously project an input state onto all the elements of an arbitrary d-dimensional frequency-bin basis, selected through appropriate spectral shaping of the pump pulse driving the process.

Our experimental results verify the theoretically predicted entropic bounds for any number of MUBs in up to 5 dimensions, and confirm that these bounds are saturated by the states that, in Ref. [17], are found to minimize the EURs. These results complement our experimental investigation [52] of the effect of inequivalent classes of MUBs [12, 13] on EURs in dimension 5. Together, this work and [52] demonstrate the potential of our scalable setup to extend the verification of uncertainty relations to higher dimensions and detect further inequivalent sets of MUBs for $d > 5$.

The remainder of this paper is structured as follows. In Section II, we summarize the main results from [17]. In Section III we describe how we implement a set of MUBs in high dimensions and the experiment verifying the numerical tight bounds on the EURs. Then, we discuss our results and compare them to the theoretical predictions from [17] and to previously known bounds. Finally, in Section IV, we draw our conclusions.

II. FRAMEWORK

Here, we concisely report the uncertainty relations for which we are going to provide experimental validations. We focus on the formulation of EURs in terms of the Shannon entropy

$$H(\hat{O}) = -\sum_j p_j \log_2 p_j \,, \tag{1}$$

where $p_j = |\langle o_j|\psi\rangle|^2$ are the Born probabilities for the measurement of the observable $\hat{O}$, with eigenvectors $\{|o_j\rangle\}_j$, on a state $|\psi\rangle$.

In terms of the Shannon entropies of two observables $\hat{A}$ and $\hat{B}$, the Maassen-Uffink [9] bound reads

$$H(\hat{A}) + H(\hat{B}) \geq -\log c \,, \tag{2}$$

where $c \equiv \max_{j,k}|\langle a_k|b_j\rangle|^2$ is the maximum overlap between the eigenstates of $\hat{A}$ and $\hat{B}$, respectively $\{|a_k\rangle\}_k$ and $\{|b_j\rangle\}_j$. In a discrete Hilbert space of dimension d, this bound is tight, meaning that it can be saturated, if the eigenstates of $\hat{A}$ and $\hat{B}$ are mutually unbiased bases (MUBs) [11, 12], i.e., if $|\langle a_k|b_j\rangle| = 1/\sqrt{d} \quad \forall\, j,k \in [0,d)$.

Given a set of m observables $\{\hat{M}_k\}_{k=l_1}^{l_m}$ in dimension d with mutually unbiased eigenstates, the general expression of the addressed inequalities reads

$$\sum_{k=l_1}^{l_m} H(\hat{M}_k) \geq \mathcal{B}_{d,m} \,, \tag{3}$$

namely, the lower bound $\mathcal{B}$ on the sum of the Shannon entropies of the observables is specific for each d and m considered. However, in general, it is not unique: as mentioned in the Introduction, in the particular case with $d = 5$ and $m = 3$, there are two distinct bounds depending on the choice of the triple $\{l_1, l_2, l_3\}$. In our notation, l_j identifies the j-th MUB in the set $\{l_j\}_{j=1}^m$.

	$m=2$	$m=3$	$m=4$	$m=5$	$m=6$
$d=3$	$\log_2 3$	3	4	-	-
$d=4$	2	3	5	7	-
$d=5$	$\log_2 5$	$4.43 \vee 2\log_2 5$	6.34	8.33	10.25

Table I. Lower bounds $\mathcal{B}$ of the EURs in Eq. 3 for dimension d three to five and m MUBs.

We express the MUBs in terms of Hadamard matrices, following the construction in Refs. [12, 13]. The explicit form is reported in Appendix A. There, every matrix represents a basis, each column being a state of the pertaining basis, and $l_j \in \{A, B, ...\} \;\forall\, j \in [1, m]$. We report in Table I the lower bounds of the uncertainty relations in Eq. (3).

Firstly, we note that, if $m = 2$, then the Maassen-Uffink relation in Eq. (2) holds in any dimension, implying that the uncertainty is minimized by the eigenstates of the addressed observables, i.e., the states of the pertaining MUBs. Henceforth, we will inspect the saturation of the uncertainty relations in Eq. (3) for each dimension $d \in [3, 5]$ with $m > 2$.

In the case $d = 3$, the set of states $|\psi\rangle_{\rm opt}$ that saturates Eq. (3) is the same for both $m = 3$ and $m = 4$ and is given by

$$|\psi\rangle_{\rm opt} = \frac{|j_1\rangle + e^{i\phi}|j_2\rangle}{\sqrt{2}} \tag{4}$$

with $j_1, j_2 = 0, 1, 2$, $j_1 \neq j_2$ and $\phi = \pi/3, \pi, 5\pi/3$.

In dimension $d = 4$, the triples of Hadamard matrices that are mutually unbiased belong to a three-parameter family [12, 13]. However, there is a unique value for each of these parameters such that four and five MUBs can be constructed. We considered this case, where the complete set of MUBs can be obtained, which is reported in Appendix A 2. Differently from the case $d = 3$, the states saturating Eq. (3) depend on the choice of the observables [17]. However, the states that minimize the uncertainty of three and four observables, also minimize the one of the complete set of MUBs. For $m = 3$, if one of the MUBs is the computational basis (A in Appendix A 2), then the expression of the optimal states is the same as the one in Eq. (4), where the parameters $j_1, j_2 \in [0, 3]$ and $\phi \in \{\pm k\pi/2\}_{k=0}^2$ depend on the choice of the other two bases. We report in Table II the values of the parameters for this case. Conversely, if $A \notin \{l_1, l_2, l_3\}$, the optimal states, in terms of the eigenstates of the computational basis, read

$$|\psi\rangle_{\rm opt} = \frac{1}{2}\sum_{j=0}^{3} e^{i\phi_j}|j\rangle, \tag{5}$$

namely, they are defined by three of the four phases ϕ_j. In Table III we fix the phase $\phi_0 = 0$ and show the relative phases of the optimal states for each triple $\{l_1, l_2, l_3\}$. In the case $m = 4$, the states that are optimal for a set $\{\bar{l}_1, \bar{l}_2, \bar{l}_3, \bar{l}_4\}$ are the same that optimize the corresponding triplet $\{\bar{l}_1, \bar{l}_2, \bar{l}_3\}$, being $\bar{l}_4$ one of the two bases left. It is worth noting that the optimal states in Eq. (5) can be recast as the expression in Eq. (4), namely as the superposition of two states, by expanding $|\psi\rangle_{\rm opt}$ over a different basis. Therefore, the set of optimal states identified in Eq. (5) arises from our convention

$\{l_1,l_2,l_3\}$	$\{l_1,l_2,l_3,l_4\}$	j_1	j_2	ϕ
ABC	$ABCD$, $ABCE$	0	1	$0,\pi$
		2	3	$0,\pi$
ABD	$ABCD$, $ABDE$	0	2	$0,\pi$
		1	3	$0,\pi$
ABE	$ABCE$, $ABDE$	0	3	$0,\pi$
		1	2	$0,\pi$
ACD	$ABCD$, $ACDE$	0	3	$\pm\pi/2$
		1	2	$\pm\pi/2$
ACE	$ABCE$, $ACDE$	0	2	$\pm\pi/2$
		1	3	$\pm\pi/2$
ADE	$ABDE$, $ACDE$	0	1	$\pm\pi/2$
		2	3	$\pm\pi/2$

Table II. Optimal states $|\psi\rangle_{\rm opt}$ in Eq. (4) saturating the bounds $\mathcal{B}_{4,3}$ and $\mathcal{B}_{4,4}$ in the EURs of Eq. (3) for triples of MUBs including the computational basis A (first column) and for the corresponding quadruples (second column).

$\{l_1,l_2,l_3\}$	$\{l_1,l_2,l_3,l_4\}$	ϕ_1	ϕ_2	ϕ_3
BCD	$ABCD$, $BCDE$	$\pi/2$	$\pi/2$	0
		$-\pi/2$	$-\pi/2$	0
		$\pi/2$	$-\pi/2$	π
		$-\pi/2$	$\pi/2$	π
BCE	$ABCE$, $BCDE$	$\pi/2$	0	$\pi/2$
		$-\pi/2$	0	$-\pi/2$
		$\pi/2$	π	$-\pi/2$
		$-\pi/2$	π	$\pi/2$
BDE	$ABDE$, $BCDE$	0	$\pi/2$	$\pi/2$
		0	$-\pi/2$	$-\pi/2$
		π	$\pi/2$	$-\pi/2$
		π	$-\pi/2$	$\pi/2$
CDE	$ACDE$, $BCDE$	π	0	0
		0	π	0
		0	0	π
		π	π	π

Table III. Optimal states $|\psi\rangle_{\rm opt}$ in Eq. (5) saturating the bounds $\mathcal{B}_{4,3}$ and $\mathcal{B}_{4,4}$ in the EURs of Eq. (3) for triples of MUBs not including the computational basis A (first column) and for the corresponding quadruples (second column). We set $\phi_0 = 0$.

of adopting the computational basis to define $|\psi\rangle_{\rm opt}$, and the fundamental structure is the one in Eq. (4), with $|j_1\rangle$ and $|j_2\rangle$ states belonging to any of the five MUBs.

In dimension $d = 5$, there are two inequivalent sets of triples of MUBs [12, 13], implying the two distinct bounds in Table I for the case $m = 3$ [52]. The states achieving the bound $\mathcal{B}^{(1)}_{5,3} = 2\log_2 5 \simeq 4.64$ are the eigenstates of the observables involved in the uncertainty relation. The lower bound $\mathcal{B}^{(2)}_{5,3} \simeq 4.43$ featured by one of the two inequivalent sets, is obtained with the states

$$|\psi\rangle_{\rm opt} = \sum_{j=0}^{4} \psi_j e^{i\phi_j}|j\rangle \tag{6}$$

such that one of the coefficients ψ_j is null and the four coefficients left are pairwise equal. In Section III, we provide experimental proof only of the bound $\mathcal{B}^{(1)}_{5,3}$ corresponding to the MUB set analyzed in [17]. The second, inequivalent bound $\mathcal{B}^{(2)}_{5,3}$ was recently identified and verified in [52], where we also inspect the pertaining minimum uncertainty states.

For $m > 3$, there is a single equivalence class of sets of MUBs [13]. Thus, for each choice of the observables $\{\hat{M}_k\}_{k=l_1}^{l_m}$ in Eq. 3 we have a single bound $\mathcal{B}_{5,m}$. However, we have, again, that the uncertainty of different sets of observables is minimized by different states. With $m = 4$ and $m = 5$, the structure of $|\psi\rangle_{\rm opt}$ is the same as the one in Eq. 6. We found and experimentally tested nine optimal states in the case $m = 4$ for the MUBs $ABCD$ and five in the case $m = 5$ for $ABCDE$. In the former scenario, the states $|\psi\rangle_{\rm opt}$ are defined by coefficients $\psi_j \in \{0, 0.19, 0.68\}$ and phases $\phi_j \in \{\pm k\pi/5\}_{k=1}^{5}$, while, in the latter, by $\psi_j \in \{0, 0.11, 0.70\}$ and the same set of phases. Finally, in the case $m = 6$, the optimal states are given again by Eq. 4, with $j_1, j_2 \in [0, 4]$ and $\phi_j \in \{\pm(2k+1)\pi/5\}_{k=0}^{2}$.

III. EXPERIMENTAL VERIFICATION OF THE EURS WITH PULSED FREQUENCY BINS

A. Experiment

In the proposed experiment, we consider a Hilbert space constructed from pulsed frequency bins—-an encoding alphabet based on the time-frequency degree of freedom of photons [53]. The d-dimensional computational basis A consists of d broadband Gaussian frequency bins, each centered at a distinct frequency. The bases mutually unbiased to A are then generated by superimposing these frequency bins with phase relationships dictated by the Hadamard matrices $\{B, C, ...\}$ in Appendix A [50, 54, 55].

Experimentally, we can estimate the probability distribution required to calculate the entropy by normalizing the counts obtained from projecting multiple copies of the input states onto the selected MUBs. Thus, we require a device capable of simultaneously projecting states from this d-dimensional Hilbert space onto all elements of an arbitrarily chosen basis. In the time-frequency domain, this can be achieved using a multi-output quantum pulse gate (mQPG) [50, 51], a high-dimensional decoder for time-frequency pulsed modes based on sum-frequency generation in a dispersion-engineered waveguide. The projection basis is determined by shaping the spectrum of the pump pulse driving the process, and the outcome of the projection onto each basis element corresponds to a probability of detecting a click in a specific output channel, each defined by a distinct output frequency.

The mQPG operation is described by a positive-operator-valued measure (POVM) $\{\pi^\gamma\}$, where each POVM element π^γ describes the measurement operator of a single channel set to project onto mode γ [51, 56, 57]. Under ideal conditions, each channel performs perfect single-mode projections $\pi^\gamma = |\gamma\rangle\langle\gamma|$. However, experimental imperfections can lead

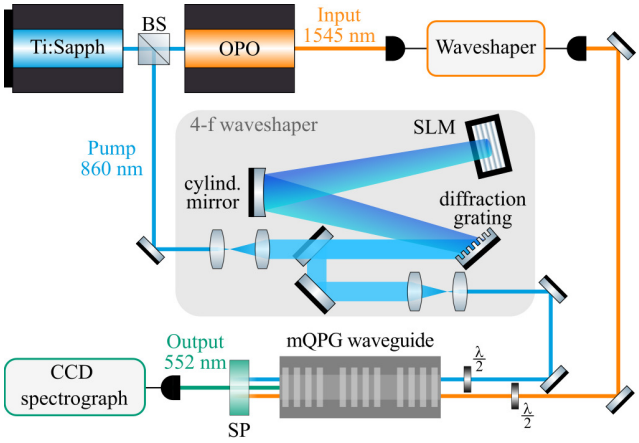

Figure 1. Schematic of the experimental setup. The signal and pump pulses, centered at 1545 nm and 860 nm respectively, are generated by a combination of a Ti:Sapphire ultrafast laser with an optical parametric oscillator (OPO). The signal pulse is shaped by a commercial waveshaper (Finisar 4000S) to generate the frequency-bin states in input. The remaining pump pulse, separated by a beam splitter (BS), is shaped as the full measurement basis using an in-house-built 4f-waveshaper consisting of a diffraction grating, a cylindrical mirror and a spatial light modulator (SLM). Both beams are coupled into the mQPG waveguide, where the signal is up-converted into the different output frequencies as a result of the mQPG projections. The output beam, centered at around 552 nm, is isolated using a short-pass (SP) filter and then detected by a commercial CCD spectrograph (Andor Shamrock 500i).

to systematic errors in the POVMs, which then are described by the more general expression $\pi^\gamma = \sum_{ij} m_{ij}^\gamma |a_i\rangle \langle a_j|$, with $|a_i\rangle$ and $|a_j\rangle$ eigenstates of the computational basis. When measuring a pure d-dimensional input state $\rho^\xi = |\xi\rangle\langle\xi|$, we will obtain output γ with probability $p^{\gamma\xi} = \mathrm{Tr}(\rho^\xi \pi^\gamma)$.

A schematic of the experimental setup is shown in Figure 1. The signal and pump pulses, centered at 1545 nm and 860 nm respectively, are generated by a combination of a Ti:Sapphire ultrafast laser with an optical parametric oscillator (OPO) at a repetition rate of 80 MHz. The signal pulse is shaped by a commercial waveshaper (Finisar 4000S) to generate the frequency-bin states in input, whereas the pump pulse is shaped by an in-house-built 4f-waveshaper to generate the d-dimensional frequency-bin basis for the measurement, with $d \in \{3, 4, 5\}$. Both beams are coupled into the mQPG waveguide, where the signal modes are up-converted into a different output channel based on their overlap with each pump mode, i.e., with each eigenstate of the chosen measurement basis. The output beam, centered at around 552 nm, is separated from the unconverted signal and pump beams by a shortpass filter and then detected by a commercial CCD spectrograph (Andor Shamrock 500i). This frequency-resolved detection allows us to separate the output channels, each centered at a distinct frequency. The number of counts detected at each output frequency indicates the number of photons measured in the corresponding mode.

For the experimental verification of the EURs found in [17]

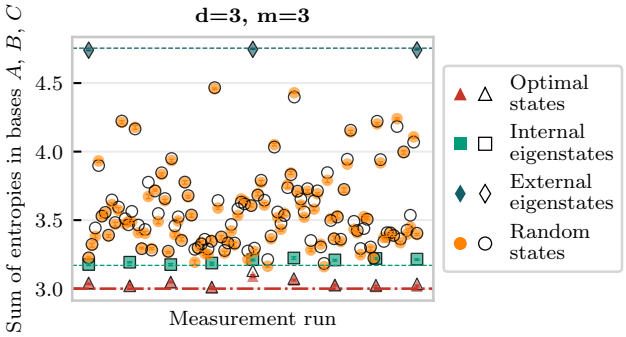

Figure 2. Sum of the entropy calculated in the MUBs A, B, C in d=3 for different types of input states: optimal states (red triangles), states from bases A, B, or C (green squares), states from the last MUB D (blue diamonds) and random states (yellow circles). The filled markers show the experimental data, whereas the hollow markers describe the predicted results based on the characterized imperfect POVMs. The dashed blue and green lines show the predicted entropy for the external and internal eigenstates, respectively. The red dash-dotted line indicates the EUR bound found in [17] for $d = 3$ and $m = 3$, which is saturated by the optimal states.

and in this work, we measure the entropy of a large sample of states for different combinations of m observables $\{\hat{M}_k\}_{k=l_1}^{l_m}$, with $2 \leq m \leq d+1$. We group the probed input states into four categories: *optimal states*, found in Ref. [17], which saturate the aforementioned entropy bounds; *internal* and *external eigenstates*, which are, respectively, the eigenstates of an observable in the set $\{\hat{M}_k\}_{k=l_1}^{l_m}$ appearing in the addressed uncertainty relation or of one of the complementary observables; *random states* generated by randomly sampling amplitude and phase coefficients from a uniform distribution. Although this method does not allow for truly uniform sampling of the parameter space, this is not relevant in the scope of this work, which concerns only the lower bound of the joint entropy distribution.

B. Results and discussion

For each probed input state and measurement basis, we calculate the entropy by estimating the probability p_i of each measurement outcome as the normalized counts in the corresponding channel. We obtain distributions of entropy values such as the one in Figure 2, which shows the sum of the entropy calculated in the first three MUBs in Appendix A for different input states from a three-dimensional Hilbert space. For each data point, the error bars indicate the 10%-90% spread of the entropy distribution obtained from a Monte Carlo simulation based on 500 samples extracted from the measured count statistics. The error bars are not visible in most points due to their narrow extent, indicating a small statistical error.

Figure 3 summarizes the experimental results for the sum of entropies $\sum_{k=l_1}^{l_m} H(\hat{M}_k)$ of d-dimensional input states measured over a set $\{\hat{M}_k\}_{k=l_1}^{l_m}$ of m MUBs, for all combinations

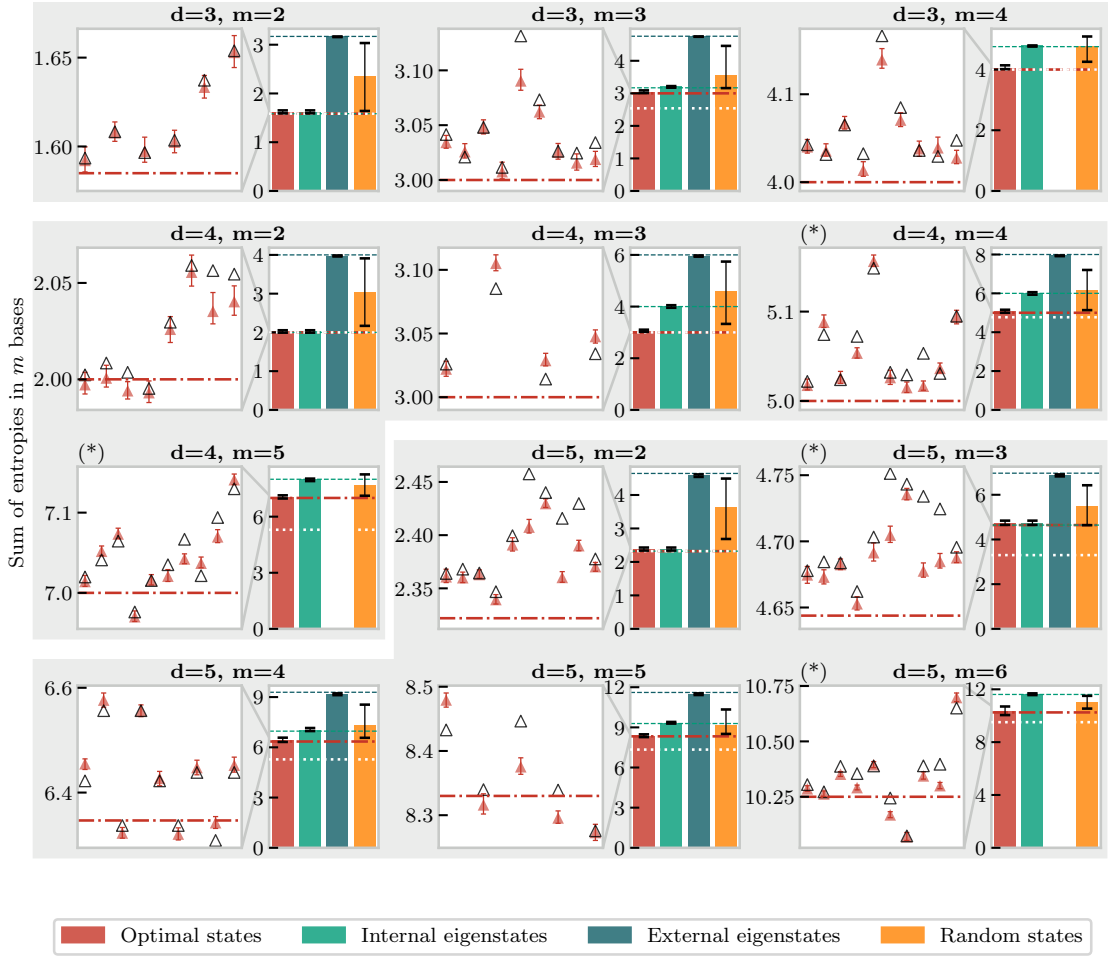

Figure 3. Measured sum of entropy in m MUBs for different dimensions d. For each combination of m and d, we only show the results for a single set of bases. Left: scatterplot showing the entropy of individual optimal states (filled triangles) and corresponding simulations (hollow triangles) in an enlarged scale. In the plots marked by (*) we only show the first ten optimal states out of a larger number of data. Right: barplot showing the mean value and the total spread of the sum of entropy for different sets of input states: from left to right, optimal states (red), internal eigenstates (green), external eigenstates (blue) and random states (yellow). The dashed blue and green lines show the predicted entropy for the external and internal eigenstates, respectively. The red dash-dotted line indicates the EUR bounds found in [17] and in [52], which is saturated by the optimal states. In contrast, the white dotted lines show the previously known EUR bounds prior to [17]. See the text for more information.

of $d \in \{3, 4, 5\}$ and $m \in \{3, \ldots, d+1\}$. The individual measurements of the optimal states are highlighted in the scatterplots in an enlarged scale. We only show the measurement results for a single set of bases for each combination of d and m, as the observed lower bounds are homogeneous over all sets of MUBs with the only exception of the case of $d = 5$ and $m = 3$. For this particular combination, in fact, we only considered a set of MUBs equivalent to the one in Ref. [17], and we verified that the EUR bound is saturated by the eigenstates of those MUBs, as expected. The case of the inequivalent set of MUBs, which leads to a different EUR bound, is analyzed in depth and experimentally verified in Ref. [52].

For each combination of d and m, the barplot shows the mean value of the sum of entropies for different sets of input states: from left to right, optimal states (red), internal eigenstates (green), external eigenstates (blue) and random states (yellow). The error bars mark the total spread of the data distribution. The results show that the optimal states saturate the entropy bounds (red dashdotted lines), while the internal eigenstates—with some exceptions—and external eigenstates do not, sitting at $(m-1)\log_2 d$ (green dashed line) and $m \log_2 d$ (blue dashed line), respectively. The exceptions are the cases with $m = 2$ and $(d = 5 \wedge m = 3)$, in which the internal eigenstates coincide with the optimal states, and the EUR bound is exactly $(m-1)\log_2 d$. In the case of random states, the mean sum of the entropies is always above the lower bound, as expected.

In the barplot, we also show (as dotted white lines) the analytic lower bounds known prior to the tight numeric ones of Ref. [17]. For $m = 2$, the bound from the Maassen-Uffink

uncertainty relation [9] is always tight. For $2 < m < d+1$, the bound found in Ref. [16] is tight only in the case $(d = 4 \wedge m = 3)$. While this is still the best analytic bound for $(d = 3 \wedge m = 3)$, $(d = 4 \wedge m = 4)$, $(d = 5 \wedge m = 3)$, $(d = 5 \wedge m = 4)$ and $(d = 5 \wedge m = 5)$, it fails to saturate the EURs. The bound found in Ref. [14] for $m = d+1$ is tight in the case $(d = 3 \wedge m = 4)$, but it is weak for $(d = 4 \wedge m = 5)$ and $(d = 5 \wedge m = 6)$. We find that our experimental data confirms these predictions, reaching the bound from [17] but not the previous bound when it is not tight.

In general, all data sets match very closely the theoretical predictions, with only minor discrepancies. However, one could be concerned that in some cases the statistical error bar is significantly smaller than this discrepancy, resulting in some data points that appear to violate the lower entropy bound. The small difference between the theoretical and measured entropy values can be explained considering the systematic error in the detection system. To verify this, we characterized the performance of the mQPG-based decoder through a quantum detector tomography [51, 58, 59] to reconstruct the true POVMs. We observed a measurement error (cross-talk) ranging from 0.1% to 2%, depending on the considered basis and dimension, with larger d generally leading to higher errors. From the reconstructed POVMs, we calculated the expected entropy that one would observe measuring the probed input states with this imperfect system, obtaining the hollow markers in Figure 2. These estimates very closely match the measured values, confirming that discrepancies with the theoretical predictions are to be attributed to the detection system.

IV. CONCLUSIONS

We provided the first experimental verification of the EURs for dimensions 3, 4 and 5, introduced in Ref. [17], in the Hilbert space formed by pulsed frequency bins and their superpositions. By performing high-dimensional time-frequency projections through an mQPG, we have probed several input states, measured their superpositions with the MUBs and retrieved the sum of the Shannon entropies of the pertaining observables $\{\hat{M}_k\}_{k=l_1}^{l_m}$ for every number of MUBs $m \in [2, d+1]$. In the case $m = 2$, our results reproduce the Maassen-Uffink uncertainty relations for Shannon entropies. Where $m > 2$, we verified that the optimal states described in Ref. [17] minimize the EURs for each d and m, and that the bounds assessed there are not achived nor violated by any other input state. Simulations based on the reconstructed POVMs of the detector have shown that the small discrepancies from the theory are explained by systematic measurement errors.

The key element that enabled this experimental verification resided in the capability of the mQPG to perform simultaneous projections onto all elements of the selected basis. It is worth noting that, while this work focused on the EUR bounds in dimension up to $d = 5$ shown in Ref. [17], the experimental setup can be straightforwardly adapted to operate in larger dimensions [50, 60], facilitating the experimental verification of possible EUR bounds in higher-dimensional Hilbert spaces and even enabling the detection of inequivalent sets of MUBs [52].

These results mark an important step toward the realization of quantum communication systems in high dimensions. A remarkable example is the one of discrete-variable quantum key distribution, where high-dimensional encodings offer increased secret key rates and resilience to noise [61], and unconditional security in real-world implementations can be guaranteed if the number of secret bits of the key is bounded via suitable EURs [62]. Additionally, extending the EURs tested in this work to entropies conditioned on a quantum memory [40] will enable novel entanglement-based high-dimensional QKD protocols, which can be implemented using a scheme similar to the one employed here [53].

V. ACKNOWLEDGEMENTS

The authors acknowledge support from the EU H2020 QuantERA ERA-NET Cofund in Quantum Technologies project QuICHE. G.C. acknowledges support from from the PNRR MUR Project PE0000023-NQSTI. C.M. acknowledges support from the PRIN MUR Project 2022SW3RPY. L.M. acknowledges support from the PRIN MUR Project 2022RATBS4 and from the U.S. Department of Energy, Office of Science, National Quantum Information Science Research Centers, Superconducting Quantum Materials and Systems Center (SQMS) under Contract No. DE-AC02-07CH11359.

Appendix A: Explicit expression of the MUBs in terms of Hadamard matrices

Following Ref. [13], here we report the Hadamard matrices defining MUBs in dimensions 3, 4 and 5. Each matrix represents a basis, where the columns are the pertaining orthonormal states.

1. $d = 3$

Complete set of MUBs in dimension $d = 3$.

$$A = \begin{pmatrix} 1 & 0 & 0 \\ 0 & 1 & 0 \\ 0 & 0 & 1 \end{pmatrix} \qquad B = \frac{1}{\sqrt{3}} \begin{pmatrix} 1 & 1 & 1 \\ 1 & \omega & \omega^2 \\ 1 & \omega^2 & \omega \end{pmatrix}$$

$$C = \frac{1}{\sqrt{3}} \begin{pmatrix} 1 & 1 & 1 \\ \omega^2 & \omega & 1 \\ 1 & \omega & \omega^2 \end{pmatrix} \qquad D = \frac{1}{\sqrt{3}} \begin{pmatrix} 1 & 1 & 1 \\ \omega & \omega^2 & 1 \\ 1 & \omega^2 & \omega \end{pmatrix}$$

with

$$\omega \equiv \exp\left(i\frac{2}{3}\pi\right).$$

2. $d = 4$

Complete set of MUBs in dimension $d = 4$.

$$A = \begin{pmatrix} 1 & 0 & 0 & 0 \\ 0 & 1 & 0 & 0 \\ 0 & 0 & 1 & 0 \\ 0 & 0 & 0 & 1 \end{pmatrix} \quad B = \frac{1}{2} \begin{pmatrix} 1 & 1 & 1 & 1 \\ 1 & 1 & -1 & -1 \\ 1 & -1 & -1 & 1 \\ 1 & -1 & 1 & -1 \end{pmatrix}$$

$$C = \frac{1}{2} \begin{pmatrix} 1 & 1 & 1 & 1 \\ 1 & 1 & -1 & -1 \\ -i & i & i & -i \\ i & -i & i & -i \end{pmatrix}$$

$$D = \frac{1}{2} \begin{pmatrix} 1 & 1 & 1 & 1 \\ i & -i & i & -i \\ -1 & -1 & 1 & 1 \\ i & -i & -i & i \end{pmatrix}$$

$$E = \frac{1}{2} \begin{pmatrix} 1 & 1 & 1 & 1 \\ i & -i & i & -i \\ i & -i & -i & i \\ -1 & -1 & 1 & 1 \end{pmatrix}$$

3. $d = 5$

Complete set of MUBs in dimension $d = 5$.

$$A = \begin{pmatrix} 1 & 0 & 0 & 0 & 0 \\ 0 & 1 & 0 & 0 & 0 \\ 0 & 0 & 1 & 0 & 0 \\ 0 & 0 & 0 & 1 & 0 \\ 0 & 0 & 0 & 0 & 1 \end{pmatrix} \qquad B = \frac{1}{\sqrt{5}} \begin{pmatrix} 1 & 1 & 1 & 1 & 1 \\ 1 & \omega & \omega^2 & \omega^3 & \omega^4 \\ 1 & \omega^2 & \omega^4 & \omega & \omega^3 \\ 1 & \omega^3 & \omega & \omega^4 & \omega^2 \\ 1 & \omega^4 & \omega^3 & \omega^2 & \omega \end{pmatrix}$$

$$C = \frac{1}{\sqrt{5}} \begin{pmatrix} 1 & 1 & 1 & 1 & 1 \\ \omega & \omega^2 & \omega^3 & \omega^4 & 1 \\ \omega^4 & \omega & \omega^3 & 1 & \omega^2 \\ \omega^4 & \omega^2 & 1 & \omega^3 & \omega \\ \omega & 1 & \omega^4 & \omega^3 & \omega^2 \end{pmatrix}$$

$$D = \frac{1}{\sqrt{5}} \begin{pmatrix} 1 & 1 & 1 & 1 & 1 \\ \omega^3 & \omega^4 & 1 & \omega & \omega^2 \\ \omega^2 & \omega^4 & \omega & \omega^3 & 1 \\ \omega^2 & 1 & \omega^3 & \omega & \omega^4 \\ \omega^3 & \omega^2 & \omega & 1 & \omega^4 \end{pmatrix}$$

$$E = \frac{1}{\sqrt{5}} \begin{pmatrix} 1 & 1 & 1 & 1 & 1 \\ \omega^2 & \omega^3 & \omega^4 & 1 & \omega \\ \omega^3 & 1 & \omega^2 & \omega^4 & \omega \\ \omega^3 & \omega & \omega^4 & \omega^2 & 1 \\ \omega^2 & \omega & 1 & \omega^4 & \omega^3 \end{pmatrix}$$

$$F = \frac{1}{\sqrt{5}} \begin{pmatrix} 1 & 1 & 1 & 1 & 1 \\ \omega^4 & 1 & \omega & \omega^2 & \omega^3 \\ \omega & \omega^3 & 1 & \omega^2 & \omega^4 \\ \omega & \omega^4 & \omega^2 & 1 & \omega^3 \\ \omega^4 & \omega^3 & \omega^2 & \omega & 1 \end{pmatrix}$$

with

$$\omega \equiv \exp\left(i\frac{2}{5}\pi\right).$$

[1] W. Heisenberg, Z. Phys. **42**, 172 (1927).
[2] H. P. Robertson, Phys. Rev. **34**, 163 (1929).
[3] M. Erba, P. Perinotti, D. Rolino, and A. Tosini, Phys. Rev. A **109**, 022239 (2024).
[4] I. I. Hirschman, Am. J. Math. **79**, 152 (1957).
[5] W. Beckner, Ann. Math **102**, 159 (1975).
[6] I. Biał ynicki Birula and J. Mycielski, Commun, math. Phys. **44**, 129 (1975).
[7] D. Deutsch, Phys. Rev. Lett. **50**, 631 (1983).
[8] K. Kraus, Phys. Rev. D **35**, 3070 (1987).
[9] H. Maassen and J. B. M. Uffink, Phys. Rev. Lett. **60**, 1103 (1988).
[10] P. J. Coles, M. Berta, M. Tomamichel, and S. Wehner, Rev. Mod. Phys. **89**, 015002 (2017).
[11] W. K. Wootters and B. D. Fields, Ann. Phys. **191**, 363 (1988).
[12] T. Durt, B.-G. Englert, I. Bengtsson, and Życzkowski, Int. J. Quantum Inf. **8**, 535 (2010).
[13] S. Brierley, S. Weigert, and I. Bengtsson, Quantum Inf. Comput. **10**, 0803 (2010).
[14] I. D. Ivanovic, J. Phys. A **25**, L363 (1992).
[15] J. Sánchez-Ruiz, Phys. Lett. A **201**, 125 (1995).
[16] A. Azarchs, arXiv:quant-ph/0412083 (2004).
[17] A. Riccardi, C. Macchiavello, and L. Maccone, Phys. Rev. A **95**, 032109 (2017).
[18] C. G. Shull, Phys. Rev. **179**, 752 (1969).
[19] J. A. Leavitt and F. A. Bills, Am. J. Phys. **37**, 905 (1969).
[20] O. Nairz, M. Arndt, and A. Zeilinger, Phys. Rev. A **65**, 032109 (2002).
[21] M. Fernández Guasti, Phys. Lett. A **448**, 128332 (2022).
[22] P. Szriftgiser, D. Guéry-Odelin, M. Arndt, and J. Dalibard, Phys. Rev. Lett. **77**, 4 (1996).
[23] W. J. Elion, M. Matters, U. Gelgenmüller, and J. E. Mooij, Nature **371**, 594 (1994).
[24] V. Giovannetti, S. Lloyd, and L. Maccone, Science **306**, 1330 (2004).
[25] V. Giovannetti, S. Lloyd, and L. Maccone, Phys. Rev. Lett. **96**, 010401 (2006).
[26] M. D. LaHaye, O. Buu, B. Camarota, and K. C. Schwab, Science **304**, 74 (2004).
[27] T. Nagata, R. Okamoto, J. L. O'Brien, K. Sasaki, and S. Takeuchi, Science **316**, 726 (2007).
[28] A. Schliesser, O. Arcizet, R. Rivière, G. Anetsberger, and T. J. Kippenberg, Nature Phys. **5**, 509 (2009).
[29] V. Cimini, E. Polino, F. Belliardo, F. Hoch, B. Piccirillo, N. Spagnolo, V. Giovannetti, and F. Sciarrino, npj Quantum Inf. **9**, 20 (2018).
[30] D. V. Tsarev, S. M. Arakelian, Y.-L. Chuang, R.-K. Lee, and A. P. Alodjants, Opt. Express **26**, 19583 (2018).
[31] S. Daryanoosh, S. Slussarenko, D. W. Berry, H. M. Wiseman, and G. J. Pryde, Nat. Commun. **9**, 4606 (2018).
[32] Z. H. Saleem, M. Perlin, A. Shaji, and S. K. Gray, Phys. Rev. A **109**, 052615 (2024).
[33] L. Maccone and A. K. Pati, Phys. Rev. Lett. **113**, 260401 (2014).
[34] S. Bagchi and A. K. Pati, Phys. Rev. A **94**, 042104 (2016).
[35] K. Wang, X. Zhan, Z. Bian, J. Li, Y. Zhang, and P. Xue, Phys. Rev. A **93**, 052108 (2016).
[36] W. Ma, B. Chen, Y. Liu, M. Wang, X. Ye, F. Kong, F. Shi, S.-M. Fei, and J. Du, Phys. Rev. Lett. **118**, 180402 (2017).
[37] L. Xiao, K. Wang, X. Zhan, Z. Bian, J. Li, Y. Zhang, P. Xue, and A. K. Pati, Opt. Express **25**, 17904 (2017).
[38] L. Xiao, B. Fan, K. Wang, A. K. Pati, and P. Xue, Phys. Rev. Res. **2**, 023106 (2020).
[39] M. Ozawa, Phys. Rev. A **67**, 042105 (2003).
[40] M. Berta, M. Christandl, R. Colbeck, J. M. Renes, and R. Renner, Nature Phys. **6**, 659 (2010).
[41] J. Erhart, S. Sponar, G. Sulyok, G. Badurek, M. Ozawa, and Y. Hasegawa, Nature Phys. **8**, 185 (2012).
[42] G. Sulyok, S. Sponar, J. Erhart, G. Badurek, M. Ozawa, and Y. Hasegawa, Phys. Rev. A **88**, 022110 (2013).
[43] G. Sulyok, S. Sponar, B. Demirel, F. Buscemi, M. J. W. Hall, M. Ozawa, and Y. Hasegawa, Phys. Rev. Lett. **115**, 030401 (2015).
[44] R. Prevedel, D. Hamel, R. Colbeck, K. Fisher, and K. J. Resh, Nature Phys. **7**, 757 (2011).
[45] C.-F. Li, J.-S. Xu, X.-Y. Xu, K. Li, and G.-C. Guo, Nature Phys. **7**, 752 (2011).
[46] A. Barchielli, M. Gregoratti, and A. Toigo, Entropy **19**, 301 (2017).
[47] Z.-Y. Ding, H. Yang, D. Wang, H. Yuan, J. Yang, and L. Ye, Phys. Rev. A **101**, 032101 (2020).
[48] L. Liu, T. Zhang, X. Yuan, and H. Lu, Frontiers in Physics **10**, 873810 (2022).
[49] W.-Z. Yan, Y. Li, Z. Hou, H. Zhu, G.-Y. Xiang, C.-F. Li, and G.-C. Guo, Phys. Rev. Lett. **132**, 080202 (2024).
[50] L. Serino, C. Eigner, B. Brecht, and C. Silberhorn, Optics Express **33**, 5577 (2025).
[51] L. Serino, J. Gil-Lopez, M. Stefszky, R. Ricken, C. Eigner, B. Brecht, and C. Silberhorn, PRX Quantum **4**, 020306 (2023).
[52] L. Serino, G. Chesi, B. Brecht, L. Maccone, C. Macchiavello, and C. Silberhorn, Phys. Rev. Res. , (2025).
[53] B. Brecht, D. V. Reddy, C. Silberhorn, and M. G. Raymer, Phys. Rev. X **5**, 041017 (2015).
[54] H.-H. Lu, M. Liscidini, A. L. Gaeta, A. M. Weiner, and J. M. Lukens, Optica **10**, 1655 (2023).
[55] A. Widomski, S. Stopiński, K. Anders, R. Piramidowicz, and M. Karpiński, Journal of Lightwave Technology **41**, 6255 (2023).
[56] B. Brecht, A. Eckstein, R. Ricken, V. Quiring, H. Suche, L. Sansoni, and C. Silberhorn, Phys. Rev. A **90**, 030302(R) (2014).
[57] V. Ansari, G. Harder, M. Allgaier, B. Brecht, and C. Silberhorn, Physical Review A **96** (2017), 10.1103/physreva.96.063817.
[58] J. S. Lundeen, A. Feito, H. Coldenstrodt-Ronge, K. L. Pregnell, C. Silberhorn, T. C. Ralph, J. Eisert, M. B. Plenio, and I. A. Walmsley, Nature Physics **5**, 27 (2009).
[59] V. Ansari, J. M. Donohue, M. Allgaier, L. Sansoni, B. Brecht, J. Roslund, N. Treps, G. Harder, and C. Silberhorn, Phys. Rev. Lett. **120**, 213601 (2018).
[60] S. De, V. Ansari, J. Sperling, S. Barkhofen, B. Brecht, and C. Silberhorn, Phys. Rev. Res. **6**, L022040 (2024).
[61] L. Sheridan and V. Scarani, Physical Review A - Atomic, Molecular, and Optical Physics **82**, 1 (2010), arXiv:1003.5464.
[62] M. Tomamichel and R. Renner, Physical Review Letters **106**, 110506 (2011).

PHYSICAL REVIEW RESEARCH 7, 033152 (2025)

Complementarity-based complementarity: The choice of mutually unbiased observables shapes quantum uncertainty relations

Laura Serino,[1] Giovanni Chesi,[2,*] Benjamin Brecht,[1] Lorenzo Maccone,[2] Chiara Macchiavello,[2] and Christine Silberhorn[1]

[1]*Integrated Quantum Optics, Institute for Photonic Quantum Systems (PhoQS), Paderborn University, Warburgerstrasse 100, 33098 Paderborn, Germany*

[2]*QUIT Group, Physics Department, University of Pavia, INFN Sez. Pavia, Via Bassi 6, 27100 Pavia, Italy*

(Received 29 July 2024; revised 20 January 2025; accepted 23 June 2025; published 13 August 2025)

Quantum uncertainty relations impose fundamental limits on the joint knowledge that can be acquired from complementary observables: Perfect knowledge of a quantum state in one basis implies maximal indetermination in all other mutually unbiased bases (MUBs). Uncertainty relations derived from joint properties of the MUBs are generally assumed to be uniform, irrespective of the specific observables chosen within a set. In this work, we demonstrate instead that the uncertainty relations can depend on the choice of observables. Through both experimental observation and numerical methods, we show that selecting different sets of three MUBs in a five-dimensional quantum system results in distinct uncertainty bounds, i.e., in varying degrees of complementarity, in terms of both entropy and variance.

DOI: 10.1103/v24q-sl6n

I. INTRODUCTION

A property of a quantum system is described by an observable, namely, a Hermitian operator $\hat{O}$. Each of the possible values o of the property $\hat{O}$ is connected to an eigenstate $|o\rangle$. The Born-rule probability that the measurement of a system property has outcome equal to the value o is given by $|\langle o|\psi\rangle|^2$, where $|\psi\rangle$ is the system state. This state of affairs formalizes the principle of complementarity [1,2]: A system can possess a definite value of a property, i.e., measurement outcomes have probability 1, only if its state is an eigenstate $|\psi\rangle = |o\rangle$ of that property. Otherwise, the value of that property is undefined, and only probabilistic predictions of measurement outcomes are possible. This implies that complementary properties exist: From a set of properties of the system, in general we can assign a definite (i.e., fully determined) value only to one.

In particular, maximally complementary properties exist: Assigning a definite value to one of them renders *all* the others maximally indeterminate; namely, each of their outcomes will have uniform probability. This happens when we consider a set of observables whose eigenstates are mutually unbiased bases (MUBs). Indeed, the square modulus of the scalar product of any two states $|a_i\rangle, |b_j\rangle$ pertaining to two different MUBs is always $|\langle a_i|b_j\rangle|^2 = 1/d$, where d is the Hilbert space dimension.

Surprisingly, it was shown [3–5] that one can have large information on more than one complementary observable provided that the value of none of them is known with certainty (which would render the values of all the others completely indetermined). Namely, if the system is prepared in a state that is a nontrivial superposition when expressed in all the MUBs, then it is possible to have nontrivial *joint* information on multiple complementary properties.

Different complementary properties (MUBs) can be grouped and classified in terms of equivalence classes of complex Hadamard matrices [6–8]. We say that two sets of MUBs are equivalent if one can be mapped into the other by unitary transformations, permutations, and phase factor multiplications. In this context, it was pointed out in Ref. [8] that in dimension $d = 5$ there are two *inequivalent* classes of triplets of MUBs. For larger dimensions, a rich and involved structure of inequivalent sets of MUBs is known to exist [7,9,10]. In Ref. [11], a notion of *operational inequivalence* of sets of MUBs has been introduced, such that the inequivalence is detected whenever distinct sets of MUBs feature a different noise robustness, used as an incompatibility quantifier.

The existence of inequivalent sets of MUBs was shown to have practical consequences on Quantum Random Access Codes, since it prevents to generalize the analytic expression of the optimal average success probability for protocols $2^d \to 1$ to protocols $n^d \to 1$ with $n \geqslant 3$ [12]. Applications have also been found in entanglement detection based on complementary observables: in Ref. [13], it was shown that the lower bound on a given correlation function, used as an entanglement witness, depends not only on the dimension and the number of measurements, but also on the choice of the specific set of MUBs.

While these contributions were mainly focused on proving and/or detecting the existence of inequivalent sets of MUBs, here we present a fundamental implication of this: their impact on the uncertainty relations (URs). The URs are the

*Contact author: giovanni.chesi@unipv.it

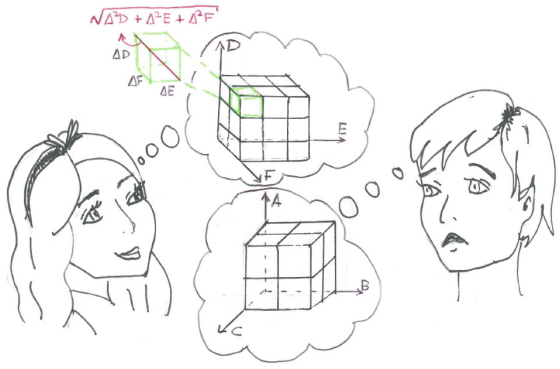

FIG. 1. Alice and Bob are both interested in joint values of observables with MUBs as eigenstates. In dimension 5, there are six of them: Bob measures observables $\hat{A}, \hat{B}, \hat{C}$, and Alice measures $\hat{D}, \hat{E}, \hat{F}$. Alice gets more information: she can divide the DEF phase space into smaller uncertainty blocks than Bob's, even though they are both looking at MUBs.

very expression of the complementary properties of quantum observables and yield a direct link between experimental observations and quantum theory. While providing experimental validation of the URs for MUBs and high-dimensional systems, we detected different minimal uncertainties for distinct triplets of MUBs in $d = 5$. Then, the inequivalence proved in Ref. [8] unveiled a finer structure of quantum URs: The information that a system can possess on three of the six complementary properties depends on *which* of the properties are considered. We show this by calculating the lower bound of the sum of the entropies or of the variances of the measurement outcomes of three complementary observables, complemented with Monte Carlo simulations, and prove that such a lower bound depends explicitly on the choice of complementary observables: complementarity-based complementarity (Fig. 1). Most importantly, the validity of distinct URs for triplets in the same complete set of MUBs opens foundational questions, finds application in a plethora of quantum protocols, and leads to experimental verification, which we report here.

II. UNCERTAINTY RELATIONS FOR INEQUIVALENT TRIPLETS OF MUBs

Consider three maximally complementary observables $\hat{A}, \hat{B}, \hat{C}$ with mutually unbiased eigenstates $\{|a_j\rangle\}_j, \{|b_j\rangle\}_j$, $\{|c_j\rangle\}_j$. One can have *partial* knowledge of all three of them if the state $|\psi\rangle$ is a nontrivial superposition when expressed in any of the bases $\{|a_j\rangle\}_j, \{|b_j\rangle\}_j, \{|c_j\rangle\}_j$. How much *joint* information on them can one obtain? We need a quantification of how uncertain the outcomes of measurements of all three observables are. This is precisely what we learn from URs. In the following, we concentrate on two quantifiers [14]. On the one hand, we consider the sum of the Shannon entropies $H(\hat{O}) = -\sum_j p_j \log_2 p_j$ of the Born probabilities $p_j = |\langle o_j|\psi\rangle|^2$ pertaining to the measurement of $\hat{O}$. The entropies are all positive quantities, so a small sum implies large *joint* knowledge. The sum of entropies for maximally complementary observables has always a nontrivial lower bound

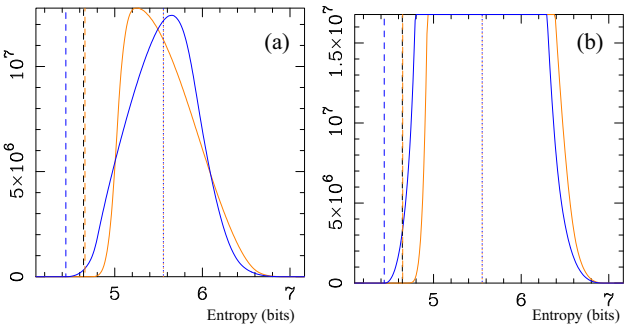

FIG. 2. Monte Carlo evaluation of the sums of entropies in (1) and (2) on pure states chosen randomly using the Haar measure. The histograms (250 bins) represent the number of states whose sum of entropies of three maximally complementary observables is equal to the value in the abscissa. (a) Simulation over 10^9 random states. (b) Detail of the tails of the distributions for a simulation over 10^{10} random states. The orange (blue) curves refer to the entropies of A, B, C (D, E, F). The black dashed line is at $2\log_2 5$ and is approached by the left tail of the orange distribution; the blue dashed line approaches the lower bound of (2). The dotted lines are the (matching) average values of the two distributions at ∼5.55.

given by the entropic uncertainty relations (EURs) [15–17]. On the other hand, we consider the sum of the variances [18] of $\hat{A}, \hat{B}, \hat{C}$. Differently from the entropy, the variance depends also on the eigenvalues of the observables, not only on the probabilities. We will choose observables with eigenvalues equal to a permutation $P(j)$ of the basis index j, i.e., $\hat{A} = \sum_j P(j)|a_j\rangle\langle a_j|$, and then minimize the variance $\Delta A^2 = \langle \hat{A}^2\rangle - \langle \hat{A}\rangle^2$ over the permutations, to avoid effects due to the arbitrariness of the eigenvalue assignments. Also, the sum of variances has a nonzero [19] lower bound for maximally complementary observables [20,21]. We now show that the UR in terms of entropies or variances of three different maximally complementary observables $\hat{A}, \hat{B}, \hat{C}$ depends on *the choice of the maximally complementary observables*.

We start from dimension $d = 5$ where there exist six maximally complementary observables $\hat{A}, \hat{B}, \hat{C}, \hat{D}, \hat{E}, \hat{F}$ with eigenvectors equal to the six MUBs [7,8] presented in the Appendix. In this case, we find that

$$H(\hat{A}) + H(\hat{B}) + H(\hat{C}) \geqslant 2\log_2 5 \simeq 4.643\,86, \qquad (1)$$

$$H(\hat{D}) + H(\hat{E}) + H(\hat{F}) \gtrsim 4.432\,23. \qquad (2)$$

Bound (1) was known [17] and was implicitly assumed to hold for every possible choice of MUB triplet, whereas bound (2), obtained numerically (see the Appendix), was found while experimentally testing the EURs. The states that minimize the first bound are eigenstates of any of the three $\hat{A}, \hat{B}, \hat{C}$, e.g., $|\psi\rangle = |a_0\rangle$. The states that minimize the second bound, instead, have a single null component when expressed in the computational basis $|a_j\rangle$, e.g., a state $\sum_j \psi_j e^{i\phi_j}|a_j\rangle$ with $\{\psi_j\} = (0.544\,88, 0.450\,67, 0, 0.450\,67, 0.544\,88)$ and $\{\phi_j\} = (0, -2\pi/5, 0, \pi, -\pi/5)$.

To validate the numerical minimization, we calculated the minimal sum of the entropies on a large number of pure states chosen randomly [22,23] with Haar measure (Fig. 2), confirming that no state beats either bound (1) or (2). We

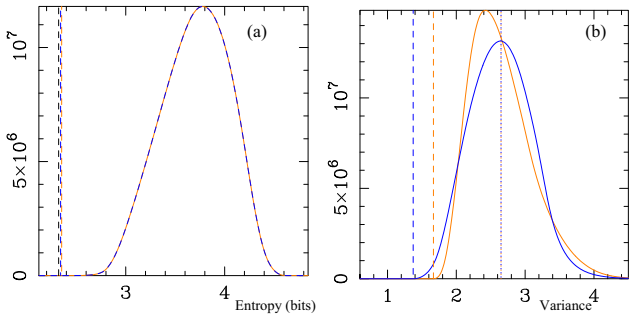

FIG. 3. (a) Histograms of the Monte Carlo evaluation of the sum of the entropies of two MUBs in dimension $d = 5$ (250 bins over 10^9 Haar distributed random pure states). As expected, all histograms match (here, the histograms refer to A, B in orange and C, D in blue). The lower bounds of the left tails (orange-blue vertical dashed lines) approach the Maassen-Uffink bound $\log_2 5$ (black dashed line). (b) Histograms (250 bins over 10^9 states) of the sum of variances of three MUBs, evaluated over A, B, C (orange) with lower bound 1.67, and D, E, F (blue) with bound 1.37.

also checked that the sum of any *two* entropies never beats the Maassen-Uffink bound [16] of $\log_2 5$ (Fig. 3) and that the sum of *four* entropies has the unique lower bound found in Ref. [17] for every choice of the MUBs, confirming that the effect presented here requires exactly three MUBs. We inspected all the $\binom{6}{3} = 20$ possible combinations of three MUBs out of six and found only the two bounds reported in Eqs. (1) and (2). Moreover, if a triplet could attain one bound, the remaining triplet would obtain the other bound. In particular, the triplets that only achieve the bound $2\log_2 5$ are the ones in the set

$$\mathcal{S}_1 \equiv \{ABC, ABF, BEF, ADE, BCD, CEF, CDF, BDE, ACE, ADF\}, \tag{3}$$

whereas the ones that achieve the bound in Eq. (2) are the triplets in the set

$$\mathcal{S}_2 \equiv \{ABD, ABE, ACF, BCE, DEF, CDE, BDF, ACD, BCF, AEF\}. \tag{4}$$

We report in Table I a list of optimal states saturating the bound in Eq. (2), one for each triplet in $\mathcal{S}_2$. We show in the Appendix that these states are all related to each other by specific unitary transformations. Moreover, we prove there that triplets belonging to the same set feature the same entropic uncertainty.

In the case $d = 4$, there is a three-parameter family of triplets of MUBs [8], but just for a specific choice of the parameters a triplet can be extended to the unique complete set, considered in Ref. [17]. Triplets selected from the complete set are all equivalent. Indeed, in this case we could not find a similar mismatch in the URs for three MUBs: in the complete set, for $d = 4$ there are five MUBs connected to five observables $(\hat{A}, \hat{B}, \hat{C}, \hat{D}, \hat{E})$, and we checked all $\binom{5}{3} = 10$ combinations of triplets $\hat{X}, \hat{Y}, \hat{Z}$ in $\{\hat{A}, \hat{B}, \hat{C}, \hat{D}, \hat{E}\}$. They all have the lower bound $H(\hat{X}) + H(\hat{Y}) + H(\hat{Z}) \geqslant 3$ identified in Ref. [17]. It is worth mentioning that, while in the case $d = 3$ the states achieving the lower bound are the same for every triplet, in $d = 4$ the optimal states depend on the choice of the MUBs. We note that they share a common structure; i.e., they all have two non-null components.

TABLE I. Optimal states saturating the bound in Eq. (2). This bound can be achieved only by the triplets in $\mathcal{S}_2$, listed here in the first column. We report one state for each triplet, having set $\phi_0 = 0$.

$\{l_1, l_2, l_3\}$	ψ_0	$\psi_1; \phi_1$	$\psi_2; \phi_2$	$\psi_3; \phi_3$	$\psi_4; \phi_4$
ABD	0.23	0.67	0.67	0.23	0
		$4\pi/5$	$-\pi/5$	π	0
ABE	0.23	0	0.23	0.67	0.67
		0	π	$\pi/5$	$-4\pi/5$
ACD	0	0.23	0.67	0.67	0.23
		0	$4\pi/5$	$\pi/5$	$\pi/5$
ACF	0.67	0.23	0.23	0.67	0
		$-3\pi/5$	$4\pi/5$	$\pi/5$	0
AEF	0.23	0.67	0.67	0.23	0
		$2\pi/5$	$\pi/5$	$-3\pi/5$	0
BCE	0.45	0.45	0.55	0	0.55
		$-\pi/5$	$2\pi/5$	0	π
BCF	0.45	0.45	0.55	0	0.55
		$-3\pi/5$	$4\pi/5$	0	$3\pi/5$
BDF	0.45	0.45	0.55	0	0.55
		π	$-4\pi/5$	0	$\pi/5$
CDE	0.55	0.55	0.45	0	0.45
		$-\pi/5$	$\pi/5$	0	$4\pi/5$
DEF	0.55	0.45	0	0.45	0.55
		$-2\pi/5$	0	π	$-\pi/5$

Interestingly, if one does not fix the parameters of the family of triplets of MUBs in $d = 4$ to get a complete set, a richer scenario of inequivalent triplets depending on three parameters can be explored. Then, different URs may be obtained, with lower bounds presumably depending on the parameters. We will not explore this case here, as our analysis focuses on the complementary properties of a same set of MUBs, but we point it out as a relevant issue for further research.

By studying the sum of variances in $d = 4$ and $d = 5$, we find URs featuring the same behavior as the one found for the EURs: In $d = 4$, the optimal states attain the same minimum for every choice of the bases, while in $d = 5$ there are two distinct lower bounds dividing the triplets of MUBs into the same two sets as for the EURs. For $d = 4$, all the URs for every choice of the three MUBs read

$$\Delta X^2 + \Delta Y^2 + \Delta Z^2 \geqslant 0.75, \tag{5}$$

with $\hat{X} \neq \hat{Y} \neq \hat{Z} \in \{\hat{A}, \hat{B}, \hat{C}, \hat{D}, \hat{E}\}$.

For $d = 5$, the UR corresponding to the EUR in Eq. (1) reads

$$\Delta X^2 + \Delta Y^2 + \Delta Z^2 \gtrsim 1.67, \tag{6}$$

with $XYZ \in \mathcal{S}_1$, while the one related to the triplets in Eq. (2) is

$$\Delta X^2 + \Delta Y^2 + \Delta Z^2 \gtrsim 1.37, \tag{7}$$

with $XYZ \in \mathcal{S}_2$.

III. EXPERIMENTAL VERIFICATION

We experimentally tested the entropic results presented in Eqs. (1) and (2) by encoding information in photonic time-frequency modes [24]. Namely, we consider a Hilbert space generated by broadband frequency bins and their superpositions encoded in coherent light pulses. In this encoding alphabet, the five-dimensional computational basis $|a_j\rangle$ (associated with observable $\hat{A}$) is defined as a set of five Gaussian-shaped frequency bins centered at different frequencies, and the MUBs are generated by superimposing the fundamental bins with different phases. We note that the chosen alphabet falls in the category of pulsed temporal modes as the superposition states overlap in both time and frequency.

We perform the projective measurements using a so-called multi-output quantum pulse gate (mQPG) [25], a high-dimensional decoder for time-frequency pulsed modes based on sum-frequency generation in a dispersion-engineered waveguide. This device projects a high-dimensional input state onto all the eigenstates of a user-chosen MUB, selected via spectral shaping of the pump pulse driving the process, and yields the result of each projection in the corresponding output channel defined by a distinct output frequency.

Mathematically, we can describe the mQPG operation as a positive-operator-valued measure (POVM) $\{\pi^\gamma\}$, where each POVM element π^γ describes the measurement operator of a single channel set to detect mode γ [25–27]. Ideally, $\pi^\gamma = |\gamma\rangle\langle\gamma|$; however, experimental imperfections lead to systematic errors in the POVMs, necessitating the more general description $\pi^\gamma = \sum_{ij} m_{ij}^\gamma |a_i\rangle\langle a_j|$, with $|a_i\rangle$ and $|a_j\rangle$ eigenstates of the computational basis. When measuring a pure input state $\rho^\xi = |\xi\rangle\langle\xi|$ from the chosen five-dimensional Hilbert space, we will obtain output γ with probability $p^{\gamma\xi} = \mathrm{Tr}(\rho^\xi \pi^\gamma)$. In the measurement process, we use an mQPG with five channels, which can be programmed to perform projections onto any arbitrary MUB in the selected Hilbert space by assigning to each channel an eigenstate of that basis. Then, for each probed input state $|\xi\rangle$, we calculate the entropy in each measurement basis by estimating the probability p_j for each measurement outcome j as the normalized counts in the corresponding channel.

A schematic of the experimental setup is shown in Fig. 4. The signal and pump pulses, centered at 1545 and 860 nm, respectively, are generated by a combination of a Ti:sapphire ultrafast laser with an optical parametric oscillator (OPO) at a repetition rate of 80 MHz. The signal pulse is shaped by a commercial waveshaper to generate the frequency-bin states in input, whereas the pump pulse is shaped by an in-house-built 4f waveshaper to generate the frequency-bin basis for the measurement. Both beams are coupled into the mQPG waveguide, where the signal modes are up-converted into a different output channel (corresponding to a distinct output frequency) based on their overlap with each pump mode, i.e., with each eigenstate of the chosen measurement basis. The output beam, centered at around 552 nm, is separated from the unconverted signal and pump beams by a shortpass (SP) filter and then detected by a commercial charged-coupled device (CCD) spectrograph (Andor Shamrock 500i). The number of counts detected at each output frequency indicates the number of photons measured in the corresponding mode.

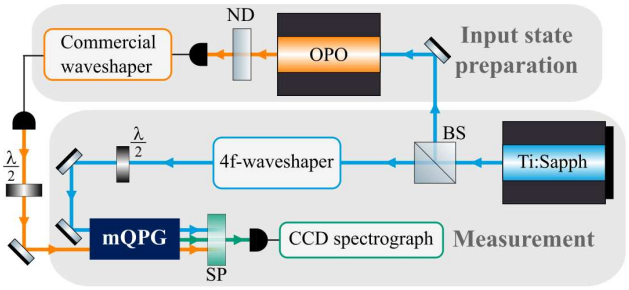

FIG. 4. Schematic of the experimental setup. The signal (1545 nm) and pump (860 nm) pulses are generated by a Ti:sapphire ultrafast laser with an OPO at a repetition rate of 80 MHz. Two waveshapers generate the frequency-bin states in input from the signal pulse and the frequency-bin basis for the measurement from the pump pulse, respectively. In the mQPG waveguide, the signal modes are up-converted into a distinct output frequency based on their overlap with each pump mode. The output beam (552 nm) is separated from the unconverted signal and pump beams by an SP filter and then detected by a commercial CCD spectrograph (Andor Shamrock 500i).

IV. RESULTS AND DISCUSSION

For the experimental verification of the bounds in Eqs. (1) and (2), we probed different types of input states and, for each state, we calculated the entropy sum $H(\hat{X}) + H(\hat{Y}) + H(\hat{Z})$ from the measured output probabilities. The results for the two MUB triplets *CDF* and *ABE* are shown as filled markers in Fig. 5, and compared to their respective lower entropy bounds from Eqs. (1) (green dashed line) and (2) (red dash-dotted line). For each input state, the error bars are calculated by sampling 500 sets of counts from a distribution with the measured mean and standard deviation of the original dataset and taking the 10%–90% spread of the corresponding entropy distribution. The error bars are not visible in most points due to their narrow extent.

The figure also shows the entropy values predicted via realistic simulations of the measurement process. These simulations are obtained by first characterizing the performance of the mQPG-based decoder through a quantum detector tomography [25,28,29] to reconstruct the actual POVMs. The average measurement error (cross-talk) per basis falls between 0.5% (for basis $\{|a_j\rangle\}_j$) and 1.9% (for basis $\{|f_j\rangle\}_j$). From the reconstructed POVMs, we calculated the expected entropy that one would observe measuring each state with this imperfect system, obtaining the hollow markers in Fig. 5. These estimates almost perfectly match the measured values, confirming that discrepancies with the theoretical predictions are to be attributed to the imperfect detection system.

The first type of probed input states are the eigenstates of all six MUBs, labeled "internal" if they are eigenstates of $\hat{X}$, $\hat{Y}$, or $\hat{Z}$, and "external" otherwise. The entropy sum of the internal eigenstates (green squares) is always equal to the value predicted in Eq. (1), which, for the triplet *CDF*, is the minimum possible entropy sum. Contrarily, the external eigenstates (blue diamonds) always maximize the entropy sum.

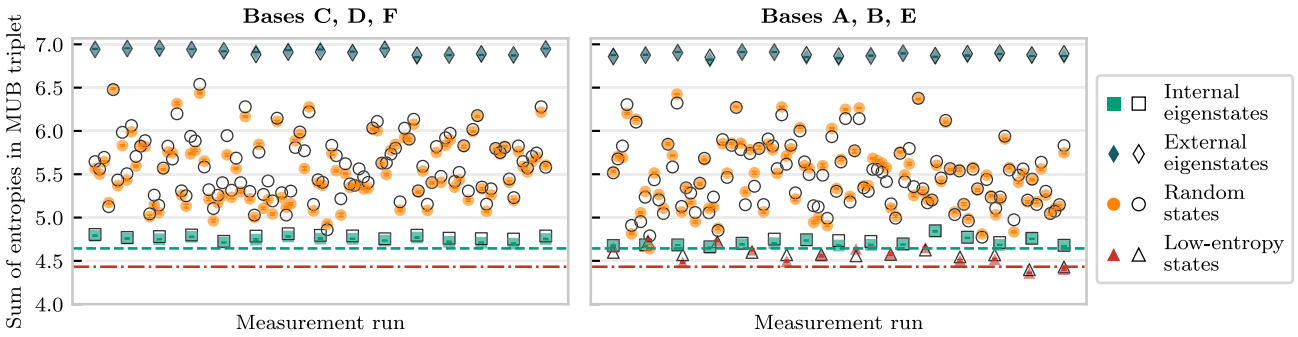

FIG. 5. Sum of the entropies calculated in $d = 5$ for the two MUB triplets *CDF* (left) and *ABE* (right) for different types of input states: eigenstates of the MUBs in the selected triplet (green squares), eigenstates of the other MUBs (blue diamonds), random states (yellow circles), and low-entropy states that violate the previous assumption of bound (1) (red triangles). The filled markers show the experimental data, whereas the hollow markers describe the predicted results based on the characterized imperfect POVMs. The dashed green line and dash-dotted red line indicate the two lower bounds (1) and (2), respectively.

Then, we probed pure random input states (orange circles), generated by sampling amplitude and phase coefficients from a uniform distribution and renormalizing the amplitudes. We note that this method does not allow for truly uniform sampling of the parameter space; however, this is not relevant in the scope of this work, as we only look at random input states to verify that they fall within the predicted entropy boundaries.

Finally, we probed states that are a superposition of four states of the computational basis $|a_i\rangle$, e.g., $\sum_j \psi_j e^{i\phi_j}|a_j\rangle$ with $\{\psi_j\} = (0.193\,23, 0.680\,19, 0, 0.680\,19, 0.193\,23)$ and $\{\phi_j\} = (-3\pi/5, \pi/5, 0, 0, 0)$ (red triangles in Fig. 5). These states were initially proven to minimize the sum of entropies in four, five, and six MUBs in $d = 5$ [17]. However, while testing this assumption, we observed that the sum of entropies in the *ABE* triplet violated bound (1), previously assumed to hold for any possible choice of MUB triplet. This contradiction led to the discovery of bound in Eq. (2) for the basis triplet *ABE*, while *CDF* maintains the known bound, revealing the immediate experimental consequences of the underlying asymmetry between sets of inequivalent MUBs.

Interestingly, while our primary goal in this demonstration was to highlight the effect of inequivalent sets of MUBs on uncertainty relations, our findings also provide an experimental verification of their existence that can, in principle, be extended to higher dimensions. In fact, while the existence and implications of inequivalent classes of MUBs have been theoretically understood, their experimental verification has remained elusive until very recently due to the subtlety of these effects, which could only be observed by a setup capable of performing simultaneous projections across a complete and arbitrary basis. Reference [30] provided an important verification in $d = 4$ using hybrid path-polarization encodings; however, their method is based on indirect estimations and lacks straightforward scalability to higher dimensions. In contrast, our demonstration relates the existence of inequivalent sets of MUBs to the simplest and most direct type of measurements. The versatility of the mQPG operating in the time-frequency degree of freedom makes our approach naturally extensible [25,31], enabling experimental verification of similar UR bounds if they are discovered in higher-dimensional systems.

V. CONCLUSIONS

In conclusion, we have shown that the URs are shaped by the inequivalence of sets of MUBs, which is a physical fundamental proof that the amount of joint information that one can have on maximally complementary observables can depend on which of them are considered, even though the overlap between the eigenstates of all maximally complementary observables is all the same, since they are MUBs. We showed that two distinct URs appear for triplets of MUBs in dimension $d = 5$, when the maximum joint information is gauged by minimizing the sum of the entropies and of the variances.

This effect has several implications that will be explored in future work. For instance, in quantum key distribution, the entropic uncertainty relations are known to provide a tight bound on the secret key rate and are crucial for security proofs. In addition, high-dimensional systems provide better key rates and larger maximum tolerable errors. Then, complementarity-based complementarity may be exploited to add a further level of security. Moreover, uncertainty relations are at the basis of many quantum information procedures (e.g., quantum metrology). Another implication refers to the foundations of quantum mechanics, where the investigation of URs in large dimensional systems can shed light on their complementary properties.

ACKNOWLEDGMENTS

The authors acknowledge support from the EU H2020 QuantERA ERA-NET Cofund in Quantum Technologies Project QuICHE. G.C. acknowledges support from the PNRR MUR Project PE0000023-NQSTI. C.M. acknowledges support from the National Research Centre for HPC, Big Data and Quantum Computing, and from the PRIN MUR Project 2022SW3RPY. L.M. acknowledges support from the PRIN MUR Project 2022RATBS4 and from the U.S. Department of Energy, Office of Science, National Quantum Information Science Research Centers, Superconducting Quantum Materials and Systems Center (SQMS) under Contract No. DE-AC02-07CH11359.

DATA AVAILABILITY

The data that support the findings of this article are not publicly available. The data are available from the authors upon reasonable request.

APPENDIX

MUBs, explicit form. In the case $d = 5$, six MUBs are known. The explicit expression of the vectors for each basis is reported below as columns of the following matrices [8]:

$$\{|a_j\rangle\}_{j=1}^5 = \begin{pmatrix} 1 & 0 & 0 & 0 & 0 \\ 0 & 1 & 0 & 0 & 0 \\ 0 & 0 & 1 & 0 & 0 \\ 0 & 0 & 0 & 1 & 0 \\ 0 & 0 & 0 & 0 & 1 \end{pmatrix}, \tag{A1}$$

$$\{|b_j\rangle\}_{j=1}^5 = \frac{1}{\sqrt{5}} \begin{pmatrix} 1 & 1 & 1 & 1 & 1 \\ 1 & \omega & \omega^2 & \omega^3 & \omega^4 \\ 1 & \omega^2 & \omega^4 & \omega & \omega^3 \\ 1 & \omega^3 & \omega & \omega^4 & \omega^2 \\ 1 & \omega^4 & \omega^3 & \omega^2 & \omega \end{pmatrix},$$

$$\{|c_j\rangle\}_{j=1}^5 = \frac{1}{\sqrt{5}} \begin{pmatrix} 1 & 1 & 1 & 1 & 1 \\ \omega & \omega^2 & \omega^3 & \omega^4 & 1 \\ \omega^4 & \omega & \omega^3 & 1 & \omega^2 \\ \omega^4 & \omega^2 & 1 & \omega^3 & \omega \\ \omega & 1 & \omega^4 & \omega^3 & \omega^2 \end{pmatrix},$$

$$\{|d_j\rangle\}_{j=1}^5 = \frac{1}{\sqrt{5}} \begin{pmatrix} 1 & 1 & 1 & 1 & 1 \\ \omega^3 & \omega^4 & 1 & \omega & \omega^2 \\ \omega^2 & \omega^4 & \omega & \omega^3 & 1 \\ \omega^2 & 1 & \omega^3 & \omega & \omega^4 \\ \omega^3 & \omega^2 & \omega & 1 & \omega^4 \end{pmatrix},$$

$$\{|e_j\rangle\}_{j=1}^5 = \frac{1}{\sqrt{5}} \begin{pmatrix} 1 & 1 & 1 & 1 & 1 \\ \omega^2 & \omega^3 & \omega^4 & 1 & \omega \\ \omega^3 & 1 & \omega^2 & \omega^4 & \omega \\ \omega^3 & \omega & \omega^4 & \omega^2 & 1 \\ \omega^2 & \omega & 1 & \omega^4 & \omega^3 \end{pmatrix},$$

$$\{|f_j\rangle\}_{j=1}^5 = \frac{1}{\sqrt{5}} \begin{pmatrix} 1 & 1 & 1 & 1 & 1 \\ \omega^4 & 1 & \omega & \omega^2 & \omega^3 \\ \omega & \omega^3 & 1 & \omega^2 & \omega^4 \\ \omega & \omega^4 & \omega^2 & 1 & \omega^3 \\ \omega^4 & \omega^3 & \omega^2 & \omega & 1 \end{pmatrix}, \tag{A2}$$

where $\omega = e^{2i\pi/5}$.

In dimension 4, we have five MUBs. Again, we display them as columns of the following matrices [8]:

$$\{|a_j\rangle\}_{j=1}^4 = \begin{pmatrix} 1 & 0 & 0 & 0 \\ 0 & 1 & 0 & 0 \\ 0 & 0 & 1 & 0 \\ 0 & 0 & 0 & 1 \end{pmatrix},$$

$$\{|b_j\rangle\}_{j=1}^4 = \frac{1}{2} \begin{pmatrix} 1 & 1 & 1 & 1 \\ 1 & 1 & -1 & -1 \\ 1 & -1 & -1 & 1 \\ 1 & -1 & 1 & -1 \end{pmatrix},$$

$$\{|c_j\rangle\}_{j=1}^4 = \frac{1}{2} \begin{pmatrix} 1 & 1 & 1 & 1 \\ 1 & 1 & -1 & -1 \\ -i & i & i & -i \\ i & -i & i & -i \end{pmatrix},$$

$$\{|d_j\rangle\}_{j=1}^4 = \frac{1}{2} \begin{pmatrix} 1 & 1 & 1 & 1 \\ i & -i & i & -i \\ -1 & -1 & 1 & 1 \\ i & -i & -i & i \end{pmatrix},$$

$$\{|e_j\rangle\}_{j=1}^4 = \frac{1}{2} \begin{pmatrix} 1 & 1 & 1 & 1 \\ i & -i & i & -i \\ i & -i & -i & i \\ -1 & -1 & 1 & 1 \end{pmatrix}. \tag{A3}$$

Numerical minimization. The numerical minimization we adopted here is very similar to the one exploited in Ref. [17]. We used the software package wolfram mathematica. We parametrized the states in dimension 5 as follows:

$$\begin{aligned} |\psi\rangle = {} & \sin\alpha_1 \sin\alpha_2 \sin\alpha_3 \sin\alpha_4 e^{i\phi_1}|0\rangle \\ & + \cos\alpha_1 \sin\alpha_2 \sin\alpha_3 \sin\alpha_4 e^{i\phi_2}|1\rangle \\ & + \cos\alpha_2 \sin\alpha_3 \sin\alpha_4 e^{i\phi_3}|2\rangle + \cos\alpha_3 \sin\alpha_4 e^{i\phi_4}|3\rangle \\ & + \cos\alpha_4 e^{i\phi_5}|4\rangle, \end{aligned} \tag{A4}$$

i.e., a parametrization yielding the normalization of the state intrinsically. Differently from Ref. [17], we checked the results of our optimizations by repeating the procedure twice: The first one on reparametrized states where the weights in Eq. (A4) were permuted with respect to the states of the basis, and the second one on each of the reparametrized states but expanded on the eigenstates of other MUBs.

For each MUB $\{|x_k\rangle\}_k$ in Eq. (A1), we retrieved the Born probabilities in terms of the coefficients in Eq. (A4) through the superpositions between the states of the MUB and the generic state $|\psi\rangle$, namely,

$$p(x_k) = |\langle x_k|\psi\rangle|^2. \tag{A5}$$

Then, we considered the Shannon entropies

$$H(\{|x_k\rangle\}) = -\sum_{k=1}^{5} p(x_k) \log_2 p(x_k) \tag{A6}$$

and the variances

$$\Delta X^2 = \langle\psi|\hat{X}^2|\psi\rangle - \langle\psi|\hat{X}|\psi\rangle^2, \tag{A7}$$

with $\hat{X} = \sum_k P(k)|x_k\rangle\langle x_k|$. We then minimized numerically the sum of three entropies and the sum of three variances for all possible triplets of distinct MUBs. The minimization was performed by using the routine NMinimize of wolfram mathematica, which finds the minimum of a function over a given set of parameters and constraints.

Effects of the inequivalence of MUBs on the EURs. Here, we inspect in more detail the effect of the inequivalence of triplets of MUBs on the pertaining EURs. In particular, we show that the combination of the MUBs in the triplets from $\mathcal{S}_1$ and $\mathcal{S}_2$ identifies two related subsets of the Born probabilities inspected so far.

The MUBs shown in the Appendix are Hadamard matrices related to each other through the unitary

$\hat{U} = \mathrm{diag}(1, \omega, \omega^4, \omega^4, \omega)$, with $\omega = \exp(i2\pi/5)$, as follows:

$$\{|c_j\rangle\} = \hat{U}\{|b_j\rangle\},$$
$$\{|e_j\rangle\} = \hat{U}^2\{|b_j\rangle\},$$
$$\{|d_j\rangle\} = \hat{U}^3\{|b_j\rangle\},$$
$$\{|f_j\rangle\} = \hat{U}^4\{|b_j\rangle\}.$$

This structure inherently prevents from mapping any triplet in the set $\mathcal{S}_1$ of Eq. (3) into a triplet in $\mathcal{S}_2$ of Eq. (4) by means of a unitary matrix [8]. In the following lemma, we show how these relations impact on the Born probabilities appearing in the URs. In particular, the proof outlines how the structure of the five-dimensional MUBs implies the same EUR in Eq. (1) [Eq. (2)] for the triplets in the same set $\mathcal{S}_1$ ($\mathcal{S}_2$).

Lemma A1. Let $\mathcal{S}_1$ and $\mathcal{S}_2$ be the two inequivalent subsets of triplets of MUBs in $d = 5$. Let

$$\mathcal{P}_1 \equiv \left\{p^{(j)}_{X_1,\psi_0}, p^{(j')}_{Y_1,\psi_0}, p^{(j'')}_{Z_1,\psi_0}\right\}_{j,j',j''} \tag{A8}$$

and

$$\mathcal{P}_2 \equiv \left\{p^{(j)}_{X_2,\psi_0}, p^{(j')}_{Y_2,\psi_0}, p^{(j'')}_{Z_2,\psi_0}\right\}_{j,j',j''} \tag{A9}$$

be the two disjoint sets of probability vectors with $X_1Y_1Z_1 \in \mathcal{S}_1$ and $X_2Y_2Z_2 \in \mathcal{S}_2$, where $p^{(j)}_{T,\psi_0}$ is the Born probability of the superposition of the jth eigenstate of a basis $T \in \{A, B, C, D, E, F\}$ with a five-dimensional pure state $|\psi_0\rangle$ and $\{p^{(j)}_{T,\psi_0}\}_{j=1}^5$ is the pertaining probability vector. Consider the unitary $U = \mathrm{diag}(1, \omega, \omega^4, \omega^4, \omega)$, with $\omega = \exp(i2\pi/5)$, and the Fourier matrix $\Phi \equiv \{b_j\}_j$. Then, the transformations in the set $\mathcal{V} \equiv \{U^N\Phi^M U^L\}_{N,L,M}$, with $N, L \in \{0, \pm 1 \mod 5, \pm 2 \mod 5\}$ and $M \in \{0, \pm 1\}$, are automorphisms of $\mathcal{P}_1$ and $\mathcal{P}_2$.

Proof. The probability $p^{(j)}_{T,\psi_0}$ reads

$$p^{(j)}_{T,\psi_0} = |\langle\psi_0|t_j\rangle|^2, \tag{A10}$$

where $\{|t_j\rangle\}_j$ are the eigenstates of T, identifying one of the MUBs. Due to the construction of the MUBs in terms of Hadamard matrices, the probabilities $p^{(j)}_{T,\psi_0}$ can always be expressed as

$$p^{(j)}_{T,\psi_0} = |\langle\psi_0|U^{n_T}\Phi^{m_T}U^l P_{jk}|a_k\rangle|^2, \tag{A11}$$

where $\{|a_j\rangle\}_j$ is the computational basis and P_{jk} is the permutation exchanging the vector $|a_k\rangle$ with $|a_j\rangle$. U being a periodic matrix such that $U^5 = I$, we have $l, n_T \in \{0, \pm 1 \mod 5, \pm 2 \mod 5\}$, while for the Fourier matrix, we just need $m_T = 0, \pm 1$. Permutations map the probability vectors $\{p^{(j)}_{T,\psi_0}\}_j$ in themselves and are therefore automorphisms for $\mathcal{P}_1$ and $\mathcal{P}_2$. Similarly, the action of $\hat{U}^l$ on the states of the computational basis reduces to the multiplication for a global phase factor, thus leaving $p^{(j)}_{T,\psi_0}$ unchanged. Conversely, the exponents m_T and n_T determine the basis T. If $m_T = 0$, the transformation $U^{n_T}\Phi^{m_T}$, again, rescales $|a_j\rangle$ by an irrelevant phase factor, while for $m_T = \pm 1$, maps it to the state of another MUB, identified by n_T. Now, we evaluate the probabilities in Eq. (A11) on a state $|\psi\rangle = V|\psi_0\rangle$, with unitary V. By definition of $\mathcal{P}_1$ and $\mathcal{P}_2$, if $V^\dagger$ is an automorphism of the set of MUBs, namely, $V^\dagger : T \to \overline{T}$, with T and $\overline{T}$ mutually unbiased, as

$$V^\dagger U^{n_T}\Phi^{m_T} = U^{n_{\overline{T}}}\Phi^{m_{\overline{T}}}, \tag{A12}$$

then it is an automorphism of $\mathcal{P}_1 \cup \mathcal{P}_2$, and

$$V^\dagger = U^{n_{\overline{T}}}\Phi^{m_{\overline{T}}-m_T}U^{n_T} \equiv U^N\Phi^M U^L \in \mathcal{V}. \tag{A13}$$

Now, we have to show that the transformations in $\mathcal{V}$ identify the two disjoint sets $\mathcal{P}_1$ and $\mathcal{P}_2$. The application of the same unitary V to the state $|\psi_0\rangle$ relates the triplets of probability vectors $\{p^{(j)}_{X,\psi}, p^{(j')}_{Y,\psi}, p^{(j'')}_{Z,\psi}\}$ and $\{p^{(j)}_{\overline{X},\psi_0}, p^{(j')}_{\overline{Y},\psi_0}, p^{(j'')}_{\overline{Z},\psi_0}\}$ through the equations

$$U^N\Phi^M U^{L+n_X}\Phi^{m_X} = U^{n_{\overline{X}}}\Phi^{m_{\overline{X}}}, \tag{A14}$$

$$U^N\Phi^M U^{L+n_Y}\Phi^{m_Y} = U^{n_{\overline{Y}}}\Phi^{m_{\overline{Y}}}, \tag{A15}$$

$$U^N\Phi^M U^{L+n_Z}\Phi^{m_Z} = U^{n_{\overline{Z}}}\Phi^{m_{\overline{Z}}}. \tag{A16}$$

Without loss of generality, we can restrict to the cases where $M = 0, L \neq 0$ and $M \neq 0, L = 0$, the remaining cases being retrieved by shifting n_X, n_Y, and n_Z by L. For the sake of simplicity, we will set the triplet XYZ in the so-called standard form, where one of the MUBs is the computational basis, say $X = \{|a_j\rangle\}_j$, implying $m_X = 0$. The proof with $m_X = \pm 1$ follows the same line of argument and leads to the same conclusions.

In the case $M = 0$, note that we can also set $N = 0$. Then, Eqs. (A14)–(A16) fix $m_{\overline{X}} = m_X = 0$, $m_{\overline{Y}} = m_Y \neq 0$, and $m_{\overline{Z}} = m_Z \neq 0$, respectively. Note that the last two must be both non-null, or we would have repetitions of the computational basis in the same triplet. Finally, Eqs. (A15) and (A16) set $\Delta n \equiv n_Z - n_Y = n_{\overline{Z}} - n_{\overline{Y}}$, implying that the application of V fixes a relation between $\{Y, Z\}$ and $\{\overline{Y}, \overline{Z}\}$. From the periodicity of U, again $\Delta n \in \{0, \pm 1 \mod 5, \pm 2 \mod 5\}$. We must have $\Delta n \neq 0$ to avoid Y and Z being the same basis. Moreover, the order in the difference Δn is irrelevant, and so is its sign. These considerations leave us with two distinct possibilities, either $\Delta n = \pm 1 \mod 5$ or $\Delta n = \pm 2 \mod 5$. However, these identify two disjoint sets of triplets, the one in $\mathcal{S}_1$, featuring $\Delta n = \pm 1 \mod 5$, and the one in $\mathcal{S}_2$, with $\Delta n = \pm 2 \mod 5$. If all the bases in the triplet are assumed to be different from $\{a_j\}_j$, then it is simple to see that one ends with a similar set of conditions for n_X, n_Y, and n_Z separating the two sets of triplets as before. Hence, U^L maps the elements of $\mathcal{P}_1$ in elements of $\mathcal{P}_1$ and the elements of $\mathcal{P}_2$ in elements of $\mathcal{P}_2$.

In the case $M \neq 0, L = 0$, we need the following identities:

$$\Phi^\dagger U\Phi = U\Phi P_{jk}U, \tag{A17}$$

$$\Phi^\dagger U^2\Phi = U^3\Phi U^2 P'_{jk}. \tag{A18}$$

Again, we will neglect the contributions of permutations and global phase shifts. From Eq. (A14), we have $m_{\overline{X}} = M$ and $n_{\overline{X}} = N$. By exploiting Eqs. (A17) and (A18), we find that the left members of Eqs. (A15) and (A16) yield

$$\begin{aligned} U^{n_{\overline{X}}}\Phi^{m_{\overline{X}}}U^{n_k}\Phi^{m_k} =& \delta_{n_k,0}(1-\delta_{n_j,0})U^{n_{\overline{X}}} + \delta_{n_k,\pm 1} \\ &\times (1-\delta_{n_j,\pm 1})U^{n_{\overline{X}}+n_k}\Phi^{m_k} \\ &+ \delta_{n_k,2}(1-\delta_{n_j,2})\delta_{m_{\overline{X}},-1}U^{n_{\overline{X}}+n_k+1}\Phi^{m_k} \\ &+ \delta_{n_k,-2}(1-\delta_{n_j,-2})\delta_{m_{\overline{X}},1}U^{n_{\overline{X}}+n_k-1}\Phi^{m_k}, \end{aligned} \tag{A19}$$

where $\delta_{a,b}$ is the Kronecker delta, $k \neq j$, and $k, j \in \{Y, Z\}$. By requiring the equality with the right members of Eqs. (A15) and (A16), we find that the deltas identify the following cases:

(i) $n_{\overline{Y}} = n_{\overline{X}} \pm 1 \mod 5$
$n_{\overline{Z}} = n_{\overline{X}} \mp 1 \mod 5$
implying $\Delta n = n_Z - n_Y = n_{\overline{Z}} - n_{\overline{Y}} = \pm 2 \mod 5$: the transformations are automorphisms of $\mathcal{P}_2$;

(ii) $n_{\overline{Y}} = n_{\overline{X}} \pm 1 \mod 5$
$n_{\overline{Z}} = n_{\overline{X}} - 2 \mod 5$
implying $\Delta n = n_{\overline{Z}} - n_{\overline{Y}} - 1$ and we have that either $\Delta n = 1 \mod 5$ or $\Delta n = -2 \mod 5$; in the first case, the transformations are automorphisms of $\mathcal{P}_1$, while in the second one those of $\mathcal{P}_2$;

(iii) $n_{\overline{Y}} = n_{\overline{X}} \pm 1 \mod 5$
$n_{\overline{Z}} = n_{\overline{X}} + 2 \mod 5$
implying $\Delta n = n_{\overline{Z}} - n_{\overline{Y}} + 1$ and we have that either $\Delta n = -1 \mod 5$ or $\Delta n = 2 \mod 5$; in the first case, the transformations are automorphisms of $\mathcal{P}_1$, while in the second one those of $\mathcal{P}_2$;

(iv) $n_{\overline{Y}} = n_{\overline{X}} - 2 \mod 5$
$n_{\overline{Z}} = n_{\overline{X}} + 2 \mod 5$
implying $\Delta n = n_{\overline{Z}} - n_{\overline{Y}} + 2 = 1 \mod 5$: the transformations are automorphisms of $\mathcal{P}_1$.

Then, the automorphisms of the whole set of triplets of probability vectors $\mathcal{P}_1 \cup \mathcal{P}_2$ are automorphisms of the disjoint sets $\mathcal{P}_1$ and $\mathcal{P}_2$. ■

Note that, while it has been proved [8] that the elements of $\mathcal{S}_1$ cannot be mapped into elements of $\mathcal{S}_2$ via unitary transformations, Lemma A1 does not imply that there are no unitaries mapping elements of $\mathcal{P}_1$ into elements of $\mathcal{P}_2$. This is a relevant distinction between the sets $\mathcal{S}_1$, $\mathcal{S}_2$ and the sets $\mathcal{P}_1$, $\mathcal{P}_2$. Lemma A1 establishes that $\mathcal{P}_1$ and $\mathcal{P}_2$ are distinct equivalence classes, which does not rule out that their elements can be unitarily related. For instance, this is trivially the case if $|\psi_0\rangle$ and $|\psi\rangle = V|\psi_0\rangle$ are states of MUBs: given two inequivalent triplets of MUBs, one can always pick two states from different MUBs providing the same triplets of probability vectors.

Since the Shannon entropies in the EURs here addressed depend on the Born probabilities only, Lemma A1 is a sufficient condition for the EUR in Eq. (1) [Eq. (2)] to hold for all the triplets in the set $\mathcal{S}_1$ ($\mathcal{S}_2$). On the other hand, the existence of distinct lower bounds is a necessary, but not sufficient, condition for the inequivalence of $\mathcal{P}_1$ and $\mathcal{P}_2$, since it implies that there is no unitary transformation that can map the optimal states saturating the EUR for the triplets in $\mathcal{S}_2$ into equivalent optimal states for the triplets in $\mathcal{S}_1$.

[1] N. Bohr, Das quantenpostulat und die neuere entwicklung der atomistik, Naturwissenschaften **16**, 245 (1928).
[2] N. Bohr, The quantum postulate and the recent development of atomic theory, Nature (London) **121**, 580 (1928).
[3] W. K. Wootters and W. H. Zurek, Complementarity in the double-slit experiment: Quantum nonseparability and a quantitative statement of Bohr's principle, Phys. Rev. D **19**, 473 (1979).
[4] D. M. Greenberger and A. Yasin, Simultaneous wave and particle knowledge in a neutron interferometer, Phys. Lett. A **128**, 391 (1988).
[5] B.-G. Englert, Fringe visibility and which-way information: An inequality, Phys. Rev. Lett. **77**, 2154 (1996).
[6] W. Tadej and K. Zyczkowski, A concise guide to complex Hadamard matrices, Open Syst. Inf. Dyn. **13**, 133 (2006).
[7] T. Durt, B.-G. Englert, I. Bengtsson, and K. Życzkowski, On mutually unbiased bases, Int. J. Quantum Inf. **08**, 535 (2010).
[8] S. Brierley, S. Weigert, and I. Bengtsson, All mutually unbiased bases in dimensions two to five, Quantum Inf. Comput. **10**, 0803 (2010).
[9] W. M. Kantor, MUBs inequivalence and affine planes, J. Math. Phys. **53**, 032204 (2012).
[10] A. Sehrawat and A. B. Klimov, Unitarily inequivalent mutually unbiased bases for n qubits, Phys. Rev. A **90**, 062308 (2014).
[11] S. Designolle, P. Skrzypczyk, F. Fröwis, and N. Brunner, Quantifying measurement incompatibility of mutually unbiases bases, Phys. Rev. Lett. **122**, 050402 (2019).
[12] E. A. Aguilar, J. J. Borkała, P. Mironowicz, and M. Pawłowski, Connections between mutually unbiased bases and quantum random access codes, Phys. Rev. Lett. **121**, 050501 (2018).
[13] B. C. Hiesmayr, D. McNulty, S. Baek, S. Singha Roy, J. Bae, and D. Chruściński, Detecting entanglement can be more effective with inequivalent mutually unbiased bases, New J. Phys. **23**, 093018 (2021).
[14] We also considered the Renyi entropies of order 2 and 1/2, but the numerics gave inconclusive results.
[15] D. Deutsch, Uncertainty in quantum measurements, Phys. Rev. Lett. **50**, 631 (1983).
[16] H. Maassen and J. B. M. Uffink, Generalized entropic uncertainty relations, Phys. Rev. Lett. **60**, 1103 (1988).
[17] A. Riccardi, C. Macchiavello, and L. Maccone, Tight entropic uncertainty relations for systems with dimension three to five, Phys. Rev. A **95**, 032109 (2017).
[18] D. A. Trifonov and S. G. Donev, Characteristic uncertainty relations, J. Phys. A: Math. Gen. **31**, 8041 (1998).
[19] Instead, the product of variances, as in the traditional Heisenberg-Robertson uncertainty relations [32], is problematic because it has no nonzero lower bound when minimizing over states: the product is null already if only one of the two variances is nonzero.
[20] D. A. Trifonov, Generalized uncertainty relations and coherent and squeezed states, J. Opt. Soc. Am. A **17**, 2486 (2000).
[21] D. A. Trifonov, Generalizations of Heisenberg uncertainty relation, Eur. Phys. J. B **29**, 349 (2002).
[22] K. Zyczkowski and M. Kuś, Random unitary matrices, J. Phys. A: Math. Gen. **27**, 4235 (1994).
[23] M. Poźniak, K. Zyczkowski, and M. Kuś, Composed ensembles of random unitary matrices, J. Phys. A: Math. Gen. **31**, 1059 (1998).
[24] B. Brecht, D. V. Reddy, C. Silberhorn, and M. G. Raymer, Photon temporal modes: A complete framework for quantum information science, Phys. Rev. X **5**, 041017 (2015).
[25] L. Serino, J. Gil-Lopez, M. Stefszky, R. Ricken, C. Eigner, B. Brecht, and C. Silberhorn, Realization of a multi-output

quantum pulse gate for decoding high-dimensional temporal modes of single-photon states, PRX Quantum **4**, 020306 (2023).

[26] B. Brecht, A. Eckstein, R. Ricken, V. Quiring, H. Suche, L. Sansoni, and C. Silberhorn, Demonstration of coherent time-frequency Schmidt mode selection using dispersion-engineered frequency conversion, Phys. Rev. A **90**, 030302(R) (2014).

[27] V. Ansari, G. Harder, M. Allgaier, B. Brecht, and C. Silberhorn, Temporal-mode measurement tomography of a quantum pulse gate, Phys. Rev. A **96**, 063817 (2017).

[28] J. S. Lundeen, A. Feito, H. Coldenstrodt-Ronge, K. L. Pregnell, C. Silberhorn, T. C. Ralph, J. Eisert, M. B. Plenio, and I. A. Walmsley, Tomography of quantum detectors, Nat. Phys. **5**, 27 (2009).

[29] V. Ansari, J. M. Donohue, M. Allgaier, L. Sansoni, B. Brecht, J. Roslund, N. Treps, G. Harder, and C. Silberhorn, Tomography and purification of the temporal-mode structure of quantum light, Phys. Rev. Lett. **120**, 213601 (2018).

[30] W.-Z. Yan, Y. Li, Z. Hou, H. Zhu, G.-Y. Xiang, C.-F. Li, and G.-C. Guo, Experimental demonstration of inequivalent mutually unbiased bases, Phys. Rev. Lett. **132**, 080202 (2024).

[31] S. De, V. Ansari, J. Sperling, S. Barkhofen, B. Brecht, and C. Silberhorn, Realization of high-fidelity unitary operations on up to 64 frequency bins, Phys. Rev. Res. **6**, L022040 (2024).

[32] H. P. Robertson, The uncertainty principle, Phys. Rev. **34**, 163 (1929).

7

State characterization through multi-output detection

Besides unlocking the new applications that we have seen in the previous chapters, the simultaneous projections enabled by the mQPG (Chapter 4) allow for improved state characterization techniques. In this chapter, we present two techniques for quantum state and pulse characterization, both of which use the unique capabilities of the mQPG and highlight its versatility for different applications. These methods contribute significantly to the high-dimensional quantum communication framework developed in this work by providing valuable means for characterizing qudits encoded in the time-frequency domain of photons.

The experimental results and methodologies presented in this chapter are based on the following publications:

[Quantum Sci. Technol. 10, 025024 (2025)] L. Serino, M. Rambach, B. Brecht, J. Romero, and C. Silberhorn, "Self-guided tomography of time-frequency qudits", *Quantum Sci. Technol.* **10**, 025024 (2025). DOI: 10.1088/2058-9565/adb0ea

[arXiv:2504.08607 (2025)] A. Bhattacharjee[†], L. Serino[†], P. Folge[†], B. Brecht, and C. Silberhorn, "Frequency-bin interferometry for reconstructing electric fields with low intensity", *arXiv:2504.08607* (2025). DOI: 10.48550/arXiv.2504.08607

[†] These authors contributed equally to the work.

7.1 Self-guided tomography

For practical applications of time-frequency encodings, precise knowledge of the prepared quantum states is essential. However, characterizing qudits—a process known as quantum state tomography—becomes inherently challenging in high dimensions, as the number of parameters to be determined grows quadratically with the dimension d [127, 128]. Standard tomography techniques, which apply the maximum-likelihood method to the results of an over-complete set of measurements, become increasingly resource-expensive [117, 129, 130] in higher dimensions. While alternative approaches like compressive tomography can reduce the number of required measurements [131–133], their algorithms are often sensitive to noise, and many practical methods require a careful error calibration of the measurement device to achieve reliable results [95, 117, 134].

Self-guided tomography (SGT) [135] is an alternative technique that addresses many of these issues. Its working principle is based on an iterative process where an estimate of the quantum state is refined through successive projective measurements that "align" the measurement state to the input. By projecting the unknown state onto a series of states (σ_+ and σ_-) perturbed in opposite directions, the measurement outcomes guide the updates to the state estimate until a precise characterization is achieved. Previously applied to the polarization [136] and spatial [137] degrees of freedom, and extended to quantum process tomography [138], SGT has demonstrated scalability to high dimensions and a powerful resilience to both statistical and environmental noise, making it particularly effective in the photon-starved regime typical of quantum optics experiments.

In our work, presented in Quantum Sci. Technol. 10, 025024 (2025) and performed in collaboration with the group of J. Romero at the University of Queensland, we demonstrate SGT in the time-frequency domain for the first time. While multi-output detection is not fundamentally required for SGT, the mQPG significantly enhances the process by simultaneously measuring the σ_+ and σ_- states, which halves the measurement time and reduces the impact of fluctuations. This approach allowed us to achieve state estimation fidelities exceeding 99% for both 3- and 5-dimensional qudits, thereby validating SGT as a highly practical and robust method for time-frequency qudit characterization.

During our analysis, we observed a notable difference compared to previous SGT demonstrations in the spatial domain [137]: while the infidelity in those experiments appeared to decrease indefinitely with more iterations, ours reached a distinct saturation value. This unexpected behavior motivated a detailed simulation study to understand its origin. We built a realistic numerical model that incorporated all the main parameters of our experiment, based on the simulated mQPG transfer function, which included the phase-matching imperfections and crosstalk effects discussed in Chapter 4, as well as the measured noise character-

ization of the detector. Our initial hypothesis was that the fidelity was limited by measurement imperfections and detector noise—after all, it seems intuitive that one can only reconstruct a state as well as one can measure it. However, we realized that this model could not explain the convergence we were seeing. The actual culprit, it turned out, was the state preparation fidelity itself. Our system was estimating the input state extremely well, even better than the measurement fidelity would suggest, but the input states themselves were not perfect. As soon as we introduced preparation infidelity into our model, we were able to reproduce the convergence behavior with remarkable accuracy. This result highlights a key strength of SGT: its iterative and stochastic nature is remarkably resilient to measurements errors, which tend to be averaged out, allowing for a state reconstruction whose fidelity is ultimately limited only by the quality of the source.

7.2 FIREFLY

The complete characterization of the spectral amplitude, phase, and coherence of ultrashort optical pulses, especially at the single-photon level, is a long-standing challenge in quantum optics. Conventional pulse characterization techniques such as frequency-resolved optical gating (FROG) [139, 140] and spectral phase interferometry for direct electric-field reconstruction (SPIDER) [141, 142] encounter difficulties with low-light-level pulses because of the high power needed by the nonlinear processes involved. While alternative methods have been developed for single-photon pulse characterization [130, 143–145], they often require a well-characterized reference pulse, computationally intensive reconstruction algorithms, and spectrally-resolved detection. Overcoming the limitation of requiring a known reference pulse to characterize the spectro-temporal structure of an unknown quantum state has been a major goal for this field.

The second publication presented in this chapter, arXiv:2504.08607 (2025), introduces a new method that solves this problem, which we labeled “frequency-bin interferometry for reconstructing electric fields with low intensity” (FIREFLY). This method directly provides spectral amplitude, phase, and coherence profiles of single-photon pulses with minimal post-processing. While not exclusively quantum, we have demonstrated its application with both weak coherent pulses and “true” quantum states from a PDC source, showcasing its remarkable speed and precision.

To understand how FIREFLY works, let us consider the challenge of reconstructing the spectral phase profile of a pulse. Since phase is a relative quantity, we need a reference to measure it. We can choose a specific frequency component of the pulse, ω_0, as our reference and define its phase as zero. To determine the phase of any other frequency component, $\omega_0 + d$, we must interfere it with our reference. Let us imagine that we can isolate these two frequency bins and

make them interfere, neglecting for the moment how exactly one could achieve that. By applying a known, controllable phase shift ϑ to the target bin and measuring the interference intensity, we can map out a sinusoidal fringe pattern, as conceptually illustrated in the top right of Fig. 1 in the included paper. The horizontal shift of this sinusoid directly reveals the original relative phase of the target bin. Furthermore, its visibility (normalized by the intensity difference between the two spectral points) describes the degree of coherence between the two frequency points, providing a complete picture of the spectral properties of the pulse at that specific frequency separation. While one could trace the entire curve to obtain this information, in practice it is sufficient to measure the intensity at just four phase settings ($\vartheta = 0, \pi/2, \pi, 3\pi/2$). As detailed in the appendix of the included paper, these four points allow one to fully determine the complex value of the interference term, which directly yields the relative phase and degree of coherence between the target and reference frequency bins.

The question remains: how can we practically interfere different frequency components? FIREFLY achieves this using a QPG, which up-converts input signal frequencies based on the spectral shape of the pump, as described by (4.1.4). By shaping the pump into two narrow frequency bins, one fixed to select our reference frequency and one to select the target frequency, we effectively select and interfere two components of the input pulse. The controllable phase shift ϑ is applied simply by changing the relative phase between the two pump bins. By scanning the target pump bin across the spectrum of the pulse, we can reconstruct the entire complex spectral profile point by point, relative to the fixed reference. This method is remarkably direct, requiring no iterative algorithms or complex data analysis beyond simple sums and subtractions. Furthermore, since the QPG is a low-noise process, the technique is highly effective even for single-photon-level signals, and its spectral resolution is limited only by the shaping resolution of the pump.

But what if the pump pulse itself has an unknown spectral phase profile? In that case, the measurement only reveals the relative phase between the input and the pump. One could characterize the pump phase profile first, but this would require another, known reference pulse. This is where the true "magic" of this method comes into play, through its extension to an mQPG. As shown in Fig. 2 of the included paper, each output channel of the mQPG performs a similar two-bin interference measurement. The key difference is that, as we can see from (4.1.7), an output channel centered at a frequency offset Δ applies an intrinsic spectral shear[1] Δ between the interfering pump and signal frequencies, due to the energy conservation.

[1]We call this an "intrinsic spectral shear" because, although no frequencies are physically sheared, the interference pattern observed in a different output channel is mathematically equivalent to the result of shearing the pump or input frequencies before they interfere. This allows us to achieve the effect of spectral shearing without the significant experimental overhead of a dedicated shearing apparatus.

The measured phase profile for each output channel $\mu(d;\Delta)$ is then a combination of the input phase profile $\phi(\omega)$ and pump phase profile $\alpha(\omega_p)$:

$$\mu(d;\Delta) = \phi(\omega_0 + d + \Delta) - \phi(\omega_0 + \Delta) - \alpha(\omega_p^{(0)} - d), \tag{7.2.1}$$

where $\omega_p^{(0)}$ is our chosen reference point for the pump spectrum. From here, we can extract both unknown phase profiles. For instance, by simply subtracting the phase profiles reconstructed from two different output channels (e.g., at $\Delta = 0$ and $\Delta = \Delta_0$), the contribution from the unknown pump pulse can be completely eliminated, leaving a phase trace that depends only on the phase profile of the input. A simple polynomial fit to this trace is usually sufficient to reconstruct the input phase, which can then be subtracted from the original measurement to reveal the phase profile of the pump pulse. Vice versa, one can shift the two profiles before subtracting them to eliminate the input dependence first, and then fit the pump phase. This reference-free technique allows for the simultaneous characterization of two unknown pulses with the effort typically required to characterize only one. As demonstrated in the paper, this approach works exceptionally well even when both pulses are at low power levels: in the publication, we demonstrate theory-experiment similarity above 95% across all retrieved profiles.

7.3 A pulsed lidar system for single photons

The versatility of the mQPG as a tool for manipulating temporal modes also opens the door to practical applications in classical measurements. In a joint work with the Department of Electrical Engineering of Paderborn University [146], we demonstrated that the capabilities of our device could be adapted to realize a pulsed lidar system compatible with single-photon-level signals. In this application, we used the mQPG to project a returning, low-intensity optical pulse onto the zeroth- and first-order Hermite-Gaussian temporal modes. By analyzing the relative weights of the outcome of these mode projections, which the mQPG yielded simultaneously in two different output channels, we could precisely determine the arrival time of the pulse [58, 147], and thus the distance to the target, with high accuracy. This work demonstrates that the mode-sorting capabilities of the mQPG, initially developed for decoding high-dimensional quantum information, provide a powerful and resource-efficient tool for classical precision metrology.

IOP Publishing Quantum Sci. Technol. 10 (2025) 025024 https://doi.org/10.1088/2058-9565/adb0ea

Quantum Science and Technology

OPEN ACCESS

RECEIVED
28 November 2024

REVISED
24 January 2025

ACCEPTED FOR PUBLICATION
31 January 2025

PUBLISHED
11 February 2025

PAPER

Self-guided tomography of time-frequency qudits

Laura Serino[1,*], **Markus Rambach**[2,3], **Benjamin Brecht**[1], **Jacquiline Romero**[2,3] and **Christine Silberhorn**[1]

[1] Paderborn University, Integrated Quantum Optics, Institute for Photonic Quantum Systems (PhoQS), Warburgerstr. 100, 33098 Paderborn, Germany
[2] Australian Research Council Centre of Excellence for Engineered Quantum Systems, Brisbane, Queensland 4072, Australia
[3] School of Mathematics and Physics, University of Queensland, Brisbane, Queensland 4072, Australia
[*] Author to whom any correspondence should be addressed.

E-mail: laura.serino@upb.de

Keywords: quantum optics, time frequency, quantum tomography, frequency conversion, qudits

Abstract

High-dimensional time-frequency encodings have the potential to significantly advance quantum information science; however, practical applications require precise knowledge of the encoded quantum states, which becomes increasingly challenging for larger Hilbert spaces. Self-guided tomography (SGT) has emerged as a practical and scalable technique for this purpose in the spatial domain. Here, we apply SGT to estimate time-frequency states using a multi-output quantum pulse gate. We achieve fidelities of more than 99% for 3- and 5-dimensional states without the need for calibration or post-processing. We demonstrate the robustness of SGT against statistical and environmental noise, highlighting its efficacy in the photon-starved regime typical of quantum information applications.

1. Introduction

The time-frequency degree of freedom of photons is gaining increasing attention in quantum information science due to its unique advantages [1–5]. It naturally supports high-dimensional encoding alphabets, allowing for the transmission of more information per photon compared to conventional binary systems [6, 7]. This increased information density enhances resilience to noise and eavesdropping in quantum cryptography protocols and, therefore, makes high-dimensional encodings particularly advantageous for secure communication [8–13]. Additionally, the time-frequency domain offers greater resilience in transmission than the polarization and spatial degrees of freedom and is uniquely compatible with single-spatial-mode optical fibers, which are integral to modern telecommunication networks.

For practical applications of time-frequency encodings in quantum information science, precise knowledge of the encoded states is essential. In high dimensions, the process of characterizing quantum states—known as quantum state tomography—becomes inherently challenging due to the large associated Hilbert space. Namely, for a single qudit, the parameter space to be characterized grows as $d^2 - 1$, where d is the dimension of the qudit [14, 15]. Standard quantum state tomography techniques, which apply the maximum-likelihood method to the results of an over-complete set of measurements [16–18], and alternative interferometric methods [19–21] become increasingly resource-expensive for large Hilbert spaces due to the significantly greater number of required measurements. Techniques such as compressive tomography [22–24] require fewer measurements for an accurate quantum state estimation; however, the estimation algorithms are sensitive to noise and become more computationally demanding for high-dimensional systems. Moreover, in practical applications with imperfect detectors, many tomography techniques require an error calibration of the experimental setup to incorporate into the reconstruction algorithm and achieve reliable results [17, 25, 26].

Self-guided tomography (SGT) [27] is an alternative technique that facilitates the estimation of a quantum state by maximizing its overlap with an iteratively updated guess without requiring any calibration or post-processing analysis. This method has been applied to the polarization [28] and spatial [29] degrees of freedom of photons, and has also been extended to perform quantum process tomography [30]. In these

IOP Publishing Quantum Sci. Technol. 10 (2025) 025024 L Serino et al

applications, SGT has demonstrated scalability to high dimensions and resilience to statistical and environmental noise, which makes it particularly effective in the photon-starved regime.

In this work, we demonstrate the advantage of SGT applied to the time-frequency domain by accurately estimating a high-dimensional input state encoded in this degree of freedom. Using a so-called multi-output quantum pulse gate (mQPG) [26], we perform time-frequency projections and iteratively update the estimated state based on the results of their outcome. We achieve a fidelity to the encoded input state above 99% in 3 and 5 dimensions, approaching the fidelity limit of the state preparation setup. Through SGT, we demonstrate the direct estimation of the quantum state without any calibration or post-processing, even in the presence of strong statistical and environmental noise.

2. Method

The problem of quantum state tomography requires characterizing an unknown input state $|\bar{\psi}\rangle$ from a chosen Hilbert space. We choose a space described by temporal modes [1], i.e. field-orthogonal wave-packet modes that encode information in the complex spectral amplitude of the electric field. Namely, we use the first d Hermite–Gaussian modes $\{|\alpha_j\rangle\}_{j=1,..,d}$ as the computational basis of our d-dimensional Hilbert space. In this space, the input state can be expressed as $|\bar{\psi}\rangle = \sum_j c_j|\alpha_j\rangle$, where c_j are complex coefficients. We note that this description intrinsically assumes a single-photon state in input and focuses solely on the temporal-mode structure of the state. We assume pure input states, as in the original formulation of SGT [27], although this technique can also be adapted to mixed states if necessary [29].

To implement SGT, we begin by generating a set of random complex coefficients c_j^0 to provide an initial guess of the target state: $|\psi^0\rangle = \sum_j c_j^0|\alpha_j\rangle$. At each iteration k of the algorithm, this estimate will be updated to a more accurate $|\psi^k\rangle = \sum_j c_j^k|\alpha_j\rangle$ based on the result of the time-frequency projections performed by the mQPG (figure 1).

The mQPG [26] serves as a mode-sorter for single-photon-level time-frequency states. Its working principle is based on sum-frequency generation in a dispersion-engineered nonlinear waveguide driven by a spectrally shaped pump pulse [31]. The mQPG operation is described by a transfer function, which is the product of the energy conservation condition, determined by the pump function, and the phase-matching function, describing momentum conservation (see inset in figure 2). By choosing a pump wavelength that is group-velocity-matched to the input wavelength in the nonlinear medium, we achieve a horizontal phase-matching function that facilitates mode-selective operation in each channel of the mQPG [17, 32]. Thus, the probability of upconversion in each channel is proportional to the complex spectral overlap between the input mode $|\bar{\psi}\rangle$ and the pump mode $|\sigma\rangle$, which can be selected via spectral shaping. Effectively, the mQPG projects a high-dimensional input state onto the selected pump modes and yields the result of each projection into a separate output channel, corresponding to a distinct output frequency that can be read out using a spectrograph.

The states for the projections at each iteration k are chosen starting from the most updated guess $|\psi^k\rangle$. We perturb each complex coefficient c_j^k in a random direction $(\Delta_k)_j \in \{1, -1, i, -i\}$ [33] with strength $\beta_k = b/(k+1)^t$, where b and t are hyperparameters of the algorithm, optimised once by trial and error in simulations. From this perturbation, we obtain the two states $|\sigma_\pm^k\rangle = |\psi^k \pm \beta_k\Delta_k\rangle$, and we assign each to a channel of a two-output mQPG. The mQPG projects $|\bar{\psi}\rangle$ onto $|\sigma_+^k\rangle$ and $|\sigma_-^k\rangle$ and yields the results of the projections as N_+ and N_- clicks detected in the respective channels.

From the pseudo-normalized quantity $\delta N = (N_+ - N_-)/(N_+ + N_-)$, we calculate the gradient $g_k = \delta N\Delta_k/2\beta_k$ which indicates the magnitude and direction of the distance vector between the target state $|\bar{\psi}\rangle$ and its estimate $|\psi^k\rangle$. We use this gradient to compute the next estimate in the iteration as $|\psi^{k+1}\rangle = |\psi^k + \alpha_k g_k\rangle$, where $\alpha_k = a/(k+1+A)^s$ determines the step size in the direction of the gradient, with a, A and s algorithm hyperparameters.

This iterative procedure is repeated for a chosen number of steps K, after which we obtain the final estimation $|\psi^K\rangle$. We then calculate the infidelity $1 - \left|\langle\psi^K|\bar{\psi}\rangle\right|^2$ to quantify the residual distance between the reconstructed state $|\psi^K\rangle$ and the target state $|\bar{\psi}\rangle$.

3. Experiment

Figure 2 shows a schematic of the experimental setup. Input and pump pulses are generated by an optical parametric oscillator (OPO) system driven by an ultrafast Ti:Sapph laser emitting 150 fs coherent pulses at a repetition rate of 80 MHz. The input pulse, centred at 1545 nm, is shaped by a commercial waveshaper (Finisar 4000S) into a random superposition $|\bar{\psi}\rangle$ of the first d Hermite–Gaussian functions, with $d \in \{3, 5\}$ dimensionality of the Hilbert space.

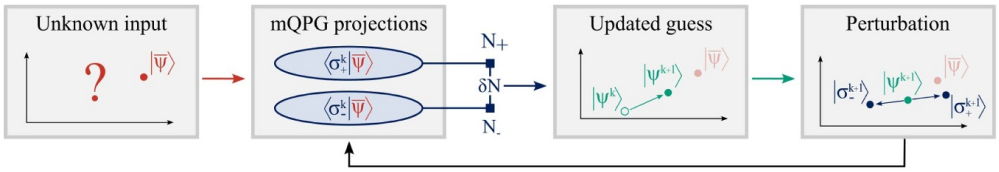

Figure 1. Schematic representation of the SGT procedure. The estimate $|\psi^k\rangle$ (initially a random guess) is iteratively updated based on the result of the projections of the true input state $|\bar{\psi}\rangle$ onto the two states $|\sigma_\pm^k\rangle$, obtained perturbing the latest estimate $|\psi^k\rangle$ in two opposite directions.

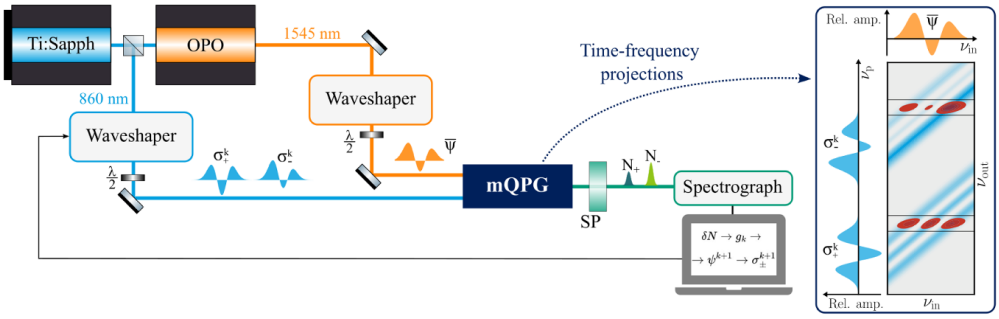

Figure 2. Schematic of the experimental setup. An optical parametric oscillator (OPO) system driven by an ultrafast Ti:Sapph laser produces the input (orange) and pump (blue) pulses. The input state $|\bar{\psi}\rangle$ is generated by a commercial waveshaper (Finisar 4000S), whereas the pump pulse is shaped by an in-house-built folded 4-f waveshaper [34] to generate $|\sigma_\pm^k\rangle$. Using two half-waveplates, we align the polarization of input and pump to horizontal and vertical, respectively, as required by the mQPG process. The mQPG projects $|\bar{\psi}\rangle$ onto $|\sigma_\pm^k\rangle$, yielding the results as N_+ and N_- upconverted photons in the two output channels. The inset shows the frequency-space representation of the mQPG projections, described by a transfer function (red), which is the product of the phase-matching function (contoured by horizontal black lines) and the energy conservation condition determined by the pump spectrum (blue). A CCD spectrograph (Andor Shamrock 500i) detects the output photons, discriminating the two output frequencies. From the pseudo-normalized difference in counts δN, we calculate the gradient g_k to determine the next estimation $|\psi^{k+1}\rangle$ which, in turn, is the starting point for $|\sigma_\pm^{k+1}\rangle$ in the following iteration.

The first estimate $|\psi^0\rangle$ of the input state is chosen randomly, and its coefficients are perturbed in two opposite directions to find the two states $|\sigma_\pm^0\rangle$ used for the mQPG projections. The pump pulse, centred at 860 nm, is shaped by an in-house-built folded 4-f waveshaper [34, 35] to generate the complex spectra of $|\sigma_+^0\rangle$ and $|\sigma_-^0\rangle$. This custom-built waveshaper is necessary because commercial waveshapers are not yet available for this wavelength range.

The mQPG waveguide used in this experiment is realized in-house in titanium in-diffused lithium niobate operated at 160 °C, with a periodic poling pattern consisting of an alternation of unpoled regions and regions which are poled with a period of 4.32 μm [26]. This pattern enables the mQPG to perform time-frequency projections in two different channels centred at two distinct frequencies. The spectra of $|\sigma_\pm^0\rangle$ in the pump pulse, therefore, are centred at two offset frequencies matched to the two output frequencies of the mQPG.

Input and pump pulses are coupled into the mQPG waveguide with a coupling efficiency of 70% and 50%, respectively. The waveguide propagation losses, below 0.1 dB at 1550 nm, are negligible in comparison. The mQPG projects the input state $|\bar{\psi}\rangle$ onto $|\sigma_+^0\rangle$ and $|\sigma_-^0\rangle$, upconverting each copy of the input state (i.e. each input photon) in the '+' or '−' channel with probability proportional to the overlap $\left|\langle\sigma_\pm^0|\bar{\psi}\rangle\right|^2$. The upconverted photons are detected by a single-photon-sensitive spectrograph (Andor Shamrock 500i), which discriminates the output frequencies and integrates over multiple pulses, providing the total counts N_+ and N_- observed in each channel during the integration period.

From these counts, we calculate the first gradient g_0 to determine the next estimate $|\psi^1\rangle$. This procedure is repeated for each iteration k, refining the estimate $|\psi^k\rangle$ closer to the true input state $|\bar{\psi}\rangle$. We perform a total of $K = 200$ iterations in $d = 3$ and $K = 300$ in $d = 5$.

For each dimensionality ($d = 3$ and $d = 5$), we repeated the SGT procedure on 100 different input states chosen randomly with Haar measure [36]. We tested this method on the same set of input states in different conditions of statistical noise quantified by $\sqrt{N}/N$, where N denotes the number of maximum counts in each channel when the input and pump states perfectly overlap. The values $N = 10^2$, $N = 10^3$ and $N = 10^4$ were

IOP Publishing Quantum Sci. Technol. 10 (2025) 025024 L Serino et al

achieved by adjusting the integration time of the spectrograph from 1 to 10 ms and 100 ms, corresponding to approximately 2.5×10^{-2} clicks per pulse; $N = 10^5$ was obtained with an integration time of 100 ms and a larger photon number in the input, resulting in approximately 2.5×10^{-2} clicks per pulse. Additionally, we performed standard tomography based on maximum-likelihood estimation [17] with a single channel of the mQPG under identical noise conditions and with the same input states for a comparative analysis.

We note that the spectrograph output was strongly affected by electronic read-out noise with a mean of 890 counts and a standard deviation $\sigma = 14$ in each channel. This was the dominant source of environmental noise during the measurements and was independent of the integration time. To limit its impact, we subtracted the minimum 'constant' background value of 820, chosen at a distance of 5σ from the mean to prevent negative count artifacts. This correction left a residual background of 70 counts per channel with the same standard deviation σ as the main source of environmental noise.

To complement the experimental data, we performed realistic simulations of the SGT process taking into account the measured electronic noise and the imperfect mQPG projections. We used these simulations to find the set of hyperparameters (b, t, a, A, s) that optimized the convergence of the estimated quantum state. We then fine-tuned these values in the experiment, observing how they affected the convergence rate of the infidelity for the same input state.

4. Results and discussion

Figure 3 shows (in colour) the median infidelity of the reconstructed states at each iteration of the process. For high photon numbers, we reach 10% infidelity after only 10 iterations in $d = 3$ and 20 iterations in $d = 5$. These values are similar to what Rambach *et al* [29] obtained in the spatial domain for the same dimensionalities, showcasing the adaptability of SGT to different experimental implementations.

However, after this value, the decrease in infidelity slows down until it reaches a plateau. This is in contrast to the results achieved in the spatial domain, where the infidelity continued to decrease indefinitely within the measured number of iterations. Notably, tuning the hyperparameters only affects the convergence speed but not the final infidelity.

The saturation of the infidelity can be attributed to a combination of two factors: systematic errors of the measurement device and imperfections in the preparation of the input states. Although we assumed ideal input preparation when calculating the infidelity of the estimated states, an infidelity of 1% in the waveshaping system that generates the input states can significantly decrease the maximum precision achievable by SGT. Additionally, although this technique is highly resilient to statistical noise due to its iterative and randomised component, it can still be affected by systematic noise from imperfect mQPG operation [17, 26, 37].

The black lines in figure 3 show the simulated results of the SGT process based on the measured electronic noise and mQPG imperfections (quantified as average cross-talk between orthogonal states [26]), in addition to an estimated infidelity in the input preparation of $(0.6 \pm 0.1)\%$ in $d = 3$ and $(0.9 \pm 0.1)\%$ in $d = 5$. We find excellent agreement between the simulation results and the experimental infidelity curve, visible both in the convergence rate and in the saturation value of the infidelity, thus supporting the assumptions on the imperfections in the input preparation.

Figure 4 illustrates the isolated effects of different types of imperfections (environmental noise, systematic errors in the measurement device and preparation infidelity) on the two datasets in $d = 5$ with $N = 10^3$ and $N = 10^4$. We always show the experimental data and realistic simulation for comparison as coloured and black solid lines, respectively. In each column, we study the effect of each particular type of imperfection by changing its value in the simulations. The dotted lines are the results of simulations in which we completely remove that source of error; the only visible improvement is observed when the preparation infidelity is eliminated (last column in figure 4). The dashed lines show the effect of an increase in the selected error source (10 times greater environmental noise, 10 times more systematic measurement imperfections, and 3 times larger preparation infidelity), keeping the others unchanged. While this leads to a larger final infidelity in general, the dataset with fewer counts is significantly more affected by an increase in the environmental noise. Overall, one can notice that the limited preparation quality of the input states represents the most significant constraint to the minimum achievable infidelity in the current experimental conditions.

Despite this technical limitation, SGT consistently achieves lower infidelity than standard maximum-likelihood tomography [17] performed with the same experimental setup in identical environmental conditions (see table 1 for detailed comparisons). Notably, the estimate of the input state is known in real-time at every step of the process without requiring post-processing.

Furthermore, SGT demonstrates superior performance even under low count rates. In both dimensionalities, we achieve infidelities of approximately 1% with only 10^3 counts per measurement. Even with as few as 100 counts per measurement, the infidelity decreases with each iteration, albeit more slowly,

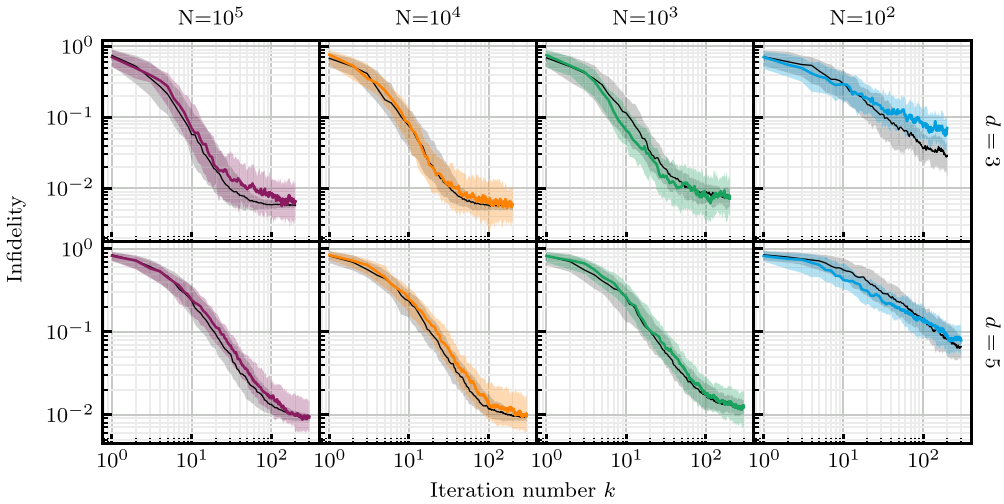

Figure 3. The coloured lines show the experimental infidelities of the reconstructed states at each iteration of the SGT algorithm for different values N of the maximum counts per iteration in each channel. The lines represent the median infidelity of the complete population of 100 different input states, whereas the shaded area shows the upper and lower quartile of the infidelities $(50 \pm 25)\%$. In close agreement with the experiment, the black lines show the results of simulations that take into account experimental imperfections, as detailed in the main text.

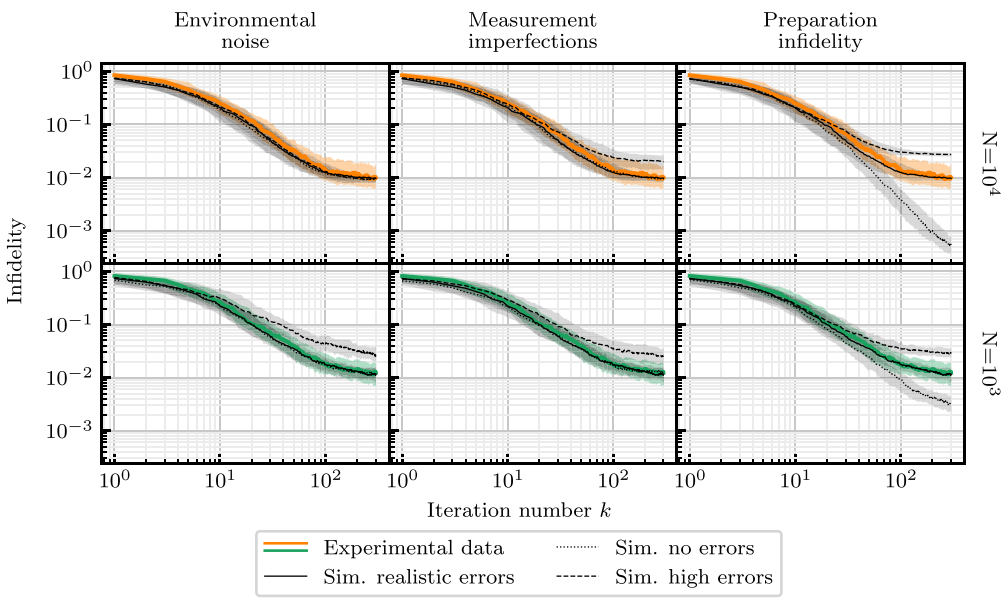

Figure 4. Effect of different sources of imperfections on the SGT convergence curve based on the same set of 100 input states in $d = 5$ for the two statistics $N = 10^3$ and $N = 10^4$. The experimental data (coloured line) and the realistic simulation (solid black line), are the same as shown in figure 3. The simulation incorporates realistic experimental errors based on the measured electronic noise and mQPG imperfections, and on the estimated infidelity in the input preparation, as detailed in the main text. The very good overlap between the experimental data and the simulation indicates a good understanding of the experimental errors in the system. In each column, we change the value of a particular type of error in the simulations: the dotted lines show what happens when we completely remove that source of error, whereas the dashed lines show the effect of an increase in that error source (10 times greater environmental noise and measurement imperfections, 3 times larger preparation infidelity). The dotted line is clearly visible only in the rightmost plots, suggesting that preparation infidelity is likely the major limiting factor in the quality of the reconstructed states. See the text for more information.

reaching 10% after approximately 100 iterations in $d = 3$ and 200 iterations in $d = 5$. This resilience to statistical noise highlights SGT as an optimal method for quantum state tomography in the photon-starved regime.

Table 1. Comparison of the final infidelity achieved through SGT and through maximum-likelihood state tomography (MLST) [17] performed with the same experimental setup in identical environmental conditions. The values indicate the median value over a set of 100 random input states, and the error shows the upper and lower quartile values of the distribution. The same set of input states was characterized with both methods.

	$d = 3$		$d = 5$	
N	SGT	MLST	SGT	MLST
10^5	$0.65^{+0.51}_{-0.29}\,\%$	$0.88^{+0.58}_{-0.47}\,\%$	$0.94^{+0.54}_{-0.33}\,\%$	$3.24^{+1.02}_{-0.52}\,\%$
10^4	$0.60^{+0.38}_{-0.24}\,\%$	$0.78^{+0.34}_{-0.49}\,\%$	$1.01^{+0.71}_{-0.36}\,\%$	$2.67^{+0.79}_{-0.72}\,\%$
10^3	$0.76^{+0.55}_{-0.35}\,\%$	$0.48^{+0.88}_{-0.22}\,\%$	$1.23^{+0.62}_{-0.55}\,\%$	$3.86^{+0.90}_{-1.02}\,\%$
10^2	$7.0^{+3.0}_{-3.4}\,\%$	$13.1^{+8.0}_{-6.0}\,\%$	$7.9^{+3.7}_{-3.0}\,\%$	$39.6^{+4.7}_{-5.3}\,\%$

5. Conclusion

We applied SGT for the first time to time-frequency qudits, showcasing the versatility of this method in different degrees of freedom. We achieved a fidelity of the estimated states above 99% in 3 and 5 dimensions without the need for calibration or post-processing. The experimental results highlight the resilience of this technique to statistical and environmental noise, favoured by its iterative character. Through realistic simulations that closely reproduce the experimental data, we infer that the ultimate fidelity of our estimates is predominantly limited by the accuracy of the input state preparation. These results demonstrate the robust and adaptable nature of this technique, paving the way for further exploration and potential applications in quantum information science.

Data availability statement

Data underlying the results presented in this paper are not publicly available at this time but may be obtained from the authors upon reasonable request.

Acknowledgments

The authors would like to thank C Ferrie for helpful and inspiring discussions. L S has received funding from the European Union's Horizon Europe research and innovation programme under Grant Agreement No 899587 (STORMYTUNE). J R and M R are supported by Australian Research Council Centre of Excellence for Engineered Quantum Systems (EQUS, CE170100009).

ORCID iDs

Laura Serino https://orcid.org/0000-0002-5954-047X
Markus Rambach https://orcid.org/0000-0002-4659-3804
Benjamin Brecht https://orcid.org/0000-0003-4140-0556
Jacquiline Romero https://orcid.org/0000-0002-5840-2606
Christine Silberhorn https://orcid.org/0000-0002-2349-5443

References

[1] Brecht B, Reddy D V, Silberhorn C and Raymer M G 2015 *Phys. Rev.* X **5** 041017
[2] Ansari V, Donohue J M, Brecht B and Silberhorn C 2018 *Optica* **5** 534–50
[3] Wang J, Sciarrino F, Laing A and Thompson M G 2020 *Nat. Photon.* **14** 273–84
[4] Raymer M G and Walmsley I A 2020 *Phys. Scr.* **95** 064002
[5] Lu H-H, Liscidini M, Gaeta A L, Weiner A M and Lukens J M 2023 *Optica* **10** 1655
[6] Leach J, Bolduc E, Gauthier D J and Boyd R W 2012 *Phys. Rev.* A **85** 060304
[7] Wang Y, Hu Z, Sanders B C and Kais S 2020 *Front. Phys.* **8** 589504
[8] Bechmann-Pasquinucci H and Tittel W 2000 *Phys. Rev.* A **61** 062308
[9] Cerf N J, Bourennane M, Karlsson A and Gisin N 2002 *Phys. Rev. Lett.* **88** 4
[10] Sheridan L and Scarani V 2010 *Phys. Rev.* A **82** 030301
[11] Lim N T, Ci C W, Cahall C and Kim J D J 2017 *Sci. Adv.* **3** e1701491
[12] Ecker S *et al* 2019 *Phys. Rev.* X **9** 1–12
[13] Cozzolino D, Da Lio B, Bacco D and Oxenløwe L K 2019 *Adv. Quantum Technol.* **2** 1900038
[14] Banaszek K, D'Ariano G M, Paris M G A and Sacchi M F 1999 *Phys. Rev.* A **61** 010304
[15] Thew R T, Nemoto K, White A G and Munro W J 2002 *Phys. Rev.* A **66** 012303
[16] Hradil Z 1997 *Phys. Rev.* A **55** R1561–4
[17] Ansari V, Harder G, Allgaier M, Brecht B and Silberhorn C 2017 *Phys. Rev.* A **96** 063817

[18] Bhattacharjee A, Folge P, Serino L, Řeháček J, Hradil Z, Silberhorn C and Brecht B 2025 Pulse characterization at the single-photon level through chronocyclic Q-function measurements *Opt. Express* **33** 5551–61
[19] Wasilewski W, Kolenderski P and Frankowski R 2007 *Phys. Rev. Lett.* **99** 123601
[20] Davis A O C, Thiel V, Karpiński M and Smith B J 2018 *Phys. Rev. Lett.* **121** 083602
[21] Thiel V, Davis A O C, Sun K, D'Ornellas P, Jin X-M and Smith B J 2020 *Opt. Express* **28** 19315–24
[22] Gross D, Liu Y-K, Flammia S T, Becker S and Eisert J 2010 *Phys. Rev. Lett.* **105** 150401
[23] Ahn D *et al* 2019 *Phys. Rev. Lett.* **122** 100404
[24] Gil-Lopez J, Teo Y S, De S, Brecht B, Jeong H, Silberhorn C and Sánchez-Soto L L 2021 *Optica* **8** 1296
[25] Cooper M, Karpiński M and Smith B J 2014 *Nat. Commun.* **5** 4332
[26] Serino L, Gil-Lopez J, Stefszky M, Ricken R, Eigner C, Brecht B and Silberhorn C 2023 *PRX Quantum* **4** 020306
[27] Ferrie C 2014 *Phys. Rev. Lett.* **113** 2–6
[28] Chapman R J, Ferrie C and Peruzzo A 2016 *Phys. Rev. Lett.* **117** 040402
[29] Rambach M, Qaryan M, Kewming M, Ferrie C, White A G and Romero J 2021 *Phys. Rev. Lett.* **126** 100402
[30] Hou Z, Tang J-F, Ferrie C, Xiang G-Y, Li C-F and Guo G-C 2020 *Phys. Rev.* A **101** 022317
[31] Brecht B, Eckstein A, Ricken R, Quiring V, Suche H, Sansoni L and Silberhorn C 2014 *Phys. Rev.* A **90** 030302(R)
[32] Eckstein A, Brecht B and Silberhorn C 2011 *Opt. Express* **19** 13770–8
[33] Utreras-Alarcón A, Rivera-Tapia M, Niklitschek S and Delgado A 2019 *Sci. Rep.* **9** 16143
[34] Monmayrant A, Weber S and Chatel B 2010 *J. Phys.* B **43** 103001
[35] Weiner A M 2000 *Rev. Sci. Instrum.* **71** 1929–60
[36] Mezzadri F 2007 *Not. Am. Math. Soc.* **54** 592–604
[37] Gil-Lopez J, Santandrea M, Roeland G, Brecht B, Eigner C, Ricken R, Quiring V and Silberhorn C 2021 *New J. Phys.* **23** 063082

Frequency-bin interferometry for reconstructing electric fields with low intensity

Abhinandan Bhattacharjee[†,*], Laura Serino[†], Patrick Folge[†], Benjamin Brecht, and Christine Silberhorn
Integrated Quantum Optics Group, Institute for Photonic Quantum Systems (PhoQS), Paderborn University, Warburger Straße 100, 33098 Paderborn, Germany and
[†] *These authors contributed equally to this work.*
[*] *abhib@mail.uni-paderborn.de*

Ultrafast single-photon pulses with tailored time-frequency properties are highly attractive for quantum information science, offering high-dimensional encoding and compatibility with integrated optics platforms. However, accurate characterization of such pulses, including spectral coherence, remains challenging because current methods require substantial experimental resources and complex reconstruction algorithms. Here, we introduce frequency-bin interferometry for reconstructing electric fields with low intensity (FIREFLY), a technique that directly provides spectral amplitude, phase, and coherence profiles of single-photon pulses without requiring intensive reconstruction algorithms. Our approach measures the two-point spectral correlation function of the pulse by interfering its different frequency components using a quantum pulse gate (QPG) driven by a reference pump pulse. We demonstrate its compatibility with quantum light by characterizing partially coherent pulses generated by a type-0 parametric down-conversion process. We also overcome this requirement of a known pump pulse by introducing spectral shear into our interferometric scheme using a multi-output QPG (mQPG). This enables simultaneous characterization of a single-photon-level input pulse alongside an unknown pump pulse. Notably, our method achieves theory-experiment similarity above 95% across all retrieved profiles, which demonstrates the reliability of this scheme for quantum information applications based on time-frequency encodings.

I. Introduction

The rapid growth in photonic quantum technology [1–3] has highlighted the importance of single-photon ultrafast pulses [4–6]. The time-frequency (TF) properties, or mode structure, of such pulses serve as a powerful resource for quantum information applications, including quantum computing [7, 8], quantum communication [9, 10], and quantum metrology [11–14]. The high-dimensionality, compatibility with integrated optics platforms, and resilience over long-distance propagation further enhance the suitability of TF mode structure for scalable quantum technologies. Harnessing these advantages requires precise and complete characterization of the TF properties, namely spectral amplitude, phase, and coherence information. Moreover, any quantum information applications demand complete information on single-photon states, hence the knowledge of spectral coherence (or purity) is particularly crucial. However, characterizing spectral coherence and phase profiles poses challenges for single-photon pulses.

Conventional pulse characterization techniques such as frequency-resolved optical gating (FROG) [15, 16], spectral phase interferometry for direct electric-field reconstruction (SPIDER) [17–19], and several of their extensions [20–26] encounter difficulties with low-light level pulses because the nonlinear processes involved in these techniques demand bright input pulses. Alternative methods, such as electro-optic shearing interferometry (EOSI) [27–29], two-photon spectral interferometry (TPSI) [30–32], homodyne tomography (HT) [33], Hong-Ou-Mandel interferometry (HOMI) [34], and chronocyclic $Q-$function tomography [35] have been used for single-photon pulse characterization. TPSI, HT, and HOMI can characterize pulses with arbitrary spectral coherence, but they require a spatially mode-matched and spectrally known reference pulse and coincidence detection. On the other hand, EOSI and $Q-$function tomography have only been demonstrated for perfectly coherent pulses. All of these techniques rely on computationally intensive reconstruction algorithms, and often struggle to detect complex spectral features such as phase jumps. Moreover, their implementations require resources such as modulators for temporal phase manipulation, interferometric stability, long measurement time, and spectrally resolved coincidence measurements.

In this article, we present frequency-bin interferometry for reconstructing electric fields with low intensity (FIREFLY), a direct, reference-free, and quantum-compatible pulse characterization technique adapted from optical coherence theory [36]. FIREFLY measures the two-point spectral correlation (TPSC) function of single-photon-level pulses and directly yields the spectral amplitude, phase, and coherence profiles without employing a complex reconstruction algorithm. Similar approaches have been widely used for characterizing mode structure and coherence information in the spatial domain [37–40]. Our scheme harnesses a quantum pulse gate (QPG) [41–45], an integrated dispersion engineered sum-frequency conversion process, to interfere different spectral components of the input pulse and extract the TPSC function by measuring the output counts. First, we demonstrate high-quality characterization of spectrally perfectly coherent pulses from a mode-locked laser attenuated to the single-photon-level. Subsequently, we use FIREFLY to characterize spectrally partially coherent quantum pulses generated by a spectrally multi-mode type-0 parametric down-conversion (PDC) process, high-

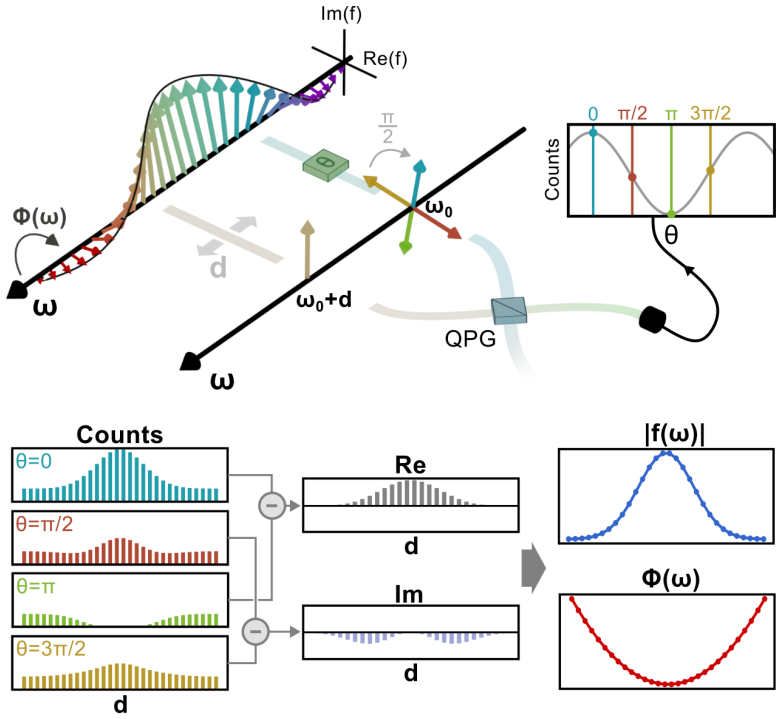

FIG. 1. Conceptual illustration of our approach for characterizing single-photon pulses by measuring their two-point spectral correlation (TPSC) function. In the illustration, the orientation of the vector represents the spectral phase, while its length corresponds to the spectral amplitude at a specific frequency. Our approach interferes different spectral components of the pulse under test using and measure the interfering count distribution as a function of their separation at different relative phase. Using these count distributions, we directly obtain the real and imaginary parts of the TPSC function, which provide the spectral amplitude and phase profiles.

lighting its compatibility with quantum light.

In the first implementation, we assume access to a characterized pump pulse, which serves as a reference pulse. We then eliminate this requirement by extending FIREFLY to a multi-output QPG (mQPG) [46] with multiple sum-frequency conversion output channels. Each output channel provides access to shifted relative phase profiles between input and pump, which we combine to reconstruct both pulses, demonstrating for the first time the simultaneous characterization of a single-photon level input pulse alongside an unknown bright pump pulse. We further showcase the practicality of this scheme by characterizing both pulses at the low light level without requiring a reference.

II. Theory

A. Concept

We consider a single-photon ultrafast pulsed field that is single-mode in both polarization and spatial degrees of freedom, with arbitrary spectral coherence. The complete TF properties of such a state are described by the two-point spectral correlation (TPSC) function $W(\omega_1, \omega_2)$, which quantifies the correlation between the complex spectral amplitudes at frequencies ω_1 and ω_2, and is defined as

$$W(\omega_1, \omega_2) = \langle f^*(\omega_1) f(\omega_2) \rangle_e, \tag{1}$$

where $f(\omega)$ is the complex spectral amplitude of the electric field at frequency ω, and $\langle\rangle_e$ represents the ensemble average. The TPSC function serves as the spectral analog of a density matrix.

For spectrally perfectly coherent pulses, $W(\omega_1, \omega_2) = f^*(\omega_1) f(\omega_2)$, and $f(\omega) = |f(\omega)| e^{i\phi(\omega)}$ completely characterizes the TF mode structure. Here, $|f(\omega)|$ and $\phi(\omega)$ represent the spectral amplitude and phase profiles, respectively. For partially coherent pulses, $W(\omega_1, \omega_2)$ yields the spectral coherence profile as a function of the frequency separation $\Delta\omega \equiv \omega_1 - \omega_2$. This approach enables the complete characterization of single-photon pulses, regardless of their spectral coherence property. Characterizing both spectral phase and coherence typically requires interfering different spectral components of a pulse, a challenging task for single-photon states. We achieve this frequency interference using a QPG, a dispersion-engineered sum-frequency conversion process realized in an integrated waveguide [41–45]. Traditionally, this device has been used as a beam splitter for TF

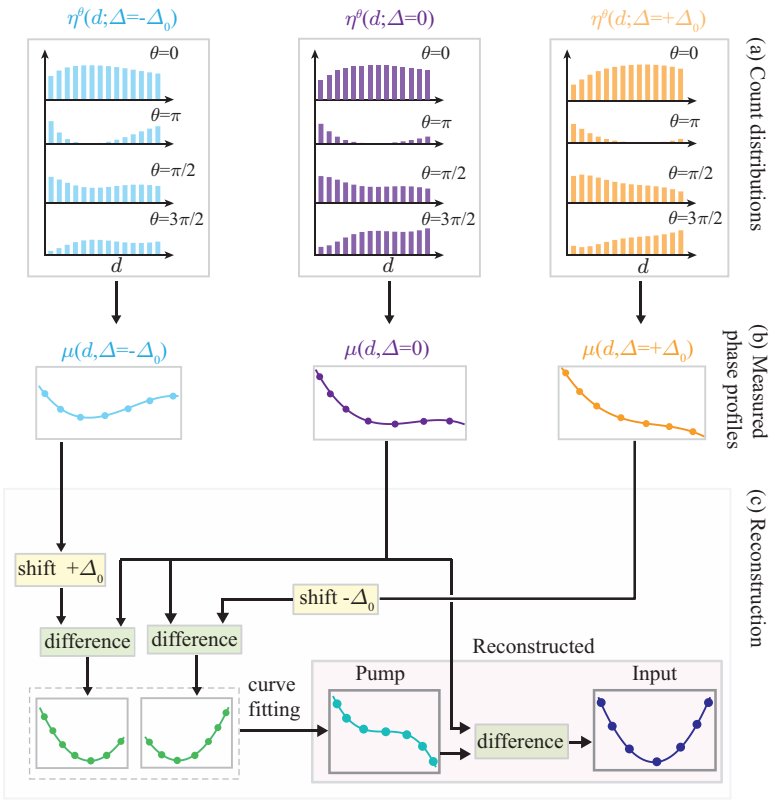

FIG. 2. Steps for characterizing the spectral phase profiles of both input and pump pulses using an mQPG. (a) Count distributions for different shearing Δ (corresponding to different mQPG output channels). (b) Phase profiles $\mu(d,\Delta)$ corresponding to different shearing Δ obtained from the above count distributions. (c) Reconstruction steps for extracting the input and pump phase profiles from $\mu(d,\Delta)$ profiles.

modes, selected by spectral shaping of the pump pulse. In this approach, we use the QPG to enable interference between input frequencies by shaping the pump as a superposition of spectral bins. By measuring the up-converted photon counts at the QPG output, we extract the TPSC function, which directly yields the spectral phase and coherence information without requiring reconstruction algorithms.

This first scheme can directly characterize a single-photon input pulse assuming prior knowledge of the pump pulse. In the next step, we eliminate this requirement, and we characterize both input and pump pulses by implementing the same scheme on an mQPG [46]. Each output channel of the mQPG applies the equivalent of a well-defined spectral shearing between pump and input frequencies. By measuring photon counts at all the output channels, we reconstruct the spectral phase profile of the pump, and we combine it with the output count data to characterize the input pulse. Our approach harnesses the QPG and mQPG as powerful tools for direct and reference-free characterization of ultrafast single-photon pulses.

B. Measurement scheme: general idea and implementation

The proposed scheme for measuring the TPSC function is illustrated in Fig. 1. In this scheme, we use a QPG to interfere complex spectral amplitudes $f(\omega_0)$ and $f(\omega_0+d)$ at frequencies ω_0 and ω_0+d, respectively, with a controlled additional relative phase θ. The resulting interference count distribution $\eta^\theta(d)$ at the output of the QPG as a function of d and θ is given by

$$\eta^\theta(d) = |f(\omega_0) + f(\omega_0+d)e^{i\theta}|^2. \quad (2)$$

This can be rewritten in terms of the TPSC function $W(\omega_0,\omega_0+d)$ as

$$\eta^\theta(d) = |f(\omega_0)|^2+|f(\omega_0+d)|^2+2\mathrm{Re}[W(\omega_0,\omega_0+d)]\cos\theta + 2\mathrm{Im}[W(\omega_0,\omega_0+d)]\sin\theta, \quad (3)$$

where $\mathrm{Re}[W(\omega_0,\omega_0+d)]$ and $\mathrm{Im}[W(\omega_0,\omega_0+d)]$ are the real and imaginary parts of $W(\omega_0,\omega_0+d)$ respectively. Therefore, for each separation d, we measure $\eta^\theta(d)$ at

$\theta \in \{0, \frac{\pi}{2}, \pi, \frac{3\pi}{2}\}$ and then extract $W(\omega_0, \omega_0 + d)$ using

$$W(\omega_0, \omega_0 + d) \propto \left[\eta^{\theta=0}(d) - \eta^{\theta=\pi}(d)\right] + i\left[\eta^{\theta=\frac{\pi}{2}}(d) - \eta^{\theta=\frac{3\pi}{2}}(d)\right]. \quad (4)$$

By varying d, this method enables direct measurement of the TPSC function $W(\omega_0, \omega_0+d)$, as shown in Fig. 1. The meaning of this measured TPSC function $W(\omega_0, \omega_0 + d)$ relies on the spectral coherence property of the pulse. For spectrally perfectly coherent pulses, $|W(\omega_0, \omega_0 + d)|$ and $\mathrm{Arg}[W(\omega_0, \omega_0 + d)]$ yield the spectral amplitude and phase profiles, respectively. On the other hand, for spectrally partially coherent pulses, $W(\omega_0, \omega_0 + d)$ represents the spectral coherence profile.

In this first scheme, prior knowledge of the spectral phase profile of the pump pulse is still necessary, as it directly transfers to the relative phase between the two interfering spectral bins. In Eq. (2), we assume that the pump phase is uniform. However, in realistic experimental conditions, the pump pulse often has a spectral phase profile, which modifies the count distribution $\eta^\theta(d)$ as

$$\eta^\theta(d) = |f(\omega_0) + f(\omega_0 + d)e^{i\theta}e^{i\alpha(\omega_p^{(0)} - d)}|^2, \quad (5)$$

where $\omega_p^{(0)}$ is the pump frequency corresponding to the input frequency ω_0, and $\alpha(\omega_p^{(0)} - d)$ is the unknown spectral phase introduced by the QPG pump. For a known $\alpha(\omega_p^{(0)} - d)$ profile, we can directly subtract it from the retrieved phase profile to extract the input spectral phase. In the more general case, where $\alpha(\omega_p^{(0)} - d)$ is unknown, we would need to characterize it along with the input phase profile. This could be achieved by applying a relative spectral shear Δ between pump and input frequencies and comparing count distributions for different shearing values; however, shearing is typically quite complex to implement experimentally.

Instead, we extend our scheme to simultaneously reconstruct both input and pump phase profiles by harnessing an mQPG. An output channel with a spectral shift of Δ relative to the central one interferes frequencies $\omega_0 + \Delta$ and $\omega_0 + \Delta + d$ in correspondence of the same pump frequencies in Eq. (5), effectively applying the equivalent of shearing between the two pulses. The resulting interference count distribution at the mQPG output is

$$\eta^\theta(d; \Delta) = |f(\omega_0 + \Delta) + f(\omega_0 + d + \Delta)e^{i\theta}e^{i\alpha(\omega_p^{(0)} - d)}|^2. \quad (6)$$

In the experiment, we use a three output mQPG with $\Delta \in \{-\Delta_0, 0, +\Delta_0\}$. By recording $\eta^\theta(d; \Delta)$ at $\theta \in \{0, \frac{\pi}{2}, \pi, \frac{3\pi}{2}\}$ (Fig. 2(a)), we reconstruct the phase profile $\mu(d; \Delta)$

$$\mu(d; \Delta) = \mathrm{Arg}\left[\frac{\eta^{\theta=0}(d; \Delta) - \eta^{\theta=\pi}(d; \Delta)}{\eta^{\theta=\frac{\pi}{2}}(d; \Delta) - \eta^{\theta=\frac{3\pi}{2}}(d; \Delta)}\right] = \phi(\omega_0 + d + \Delta) - \alpha(\omega_0^{(p)} - d) - \phi(\omega_0 + \Delta). \quad (7)$$

This expression relates the measured phase profile $\mu(d; \Delta)$ to both input and pump spectral phase profiles. If the pump spectral phase profile $\alpha(\omega_0^{(p)} - d)$ is known, $\mu(d; \Delta)$ directly provides the input phase profile $\phi(\omega_0 + d + \Delta)$. By analyzing $\mu(d; \Delta)$ profiles (Fig. 2(b)), we use a straightforward algorithm (Fig. 2(c)) to extract the pump spectral phase with the only assumption that it follows a polynomial function, which is commonly used in pulse characterization experiments. Once the pump phase is determined, we subtract it from the measured $\mu(d; \Delta)$ to obtain the input phase profile.

This approach eliminates the need for an iterative algorithm by replacing it with simple curve fitting of the pump profile, allowing for direct and straightforward reconstruction of the spectral phase profiles of both pulses. Moreover, this method also enables the retrieval of the spectral amplitude profiles (see the supplementary material).

III. Experiment and Results

A. Characterization of spectrally perfectly and partially coherent pulses

Figure 3 shows the schematic of the experimental setup. A Ti:Sapphire laser, centered at 860 nm, drives an optical parametric oscillator (OPO) to generate spectrally coherent input pulses at 1545 nm. These pulses are attenuated to a mean photon number of 0.1 per pulse using a neutral density (ND) filter, which allows them to be approximated as single-photon pulses. The spectral amplitude and phase profiles are customized using a waveshaper, while the same Ti:Sapphire laser also serves as the pump for the QPG. Additional details are given in the Appendix Sec. VI C.

We first characterize these single-photon perfectly coherent pulses. Figures 4(a) and 4(b) show the measured $|W(\omega_0, \omega_0 + d)|$ and $\mathrm{Arg}[W(\omega_0, \omega_0 + d)]$, respectively, along with their theoretical predictions for different input pulses. In the supplementary material, we present the step-by-step reconstruction of $|W(\omega_0, \omega_0+d)|$ and $\mathrm{Arg}[W(\omega_0, \omega_0 + d)]$ from the measured count distributions.

For a quantitative comparison, we evaluate the similarity S between theoretical and experimental profiles. We find that S exceeds 97% for each experimental profile, indicating an excellent agreement with the theory. The high signal to noise ratio of the recorded count distribution ensures almost negligible statistical errors in the reconstructed spectral amplitude and phase profiles. The small deviations in the reconstructed profiles from the expected profiles can be attributed to the experimental imperfections, such as the imperfections in shaping and finite width of pump frequency bins, which effectively lowers the measurement resolution. Each single-photon photon pulse characterization takes a measurement time of 25 minutes, though this can be reduced to just a few

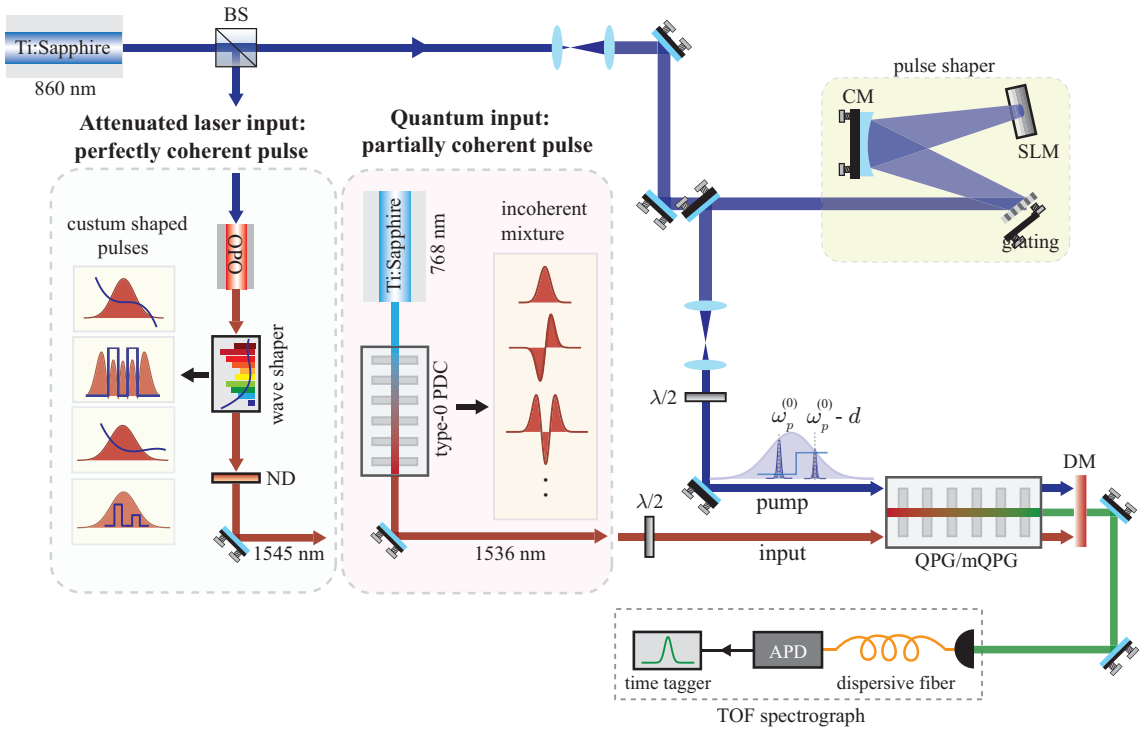

FIG. 3. Schematic of the experimental setup. A Ti:Sapphire laser (860 nm) pumps an OPO process to generate spectrally perfectly coherent telecom input pulses (1545 nm). A commercial waveshaper applies custom-designed spectral phase and amplitude profiles to the telecom, which we want to characterize. An ND filter attenuates the input to single-photon-level. To apply this method on a quantum light source, we replace the attenuated OPO pulses by an integrated type-0 PDC. The remaining 860 nm pulse is used as a pump, shaped by an in-house-built pulse shaper. Both input and pump pulses are sent to either the QPG or mQPG waveguide to characterize only the input or both pulses. A time-of-flight spectrograph detects the output pulses. BS: beam splitter, SLM: spatial light modulator, DM: dichroic mirror, CM: cylindrical mirror, OPO: optical parametric oscillator, PDC: parametric down-conversion.

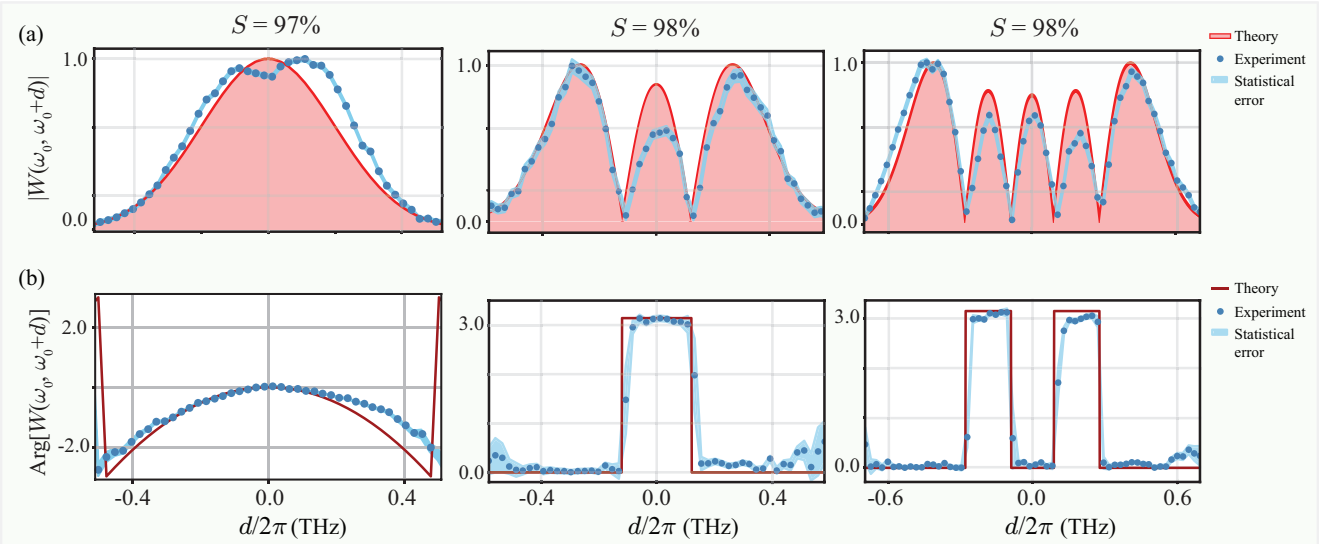

FIG. 4. Characterization of single-photon level spectrally perfectly coherent pulses. (a) Measured and theoretical $|W(\omega_0, \omega_0+d)|$ profiles, which represent the functional form of spectral amplitude profile. The maximum of $|W(\omega_0, \omega_0+d)|$ is normalized to 1. (b) Measured and theoretical $\mathrm{Arg}[W(\omega_0, \omega_0+d)]$ profiles, which represent the spectral phase profile.

seconds for bright input pulses. This demonstration highlights the ability of our scheme to characterize spectrally coherent pulses with high precision, including challenging features like phase jumps, a challenging task for existing schemes.

To demonstrate the suitability of our scheme for quantum light, we apply it to a type-0 integrated parametric down-conversion (PDC) source. The experimental details of the source are provided in the Appendix Sec. VI C. This source exhibits strong spectral-temporal correlations between the generated photon pairs, while each photon has large spectral and temporal widths. As a consequence, the quantum pulses generated by PDC have spectral and temporal bandwidths that are much broader than their corresponding coherence widths, resulting in partially coherent pulses. To further illustrate this partial coherence, the expected two-dimensional TPSC function is shown in Fig. 5(a), which clearly reveals that the spectrum is significantly broader than the coherence profile. Additional details on the TF characteristics of the type-0 PDC process are provided in the supplementary material.

Figures 5(c) and (d) show the measured $|W(\omega_0, \omega_0+d)|$ and $\mathrm{Arg}[W(\omega_0, \omega_0+d)]$ alongside their theoretical predictions. In Fig. 5(c), the measured $W(\omega_0, \omega_0+d)$ is plotted together with the expected spectrum $S(\omega_0 - d)$ (dashed green line), to highlight that the measured coherence profile is significantly narrower than the expected spectrum, demonstrating the low spectral coherence of the PDC pulses. A quantitative comparison between the theoretical and experimental profiles yields a similarity $S \approx 98\%$. This demonstrates the effectiveness of our scheme for quantum pulses with low spectral coherence. The data accumulation time of 30 minutes yields high signal to noise ratio, such that the statistical errors in the reconstructed profiles are almost negligible. The flexibility of this scheme for characterizing pulses is showcased with varying degrees of coherence in the supplementary section.

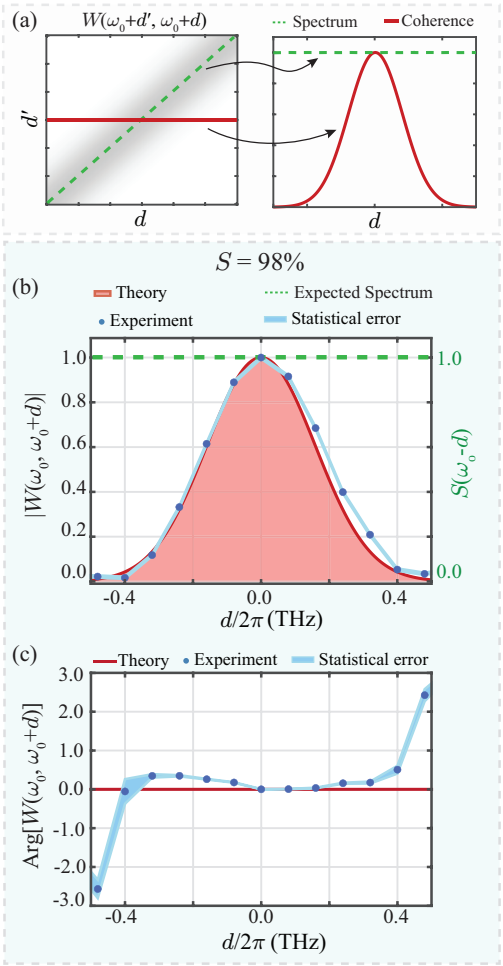

FIG. 5. (a) Illustrates the expected two-dimensional TPSC function $W(\omega_0 + d', \omega_0 + d)$ for partially coherent quantum pulses from a type-0 PDC (left). We plot the spectrum (green dashed line) and coherence profile (red solid curve) together to highlight that coherence width is much narrower than the spectral bandwidth (right). (b) Measured and theoretical spectral coherence profiles $|W(\omega_0, \omega_0 + d)|$ alongside the expected spectrum $S(\omega_0 - d)$. The maximum of each profile is normalized to 1. (c) Measured and theoretical $\mathrm{Arg}[W(\omega_0, \omega_0 + d)]$ profiles.

B. Simultaneous characterization of spectral phase profiles of input and pump pulses

Finally, to showcase the capability of this scheme for characterizing single-photon level pulses without prior knowledge of pump pulse, in the experimental setup in Fig. 3 we replace the QPG with an mQPG. The perfectly coherent input pulses from the OPO are attenuated to a mean photon number of 1.0 per pulse, while the Ti:Sapphire laser pumps the mQPG. Data accumulation takes around 30 minutes.See the Appendix Sec. VI C for further details.

Figure 6(a) shows the measured spectral phase profiles $\mu(d; \Delta)$ for different shearing values Δ, corresponding to different input and pump phase shapes. We find a good agreement with the expected profiles. These measured profiles are then processed using the algorithm illustrated in Fig. 2 to retrieve the input and pump phase profiles. Figure 6(b) shows the retrieved input and pump phase profiles and compares them with their corresponding theoretical predictions, showing a similarity above 96%, even for complicated input phase structures. These results mark a major step toward self-referenced spectral phase characterization at the single-photon level, eliminating the limitation of requiring a known pump or reference pulse in existing phase characterization techniques. Moreover, the scheme remains applicable to single-photon pulses or lower fluxes with increased accumulation time.

So far, we have operated with pump pulses of 62 pJ

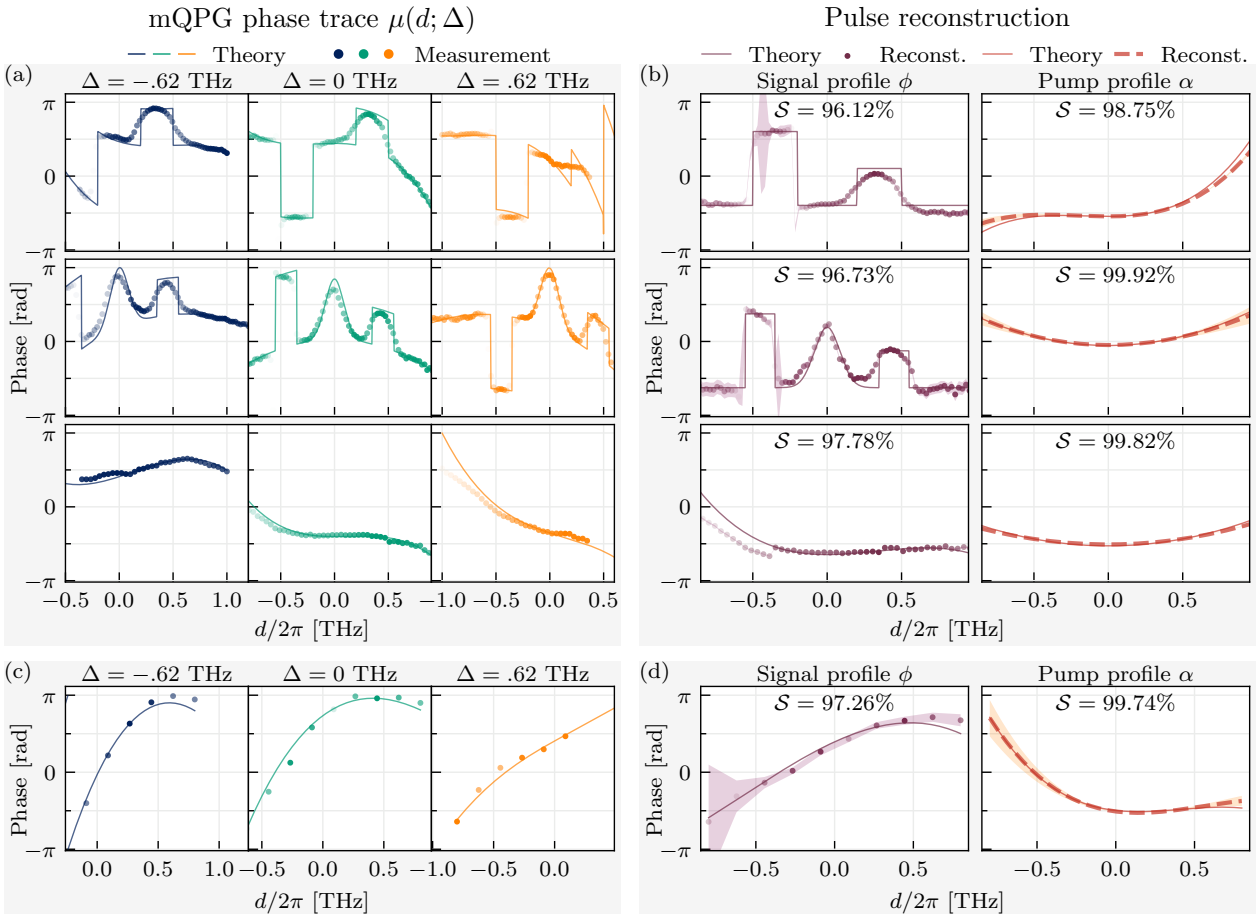

FIG. 6. (a) Theoretical and measured phase traces, $\mu(d;\Delta)$, for $\Delta = -0.62$, 0, and 0.62 THz, corresponding to different spectral phase profiles of single-photon-level input pulses and bright pump pulses. (b) Reconstructed spectral phase profiles of the input and pump pulses for various shapes, shown alongside theoretical predictions. Shaded regions in the reconstructed profiles indicate statistical errors. (c) Theoretical and measured mQPG phase traces, $\mu(d;\Delta)$, for $\Delta = -0.62$, 0, and 0.62 THz, corresponding to low-light-level input and pump pulses. (d) Reconstructed spectral phase profiles of the pump and input pulses for different shapes, shown with theoretical predictions. Shaded regions in the reconstructed profiles indicate statistical errors.

per pulse. To showcase the feasibility of our approach in extreme low-light conditions, we attenuate both the input and pump pulses to 1.25 fJ per pulse (10^4 photons per pulse). As expected, the reduced photon flux, or pulse energy, increases the measurement time to approximately 60 minutes. Figure 6(c) presents the measured phase profiles for different shearing alongside their theoretical predictions. Figure 6(d) shows the reconstructed input and pump phase profiles, indicating excellent agreement with theoretical predictions, with similarity S above 97%. This demonstration highlights the applicability of our method for scenarios where simultaneous spectral phase characterization of two low-energy pulses at different wavelengths is required, such as in quantum metrology applications.

IV. Conclusion and Discussion

In conclusion, we have developed FIREFLY, a method for characterizing single-photon-level ultrafast pulses by measuring their TPSC functions using a QPG. This approach enables high-quality characterization of the spectral amplitude and phase profiles for spectrally coherent pulses. We have also applied our scheme to quantum light by analysing the spectral coherence profile of partially coherent pulses generated from a mutimode type-0 PDC process. Importantly, we have then eliminated the

requirement for a spectrally known pump or reference pulse by extending FIREFLY to an mQPG. As proof of principle, we have demonstrated the simultaneous characterization of the spectral phase profiles for both single-photon input and bright pump pulses with complex spectral shapes. Remarkably, our approach even works for both pulses at the low-light-level.

Unlike most existing schemes, our method can characterize complex phase structures and coherence profiles without a requiring reconstruction algorithm or setup reconfiguration. Additionally, the use of the mQPG to characterize single-photon-level pulses without a known reference pulse enhances experimental resource efficiency and ensures compatibility with the integrated optics platform. These features make our scheme readily suitable for quantum communication and metrology protocols that require fast characterization of single-photon pulses, as well as for deep-space communication in high-loss and turbulent environments.

Further improvements, such as adopting periodic poling modulation techniques [47] in the mQPG fabrication and replacing the time-of-flight (TOF) spectrograph with a spectral-filtering-based detection scheme, can enhance efficiency by nearly 1000 fold. These improvements enable single-photon pulse characterization within seconds.

In our experiment, the QPG and the mQPG facilitate the characterization of single-photon-level telecom pulses through detection of the visible output photons, thereby eliminating the need for single-photon sensitive telecom detectors. This approach can be extended to input pulses of any wavelength [48], facilitating pulse characterization in spectral regions where single-photon-sensitive detectors are resource demanding. While our current FIREFLY implementation is optimal for characterizing input pulses with temporal widths ranging from 100 fs to 20 ps, this range can be extended by tailoring the dispersion properties of the waveguide [48]. Furthermore, advances in thin-film lithium niobate technology [49] offer greater flexibility in modulating dispersion properties with tailored waveguide geometries, which can enable (m)QPGs compatible with sub-femtosecond input pulses across any spectral range. These developments can make our scheme valuable for diverse applications in quantum information science and beyond, including ultrafast optics and spectroscopy.

V. Acknowledgements

We acknowledge the European Union's Horizon Europe research and innovation programme under grant agreement No 899587 (STORMYTUNE) for the funding.

VI. Data Availability

All data required for evaluating our conclusions are present in the paper and supplementary material. Additional data related to this paper may be requested from the corresponding author

[1] J. L. O'brien, A. Furusawa, and J. Vučković, Nature Photonics **3**, 687 (2009).
[2] F. Flamini, N. Spagnolo, and F. Sciarrino, Reports on Progress in Physics **82**, 016001 (2018).
[3] E. Pelucchi, G. Fagas, I. Aharonovich, D. Englund, E. Figueroa, Q. Gong, H. Hannes, J. Liu, C.-Y. Lu, N. Matsuda, *et al.*, Nature Reviews Physics **4**, 194 (2022).
[4] B. Brecht, D. V. Reddy, C. Silberhorn, and M. G. Raymer, Phys. Rev. X **5**, 041017 (2015).
[5] V. Ansari, J. M. Donohue, B. Brecht, and C. Silberhorn, Optica **5**, 534 (2018).
[6] M. Karpiński, A. O. Davis, F. Sośnicki, V. Thiel, and B. J. Smith, Advanced Quantum Technologies **4**, 2000150 (2021).
[7] P. C. Humphreys, B. J. Metcalf, J. B. Spring, M. Moore, X.-M. Jin, M. Barbieri, W. S. Kolthammer, and I. A. Walmsley, Physical review letters **111**, 150501 (2013).
[8] N. C. Menicucci, S. T. Flammia, and O. Pfister, Physical review letters **101**, 130501 (2008).
[9] F. Bouchard, D. England, P. J. Bustard, K. Heshami, and B. Sussman, PRX Quantum **3**, 010332 (2022).
[10] F. Bouchard, D. England, P. J. Bustard, K. L. Fenwick, E. Karimi, K. Heshami, and B. Sussman, Physical Review Applied **15**, 024027 (2021).
[11] S. Mukamel, M. Freyberger, W. Schleich, M. Bellini, A. Zavatta, G. Leuchs, C. Silberhorn, R. W. Boyd, L. L. Sánchez-Soto, A. Stefanov, *et al.*, Journal of physics B: Atomic, molecular and optical physics **53**, 072002 (2020).
[12] J. M. Donohue, V. Ansari, J. Řeháček, Z. Hradil, B. Stoklasa, M. Paúr, L. L. Sánchez-Soto, and C. Silberhorn, Physical review letters **121**, 090501 (2018).
[13] V. Giovannetti, S. Lloyd, and L. Maccone, Nature photonics **5**, 222 (2011).
[14] M. Barbieri, PRX Quantum **3**, 010202 (2022).
[15] R. Trebino and D. J. Kane, J. Opt. Soc. Am. A **10**, 1101 (1993).
[16] K. DeLong, R. Trebino, J. Hunter, and W. White, JOSA B **11**, 2206 (1994).
[17] I. A. Walmsley and V. Wong, JOSA B **13**, 2453 (1996).
[18] C. Iaconis and I. A. Walmsley, Optics letters **23**, 792 (1998).
[19] P. Londero, M. E. Anderson, C. Radzewicz, C. Iaconis, and I. A. Walmsley, Journal of Modern Optics **50**, 179 (2003).
[20] D. N. Fittinghoff, J. L. Bowie, J. N. Sweetser, R. T. Jennings, M. A. Krumbügel, K. W. DeLong, R. Trebino, and I. A. Walmsley, Optics letters **21**, 884 (1996).
[21] L. Gallmann, G. Steinmeyer, D. Sutter, T. Rupp, C. Iaconis, I. Walmsley, and U. Keller, Optics Letters **26**, 96 (2001).
[22] M. Kacprowicz, W. Wasilewski, and K. Banaszek, Applied Physics B **91**, 283 (2008).

[23] D. Reid, P. Loza-Alvarez, C. Brown, T. Beddard, and W. Sibbett, Optics letters **25**, 1478 (2000).
[24] G. Stibenz and G. Steinmeyer, Optics express **13**, 2617 (2005).
[25] A. Pasquazi, M. Peccianti, Y. Park, B. E. Little, S. T. Chu, R. Morandotti, J. Azaña, and D. J. Moss, Nature Photonics **5**, 618 (2011).
[26] C. Bourassin-Bouchet and M.-E. Couprie, Nature communications **6**, 6465 (2015).
[27] A. O. Davis, V. Thiel, M. Karpiński, and B. J. Smith, Physical Review A **98**, 023840 (2018).
[28] A. O. Davis, V. Thiel, M. Karpiński, and B. J. Smith, Physical review letters **121**, 083602 (2018).
[29] A. Golestani, A. O. Davis, F. Sośnicki, M. Mikołajczyk, N. Treps, and M. Karpiński, Physical Review Letters **129**, 123605 (2022).
[30] V. Thiel, A. O. C. Davis, K. Sun, P. D'Ornellas, X.-M. Jin, and B. J. Smith, Opt. Express **28**, 19315 (2020).
[31] M. Lipka and M. Parniak, Physical Review Letters **127**, 163601 (2021).
[32] G. Thekkadath, B. Bell, R. Patel, M. Kim, and I. Walmsley, Physical Review Letters **128**, 023601 (2022).
[33] Z. Qin, A. S. Prasad, T. Brannan, A. MacRae, A. Lezama, and A. Lvovsky, Light: Science & Applications **4**, e298 (2015).
[34] W. Wasilewski, P. Kolenderski, and R. Frankowski, Physical review letters **99**, 123601 (2007).
[35] A. Bhattacharjee, L. Serino, J. Řeháček, Z. Hradil, C. Silberhorn, and B. Brecht, arXiv preprint arXiv:2408.12306 (2024).
[36] L. Mandel, *Optical Coherence and Quantum Optics* (Cambridge University Press, 1995).
[37] G. Kulkarni, R. Sahu, O. S. Magaña-Loaiza, R. W. Boyd, and A. K. Jha, Nature communications **8**, 1054 (2017).
[38] C. Iaconis and I. A. Walmsley, Optics letters **21**, 1783 (1996).
[39] R. Rezvani Naraghi, H. Gemar, M. Batarseh, A. Beckus, G. Atia, S. Sukhov, and A. Dogariu, Optics letters **42**, 4929 (2017).
[40] A. Bhattacharjee, S. Aarav, and A. K. Jha, Applied Physics Letters **113**, 051102 (2018).
[41] V. Ansari, G. Harder, M. Allgaier, B. Brecht, and C. Silberhorn, Phys. Rev. A **96**, 063817 (2017).
[42] M. Allgaier, G. Vigh, V. Ansari, C. Eigner, V. Quiring, R. Ricken, B. Brecht, and C. Silberhorn, Quantum Science and Technology **2**, 034012 (2017).
[43] V. Ansari, J. M. Donohue, M. Allgaier, L. Sansoni, B. Brecht, J. Roslund, N. Treps, G. Harder, and C. Silberhorn, Physical review letters **120**, 213601 (2018).
[44] J. Gil-Lopez, Y. S. Teo, S. De, B. Brecht, H. Jeong, C. Silberhorn, and L. L. Sánchez-Soto, Optica **8**, 1296 (2021).
[45] V. Ansari, J. M. Donohue, B. Brecht, and C. Silberhorn, Optics Express **28**, 28295 (2020).
[46] L. Serino, J. Gil-Lopez, M. Stefszky, R. Ricken, C. Eigner, B. Brecht, and C. Silberhorn, PRX quantum **4**, 020306 (2023).
[47] M. Chou, K. Parameswaran, M. M. Fejer, and I. Brener, Optics letters **24**, 1157 (1999).
[48] F. Roeder, A. Gnanavel, R. Pollmann, O. Brecht, M. Stefszky, L. Padberg, C. Eigner, C. Silberhorn, and B. Brecht, New Journal of Physics **26**, 123025 (2024).
[49] D. Zhu, L. Shao, M. Yu, R. Cheng, B. Desiatov, C. Xin, Y. Hu, J. Holzgrafe, S. Ghosh, A. Shams-Ansari, *et al.*, Advances in Optics and Photonics **13**, 242 (2021).
[50] C. Dorrer and I. A. Walmsley, JOSA B **19**, 1019 (2002).

Appendix

A. Quantum pulse gate (QPG) and its implementation for measuring the TPSC function

The proposed method in Sec. II B for measuring the TPSC function of pulses employs a quantum pulse gate (QPG). The implementation of this scheme is illustrated in Fig. 1(a). In this scheme, we consider the pump profile is known prior to shaping. The QPG projects a single-photon-level input pulse, described by its complex spectral amplitude $f(\omega)$, onto any desired TF function decided by the pump TF mode $E_p(\omega_p)$, where ω_p is the pump frequency. The up-converted QPG output is centered at frequency ω_{out} and the energy conservation in this process fixes the relationship $\omega_{out} = \omega + \omega_p$. The total output counts η at the output ω_{out} are given by following overlap integral

$$\eta \propto \left| f(\omega) E_p^*(\omega_{out} - \omega) d\omega \right|^2 . \tag{1}$$

This expression of η is valid if both input and pump pulses are described by their complex spectral amplitudes. For partially coherent input pulses, η in terms of the TPSC function $W(\omega_1, \omega_2)$ is given by

$$\eta^\theta(\omega_{out}) \propto \iint W(\omega_1, \omega_2) E_p(\omega_{out} - \omega_1) \times E_p^*(\omega_{out} - \omega_2) d\omega_1 d\omega_2. \tag{2}$$

To measure the TPSC function $W(\omega_0, \omega_0 + d)$, we need to interfere the complex spectral amplitudes $f(\omega_0)$ and $f(\omega_0 + d)$ at frequencies ω_0 and $\omega_0 + d$ respectively, using a QPG. We start with a spectrally characterized pump pulse and shape it with a complex spectral amplitude $E_p(\omega_p) = \delta(\omega_p - \omega_p^{(0)}) + e^{i\theta}\delta(\omega_p - \omega_p^{(0)} + d)$, where $\omega_p^{(0)}$ is the pump central frequency, d is the bin separation and θ is the relative phase difference between the bins. As shown in Fig. 1(b), the pump profile $E_p(\omega_p)$ up-converts a pair of spectral bins from the input to the same QPG output frequency ω_{out}. As a result, the up-converted spectral bins interfere and the information is encoded in the total output counts of the QPG.

The total count distribution $\eta^\theta(d)$ as a function of d at the output ω_{out} can be written by substituting $E_p(\omega_p)$ into Eq. (2):

$$\eta^\theta(d) = S(\omega_0) + S(\omega_0 + d) + 2\mathrm{Re}[W(\omega_0, \omega_0 + d)] \times \cos\theta + 2\mathrm{Im}[W(\omega_0, \omega_0 + d)] \sin\theta, \tag{3}$$

In the above expression, we replace $\omega_{p1,2} = \omega_{out} - \omega_{1,2}$ and define $\omega_0 = \omega_{out} - \omega_p^{(0)}$. In order to extract $W(\omega_0, \omega_0 + d)$, we measure $\eta^\theta(d; \omega_{out})$ at $\theta = 0, \pi/2, \pi$,

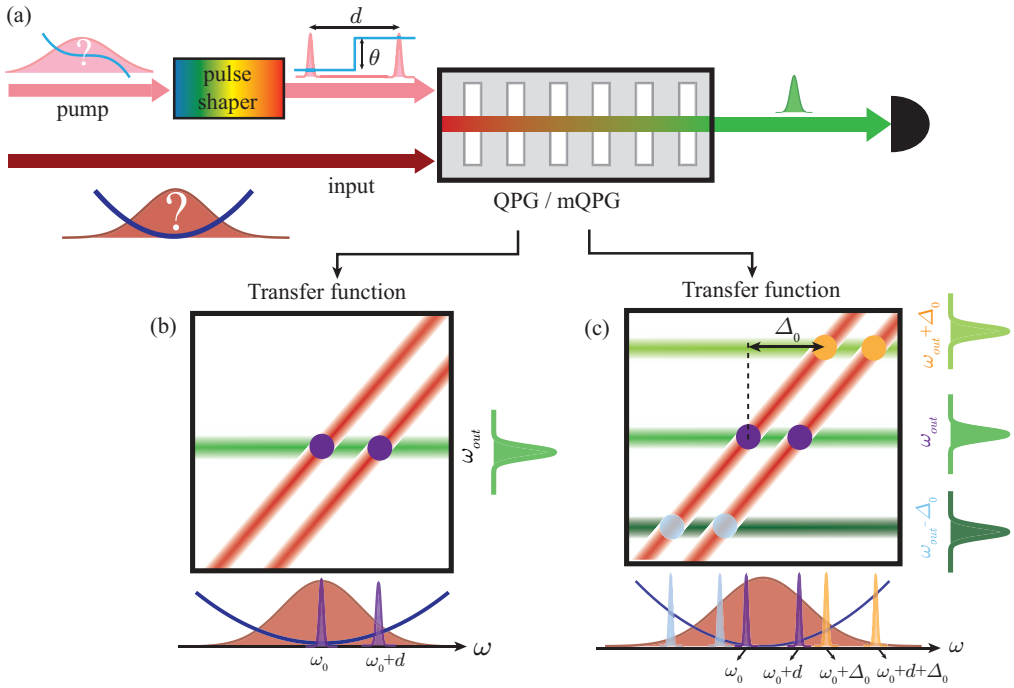

FIG. 1. (a) Schematic of the proposed method for measuring TPDC function using a QPG and simultaneous characterization of input and pump pulses using mQPG. (b) Depicts the transfer function of QPG: the superposition of the frequency bin shape of pump up-converts input frequency bins at ω_0 and $\omega_0 + d$ into a single QPG output frequency ω_{out}. The output counts provides resulting interference counts between the bins. (c) Depicts the transfer function: input frequency bins with separation d for different shearing Δ up-converts into different mQPG output frequencies.

and $3\pi/2$ and obtain the real and imaginary parts of $W(\omega_0, \omega_0 + d)$

$$\mathrm{Re}[W(\omega_0, \omega_0 + d)] \propto \eta^{\theta=0}(d) - \eta^{\theta=\pi}(d), \tag{4}$$

$$\mathrm{Im}[W(\omega_0, \omega_0 + d)] \propto \eta^{\theta=\frac{\pi}{2}}(d) - \eta^{\theta=\frac{3\pi}{2}}(d). \tag{5}$$

By combining $\mathrm{Re}[W(\omega_0, \omega_0 + d)]$ and $\mathrm{Im}[W(\omega_0, \omega_0 + d)]$, we directly find $W(\omega_0, \omega_0 + d)$.

$$W(\omega_0, \omega_0 + d) = \mathrm{Re}[W(\omega_0, \omega_0 + d)] + i\mathrm{Im}[W(\omega_0, \omega_0 + d)]. \tag{6}$$

B. Algorithm for simultaneously characterizing input and pump pulses

In this case, we consider that input and pump pulses are described by their respective complex spectral amplitudes $f(\omega)$ and $g(\omega_p)$, where ω and ω_p are the input and pump frequencies. Our objective is to characterize the spectral phase profiles $\phi(\omega)$ and $\alpha(\omega_p)$ of input and pump respectively. For simplicity, we assume that the spectral amplitude of the pump pulse is uniform.

As outlined in main manuscript Sec. II B, we extend the above TPSC measurement scheme to an mQPG, which introduces a spectral shear Δ between input and pump frequencies. Figure 1(a) shows the illustration of this scheme with an mQPG with three output channels centered at $\omega_{out} + \Delta$, where $\Delta \in \{-\Delta_0, 0, +\Delta_0\}$. Figure 1(c) depicts that the output channel with frequency $\omega_{out} + \Delta$ enables the inteference of input frequencies $\omega_0 + \Delta$ and $\omega_0 + d + \Delta$ by still shaping the pump with the amplitude $E_p(\omega_p) = \delta(\omega_p - \omega_p^{(0)}) + e^{i\theta}\delta(\omega_p - \omega_p^{(0)} + d)$. By measuring the count distribution $\eta(d; \Delta)$ for $\theta \in \{0, \pi/2, pi, 3\pi/2\}$, we obtain the phase profile $\mu(d; \Delta)$ using

$$\begin{aligned}\mu(d;\Delta) &= \mathrm{Arg}\left[\frac{\eta^{\theta=\frac{\pi}{2}}(d;\Delta) - \eta^{\theta=\frac{3\pi}{2}}(d;\Delta)}{\eta^{\theta=0}(d;\Delta) - \eta^{\theta=\pi}(d;\Delta)}\right] \\ &= \phi(\omega_0 + d + \Delta) - \alpha(\omega_p^{(0)} - d) - \phi(\omega_0 + \Delta).\end{aligned} \tag{7}$$

This profile encodes both input and pump phase profiles. We retrieve the above phase profile for different Δ values. From these phase profiles, we first reconstruct the pump spectral phase profile by shifting the $\mu(d; \Delta)$ by $-\Delta$ and subtract it from $\mu(d; 0)$

$$\Delta\alpha(d) = \mu(d;0) - \mu(d-\Delta;\Delta) = \alpha(\omega_p^{(0)} - d + \Delta) - \alpha(\omega_p^{(0)} - d). \tag{8}$$

The above profile is independent of the input spectral phase profile $\phi(\omega_0 + d)$ and depends only on the pump phase difference profile $\alpha(\omega_p^{(0)} - d) - \alpha(\omega_p^{(0)} - d + \Delta_0)$.

Notably, the SPIDER algorithm [17, 18, 50] also provides the same phase difference profile while characterizing a single pulse. Thus, inspired by SPIDER and as a proof of principle, we impose the assumption that the pump phase profile $\alpha(\omega_p^{(0)} - d)$ is a polynomial function of the form $\alpha(\omega_p^{(0)} - d) = a \cdot (\omega_p^{(0)} - d)^2 + b \cdot (\omega_p^{(0)} - d)^3$, which is reasonable in pulse characterization experiments. In the experiment, we implement shearing values $\Delta \in \{-\Delta_0, +\Delta_0\}$, which yields two distinct $\Delta\alpha(d)$ profiles. A polynomial curve fitting, with a known Δ_0, is then used on $\Delta\alpha(d)$ profiles to extract $\alpha(\omega_p^{(0)} - d)$. For small Δ_0, as is the case for SPIDER, the phase difference profile in Eq. (8) would directly map the derivative of $\alpha(\omega_p^{(0)} - d)$ [50]. Next, we obtain the input phase profile $\phi(\omega_0 + d)$ as

$$\phi(\omega_0 + d) = \mu(d; 0) - \alpha(\omega_p^{(0)} - d) + \phi(\omega_0). \qquad (9)$$

Here, $\phi(\omega_0)$ introduces a constant offset to the reconstructed $\phi(\omega_0 + d)$ profile. Fig. 2 illustrates the steps of this phase retrieval scheme. Thus, by measuring the interference counts corresponding to different shearing values (at different mQPG output channels), we characterize the spectral phase profiles of both input and pump pulses.

C. Experimental details

We first describe the setup for characterizing single-photon level, spectrally perfectly coherent pulses. A Ti:Sapphire pulsed laser of central wavelength 860 nm and repetition rate 80 MHz drives an OPO process to generate input pulses centered at 1545 nm. The residual 860 nm pulses serve as the pump and are directed to a in-house-built 4f-line pulse shaper to "carve out" a superposition of frequency bins with a well-defined separation and relative phase. The bin width ranges from 30 to 60 GHz. A commercial wave shaper (Finisar 4000S) is used to apply phase and amplitude profiles to produce custom-shaped coherent input pulses. After shaping, the input pulses are attenuated to mean photon of 0.1 per pulse using a neutral density filter.

Both the input and pump pulses are sent to a periodically poled, titanium-indiffused $LiNbO_3$ QPG waveguide, 4 cm in length with a poling period of 4.32 μm, operated at 433 K. The waveguide supports only the fundamental spatial mode for the input pulse, and appropriate care is taken to couple the pump pulse in the fundamental mode. The coupling efficiency for both input and pump pulses is approximately 70% and 50% respectively. The up-converted QPG output pulses, centered around 552 nm (543 THz), are separated from the residual input and pump pulses using a dichroic mirror. We detect the up-converted output counts using a time-of-flight (TOF) single-photon spectrograph with an effective resolution of 300 GHz. The spectrograph consist of a dispersive fiber, an avalanche photodiode (APD), and a time-to-digital converter (TDC). We keep the integration time per measurement point ranges between $3 - 7$ seconds . We note that due to the imperfections in QPG phase-matching, additional sidelobes of the phase-matching can reduce the QPG operation fidelity. To mitigate this, narrow band spectral filtering of the output photons is required prior to photon counting. Here, the TOF spectrograph implements both spectral filtering and photon counting over the filtered photons in a single device. Alternatively, one can use a narrow spectral filter alongside a single-photon detector to achieve the same goal and with a higher detection efficiency.

For characterizing spectrally partially coherent quantum pulses, the combination of Ti:Sapphire pulsed laser and OPO is replaced by an integrated type-0 PDC source, realized in a 1-cm-long periodically pole titanium-indiffused $LiNbO_3$ waveguide operating at 443 K. The PDC process is pumped by a pulsed laser centered at 768 nm with a spectral bandwidth of 0.25 THz, generating partially coherent pulses centered at 1536 nm, which are sent to the QPG waveguide. A combination of narrow spectral filter and APD is used photon counting at the QPG output. The rest of the setup remains the same as the above.

We now describe the setup for the simultaneous characterization of input and pump pulses. In this setup, we use an mQPG instead of a QPG. Using a Ti:Sapphire pulsed laser combined with an OPO, we generate spectrally coherent input pulses centered at 1545 nm. A in-house-built pulse shaper applies spectral phase profiles to the pump pulses, while a commercial waveshaper (Finisar 4000S) applies custom-shaped phase profiles to the input pulses. We attenuate the input pulses to a mean photon number of 1.0 per pulse. The mQPG used in this experiment is a 4-cm-long titanium-indiffused $LiNbO_3$ waveguide operated at 433 K with a super-poling structure consisting of unpoled regions alternating to periodically poled regions with a poling period of 4.32 μm. This poling structure generates three output frequency channels centered around 551.48 nm (543.62 THz), 552 nm (543 THz), and 552.62 nm (542.38 THz), corresponding to a shearing value of $\Delta_0/2\pi$ =0.62 THz. The TOF spectrograph spectrally separates each channel and performs parallel measurements of total counts. This configuration can be replaced by combination of three spectral filters and single-photon detectors, which can boost the detection efficiency by up to two orders of magnitude.

Supplementary Material: Frequency-bin interferometry for reconstructing electric fields with low intensity

Abhinandan Bhattacharjee†, Laura Serino†, Patrick Folge†, Benjamin Brecht, and Christine Silberhorn
Integrated Quantum Optics Group, Institute for Photonic Quantum Systems (PhoQS), Paderborn University, Warburger Straße 100, 33098 Paderborn, Germany and
† *These authors contributed equally to this work.*
* *abhib@mail.uni-paderborn.de*

I. Retrieval of spectral amplitude with an unknown pump pulse

In this section, we present the steps for characterizing the spectral amplitude profile of the input pulse with an unknown pump pulse using a multi-output quantum pulse gate (mQPG). The input and pump pulses are described by their respective complex spectral amplitudes $f(\omega)$ and $g(\omega_p)$, where ω and ω_p are input and pump frequencies. In the proposed scheme, we introduce a spectral shear Δ, to the input frequencies and interfere $\omega_0 + \Delta$ and $\omega_0 + d + \Delta$ by shaping the pump with a complex spectral amplitude amplitude $E_p(\omega_p) = \delta(\omega_p - \omega_p^{(0)}) + e^{i\theta}\delta(\omega_p - \omega_p^{(0)} + d)$. This interference can be measured at an output frequency shifted by Δ relative to ω_{out} of a multi-output QPG. The resulting interference count distribution $\eta(d;\Delta)$ is given by:

$$\eta^{\theta}(d;\Delta) = |f(\omega_0+\Delta)g(\omega_p^{(0)}) + f(\omega_0+d+\Delta)g(\omega_p^{(0)}-d)e^{i\theta}e^{i\alpha(\omega_p^{(0)}-d)}|^2. \tag{1}$$

We record $\eta^{\theta}(d;\Delta)$ at 0, $\pi/2$, π, and $3\pi/2$. These measurements yield the amplitude profile

$$A(d;\Delta) = |f(\omega_0)||g(\omega_p^{(0)})||f(\omega_0+d+\Delta)||g(\omega_p^{(0)}-d)|. \tag{2}$$

The product $|f(\omega_0)||g(\omega_p^{(0)})|$ is a constant scaling factor, K. The above profile is simplified as the product of spectral amplitudes of the input and pump pulses. We note that the pump spectral amplitude $|g(\omega_0+d)|$ can be characterized by directly measuring the pump spectrum, $S(\omega_p) = |g(\omega_p)|^2$, using a spectrograph. From the measured spectrum, the input spectral amplitude can be retrieved as

$$|f(\omega_0+d+\Delta)| = \frac{1}{K}\frac{A(d;\Delta)}{\sqrt{S(\omega_p^{(0)}+d)}}. \tag{3}$$

Alternatively, the spectral amplitudes of both input and pump can be characterized simultaneously measuring $\eta^{\theta}(d;\Delta)$ at different values of Δ corresponding to each out channel of the mQPG. These measurements provide the amplitude profiles $A(d;-\Delta_0)$, $A(d;0)$, and $A(d;+\Delta_0)$ for $\Delta = -\Delta_0$, 0, and $+\Delta_0$ respectively. The ratio

$$A_{\pm}(d) = \frac{A(d\pm\Delta_0;0)}{A(d;\pm\Delta_0)} = c\frac{g(\omega_p^{(0)}-d\mp\Delta_0)}{g(\omega_p^{(0)}-d)}. \tag{4}$$

only depends on the pump amplitude ratios and independent of the input amplitude.

For proof of principle, we assume that the pump has a Gaussian spectral amplitude of unknown bandwidth and center, which is a reasonable assumption in typical pulse characterization experiments. Using a curve-fitting on the $A_{\pm}(d)$ profiles for a known Δ_0, we retrieve $g(\omega_p^{(0)}-d)$. The input amplitude profile $|f(\omega_0+d)|$ then can be retrieved as

$$|f(\omega_0+d)| = K\frac{A(d;0)}{|g(\omega_p^{(0)}-d)|}, \tag{5}$$

where K is a scaling constant. This retrieval approach is analogous to that of the simultaneous phase characterization of both input and pump pulses.

II. Retrieval of spectral and phase profiles from the measured data

In this section, we outline the procedure for retrieving the spectral amplitude and phase profiles from the measured data. The analysis focuses on a spectrally perfectly coherent input pulse, as depicted in the first column of Fig. 4(a)

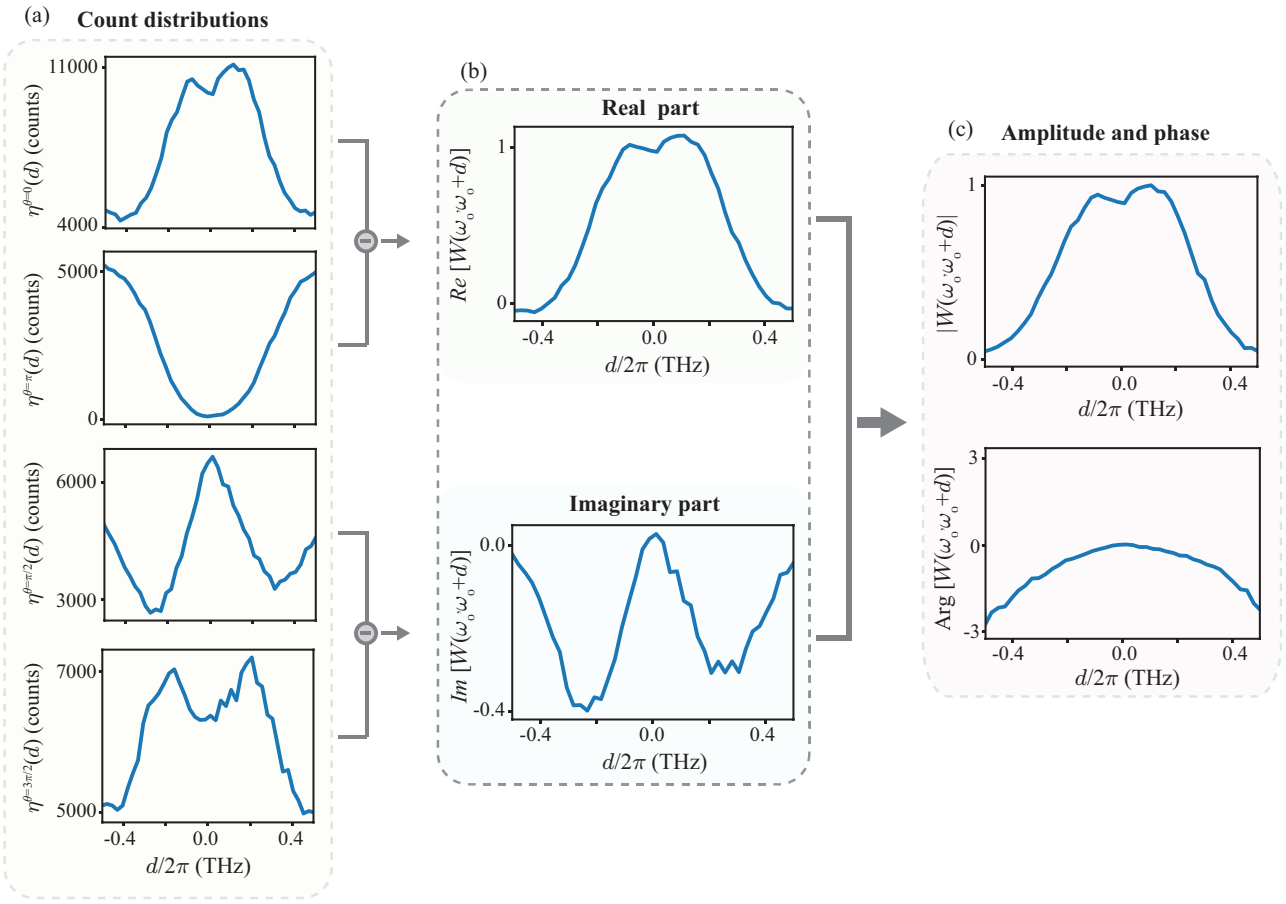

FIG. 1. (a) Measured count distributions $\eta^{\theta}(d)$ at $\theta = 0, \pi, \pi/2$, and $3\pi/2$. (b) Real and imaginary profiles of $W(\omega_0, \omega_0 + d)$. (c) Amplitude $|W(\omega_0 - d, \omega_0 + d)|$ and Arg$[W(\omega_0 - d, \omega_0 + d)]$ profiles of $W(\omega_0 - d, \omega_0 + d)$.

in the main manuscript. Figure 1 shows the measured count distributions $\eta^{\theta}(d)$ at $\theta = 0, \pi/2, \pi, 3\pi/2$. The difference in count distributions yield the real and imaginary parts of the two-point spectral correlation (TPSC) function $W(\omega_0, \omega_0 + d)$ as shown in Fig. 1(b). By combining them, we retrieve the spectral amplitude $|W(\omega_0, \omega_0 + d)|$and phase Arg$[W(\omega_0, \omega_0 + d)]$ profiles as shown in Fig. 1(c).

III. Characterizing partially coherent pulses with tunable time-frequency coherence

In this section, we focus on characterizing the spectral coherence profile of different spectrally partially coherent single-photon-level pulses generated by incoherently mixing perfectly coherent pulses from an OPO in post-processing. The incoming pulses are shaped into different Hermite-Gaussian (HG) modes $\mathrm{HG_n}(\omega)$ and the corresponding TPSC functions, $W_n(\omega_0 - d, \omega_0 + d)$, are measured. To realize a partially coherent pulse in the post-processing, we incoherently add the measured $W_n(\omega_0 - d, \omega_0 + d)$ data with weights λ_n, forming $W(\omega_0 - d, \omega_0 + d) = \sum_n \lambda_n W_n(\omega_0 - d, \omega_0 + d)$ corresponding to a partially coherent pulse. In experiment, we keep the input mean photon number at 0.1 photons per pulse. The total data accumulation time for each partially coherent pulse takes around 120 minutes.

Figure 2(a) shows the mode distribution λ_n as a function of the mode index n for different incoherent mixtures. Here, we are interested in the relative proportion of individual HG pulses; an appropriate normalization of λ_n is not necessary. Figure 2(b) show the corresponding measured $W(\omega_0 - d, \omega_0 + d)$ along with the theoretical predictions. The dashed green curves in Fig. 2(b) represent the expected spectrum $S(\omega_0 - d)$ for corresponding to each partially coherent pulses. Furthermore, we see that $W(\omega_0 - d, \omega_0 + d)$ becomes narrower with the increases in the number of HG modes in the incoherent mixture, indicating a decrease in the spectral coherence. A quantitative comparison between theoretical and experimental results yields similarity $S \approx 99\%$ in both cases, demonstrating the accurate

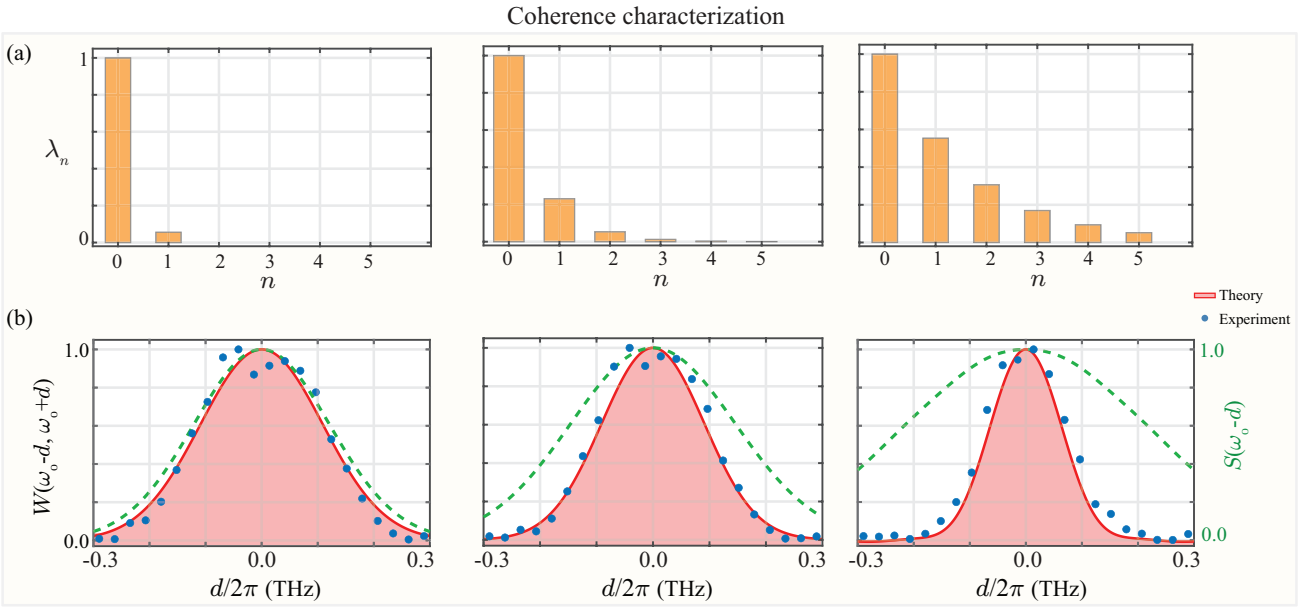

FIG. 2. (a) Mode distribution λ_n for different incoherent mixtures. (b) $W(\omega_0 - d, \omega_0 + d)$ profiles for different incoherent mixtures alongside theoretical predictions. The green dashed curves represent the expected spectrum $S(\omega_0 - d)$ for each incoherent mixture.

coherence characterization capability of this scheme.

IV. Time-frequency characteristics of type-0 parametric down-conversion (PDC) process

In this section, we describe the time-frequency (TF) properties of the type-0 PDC process and explain how it generates spectrally partially coherent pulses. A Gaussian pump pulse, centered at frequency $\omega_{pump}^{(0)}$ with a spectral bandwidth σ_p, drives the type-0 PDC process, producing signal and idler photon pairs centered at frequencies $\omega_s^{(0)}$ and $\omega_i^{(0)}$, respectively. The energy conservation condition of this process imposes the relationship $\omega_{pump} = \omega_s + \omega_i$, where, ω_{pump}, ω_s, and ω_i represent the frequencies of pump, signal, and idler photons, respectively,

The joint spectral amplitude (JSA), which fully describes the complete TF structure of signal-idler pair, is expressed as

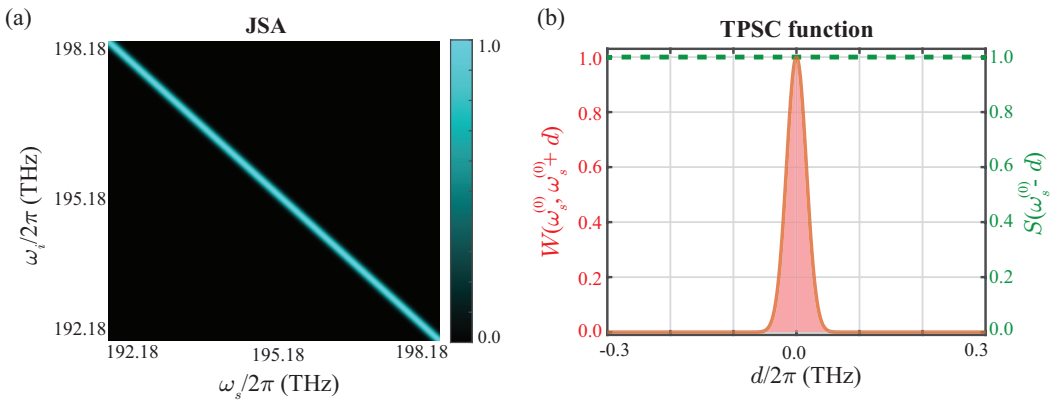

FIG. 3. (a) Joint spectral amplitude (JSA) of our type-0 PDC source. (b) TPSC function $W(\omega_s^{(0)}, \omega_s^{(0)} + d)$ of signal evaluated from the above JSA. The corresponding spectrum (green dashed line) $S(\omega_0 - d)$ is also plotted for comparison.

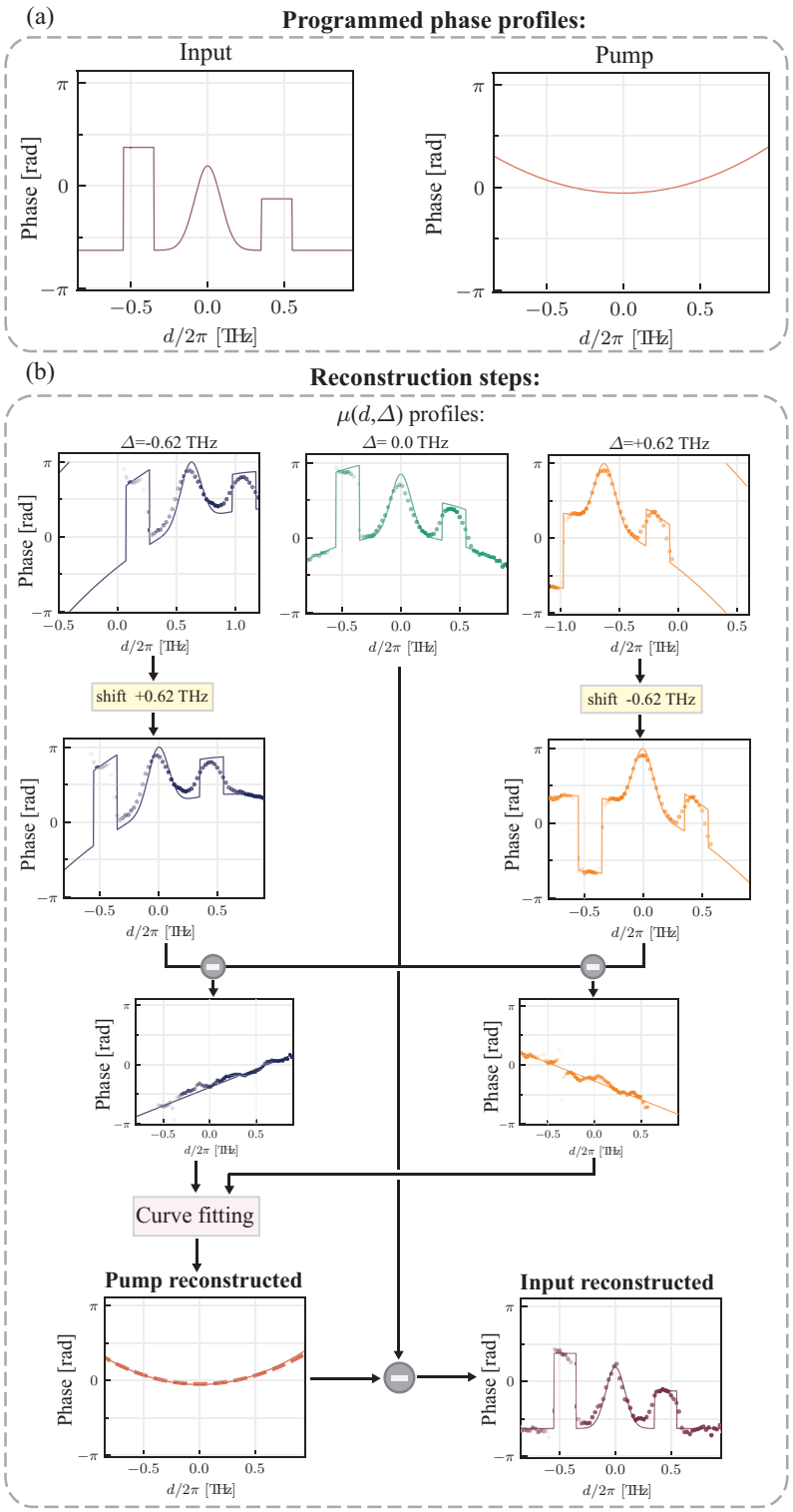

FIG. 4. (a) Spectral phase profiles programmed by input and pump pulse shapers. (b) Steps for reconstructing the spectral phase profiles of input and pump pulses from the measured data. The solid curves represent theoretical predictions and dots represent the measured and reconstructed profiles.

$$\psi(\omega_s,\omega_i) = N \exp\left[-\frac{\left(\omega_s+\omega_i-\omega_s^{(0)}-\omega_i^{(0)}\right)^2}{4\sigma_p^2}\right]\Phi(\omega_s,\omega_i), \tag{6}$$

where, $\Phi(\omega_s,\omega_i)$ represents the phase-matching function determined by the material properties of the $LiNbO_3$ waveguide used in our experiment to realize the type-0 PDC process. Figure 3(a) shows the JSA $\psi(\omega_s,\omega_i)$ corresponding to our type-0 PDC setup, showcasing the strong spectral correlation between signal and idler photons. Here, we see that signal and idler photons are spectrally identical.

The JSA $\psi(\omega_s,\omega_i)$ can be decomposed into Schmidt modes $\{f_n(\omega)\}$ as

$$\psi(\omega_s,\omega_i) = \sum_n \lambda_n f_n(\omega_s) f_n(\omega_i), \tag{7}$$

where, λ_n is the Schmidt coefficient correspond to each Schmidt mode $f_n(\omega)$. To determine the TF structure of the signal photons alone, we trace out the idler photons from the JSA. This is described by the TPSC function $W(\omega_s,\omega_s')$

$$W(\omega_s,\omega_s') = \int \psi(\omega_s,\omega_i)\psi^*(\omega_s',\omega_i)d\omega_i = \sum_n |\lambda_n|^2 f_n(\omega_s) f_n^*(\omega_s'), \tag{8}$$

This TPSC function represents an incoherent mixture of Schmidt modes $\{f_n(\omega_s)\}$, weighted by $\{\lambda_n\}$. This incoherent mixture leads to the generation of spectrally partially coherent signal pulses. Figure 3(b) compares the one-dimensional TPSC function $W(\omega_s^{(0)}\omega_s^{(0)}-d)$ with the spectrum $S(\omega_s^{(0))}-d)$. The significantly narrower width of the TPSC function, relative to the spectrum, highlights the low spectral coherence of the signal pulses.

V. Reconstruction of spectral phase profiles of input and pump pulses

Figure 4(a) shows the spectral phase profiles of input and pump pulses programmed through respective pulse shapers that we want to characterize. Figure 4(b) shows the reconstruction steps. First, following the methodology described in Sec. II, we reconstruct the phase profiles $\mu(d;\Delta)$ as shown in Fig. 4(b) (top row) by measuring count distributions at different mQPG output channels characterized by $\Delta = -0.62, 0$, and $+0.62$ THz alongside the corresponding theoretical predictions.

To retrieve the input and pump phase profiles, we use the algorithm illustrated in Fig.2 of the main text. Specifically, we introduce spectral shifts of $+0.62$ THz and -0.62 THz to $\mu(d;\Delta=-0.62)$ and $\mu(d;\Delta=+0.62)$, respectively. By subtracting these shifted profiles from $\mu(d;0)$ and then employing a curve-fitting algorithm, we retrieve the pump phase profile, $\alpha(\omega_p^{(0)}-d)$, which is shown in Fig. 4(b) (last row left figure). Next, we subtract the obtained pump profile $\alpha(\omega_p^{(0)}-d)$ from $\mu(d;0)$ to retrieve the input phase profile, see last row right plot in Fig. 4(b). This data set is presented in the main text in Fig.6(a) and (b).

8

Conclusion and outlook

8.1 Conclusion

In this thesis, we have explored the foundational elements of and experimentally realized a high-dimensional quantum communication framework using time-frequency qudits. We have directly addressed the main challenges regarding the generation and detection of these complex photonic states by developing its two core building blocks: a programmable source of high-dimensional entangled states and a programmable high-dimensional quantum decoder. In realizing and characterizing these devices, we have demonstrated a versatile platform that not only enables high-dimensional quantum communication, but also opens the door to new lines of research, from the investigation of fundamental quantum properties to the development of practical tools for state characterization and precision measurements.

The first objective of our work was the development of a programmable source for high-dimensional entangled time-frequency states. While previous works had generated such states, achieving programmability of the entanglement dimension while ensuring the generation of maximally entangled states was a significant challenge. Through the precise engineering of parametric down-conversion in a nonlinear waveguide, we achieved unprecedented, real-time control over the modal structure of time-frequency-entangled qudits. We characterized our source, demonstrating that it allows for the generation of maximally entangled time-frequency qudits with a dimensionality that is programmably tunable from $d = 1$ (decorrelated state) up to $d = 20$ [148]. This capability provides a crucial, versatile resource for adapting to the specific requirements of different high-

dimensional quantum protocols, overcoming the fixed dimensionality of previous sources.

This programmable source provides a powerful platform for exploring high-dimensional quantum protocols, moving beyond state generation to enable fundamental tests of quantum mechanics. We demonstrated this directly in a collaborative work with Heriot-Watt University and Lund University [109], where the high-fidelity entangled states produced by our source were used to certify a violation of high-dimensional Bell inequalities for dimensions up do $d = 8$. Remarkably, this was achieved using only joint spectral intensity measurements, demonstrating that intensity correlations alone can probe phase-sensitive superposition states, and offering a practical route for future Bell tests in high dimensions.

The second cornerstone, which became the central technology for the remainder of this thesis, was the realization of a versatile high-dimensional quantum decoder: the multi-output quantum pulse gate (mQPG). This device was designed to overcome a major bottleneck in the field: the challenge of performing efficient, single-shot projective measurements in arbitrary high-dimensional bases. We demonstrated this feature by characterizing the mQPG's performance in a five-dimensional Hilbert space of Hermite-Gaussian (HG) modes through quantum detector tomography, showing projections in all six possible mutually unbiased bases (MUBs) with an average fidelity of 96% [95]. This characterization also enabled extremely accurate maximum-likelihood quantum state tomography, achieving a fidelity of 98% in the reconstructed states [95].

Moreover, we showcased the versatility of the mQPG by showing its operation with three distinct time-frequency mode bases: HG modes, pulsed frequency bins, and ultrafast time bins, with the basis selection achieved solely through spectral reconfiguration of the pump [60]. This established the mQPG as a truly general decoder for time-frequency encodings, capable of interfacing between different systems that might rely on different alphabets, a critical feature for future high-dimensional quantum networks.

The most immediate application of the mQPG's ability to perform simultaneous projections onto arbitrary states was the one that motivated its creation: high-dimensional quantum key distribution (HD-QKD). Using pulsed frequency bins in dimension $d = 3$, we implemented a complete prepare-and-measure HD-QKD system. Here, the capability of the mQPG to project onto arbitrary superpositions of frequency bins was fundamental to building our decoder for the control basis, while the fact that unconverted photons pass through unaffected allowed us to simultaneously measure the key basis. In a proof-of-principle experiment, we demonstrated an asymptotic secret key fraction of 1.18 bits per photon, surpassing the fundamental limit for qubit-based systems and validating the enhanced security and information capacity promised by high-dimensional alphabets.

However, as is often the case in research, the development of such a versatile tool opened the door to explorations far beyond our initial focus. We found that the mQPG, by providing access to the full probability distribution of measurement outcomes in multiple MUBs, could be used to probe fundamental properties of quantum mechanics. In a collaborative work with the University of Pavia [149], we leveraged these high-dimensional projections to experimentally verify entropic uncertainty relations (EURs) for multiple MUBs in 3, 4, and 5 dimensions, which were previously only proven numerically. In what felt like a traditional story of theory and experiment, we found that in a particular case (three bases in five dimensions) the experimental data did not match the theoretical predictions. After confirming the results, we realized this discrepancy arose from a known asymmetry in sets of MUBs: choosing inequivalent sets of MUBs for measuring uncertainty relations can lead to different minimum uncertainty bounds [150]. With these works, we not only uncovered a fascinating new aspect of quantum complementarity, but also developed a framework that can be used to probe EURs and inequivalent sets of MUBs in even higher dimensions.

Beyond fundamental science, we discovered that the multi-output nature of our platform could be leveraged to improve existing applications and develop new ones entirely. We used our system for self-guided tomography (SGT), a technique that for the first time we applied to the time-frequency domain, demonstrating state estimation fidelities exceeding 99% in up to five dimensions without the need for additional calibration or post-processing [151]. We verified the technique's robustness against both statistical and environmental noise. This resilience is particularly beneficial in the photon-starved regimes typical of quantum information applications, making SGT a highly practical and scalable method for the characterization of unknown high-dimensional quantum states in real-world scenarios where experimental conditions are not ideal.

Taking this a step further, we developed a new pulse characterization technique, FIREFLY, which harnesses the multi-channel structure of the mQPG to perform interferometric measurements between different frequency bins. This enables the simultaneous characterization of the spectral amplitude, phase, and coherence profiles of single-photon pulses, and even the characterization of two unknown pulses, overcoming a long-standing limitation in ultrashort pulse measurement that required a well-characterized reference pulse [130]. The utility of this method was immediately apparent in our own work, as we used it as a diagnostic tool to precisely characterize and compensate for the higher-order spectral phase of the pulses used in our experiments, which was crucial for achieving high-fidelity projections. Indeed, the versatility of the underlying multi-channel detection platform is not limited to quantum applications: in a joint work with the Department of Electrical Engineering, we adapted the principles of time-frequency mode sorting to realize a high-precision pulsed lidar system for single-photon-level signals [146].

8.2 Outlook

The successful implementation and characterization of our programmable source and decoder represents a significant step forward for high-dimensional quantum communication and. More in general, this work has provided a complete and versatile toolbox for the experimental implementation of time-frequency qudits.

The most direct next step would be to combine our fully programmable source and our reconfigurable decoder, opening the door to a plethora of future experiments. One could use this combination to realize entanglement-based HD-QKD, which would allow for an experimental investigation into how the secret key rate scales with the dimensionality of the encoding alphabet. Beyond HD-QKD, this combined platform is perfectly suited for exploring the interesting properties of high-dimensional entanglement through projections onto complete sets of MUBs.

Of course, it would be exciting to address even higher dimensions. For this, moving to a versatile platform like thin-film lithium niobate would be highly beneficial, paving the way for more compact, efficient, and scalable integrated devices. Integrating resonant structures could also offer enhanced control and efficiency, pushing the boundaries of what is possible.

It would also be incredibly rewarding to see these technologies find their way into practical applications beyond mere research interest. The advancements demonstrated here have the potential to be applied in areas such as efficient deep-space communication and robust quantum cryptography, offering new insights into fundamental quantum mechanics while addressing practical challenges. We started this journey with quantum communication in mind and, along the way, found applications in fundamental tests of quantum mechanics, new characterization methods, and even improved classical measurements. This is the exciting nature of research: you set out with a goal, and in building the tools to reach it, you discover they can take you to places you never expected. Who knows what's next?

A

Derivation of modulated phase-matching function

This appendix details the mathematical derivations for the phase-matching functions of modulated poling structures, as introduced in Section 2.3.2.

A.1 Fourier series and transforms

In the context of the spatial nonlinearity profile $d(z)$ and phase mismatch $\Delta\beta$, we define the Fourier transform $\mathcal{F}$ and its inverse $\tilde{\mathcal{F}}$ as

$$\Phi(\Delta\beta) = \mathcal{F}\{d(z)\} = \int_{-\infty}^{\infty} d(z)\, e^{i\Delta\beta z}\, \mathrm{d}z\,, \tag{A.1.1}$$

$$d(z) = \tilde{\mathcal{F}}\{\Phi(\Delta\beta)\}\, \frac{1}{2\pi} \int_{-\infty}^{\infty} \Phi(\Delta\beta)\, e^{-i\Delta\beta z}\, \mathrm{d}\Delta\beta\,, \tag{A.1.2}$$

where the $1/2\pi$ factor is due to the asymmetric definition we adopt. Note that this is opposite to the more common convention used for time-frequency Fourier transforms in Sec. 2.1.2, which assigns the negative exponent to the direct transform and the positive one to the inverse transform.

With this definition, the Fourier transform of a product of two functions $f(z)$ and $g(z)$ is given by the convolution theorem:

$$\mathcal{F}\{f(z)\cdot g(z)\} = \frac{1}{2\pi}\left(\hat{f} * \hat{g}\right)(\Delta\beta), \tag{A.1.3}$$

where, again, the factor $\frac{1}{2\pi}$ derives from the asymmetry in the Fourier transform we adopt here, and $*$ denotes the convolution integral:

$$\left(\hat{f} * \hat{g}\right)(\Delta\beta) = \int_{-\infty}^{\infty} \hat{f}(\xi)\hat{g}(\Delta\beta - \xi)\, d\xi\,. \tag{A.1.4}$$

Conversely, the Fourier transform of the convolution of two functions $f(z)$ and $g(z)$ is

$$\mathcal{F}\{(f * g)(z)\} = \mathcal{F}\{f(z)\}\cdot\mathcal{F}\{g(z)\}\,. \tag{A.1.5}$$

Any periodic function $d(z)$ with period Λ can be expressed as a complex exponential Fourier series:

$$d(z) = \sum_{n=-\infty}^{+\infty} c_n\, e^{i\frac{2\pi n z}{\Lambda}},$$

where the coefficients c_n are given by

$$c_n = \frac{1}{\Lambda}\int_{\Lambda} d(z)\, e^{-i\frac{2\pi n z}{\Lambda}}\, \mathrm{d}z\,.$$

Notice that, with this definition, c_0 is the mean value of $d(z)$ over one period. The Fourier transform of this periodic function is a Dirac comb:

$$\mathcal{F}\{d(z)\} = 2\pi \sum_{n=-\infty}^{+\infty} c_n\, \delta\left(\Delta\beta - \frac{2\pi n}{\Lambda}\right). \tag{A.1.6}$$

This result is fundamental to our analysis, as it implies that any periodic (repeated) structure in the nonlinear profile generates a Dirac comb in the phase-matching function.

A.2 Poling with phase reversal

The nonlinear profile for phase-reversal poling is the product of the QPM square wave $s(z/\lambda)$ and a slower modulating square wave $s_D(z/\gamma)$ with duty cycle D:

$$\begin{aligned} d(z) &= s\left(\frac{z}{\Lambda}\right)\cdot s_D\left(\frac{z}{\Gamma}\right) \\ &= \sum_{n\,\mathrm{odd}} \frac{2}{i\pi n} e^{i\frac{2\pi}{\Lambda}nz}\cdot\left[(2D-1) + \sum_{m\neq 0}\frac{1}{i\pi m}\left(1-\mathrm{e}^{-i2\pi mD}\right)e^{i\frac{2\pi}{\Gamma}mz}\right]. \end{aligned} \tag{A.2.1}$$

Its Fourier transform $\mathcal{F}\{d(z)\}$ is found by applying the convolution theorem to the Fourier series of the two functions:

$$\begin{aligned}\mathcal{F}\{d(z)\} =& \frac{1}{2\pi}\mathcal{F}\left\{\sum_{n\,\text{odd}}\frac{2}{i\pi n}e^{i\frac{2\pi}{\Lambda}nz}\right\} * \mathcal{F}\left\{(2D-1)+\sum_{m\neq 0}\frac{1}{i\pi m}\left(1-\mathrm{e}^{-i2\pi mD}\right)e^{i\frac{2\pi}{\Gamma}mz}\right\}\\ =& 2\pi\sum_{n\,\text{odd}}\frac{2}{i\pi n}\delta\left(\Delta\beta-\frac{2\pi}{\Lambda}n\right)\\ & * \left[(2D-1)\,\delta(\Delta\beta)+\sum_{m\neq 0}\frac{1}{i\pi m}\left(1-e^{-i2\pi mD}\right)\delta\left(\Delta\beta-\frac{2\pi}{\Gamma}m\right)\right]\\ =& 2\pi\sum_{n\,\text{odd}}\frac{2}{i\pi n}\Bigg[(2D-1)\,\delta\left(\Delta\beta-\frac{2\pi}{\Lambda}n\right)\\ & -\sum_{m\neq 0}\frac{1}{i\pi m}\left(1-e^{-i2\pi mD}\right)\delta\left(\Delta\beta-\frac{2\pi}{\Lambda}n-\frac{2\pi}{\Gamma}m\right)\Bigg],\end{aligned} \tag{A.2.2}$$

where each peak in eq. (2.3.18) is split into multiple peaks at positions $\Delta\beta' = 2\pi m/\Gamma$ with heights given by the coefficients

$$c_m(D) = \begin{cases} 2D-1, & m=0\,,\\ -\dfrac{1-e^{-i2\pi mD}}{i\pi m}, & m\neq 0\,. \end{cases} \tag{A.2.3}$$

The values of these coefficients as a function of the duty cycle D are studied in Figure 2.14. Note that the sum of all the corresponding intensities is unchanged, i.e., the total efficiency of the phase-matching across all frequencies remains constant.

This yields a series of delta functions at positions $\Delta\beta = \frac{2\pi}{\Lambda}n + \frac{2\pi}{\Gamma}m$, with the relative heights given by the coefficients in Eq. (A.2.3). Substituting this into the general expression for $\Phi(\Delta\beta)$ in eq. (2.3.16) and applying the same approximation as for QPM gives the final result in eq. (2.3.22):

$$\Phi(\Delta\beta') \approx L\,\frac{2}{i\pi}\sum_m c_m(D)\,\operatorname{sinc}\left(\left(\Delta\beta'-\frac{2\pi}{\Gamma}m\right)\frac{L}{2}\right)e^{i\left(\Delta\beta'-\frac{2\pi}{\Gamma}m\right)\frac{L}{2}}. \tag{A.2.4}$$

This expression describes a train of sinc functions, each identical to eq. (2.3.21), separated by $2\pi/\Gamma$. These peaks reach maximum heights in the region near $\Delta\beta' = 0$ and fade away from this region.

In the special case of $D = 0.5$, the symmetry of the square wave results in the vanishing of the central peak at $\Delta\beta' = 0$, similarly to the case of QPM. In this case, the terms with $m = \pm 1$ are dominant and correspond to two identical sinc functions centered at $\Delta\beta' = \pm 2\pi/\Gamma$. This case is analyzed in Figure 2.19, showing that the line corresponding to $\Delta\beta' = 0$ travels back and forth between the same two points due to the sign of the nonlinearity, which flips at regular intervals. This phase reversal acts exactly when the lines corresponding to

$\Delta\beta' = \pm 2\pi/\Gamma$ would start decreasing in amplitude, causing them to constantly increase.

Another noteworthy case is that of $D = 0.265$, in which the central peak has equal height to the two side peaks, leading to three identical dominant peaks at $\Delta\beta' = 0$ and $\Delta\beta' = \pm 2\pi/\Gamma$. In principle, additional phase reversal modulations with varying periods and duty cycles can be combined to generate different phase-matching structures. For instance, superimposing two symmetric square waves ($D = 0.5$) with periods Γ and 2Γ and a phase difference of γ generates a nonlinear profile

$$\begin{aligned} d(z) &= s\left(\frac{z}{\Lambda}\right) \cdot s\left(\frac{z}{\Gamma}\right) \cdot s\left(\frac{z-\gamma}{2\Gamma}\right) \\ &= \sum_{n\,\mathrm{odd}} \frac{2}{i\pi n} e^{i\frac{2\pi}{\Lambda}nz} \cdot \sum_{m\,\mathrm{odd}} \frac{2}{i\pi m} e^{i\frac{2\pi}{\Gamma}mz} \cdot \sum_{p\,\mathrm{odd}} \frac{2}{i\pi p} e^{i\frac{2\pi}{2\Gamma}p(z-\gamma)} \\ &= \sum_{n\,\mathrm{odd}} \frac{2}{i\pi n} e^{i\frac{2\pi}{\Lambda}nz} \cdot \sum_{k\,\mathrm{odd}} c_k e^{i\frac{2\pi}{2\Gamma}kz}, \end{aligned} \tag{A.2.5}$$

with

$$c_k = \sum_{m\,\mathrm{odd}} \frac{-4e^{-i\pi(k-2m)\frac{\gamma}{\Gamma}}}{\pi^2(k-2m)m}. \tag{A.2.6}$$

The Fourier transform of this nonlinear profile is

$$\begin{aligned} \mathcal{F}\{d(z)\} =& \frac{1}{2\pi}\mathcal{F}\left\{\sum_{n\,\mathrm{odd}} \frac{2}{i\pi n} e^{i\frac{2\pi}{\Lambda}nz}\right\} * \mathcal{F}\left\{\sum_{k\,\mathrm{odd}} e^{i\frac{2\pi}{2\Gamma}kz} c_k\right\} \\ =& 2\pi \sum_{n\,\mathrm{odd}} \frac{2}{i\pi n}\delta\left(\Delta\beta - \frac{2\pi}{\Lambda}n\right) * \sum_{k\,\mathrm{odd}} c_k \delta\left(\Delta\beta - \frac{2\pi}{2\Gamma}k\right), \end{aligned} \tag{A.2.7}$$

which describes a delta comb centered around each QPM peak, with delta in position $\Delta\beta' = \pi k/\Gamma$ and a height modulated by the coefficient c_k. Particularly, for $\gamma = .114\Gamma$, the four peaks at $k = \pm 1$ and $k = \pm 3$ are dominant and have equal heights.

A.3 Super-poling

Consider a poling profile that alternates between poled and unpoled regions with a period Γ (the *super-poling* period). If each poled region has length l (the *unit active length*), each corresponding unpoled region will have length $\Gamma - l$. The resulting nonlinear profile $d(z)$ is that of a square wave (from the poled regions) multiplied by a rectangular function—defined in eq.(2.3.15)—which selects a length l at regular intervals Γ, all superimposed on a flat background of value 1:

$$d(z) = 1 + \left(s\left(\frac{z}{\Lambda}\right) - 1\right) \cdot \sum_{m=-\infty}^{\infty} \Pi\left(\frac{z - m\Gamma}{l}\right). \tag{A.3.1}$$

Taking the Fourier transform, and using the linearity property (the Fourier transform of a sum is the sum of the Fourier transforms), we obtain

$$\begin{aligned}\mathcal{F}\{d(z)\} =&\mathcal{F}\{1\} + \frac{1}{2\pi}\left(\mathcal{F}\left\{s\left(\frac{z}{\Lambda}\right)\right\} - \mathcal{F}\{1\}\right) * \sum_m \mathcal{F}\left\{\Pi\left(\frac{z-m\Gamma}{l}\right)\right\} \\ =&2\pi\delta(\Delta\beta) + \left[\sum_{n\,\text{odd}} \frac{2}{i\pi n}\delta\left(\Delta\beta - \frac{2\pi}{\Lambda}n\right) - \delta(\Delta\beta)\right] \\ &* \left[l\,\text{sinc}\left(\frac{\Delta\beta l}{2}\right)e^{i\frac{\Delta\beta l}{2}} \cdot \frac{2\pi}{\Gamma}\sum_m \delta\left(\Delta\beta - \frac{2\pi}{\Gamma}m\right)\right] \\ =&2\pi\delta(\Delta\beta) - 2\pi\frac{l}{\Gamma}\sum_m \delta\left(\Delta\beta - \frac{2\pi}{\Gamma}m\right)\cdot\text{sinc}\left(\frac{2\pi m}{\Gamma}\frac{l}{2}\right)e^{i\frac{2\pi m}{\Gamma}\frac{l}{2}} \\ &+ 2\pi\frac{l}{\Gamma}\sum_{n\,\text{odd}}\frac{2}{i\pi n}\sum_m \delta\left(\Delta\beta - \frac{2\pi}{\Lambda}n - \frac{2\pi}{\Gamma}m\right)\cdot\text{sinc}\left(\frac{2\pi m}{\Gamma}\frac{l}{2}\right)e^{i\frac{2\pi m}{\Gamma}\frac{l}{2}}.\end{aligned} \tag{A.3.2}$$

Although this expression appears complex, it only comprises a sum of delta functions. When substituted back into eq.(2.3.16), these delta functions define the center positions of the resulting sinc-shaped phase-matching peaks. The first term, $2\pi\delta(\Delta\beta)$, results in a sinc function at $\Delta\beta = 0$ (the center of the birefringent phase-matching). The second term corresponds to a Dirac comb with a period of $2\pi/\Gamma$, modulated by a sinc envelope centered at $\Delta\beta = 0$. This term derives from the alternating unpoled regions, and it is analogous to the diffraction pattern of light scattered by a grating with rectangular slits. Notably, the Dirac comb also contains a contribution at $\Delta\beta = 0$ that cancels part of the contribution from the flat background, thereby conserving the overall efficiency across all frequencies. The last term contains the same Dirac comb modulated by a sinc envelope, but this time centered around each QPM peak. Particularly, in the region near $n = 1$ we will have phase-matching peaks at positions $\Delta\beta' = 2\pi m/\Gamma$ with heights determined by the coefficients

$$c_m\left(\frac{l}{\Gamma}\right) = \frac{l}{\Gamma}\,\text{sinc}\left(\frac{2\pi m}{\Gamma}\frac{l}{2}\right)e^{i\frac{2\pi m}{\Gamma}\frac{l}{2}}. \tag{A.3.3}$$

The values of these coefficients as a function of the poled waveguide fraction l/Γ are studied in Figure 2.16. The cross-hatched region indicates the fraction $1 - l/\Gamma$ of phase-matching efficiency that is "lost" due to the unpoled fraction of the waveguide.

By focusing on the region near $n = 1$ and defining the shifted variable $\Delta\beta'$, we obtain

$$\begin{aligned}\Phi(\Delta\beta') \approx& L\frac{2i}{\pi}\frac{l}{\Gamma}\sum_m c_m\left(\frac{l}{\Gamma}\right)\text{sinc}\left(\left(\Delta\beta' - \frac{2\pi}{\Gamma}m\right)\frac{L}{2}\right)e^{i\left(\Delta\beta' - \frac{2\pi}{\Gamma}m\right)\frac{L}{2}} \\ \approx& L\frac{2i}{\pi}\frac{l}{\Gamma}\,\text{sinc}\left(\frac{\Delta\beta' l}{2}\right)e^{i\frac{\Delta\beta' l}{2}}\sum_m \text{sinc}\left(\left(\Delta\beta' - \frac{2\pi}{\Gamma}m\right)\frac{L}{2}\right)e^{i\left(\Delta\beta' - \frac{2\pi}{\Gamma}m\right)\frac{L}{2}},\end{aligned} \tag{A.3.4}$$

where we assumed a slowly-varying envelope, i.e., $l \ll L$. Comparing this with the QPM expression in eq. (2.3.21), we notice that the phase-matching peak is split into multiple sinc-shaped peaks of identical width $2\pi/L$, separated by $2\pi/\Gamma$, with their heights modulated by a sinc envelope of width $2\pi/l$. The comb and the envelope are both centered at $\Delta\beta' = 0$, giving rise to a symmetric phase-matching structure. The number of peaks within the full width at half maximum (FWHM) of the sinc envelope can be approximated as Γ/l, which is the inverse of the total poled fraction of the waveguide. In the limit case where $l = \Gamma$, the poling structure is continuous and eq. (2.3.24) reduces to eq. (2.3.21).

Figure 2.20 shows the amplitude and phase of the phase-matching function at different points along the waveguide. Up to the first unpoled region, the phase-matching is determined by the QPM behavior. In the unpoled regions, the sign of the nonlinearity is unchanging, and the Φ lines start moving on the narrow circles dictated by the birefringent phase-matching case, so that their amplitude does not change significantly. When the next poled section starts, the amplitude starts increasing or decreasing depending on the phase that the Φ lines had accumulated while rotating, leading to multiple phase-matching peaks at regular intervals of $\Delta\beta'$.

An alternative approach involves restarting the poling at every interval Γ for a length l (instead of periodically "erasing" it), leading to

$$\begin{aligned} d(z) &= 1 + \sum_m \left(s\left(\frac{z - m\Gamma}{\Lambda}\right) - 1 \right) \cdot \Pi\left(\frac{z - m\Gamma}{l}\right) \\ &= 1 + \sum_m \delta(z - m\Gamma) * \left[\left(s\left(\frac{z}{\Lambda}\right) - 1 \right) \cdot \Pi\left(\frac{z}{l}\right) \right], \end{aligned} \tag{A.3.5}$$

with Fourier transform

$$\begin{aligned} \mathcal{F}\{d(z)\} =& \mathcal{F}\{1\} + \frac{1}{2\pi} \sum_m \mathcal{F}\{\delta(z - m\Gamma)\} \cdot \left[\left(\mathcal{F}\left\{ s\left(\frac{z}{\Lambda}\right) \right\} - \mathcal{F}\{1\} \right) * \mathcal{F}\left\{ \Pi\left(\frac{z}{l}\right) \right\} \right] \\ =& 2\pi\delta(\Delta\beta) + \frac{2\pi}{\Gamma} \sum_m \delta\left(\Delta\beta - \frac{2\pi}{\Gamma} m\right) \\ & \cdot \left[\left(\sum_{n\,\text{odd}} \frac{2}{i\pi n} \delta\left(\Delta\beta - \frac{2\pi}{\Lambda} n\right) - \delta(\Delta\beta) \right) * l\,\text{sinc}\left(\frac{\Delta\beta l}{2}\right) e^{i\frac{\Delta\beta l}{2}} \right] \\ =& 2\pi\delta(\Delta\beta) - 2\pi \frac{l}{\Gamma} \sum_m \delta\left(\Delta\beta - \frac{2\pi}{\Gamma} m\right) \cdot \text{sinc}\left(\frac{2\pi m}{\Gamma} \frac{l}{2}\right) e^{i\frac{2\pi m}{\Gamma}\frac{l}{2}} \\ & + 2\pi \frac{l}{\Gamma} \sum_{n\,\text{odd}} \frac{2}{i\pi n} \sum_m \delta\left(\Delta\beta - \frac{2\pi}{\Gamma} m\right) \\ & \cdot \text{sinc}\left(\left(\frac{2\pi}{\Gamma} m - \frac{2\pi}{\Lambda} n \right) \frac{l}{2} \right) e^{i\left(\frac{2\pi}{\Gamma} m - \frac{2\pi}{\Lambda} n\right)\frac{l}{2}}. \end{aligned} \tag{A.3.6}$$

With the same approximations as before, we obtain

$$\Phi(\Delta\beta') \approx L\,\frac{2i}{\pi}\sum_m \operatorname{sinc}\left(\left(\Delta\beta-\frac{2\pi}{\Gamma}m\right)\frac{L}{2}\right)e^{i\left(\Delta\beta-\frac{2\pi}{\Gamma}m\right)\frac{L}{2}} \cdot\frac{l}{\Gamma}\operatorname{sinc}\left(\frac{\Delta\beta' l}{2}\right)e^{i\frac{\Delta\beta' l}{2}}, \tag{A.3.7}$$

which differs from eq. (2.3.24) only in the alignment of the Dirac comb. In particular, when $\Gamma = k\Lambda$ (with $k \in \mathbb{Z}$), the Dirac train aligns with the sinc envelope and the expressions become identical. If instead $\Gamma = (k+\frac{1}{2})\Lambda$, a symmetric structure with two equal peaks around $\Delta\beta' = 0$ emerges; in the limit $l = \Gamma$, when the waveguide is completely poled, this structure will lead to the same phase-matching profile as a phase-reversal modulation with duty cycle $D = 0.5$ in Figure 2.19.

B

Miscellanea

B.1 Recipe for MUBs

B.1.1 MUBs in prime power dimensions

For a prime odd dimension d, Ivanovic [21] showed that one can find $d+1$ MUBs, which include the fundamental basis $\{|0\rangle, |1\rangle, \ldots, |d-1\rangle\}$ and d superposition bases. If we define $\left|v_k^{(r)}\right\rangle$ as the element k of basis r, then the elements of the fundamental basis are $\left|v_k^{(0)}\right\rangle = |k\rangle$, whereas its MUBs are

$$\left|v_k^{(r)}\right\rangle = \frac{1}{\sqrt{d}} \sum_{l=0}^{d-1} \omega^{rl^2+kl} |l\rangle, \quad \omega = e^{\frac{2\pi i}{d}}, \quad r = 1, \ldots, d, \tag{B.1.1}$$

in which the components of the vectors all have magnitude $1/\sqrt{d}$ and a phase that is a d-th root of unity.

Wootters and Fields [22] extended this to odd prime powers $d = p^n$, $p \neq 0$, finding the d MUBs as

$$\left|v_k^{(r)}\right\rangle = \frac{1}{\sqrt{d}} \sum_{l=0}^{d-1} \omega^{\mathrm{Tr}\{rl^2+kl\}} |l\rangle, \quad \omega = e^{\frac{2\pi i}{p}}, \quad r = 1, \ldots, d, \tag{B.1.2}$$

where the trace is defined as

$$\mathrm{Tr}(\alpha) = \alpha + \alpha^p + \alpha^{p^2} + \cdots + \alpha^{p^{n-1}}. \tag{B.1.3}$$

In the same work, Wootters and Fields also showed the different construction required for even prime powers $d = 2^n$.

B.1.2 Circulant MUBs

Combescure [118] showed another construction of MUBs for prime dimensions d from circulant Hadamard matrices. In this formulation, each basis is generated from a fixed vector by cyclically shifting its components. The fundamental (computational) basis remains $\{\left|v_k^{(0)}\right\rangle = |k\rangle\}$, while the remaining $d-1$ bases, labeled by $r = 1, \ldots, d-1$, are defined by

$$\left|v_k^{(r)}\right\rangle = \frac{1}{\sqrt{d}} \sum_{l=0}^{d-1} \omega^{\frac{rl(l+1)}{2} - kl} |l\rangle \,, \quad \omega = e^{\frac{2\pi i}{d}} \,, \quad j = 0, \ldots, d-1 \,. \tag{B.1.4}$$

B.2 Spectral formulas

In this thesis, we define a Gaussian spectrum centered at ω_0 with standard deviation σ as

$$\text{Gauss}(\omega; \omega_0, \sigma) = \frac{1}{\sqrt{\sigma\sqrt{\pi}}} e^{-\frac{(\omega-\omega_0)^2}{2\sigma^2}} \,, \tag{B.2.1}$$

where the FWHM is related to the standard deviation through $\text{FWHM} = \sigma \cdot 2\sqrt{2\ln(2)}$.

HG modes are defined as

$$\text{HG}_n(\omega; \omega_0, \sigma) = \frac{1}{\sqrt{2^n n! \sqrt{\pi}\,\sigma}} H_n\left(\frac{\omega - \omega_0}{\sigma}\right) e^{-\frac{(\omega-\omega_0)^2}{2\sigma^2}} \,, \tag{B.2.2}$$

where H_n is the Hermite polynomial of order n. Note that $\text{HG}_0(\omega) = \text{Gauss}(\omega)$.

We define Gaussian frequency bins in d dimensions as Gaussian spectra centered at different frequencies spaced by $\Delta\omega$:

$$\text{FB}_n(\omega; \omega_0, \sigma, \Delta\omega) = \text{HG}_0\left(\omega; \omega_0 + \left(n - \frac{d-1}{2}\right)\Delta\omega, \sigma\right) . \tag{B.2.3}$$

This definition maintains the overall central frequency at ω_0. We choose the frequency separation large enough to minimize inter-bin overlap in order to have effectively orthogonal modes.

Gaussian time bins are instead defined as overlapping Gaussian spectra with different linear phases, which map to different delays separated by Δt:

$$\text{TB}_n(\omega; \omega_0, \sigma, \Delta t) = \text{HG}_0(\omega; \omega_0, \sigma) \cdot e^{i\,2\pi(\omega-\omega_0)\cdot\left(n - \frac{d-1}{2}\right)\cdot\Delta t} \,. \tag{B.2.4}$$

Here as well, the time separation is chosen large enough with respect to the time width ($\propto 1/\sigma$) to prevent overlaps between different bins and ensure orthogonality.

Finally, in this thesis, we define the sinc function as

$$\operatorname{sinc}(x) = \begin{cases} \dfrac{\sin(x)}{x} & x \neq 0\,, \\ 1 & x = 0\,. \end{cases} \tag{B.2.5}$$

With this expression, the null-to-null bandwidth (i.e., the distance between the two central zeroes) is $\Delta x = 2\pi$.

Bibliography

[1] G. P. Agrawal, *Fiber-optic communication systems*, 3. ed, Wiley Series in Microwave and Optical Engineering (Wiley-Interscience, New York, NY, 2002) (cit. on p. xi).

[2] S. Barnett, *Quantum information* (Oxford University Press, Inc., USA, 2009) (cit. on pp. xi, 1, 15).

[3] M. A. Nielsen and I. L. Chuang, *Quantum computation and quantum information* (Cambridge University Press, 2010) (cit. on pp. xi, 1).

[4] N. J. Cerf, M. Bourennane, A. Karlsson, and N. Gisin, "Security of Quantum Key Distribution Using d-Level Systems", Phys. Rev. Lett. **88**, 4 (2002) (cit. on pp. xii, 8, 19, 20, 133).

[5] L. Sheridan and V. Scarani, "Security proof for quantum key distribution using qudit systems", Phys. Rev. A **82**, 1–4 (2010) (cit. on pp. xii, 8, 19, 20, 72, 133).

[6] B. P. Lanyon, M. Barbieri, M. P. Almeida, T. Jennewein, T. C. Ralph, K. J. Resch, G. J. Pryde, J. L. O'Brien, A. Gilchrist, and A. G. White, "Simplifying quantum logic using higher-dimensional Hilbert spaces", Nat. Phys. **5**, 134–140 (2009) (cit. on p. xii).

[7] T. Durt, B.-G. Englert, I. Bengtsson, and K. Zyczkowski, "On mutually unbiased bases", Int. J. Quantum Inf. **08**, 535–640 (2010) (cit. on pp. xii, 8, 145).

[8] J. L. O'Brien, A. Furusawa, and J. Vučković, "Photonic quantum technologies", Nat. Photonics **3**, 687–695 (2009) (cit. on p. xii).

[9] C. D. Bruzewicz, J. Chiaverini, R. McConnell, and J. M. Sage, "Trapped-ion quantum computing: Progress and challenges", Appl. Phys. Rev. **6**, 021314 (2019) (cit. on p. xii).

[10] R. Hanson, L. P. Kouwenhoven, J. R. Petta, S. Tarucha, and L. M. K. Vandersypen, "Spins in few-electron quantum dots", Rev. Mod. Phys. **79**, 1217–1265 (2007) (cit. on p. xii).

[11] M. Kjaergaard, M. E. Schwartz, J. Braumüller, P. Krantz, J. I.-J. Wang, S. Gustavsson, and W. D. Oliver, "Superconducting Qubits: Current State of Play", Annu. Rev. Condens. Matter Phys. **11**, 369–395 (2020) (cit. on p. xii).

[12] M. Ringbauer, M. Meth, L. Postler, R. Stricker, R. Blatt, P. Schindler, and T. Monz, "A universal qudit quantum processor with trapped ions", Nat. Phys. **18**, 1053–1057 (2022) (cit. on p. xii).

[13] P. Hrmo, B. Wilhelm, L. Gerster, M. W. van Mourik, M. Huber, R. Blatt, P. Schindler, T. Monz, and M. Ringbauer, "Native qudit entanglement in a trapped ion quantum processor", Nat. Commun. **14**, 2242 (2023) (cit. on p. xii).

[14] D. Cozzolino, B. Da Lio, D. Bacco, and L. K. Oxenløwe, "High-Dimensional Quantum Communication: Benefits, Progress, and Future Challenges", Adv. Quantum Technol. **2** (2019) (cit. on pp. xii, 7, 28, 133).

[15] H. J. Kimble, "The quantum internet", Nature **453**, 1023–1030 (2008) (cit. on p. xii).

[16] B. Brecht, D. V. Reddy, C. Silberhorn, and M. G. Raymer, "Photon temporal modes: a complete framework for quantum information science", Phys. Rev. X **5**, 041017 (2015) (cit. on pp. xii, 26, 28, 29, 72, 95).

[17] V. Scarani, H. Bechmann-Pasquinucci, N. J. Cerf, M. Dušek, N. Lütkenhaus, and M. Peev, "The security of practical quantum key distribution", Rev. Mod. Phys. **81**, 1301–1350 (2009) (cit. on pp. 1, 9, 13, 16, 18, 22, 137).

[18] C. E. Shannon, "A mathematical theory of communication", Bell Syst. Tech. J. **27**, 379–423 (1948) (cit. on p. 2).

[19] W. K. Wootters and W. H. Zurek, "A single quantum cannot be cloned", Nature **299**, 802–803 (1982) (cit. on p. 4).

[20] J. S. Bell, "On the Einstein Podolsky Rosen paradox", Phys. Phys. Fizika **1**, 195–200 (1964) (cit. on p. 6).

[21] I. D. Ivonovic, "Geometrical description of quantal state determination", J. Phys. A: Math. Gen. **14**, 3241 (1981) (cit. on pp. 7, 205).

[22] W. K. Wootters and B. D. Fields, "Optimal state-determination by mutually unbiased measurements", Ann. Phys. **191**, 363–381 (1989) (cit. on pp. 7, 205).

[23] S. Brierley, S. Weigert, and I. Bengtsson, "All mutually unbiased bases in dimensions two to five", Quantum Info. Comput. **10**, 803–820 (2010) (cit. on pp. 7, 145).

[24] S. Designolle, P. Skrzypczyk, F. Fröwis, and N. Brunner, "Quantifying Measurement Incompatibility of Mutually Unbiased Bases", Phys. Rev. Lett. **122**, 050402 (2019) (cit. on p. 8).

[25] S. Wiesner, "Conjugate coding", SIGACT News **15**, 78–88 (1983) (cit. on p. 8).

[26] C. H. Bennett and G. Brassard, "Quantum cryptography: Public key distribution and coin tossing", Theor. Comput. Sci., Theoretical Aspects of Quantum Cryptography – celebrating 30 years of BB84 **560**, 7–11 (2014) (cit. on pp. 8, 10, 133).

[27] A. K. Ekert, "Quantum cryptography based on bell's theorem", Phys. Rev. Lett. **67**, 661–663 (1991) (cit. on p. 8).

[28] D. Mayers, “Unconditional security in quantum cryptography”, in Advances in cryptology — crypto ’96 (1996), pp. 343–357 (cit. on p. 8).
[29] D. Mayers, “Unconditional security in quantum cryptography”, J. ACM **48**, 351–406 (2001) (cit. on p. 8).
[30] D. Deutsch, A. K. Ekert, R. Jozsa, C. Macchiavello, S. Popescu, and A. Sanpera, “Quantum privacy amplification and the security of quantum cryptography”, Phys. Rev. Lett. **77**, 2818–2821 (1996) (cit. on p. 8).
[31] H.-K. Lo and H. F. Chau, “Unconditional security of quantum key distribution over arbitrarily long distances”, Science **283**, 2050–2056 (1999) (cit. on p. 8).
[32] P. W. Shor and J. Preskill, “Simple Proof of Security of the BB84 Quantum Key Distribution Protocol”, Phys. Rev. Lett. **85**, 441–444 (2000) (cit. on p. 8).
[33] K. Brádler, M. Mirhosseini, R. Fickler, A. Broadbent, and R. Boyd, “Finite-key security analysis for multilevel quantum key distribution”, New J. Phys. **18**, 073030 (2016) (cit. on pp. 8, 19, 133, 137).
[34] G. S. Vernam, “Cipher printing telegraph systems: For secret wire and radio telegraphic communications”, J. Am. Inst. Electr. Eng. **45**, 109–115 (1926) (cit. on p. 9).
[35] C. E. Shannon, “Communication theory of secrecy systems”, Bell Syst. Tech. J. **28**, 656–715 (1949) (cit. on p. 9).
[36] I. Csiszar and J. Korner, “Broadcast channels with confidential messages”, IEEE Trans. Inf. Theory **24**, 339–348 (1978) (cit. on p. 16).
[37] N. Wyderka, G. Chesi, H. Kampermann, C. Macchiavello, and D. Bruß, “High-dimensional quantum key distribution rates for multiple measurement bases”, 2025, arXiv:2501.05890 [quant-ph], pre-published (cit. on pp. 19, 21, 133, 137, 139).
[38] D. Bruß, “Optimal eavesdropping in quantum cryptography with six states”, Phys. Rev. Lett. **81**, 3018–3021 (1998) (cit. on p. 19).
[39] H. Bechmann-Pasquinucci and N. Gisin, “Incoherent and coherent eavesdropping in the six-state protocol of quantum cryptography”, Phys. Rev. A **59**, 4238–4248 (1999) (cit. on p. 19).
[40] R. Y. Q. Cai and V. Scarani, “Finite-key analysis for practical implementations of quantum key distribution”, New J. Phys. **11**, 045024 (2009) (cit. on pp. 21, 139).
[41] W.-Y. Hwang, “Quantum Key Distribution with High Loss: Toward Global Secure Communication”, Phys. Rev. Lett. **91**, 057901 (2003) (cit. on pp. 22, 139).
[42] Z. Y. Ou and Y. J. Lu, “Cavity enhanced spontaneous parametric down-conversion for the prolongation of correlation time between conjugate photons”, Phys. Rev. Lett. **83**, 2556–2559 (1999) (cit. on pp. 25, 72).
[43] Z. Xie, T. Zhong, S. Shrestha, X. A. Xu, J. Liang, Y. X. Gong, J. C. Bienfang, A. Restelli, J. H. Shapiro, F. N. Wong, and C. W. Wong, “Harnessing high-

dimensional hyperentanglement through a biphoton frequency comb", Nat. Photonics **9**, 536–542 (2015) (cit. on pp. 25, 72).

[44] C. Bernhard, B. Bessire, T. Feurer, and A. Stefanov, "Shaping frequency-entangled qudits", Phys. Rev. A **88**, 032322 (2013) (cit. on pp. 25, 72).

[45] F. Graffitti, P. Barrow, A. Pickston, A. M. Brańczyk, and A. Fedrizzi, "Direct generation of tailored pulse-mode entanglement", Phys. Rev. Lett. **124**, 053603 (2020) (cit. on pp. 25, 72).

[46] R. B. Jin, R. Shimizu, M. Fujiwara, M. Takeoka, R. Wakabayashi, T. Yamashita, S. Miki, H. Terai, T. Gerrits, and M. Sasaki, "Simple method of generating and distributing frequency-entangled qudits", Quantum Sci. Technol. **1**, 015004 (2016) (cit. on pp. 25, 72).

[47] K.-C. Chang, X. Cheng, M. C. Sarihan, A. K. Vinod, Y. S. Lee, T. Zhong, Y. X. Gong, Z. Xie, J. H. Shapiro, F. N. Wong, and C. W. Wong, "648 Hilbert-space dimensionality in a biphoton frequency comb: entanglement of formation and Schmidt mode decomposition", npj Quantum Inf. **7** (2021) (cit. on pp. 25, 72).

[48] B. Brecht, A. Eckstein, R. Ricken, V. Quiring, H. Suche, L. Sansoni, and C. Silberhorn, "Demonstration of coherent time-frequency Schmidt mode selection using dispersion-engineered frequency conversion", Phys. Rev. A **90**, 1–5 (2014) (cit. on pp. 25, 33, 72, 94, 95).

[49] V. Ansari, J. M. Donohue, M. Allgaier, L. Sansoni, B. Brecht, J. Roslund, N. Treps, G. Harder, and C. Silberhorn, "Tomography and Purification of the Temporal-Mode Structure of Quantum Light", Phys. Rev. Lett. **120**, 213601 (2018) (cit. on pp. 25, 28, 94).

[50] H.-H. Lu, J. M. Lukens, N. A. Peters, O. D. Odele, D. E. Leaird, A. M. Weiner, and P. Lougovski, "Electro-optic frequency beam splitters and tritters for high-fidelity photonic quantum information processing", Phys. Rev. Lett. **120**, 030502 (2018) (cit. on pp. 25, 72, 94).

[51] I. Vagniluca, B. Da Lio, D. Rusca, D. Cozzolino, Y. Ding, H. Zbinden, A. Zavatta, L. K. Oxenløwe, and D. Bacco, "Efficient Time-Bin Encoding for Practical High-Dimensional Quantum Key Distribution", Phys. Rev. Applied **14**, 1 (2020) (cit. on pp. 25, 28, 94).

[52] H.-h. Lu, N. A. Peters, A. M. Weiner, and J. M. Lukens, "Characterization of Quantum Frequency Processors", IEEE J. Select. Topics Quantum Electron. **29**, 1–14 (2023) (cit. on pp. 25, 94).

[53] K. J. Blow, R. Loudon, S. J. D. Phoenix, and T. J. Shepherd, "Continuum fields in quantum optics", Phys. Rev. A **42**, 4102–4114 (1990) (cit. on pp. 27, 28).

[54] C. Fabre and N. Treps, "Modes and states in quantum optics", Rev. Mod. Phys. **92**, 035005 (2020) (cit. on p. 27).

[55] G. C. Berkhout, M. P. Lavery, J. Courtial, M. W. Beijersbergen, and M. J. Padgett, "Efficient sorting of orbital angular momentum states of light", Phys. Rev. Lett. **105**, 8–11 (2010) (cit. on p. 28).

[56] K. Huang, H. Liu, S. Restuccia, M. Q. Mehmood, S. T. Mei, D. Giovannini, A. Danner, M. J. Padgett, J. H. Teng, and C. W. Qiu, "Spiniform phase-encoded metagratings entangling arbitrary rational-order orbital angular momentum", Light Sci Appl **7**, 17156–17157 (2018) (cit. on p. 28).

[57] M. Mirhosseini, O. S. Magaña-Loaiza, M. N. O'Sullivan, B. Rodenburg, M. Malik, M. P. Lavery, M. J. Padgett, D. J. Gauthier, and R. W. Boyd, "High-dimensional quantum cryptography with twisted light", New J. Phys. **17**, 1–12 (2015) (cit. on p. 28).

[58] J. M. Donohue, V. Ansari, J. Řeháček, Z. Hradil, B. Stoklasa, M. Paúr, L. L. Sánchez-Soto, and C. Silberhorn, "Quantum-Limited Time-Frequency Estimation through Mode-Selective Photon Measurement", Phys. Rev. Lett. **121**, 1–6 (2018) (cit. on pp. 28, 169).

[59] M. G. Raymer and I. A. Walmsley, "Temporal modes in quantum optics: Then and now", Phys. Scr. **95**, 064002 (2020) (cit. on pp. 28, 29).

[60] L. Serino, C. Eigner, B. Brecht, and C. Silberhorn, "Programmable time-frequency mode-sorting of single photons with a multi-output quantum pulse gate", Opt. Express **33**, 5577 (2025) (cit. on pp. 31, 194).

[61] R. W. Boyd, edited by R. W. Boyd, Fourth Edition (Academic Press, 2020), pp. 1–64 (cit. on pp. 33, 47, 50).

[62] M. Santandrea, "Design of nonlinear integrated devices for quantum optics applications", PhD thesis (2019) (cit. on pp. 33, 49).

[63] B. Brecht, "Engineering ultrafast quantum frequency conversion", PhD thesis (2014) (cit. on pp. 34–37, 95).

[64] A. Christ, B. Brecht, W. Mauerer, and C. Silberhorn, "Theory of quantum frequency conversion and type-II parametric down-conversion in the high-gain regime", New J. Phys. **15**, 053038 (2013) (cit. on p. 35).

[65] N. Quesada and J. E. Sipe, "Why you should not use the electric field to quantize in nonlinear optics", Opt. Lett. **42**, 3443 (2017) (cit. on p. 35).

[66] E. Schmidt, "Zur Theorie der linearen und nichtlinearen Integralgleichungen", Math. Ann. **63**, 433–476 (1907) (cit. on p. 39).

[67] H. Everett, ""Relative State" Formulation of Quantum Mechanics", Rev. Mod. Phys. **29**, 454–462 (1957) (cit. on p. 39).

[68] A. Ekert and P. L. Knight, "Entangled quantum systems and the Schmidt decomposition", Am. J. Phys. **63**, 415–423 (1995) (cit. on p. 39).

[69] C. K. Law, I. A. Walmsley, and J. H. Eberly, "Continuous frequency entanglement: Effective finite hilbert space and entropy control", Phys. Rev. Lett. **84**, 5304–5307 (2000) (cit. on pp. 39, 74).

[70] T. Tamir, ed., *Guided-wave optoelectronics*, 1st, Vol. 26, Springer Series in Electronics and Photonics (Springer-Verlag, Berlin, Heidelberg, 1988) (cit. on p. 43).

[71] D. Marcuse, *Theory of dielectric optical waveguides*, 2nd (Academic Press, San Diego, 1991) (cit. on p. 43).

[72] D. Smirnova and Y. S. Kivshar, "Multipolar nonlinear nanophotonics", Optica **3**, 1241–1255 (2016) (cit. on p. 47).

[73] B. Sain, C. Meier, and T. Zentgraf, "Nonlinear optics in all-dielectric nanoantennas and metasurfaces: a review", Adv. Photonics **1**, 024002 (2019) (cit. on p. 47).

[74] D. Zhu, L. Shao, M. Yu, R. Cheng, B. Desiatov, C. J. Xin, Y. Hu, J. Holzgrafe, S. Ghosh, A. Shams-Ansari, E. Puma, N. Sinclair, C. Reimer, M. Zhang, and M. Lončar, "Integrated photonics on thin-film lithium niobate", Adv. Opt. Photon. **13**, 242 (2021) (cit. on p. 47).

[75] M. Houde, L. Beaudoin, K. Hirota, R. Nehra, and N. Quesada, "Ultrashort-pulse-pumped, single-mode type-0 squeezers in lithium niobate nanophotonics", (2024), pre-published (cit. on p. 47).

[76] A. B. U'Ren, C. Silberhorn, K. Banaszek, I. A. Walmsley, R. Erdmann, W. P. Grice, and M. G. Raymer, "Generation of pure-state single-photon wavepackets by conditional preparation based on spontaneous parametric downconversion", Laser Physics **15**, 146–161 (2005) (cit. on p. 50).

[77] D. S. Hum and M. M. Fejer, "Quasi-phasematching", C. R. Phys. **8**, 180–198 (2007) (cit. on p. 52).

[78] T. F. Weiss and A. Peruzzo, "Nonlinear domain engineering for quantum technologies", Appl. Phys. Rev. **12**, 011318 (2025) (cit. on p. 52).

[79] M. H. Chou, K. R. Parameswaran, M. M. Fejer, and I. Brener, "Multiple-channel wavelength conversion by use of engineered quasi-phase-matching structures in LiNbO_3 waveguides", Opt. Lett. **24**, 1157 (1999) (cit. on pp. 52, 54, 94).

[80] M. Silver, Y. P. Huang, C. Langrock, M. M. Fejer, P. Kumar, and G. S. Kanter, "Three-Signal Temporal-Mode Selective Upconversion Demultiplexing", IEEE Photon. Technol. Lett. **31**, 1749–1752 (2019) (cit. on pp. 54, 94).

[81] A. M. Brańczyk, A. Fedrizzi, T. M. Stace, T. C. Ralph, and A. G. White, "Engineered optical nonlinearity for quantum light sources", Opt. Express **19**, 55 (2011) (cit. on pp. 54, 56).

[82] M. Asobe, O. Tadanaga, H. Miyazawa, Y. Nishida, and H. Suzuki, "Multiple quasi-phase-matched device using continuous phase modulation of $\chi^{(2)}$ grating and its application to variable wavelength conversion", IEEE J. Quantum Electron. **41**, 1540–1547 (2005) (cit. on p. 54).

[83] N. Quesada and A. M. Brańczyk, "Gaussian functions are optimal for waveguided nonlinear-quantum-optical processes", Phys. Rev. A **98**, 043813 (2018) (cit. on p. 56).

[84] P. B. Dixon, J. H. Shapiro, and F. N. C. Wong, "Spectral engineering by Gaussian phase-matching for quantum photonics", Opt. Express **21**, 5879–5890 (2013) (cit. on p. 56).

[85] A. Dosseva, Ł. Cincio, and A. M. Brańczyk, "Shaping the joint spectrum of down-converted photons through optimized custom poling", Phys. Rev. A **93**, 1–7 (2016) (cit. on p. 56).

[86] J.-L. Tambasco, A. Boes, L. G. Helt, M. J. Steel, and A. Mitchell, "Domain engineering algorithm for practical and effective photon sources", Opt. Express **24**, 19616 (2016) (cit. on p. 56).

[87] K. Liu, C. R. Ye, S. Khan, and V. J. Sorger, "Review and perspective on ultrafast wavelength-size electro-optic modulators", Laser Photonics Rev. **9**, 172–194 (2015) (cit. on p. 62).

[88] G. Sinatkas, T. Christopoulos, O. Tsilipakos, and E. E. Kriezis, "Electro-optic modulation in integrated photonics", J. Appl. Phys. **130**, 010901 (2021) (cit. on p. 62).

[89] A. M. Weiner, "Femtosecond pulse shaping using spatial light modulators", Rev. Sci. Instrum. **71**, 1929–1960 (2000) (cit. on pp. 62, 66).

[90] A. Monmayrant, S. Weber, and B. Chatel, "A newcomer's guide to ultrashort pulse shaping and characterization", J. Phys. B: At. Mol. Opt. Phys. **43** (2010) (cit. on pp. 62, 66).

[91] J. C. Vaughan, T. Hornung, T. Feurer, and K. A. Nelson, "Diffraction-based femtosecond pulse shaping with a two-dimensional spatial light modulator", Opt. Lett. **30**, 323 (2005) (cit. on pp. 62, 66).

[92] E. Frumker and Y. Silberberg, "Phase and amplitude pulse shaping with two-dimensional phase-only spatial light modulators", J. Opt. Soc. Am. B **24**, 2940–2947 (2007) (cit. on p. 62).

[93] M. M. Wefers and K. A. Nelson, "Analysis of programmable ultrashort waveform generation using liquid-crystal spatial light modulators", J. Opt. Soc. Am. B **12**, 1343–1362 (1995) (cit. on p. 67).

[94] V. Ansari, E. Roccia, M. Santandrea, M. Doostdar, C. Eigner, L. Padberg, I. Gianani, M. Sbroscia, J. M. Donohue, L. Mancino, et al., "Heralded generation of high-purity ultrashort single photons in programmable temporal shapes", Opt. Express **26**, 2764–2774 (2018) (cit. on p. 72).

[95] L. Serino, J. Gil-Lopez, M. Stefszky, R. Ricken, C. Eigner, B. Brecht, and C. Silberhorn, "Realization of a multi-output quantum pulse gate for decoding high-dimensional temporal modes of single-photon states", PRX Quantum **4**, 020306 (2023) (cit. on pp. 72, 166, 194).

[96] P. C. Humphreys, B. J. Metcalf, J. B. Spring, M. Moore, X.-M. Jin, M. Barbieri, W. S. Kolthammer, and I. A. Walmsley, "Linear optical quantum computing in a single spatial mode", Phys. Rev. Lett. **111**, 150501 (2013) (cit. on p. 72).

[97] H.-H. Lu, J. M. Lukens, N. A. Peters, B. P. Williams, A. M. Weiner, and P. Lougovski, "Quantum interference and correlation control of frequency-bin qubits", Optica **5**, 1455–1460 (2018) (cit. on p. 72).

[98] C. L. Morrison, F. Graffitti, P. Barrow, A. Pickston, J. Ho, and A. Fedrizzi, "Frequency-bin entanglement from domain-engineered down-conversion", APL Photonics **7**, 066102 (2022) (cit. on p. 72).

[99] F. Chiriano, J. Ho, C. L. Morrison, J. W. Webb, A. Pickston, F. Graffitti, and A. Fedrizzi, "Hyper-entanglement between pulse modes and frequency bins", Opt. Express **31**, 35131–35142 (2023) (cit. on p. 72).

[100] M. A. Finger, N. Y. Joly, P. S. J. Russell, and M. V. Chekhova, "Characterization and shaping of the time-frequency schmidt mode spectrum of bright twin beams generated in gas-filled hollow-core photonic crystal fibers", Phys. Rev. A **95**, 053814 (2017) (cit. on p. 72).

[101] N. B. Lingaraju, H.-H. Lu, S. Seshadri, P. Imany, D. E. Leaird, J. M. Lukens, and A. M. Weiner, "Quantum frequency combs and hong–ou–mandel interferometry: the role of spectral phase coherence", Opt. Express **27**, 38683 (2019) (cit. on p. 72).

[102] G. Maltese, M. I. Amanti, F. Appas, G. Sinnl, A. Lemaître, P. Milman, F. Baboux, and S. Ducci, "Generation and symmetry control of quantum frequency combs", npj Quantum Inf. **6** (2020) (cit. on p. 72).

[103] H.-H. Lu, M. Liscidini, A. L. Gaeta, A. M. Weiner, and J. M. Lukens, "Frequency-bin photonic quantum information", Optica **10**, 1655 (2023) (cit. on p. 72).

[104] A. Christ, C. Lupo, M. Reichelt, T. Meier, and C. Silberhorn, "Theory of filtered type-ii parametric down-conversion in the continuous-variable domain: quantifying the impacts of filtering", Phys. Rev. A **90**, 023823 (2014) (cit. on p. 72).

[105] E. Meyer-Scott, N. Montaut, J. Tiedau, L. Sansoni, H. Herrmann, T. J. Bartley, and C. Silberhorn, "Limits on the heralding efficiencies and spectral purities of spectrally filtered single photons from photon-pair sources", Phys. Rev. A **95**, 061803(R) (2017) (cit. on p. 72).

[106] L. Mandel and E. Wolf, *Optical coherence and quantum optics* (Cambridge University Press, Cambridge, 1995) (cit. on p. 76).

[107] W. Mauerer, M. Avenhaus, W. Helwig, and C. Silberhorn, "How colors influence numbers: Photon statistics of parametric down-conversion", Phys. Rev. A **80**, 053815 (2009) (cit. on p. 76).

[108] A. Christ, K. Laiho, A. Eckstein, K. N. Cassemiro, and C. Silberhorn, "Probing multimode squeezing with correlation functions", New J. Phys. **13**, 033027 (2011) (cit. on p. 76).

[109] K. Dekkers, L. Serino, N. D'Alessandro, A. Bhattacharjee, B. Brecht, A. Tavoli, C. Silberhorn, and J. Leach, "Observing High-dimensional Nonlocality using Multi-Outcome Spectral Measurements", 2025, arXiv:2506.20796 [quant-ph], pre-published (cit. on pp. 77, 78, 194).

[110] D. Collins, N. Gisin, N. Linden, S. Massar, and S. Popescu, "Bell inequalities for arbitrarily high-dimensional systems", Phys. Rev. Lett. **88**, 404041–404044 (2002) (cit. on p. 78).

[111] D. V. Reddy and M. G. Raymer, "High-selectivity quantum pulse gating of photonic temporal modes using all-optical Ramsey interferometry", Optica **5**, 423 (2018) (cit. on pp. 94, 95).

[112] A. Eckstein, B. Brecht, and C. Silberhorn, "A quantum pulse gate based on spectrally engineered sum frequency generation", Opt. Express **19**, 13770 (2011) (cit. on p. 95).

[113] D. V. Reddy, M. G. Raymer, and C. J. McKinstrie, "Efficient sorting of quantum-optical wave packets by temporal-mode interferometry", Opt. Lett. **39**, 2924–2927 (2014) (cit. on p. 95).

[114] D. V. Reddy, M. G. Raymer, and C. J. McKinstrie, "Sorting photon wave packets using temporal-mode interferometry based on multiple-stage quantum frequency conversion", Phys. Rev. A **91**, 012323 (2015) (cit. on p. 95).

[115] P. Folge, M. Stefszky, B. Brecht, and C. Silberhorn, "Harnessing Multi-output Quantum Pulse Gates", Phys. Rev. Appl. **10**, 1 (2024) (cit. on p. 99).

[116] J. S. Lundeen, A. Feito, H. Coldenstrodt-Ronge, K. L. Pregnell, C. Silberhorn, T. C. Ralph, J. Eisert, M. B. Plenio, and I. A. Walmsley, "Tomography of quantum detectors", Nat. Phys. **5**, 27–30 (2009) (cit. on p. 101).

[117] V. Ansari, G. Harder, M. Allgaier, B. Brecht, and C. Silberhorn, "Temporal-mode measurement tomography of a quantum pulse gate", Phys. Rev. A **96** (2017) (cit. on pp. 101, 166).

[118] M. Combescure, "Circulant matrices, Gauss sums and mutually unbiased bases. I: The prime number case.", Cubo **11**, 73–86 (2009) (cit. on pp. 103, 206).

[119] W. Heisenberg, "Uber den anschaulichen inhalt der quantentheoretischen kinematik und mechanik", Z. Phys. **42**, 172 (1927) (cit. on p. 144).

[120] W. Beckner, "Inequalities in fourier analysis", Ann. Math. **102**, 159 (1975) (cit. on p. 144).

[121] I. Białynicki-Birula and J. Mycielski, "Uncertainty relations for information entropy in wave mechanics", Commun. Math. Phys. **44**, 129 (1975) (cit. on p. 144).

[122] D. Deutsch, "Uncertainty in quantum measurements", Phys. Rev. Lett. **50**, 631 (1983) (cit. on p. 144).

[123] K. Kraus, "Complementary observables and uncertainty relations", Phys. Rev. D **35**, 3070 (1987) (cit. on p. 144).

[124] H. Maassen and J. B. M. Uffink, "Generalized entropic uncertinty relations", Phys. Rev. Lett. **60**, 1103 (1988) (cit. on pp. 144, 146).

[125] A. Riccardi, C. Macchiavello, and L. Maccone, "Tight entropic uncertainty relations for systems with dimension three to five", Phys. Rev. A **95**, 1–7 (2017) (cit. on pp. 144, 146).

[126] W.-Z. Yan, Y. Li, Z. Hou, H. Zhu, G.-Y. Xiang, C.-F. Li, and G.-C. Guo, "Experimental demonstration of inequivalent mutually unbiased bases", Phys. Rev. Lett. **132**, 080202 (2024) (cit. on p. 145).

[127] K. Banaszek, G. M. D'Ariano, M. G. A. Paris, and M. F. Sacchi, "Maximum-likelihood estimation of the density matrix", Phys. Rev. A **61**, 010304 (1999) (cit. on p. 166).

[128] R. T. Thew, K. Nemoto, A. G. White, and W. J. Munro, "Qudit quantum-state tomography", Phys. Rev. A **66**, 012303 (2002) (cit. on p. 166).

[129] Z. Hradil, "Quantum-State Estimation", Phys. Rev. A **55**, R1561–R1564 (1997) (cit. on p. 166).

[130] A. Bhattacharjee, P. Folge, L. Serino, J. Řeháček, Z. Hradil, C. Silberhorn, and B. Brecht, "Pulse characterization at the single-photon level through chronocyclic q-function measurements", Opt. Express **33**, 5551–5561 (2025) (cit. on pp. 166, 167, 195).

[131] D. Gross, Y.-K. Liu, S. T. Flammia, S. Becker, and J. Eisert, "Quantum state tomography via compressed sensing", Phys. Rev. Lett. **105**, 150401 (2010) (cit. on p. 166).

[132] D. Ahn, Y. S. Teo, H. Jeong, F. Bouchard, F. Hufnagel, E. Karimi, D. Koutný, J. Řeháček, Z. Hradil, G. Leuchs, and L. L. Sánchez-Soto, "Adaptive compressive tomography with no a priori information", Phys. Rev. Lett. **122**, 100404 (2019) (cit. on p. 166).

[133] J. Gil-Lopez, Y. S. Teo, S. De, B. Brecht, H. Jeong, C. Silberhorn, and L. L. Sánchez-Soto, "Universal Compressive Tomography In The Time-Frequency Domain", Optica **8**, 1296 (2021) (cit. on p. 166).

[134] M. Cooper, M. Karpiński, and B. J. Smith, "Local mapping of detector response for reliable quantum state estimation", Nat. Commun. **5**, 4332 (2014) (cit. on p. 166).

[135] C. Ferrie, "Self-guided quantum tomography", Phys. Rev. Lett. **113**, 2–6 (2014) (cit. on p. 166).

[136] R. J. Chapman, C. Ferrie, and A. Peruzzo, "Experimental demonstration of self-guided quantum tomography", Phys. Rev. Lett. **117**, 040402 (2016) (cit. on p. 166).

[137] M. Rambach, M. Qaryan, M. Kewming, C. Ferrie, A. G. White, and J. Romero, "Robust and Efficient High-Dimensional Quantum State Tomography", Phys. Rev. Lett. **126**, 100402 (2021) (cit. on p. 166).

[138] Z. Hou, J.-F. Tang, C. Ferrie, G.-Y. Xiang, C.-F. Li, and G.-C. Guo, "Experimental realization of self-guided quantum process tomography", Phys. Rev. A **101**, 022317 (2020) (cit. on p. 166).

[139] R. Trebino and D. J. Kane, "Using phase retrieval to measure the intensity and phase of ultrashort pulses: frequency-resolved optical gating", J. Opt. Soc. Am. A **10**, 1101–1111 (1993) (cit. on p. 167).

[140] K. DeLong, R. Trebino, J. Hunter, and W. White, "Frequency-resolved optical gating with the use of second-harmonic generation", J. Opt. Soc. Am. B **11**, 2206–2215 (1994) (cit. on p. 167).

[141] I. A. Walmsley and V. Wong, "Characterization of the electric field of ultrashort optical pulses", J. Opt. Soc. Am. B **13**, 2453–2463 (1996) (cit. on p. 167).

[142] C. Iaconis and I. A. Walmsley, "Spectral phase interferometry for direct electric-field reconstruction of ultrashort optical pulses", Opt. Lett. **23**, 792–794 (1998) (cit. on p. 167).

[143] W. Wasilewski, P. Kolenderski, and R. Frankowski, "Spectral density matrix of a single photon measured", Phys. Rev. Lett. **99**, 123601 (2007) (cit. on p. 167).

[144] A. O. Davis, V. Thiel, M. Karpiński, and B. J. Smith, "Measuring the single-photon temporal-spectral wave function", Phys. Rev. Lett. **121**, 083602 (2018) (cit. on p. 167).

[145] V. Thiel, A. O. C. Davis, K. Sun, P. D'Ornellas, X.-M. Jin, and B. J. Smith, "Single-photon characterization by two-photon spectral interferometry", Opt. Express **28**, 19315–19324 (2020) (cit. on p. 167).

[146] S. Kruse, L. Serino, P. Folge, D. E. Oviedo, A. Bhattacharjee, M. Stefszky, J. C. Scheytt, B. Brecht, and C. Silberhorn, "A Pulsed Lidar System with Ultimate Quantum Range Accuracy", IEEE Photon. Technol. Lett. **35**, 769–772 (2023) (cit. on pp. 169, 195).

[147] V. Ansari, B. Brecht, J. Gil-Lopez, J. M. Donohue, J. Řeháček, Z. Hradil, L. L. Sánchez-Soto, and C. Silberhorn, "Achieving the Ultimate Quantum Timing Resolution", PRX Quantum **2**, 1–8 (2021) (cit. on p. 169).

[148] L. Serino, W. Ridder, A. Bhattacharjee, J. Gil Lopez, B. Brecht, and C. Silberhorn, "Orchestrating time and color: a programmable source of high-dimensional entanglement", Optica Quantum **2**, 339–345 (2024) (cit. on p. 193).

[149] L. Serino, G. Chesi, B. Brecht, L. Maccone, C. Macchiavello, and C. Silberhorn, "Experimental entropic uncertainty relations in dimensions three to five", 2025, arXiv:2507.05025 [quant-ph], pre-published (cit. on p. 195).

[150] L. Serino, G. Chesi, B. Brecht, L. Maccone, C. Macchiavello, and C. Silberhorn, "Complementarity-based complementarity: the choice of mutually unbiased observables shapes quantum uncertainty relations", Phys. Rev. Res. **7**, 033152 (2025) (cit. on p. 195).

[151] L. Serino, M. Rambach, B. Brecht, J. Romero, and C. Silberhorn, "Self-guided tomography of time-frequency qudits", Quantum Sci. Technol. **10**, 025024 (2025) (cit. on p. 195).

Acknowledgments

Looking back on these years, I see how much this thesis came from countless conversations, shared ideas, and moments of support. My journey to this point would not have been possible without the many people who were part of it, and I am happy to finally have the chance to thank them here.

First and foremost, my deepest gratitude goes to my supervisor, Christine. Thank you for being an exceptional mentor, for teaching me not to be afraid to ask the "stupid questions", for trusting me with fascinating projects, and for giving me the freedom to explore my own ideas while providing the guidance to turn them into reality. I am also deeply grateful to my group leader, Benni, for being a constant reference, for his invaluable advice and support, and for always pushing me to be my best.

I owe a special thanks to those who were there through my first years in Paderborn. To Jano, for his contagious optimism and for patiently leading me into the exciting world of QPGs when I was just starting out. To Vahid, even though our paths crossed shortly, I am so glad you were there to help me with debugging. And to the "newbies", Franz, Dana, Patrick, and Federico: starting this journey with you was a lot of fun and made moving to a new country during a pandemic much less lonely. I will always think back to our adventures with a smile, especially to how we consistently ended up grilling in the rain or falling asleep in the back of a conference bus.

So many people made daily life in the office much brighter. I am grateful to Abhinandan for the constant exchanges from which I learned so much, and for trying to explain the rules of cricket (I still don't get it). And Patrick, you deserve a second mention here for sharing my enthusiasm for cool science, for the countless discussions that really made me enjoy working together, and for all the artistic counseling. To René, thank you for sharing my terrible sense of humor; you were the best lab co-dictator I could have ever wished for, and I am grateful you were always there to help me with brainstorming.

I am grateful for the "lunch crew"—Michael, Federico, Fabian, Ankita, Alejandra, and Cheeranjiv—for the fun chats that provided a much-needed break from work. Ankita also deserves a second mention for teaching me how to make kimchi. I

also want to thank Kai for always taking care of everyone, and for single-handedly increasing my tolerance for spicy food to the point that I now genuinely enjoy it. Thank you to our secretaries, especially Petra and Rita, for making the German bureaucracy bearable, for their patience every time I forgot to sign a form, and simply for being such wonderful people. Thank you to everyone in the group for creating such a wonderful and supportive atmosphere to work in.

This work would not have been possible without the support of our collaborators. I am especially grateful to Giovanni, Nikolai, Markus, and Kiki for the stimulating discussions and wonderful collaborations. A special thank you goes to Georg for going above and beyond to repair our laser.

Outside the lab, I am grateful for my friends, who were a constant source of happiness. Thank you to Michael, Marcello, Angelina, Tanya, and Jan for the countless fun board game nights and for the constant flow of snacks. My thanks also go to my "Italian" friends—Alessandra, Valeria, Alessandro, Sabrina, Erica, Christian, and Federico—for not letting the distance (or my terrible timing in replying to texts) separate us.

I would like to thank my family, for encouraging me to always pursue what I enjoyed and for believing I had the capabilities to do it.

Finally, my deepest gratitude goes to Matteo. Thank you for your love, support, and infinite patience in these years, and thank you for believing in me more than I ever believed in myself. I am so happy you were by my side through all of this.